THE UNIVERSITY *of* EDINBURGH

Gauge Fixed Gluonic Observables and Neutral Kaon Mixing on the Lattice

Renwick James Hudspith

Doctor of Philosophy
The University of Edinburgh
August 2013

Abstract

This thesis presents gauge fixed gluonic observable and neutral Kaon mixing matrix element measurements using nf=2+1 Domain Wall Fermion (DWF) configurations. These were generated with the Iwasaki gauge action by the RBC and UKQCD collaborations.

Results from the first measurement of the QCD strong coupling with these ensembles using the triple gluon vertex are shown. We find that while a very accurate measurement of the coupling is possible using this technique, the systematic error from the perturbative matching at current lattice scales is large. We also discuss the utilisation of this method as a probe for possible Technicolor theories.

The calculation of the QCD strong coupling constant from the triple gluon vertex required an implementation of a fast code to fix lattice gauge configurations. I provide details on my implementation of a parallel and optimised Fourier-accelerated algorithm for both Landau and Coulomb gauge fixing.

I include the first calculation of the highly accurate W0-scale using these ensembles, allowing for percent-level scale setting. I show results from a wide variety of smearing methods and present the first gluonic measurement of different smearing radii.

This thesis also details the first nf=2+1 measurement of the BSM neutral Kaon mixing renormalised matrix elements from lattice simulations with almost exact chiral symmetry in the valence sector and the sea.

Declaration

I declare that this thesis was composed by myself, that the work contained herein is my own except where explicitly stated otherwise in the text, and that this work has not been submitted for any other degree or professional qualification.

I have used throughout this work $16^3 \times 32 \times 16$, $24^3 \times 64 \times 16$ and $32^3 \times 64 \times 16$ nf=2+1 Flavor Domain Wall Fermion Iwasaki gauge ensembles generated by the RBC and UKQCD collaborations. And $32^3 \times 64$ and $48^3 \times 80$ SU(2) nf=2 Adjoint fermions, Wilson action ensembles generated by HiRep.

I have written a stand-alone, thread-parallel $SU(N_c)$-generic gauge fixing, smearing and two and three point gluonic correlator and vertex function measurement code which can be compiled into a library. All of the matrix operations and all algorithms used in the measurement of the triple gluon vertex, the production of smeared ensembles and the computation of the Wilson flow were generated using this code.

I performed one of two independent analyses of our measurement of $K_0 - \overline{K}_0$ mixing in and beyond the Standard Model, my analysis code was written using the UKHadron libraries which were principally developed by Peter Boyle. For the coarse ensemble of this analysis, my code was used to perform the Coulomb gauge fixing and I performed the contractions using UKHadron. The analysis for both of the methods to compute the QCD strong coupling were also written using the UKHadron libraries. I have produced and maintained several features in these libraries, including the incorporation of my own library.

Inversions and contractions to determine correlation functions were performed by the UKHadron and Columbia Physics System (CPS) libraries. The non-perturbative renormalisation matrices for the $K_0 - \overline{K}_0$ mixing analysis were computed by N.Garron and A.Lytle.

Parts of this work have been published in [43].

Parts of this work have been published in [18].

(*Renwick James Hudspith, August 2013*)

Acknowledgements

First I would like to thank my supervisor Peter Boyle for consistently useful advice. I would also like to thank collaborators L. del Debbio, R.Arthur, N. Garron, A.Lytle and S. Hashimoto for their help and patience. I would also like to thank the STFC for their funding.

Contents

List of Figures

List of Tables

Chapter 1

Introduction

This thesis aims to present several new measurements of quantities such as the strong coupling α_s, the Wilson flow parameter W_0 and matrix elements for neutral Kaon mixing in and beyond the Standard Model (SM) of particle physics. We perform these measurements using lattice field theory simulations with $N_f = 2+1$ Domain Wall Fermions (DWF). Within these measurements we investigate new strategies for improvement.

The strong coupling of non-abelian field theories α_s in the massless limit is the only free parameter of the theory and thus determines the physics. The value of the coupling at some scale must be determined experimentally. Theoretical predictions of measureable quantities such as cross-sections generally are expressed as a power series in terms of the coupling and so accurate determination of the coupling is vital for accurate theoretical predictions.

Lattice field theory allows for several evaluations of the coupling. In Chapter 3 we will evaluate it via the triple gluon vertex, which is computationally fast as long as a fast Landau gauge-fixing code is available. We will detail the implementation of our Fourier-Accelerated Landau gauge fixing code in Chapter 6, which was a vital step in our determination of the coupling. We require the gauge to be fixed so that we can use continuum perturbation theory results to relate our measurement to a scheme in which most results are quoted, that of $\overline{\text{MS}}$.

Our measurement of the coupling is the first performed using the ensembles generated by RBC/UKQCD [14]. We will investigate our determination in two different schemes, the exceptional ($\widetilde{\text{MOMgg}}$) [51] and the non-exceptional

(MOMggg) [98]. The measurement using the MOMggg scheme will be the first using the projector and matching of [98]. We will investigate the rôle Gribov copies (local minima of the gauge fixing functional) play in the evaluation, as well as investigating the required gauge fixing accuracy for our results.

We have also considered different definitions of the gauge fields away from the standard "Hermitian projection" by taking the exact logarithm of the $SU(N_c)$ link matrices to define the gauge fields, to this end we introduce a new method for taking the Logarithm exactly of link matrices as detailed in Appendix A. We will investigate the computational costs and possible benefits of using an exact field definition.

Link smearing is a useful technique for reducing the UV fluctuations of the gauge fields in dynamical simulations [73] and can be used for topological charge evaluations [14]. In Chapter 4, we start by showing that the general smearing transformation is a simple evaluation for the integration of the Wilson flow equation. We then illustrate the connection between different smearing transformations (APE, STOUT and LOG) and show their equivalence under a weak-field approximation. We then define perturbatively at leading order the smearing radius and provide a Landau gauge-fixed gluonic measurement of it to see whether a strongly coupled evaluation is comparable to the perturbative prediction.

We continue in Chapter 4 to discuss the Wilson flow, and its dimensionful parameter W_0. We discuss how the unphysical Wilson flow parameter $W(t)$ can be used to deduce the lattice scale (defined by the lattice spacing) of a simulation. We present the first measurement of the paramter W_0 using DWF simulations, and argue that the Wilson flow scale setting procedure can be used to obtain sub-percent lattice spacing evaluations. Such accuracy in determining the lattice spacing will be necessary in present and future simulations if percent-scale (and below) errors for measurements of physically important quantities such as the Kaon bag parameter B_K are to be achieved.

In the SM, neutral Kaons can change to anti-Kaons via the weak interaction. The Cabbibo-Kobayashi-Maskawa (CKM) [48, 112] matrix prescribes how quarks change their flavour whilst propagating and is a unitary 3×3 matrix, its elements are fundamental parameters of the standard model. The CKM matrix has a complex phase that allows for charge-parity (CP) symmetry breaking, a related parameter ϵ can be directly measured by experiment and compared to theoretical

predictions. The theoretical prediction for the quantity ϵ depends on perturbative terms plus a non-perturbative hadronic matrix element that can be computed using lattice techniques. This matrix element is directly related to the quantity B_K, and it is the error on B_K that is dominant for the theoretical uncertainties in ϵ. In Chapter 5 we will provide a determination of the SM bag parameter B_K as part of this thesis, as well as matrix elements that could appear in theories Beyond the Standard Model (BSM).

In the SM, Kaon mixing only occurs via the weak interaction. In possible BSM scenarios, different, heavy particles can cause this flavour changing of quarks. Just as in the SM, the effect of these particles can be split into perturbative and non-perturbative contributions. The perturbative part is model dependent but the non-perturbative part describes the low energy QCD physics and is model independent. The low energy matrix elements can be measured on the lattice, and with some assumptions can be used to constrain the scale of new physics.

In this thesis we measure the SM and BSM bag parameters, and arguably more importantly the ratios of the SM to BSM matrix elements, using DWF which have specific advantage over other fermion discretisations by having good chiral symmetry. In this work we provide the first continuum limit evaluation of the ratios and bag parameters using $N_f = 2 + 1$ dynamical DWF simulations.

Chapter 2

Background theory

The Lagrangian density for Minkowskian, strongly coupled, interacting gauge fields (with field strength tensor $F_{\mu\nu}(x)$) with "N_f" flavours of Dirac fermions ($\Psi(x)$) is,

$$\mathfrak{L}(x) = -\frac{1}{2}\mathrm{Tr}\left[F_{\mu\nu}(x)F^{\mu\nu}(x)\right] + \sum_{i}^{N_f} \bar{\Psi}^i(x)(i\gamma^\mu D_\mu - m^{(i)})\Psi^i(x). \tag{2.1}$$

Where $D_\mu = \partial_\mu + igA_\mu(x)$, $A_\mu(x)$ is our gauge field and g our theory's coupling strength. The field strength tensor is defined as,

$$F_{\mu\nu}(x) = \partial_\mu A_\nu(x) - \partial_\nu A_\mu(x) + ig\left[A_\mu(x), A_\nu(x)\right]. \tag{2.2}$$

For a four dimensional theory the action is $S(A_\mu, \Psi^i, \bar{\Psi}^i) = \int d^4x \mathfrak{L}(x)$. The path integral representation treats the theory as a statistical ensemble with weights of paths of particles given by the exponential of the action. Introducing the generating functional W for a single flavour of fermion,

$$W[\eta, \bar{\eta}, J] = \int \mathcal{D}A_\mu \mathcal{D}\Psi \mathcal{D}\bar{\Psi} e^{i\int d^4x \mathfrak{L} + J^\mu A_\mu + \bar{\eta}\Psi + \bar{\Psi}\eta}, \tag{2.3}$$

with source terms $\eta, \bar{\eta}, J^\mu$ and the integral is over all field paths. We can define a measurement of the (time ordered) observable $\mathcal{O}$ (normalised by the partition function Z) by functionally differentiating the generating functional (the indices

j, k and l are dependent on the operator),

$$\begin{aligned}\langle 0|\mathcal{O}|0\rangle &= \frac{1}{Z}\frac{\delta^j}{\delta J^j}\frac{\delta^k}{\delta \eta^k}\frac{\delta^l}{\delta \bar{\eta}^l}W[\eta,\bar{\eta},J]|_{J=\eta=\bar{\eta}=0},\\ &= \frac{1}{Z}\int \mathcal{D}A_\mu \prod_i^{N_f}\mathcal{D}\bar{\Psi}^i\mathcal{D}\Psi^i\mathcal{O}e^{iS(A_\mu,\bar{\Psi}^i,\Psi^i)},\\ Z &= \int \mathcal{D}A_\mu \prod_i^{N_f}\mathcal{D}\bar{\Psi}^i\mathcal{D}\Psi^i e^{iS(A_\mu,\bar{\Psi}^i,\Psi^i)}.\end{aligned} \tag{2.4}$$

The gauge and fermionic contributions to the path integral can be separated and the fermionic fields, being Grassmann variables can be integrated out giving the usual fermionic determinant (det) and exponential weight of just the gauge action,

$$\langle 0|\mathcal{O}|0\rangle = \frac{1}{Z}\int \mathcal{D}A_\mu \mathcal{O}\prod_i^{N_f}\det\left(i\gamma_\mu D_\mu + m^{(i)}\right)e^{iS(A_\mu)}. \tag{2.5}$$

We perform a Wick rotation to Euclidean space from Minkowski, we work with an imaginary time direction which alters the gamma matrices $\gamma_0^E = \gamma_0, \gamma_j^E = -i\gamma_j (j = 1, 2, 3)$ (from now on I will work in Euclidean space and drop the label E). This turns our path integral observable measurement into,

$$\langle 0|\mathcal{O}|0\rangle = \frac{1}{Z}\int \mathcal{D}A_\mu \mathcal{O}\prod_i^{N_f}\det\left(\gamma_\mu D_\mu + m^{(i)}\right)e^{-S(A_\mu)}. \tag{2.6}$$

This integral has infinite degrees of freedom and can only be treated by either perturbative expansion or numerical integration of a discretised and finite number of degrees of freedom. We move the theory onto a discrete space-time lattice which regularises the theory. The Euclidean generating functional (Eq.2.3) for one flavour of fermion becomes (where $M = (\gamma_\mu D_\mu + m)$),

$$W[J,\eta,\bar{\eta}] = \int \mathcal{D}A_\mu \det(M)\, e^{-S(A_\mu)-\int d^4x\, \bar{\eta}(M)^{-1}\eta + JA_\mu}. \tag{2.7}$$

The path integral can be computed using importance sampling, as the path integral only has a finite number of degrees of freedom. Our correlation function can be written as,

$$\langle \mathcal{O}\rangle = \lim_{N\to\infty}\frac{1}{N}\sum_{i=1}^{N}\mathcal{O}(i) + O\left(\frac{1}{\sqrt{N}}\right). \tag{2.8}$$

With $\mathcal{O}(i)$ being a randomly sampled value from the probability distribution of $\mathcal{O}$, this describes a Monte Carlo integration procedure.

Quark fields in the observable $\mathcal{O}$ are contracted together according to Wick's theorem, and will be equivalent to a product of propagators, $S = M^{-1}$. The probability distribution of our lattice fields is,

$$P(U) = \frac{1}{Z} e^{-S(A_\mu)} \prod_i^{N_f} \det(M^{(i)}). \tag{2.9}$$

Where U corresponds to the field of gauge links and M is the Dirac matrix. Both of which will be discussed below, suffice to say that including an unbiased estimate of the fermionic determinant in the importance sampling is by far the most expensive part of dynamical simulations, setting this determinant to 1 is called the quenched approximation.

An in depth discussion of the creation of gauge fields weighted with such a probability distribution is beyond the scope of this thesis. All computations performed in this thesis will be dynamical configurations generated with the (Rational) Hybrid Monte Carlo algorithm (r)hmc [57, 71], which generates a sequence of gluonic configurations in a Markov chain that importance samples the path integral. This chain introduces a fictitious Monte Carlo time, it is with this index that we use to identify configurations.

The gauge theory of $SU(3)$ with $N_f = 6$, is what we call Quantum Chromodynamics (QCD). There is a large mass hierarchy in this theory between the heaviest quark (the Top) and the lightest (the Up and the Down), this means that for simulations of QCD with energy around that of the fourth quark mass, the Charm ($\approx 1.6GeV$) and $N_f = 2 + 1$ i.e. two light degenerate quarks (the up and the down) and one heavy (the strange) has to a good approximation the same physics as that of fully-fledged QCD.

2.1 Lattice gauge fields

Our discretised lattice is a set of fields which may live on the lattice "sites" or between sites on "links" depending on their spin. Gauge fields ($A_\mu\left(x + a\frac{\hat{\mu}}{2}\right)$) on the lattice are encoded via their parallel transport matrices ($U_\mu\left(x + a\frac{\hat{\mu}}{2}\right)$) between neighbouring sites and are the links, as in the equation (where a is the theory's

lattice spacing, i.e. the distance between the sites, and g_0 is the theory's bare interaction strength),

$$U_\mu\left(x + a\frac{\hat{\mu}}{2}\right) = e^{iag_0 A_\mu\left(x + a\frac{\hat{\mu}}{2}\right)}. \tag{2.10}$$

The links exist in the Lie group, $U_\mu\left(x + a\frac{\hat{\mu}}{2}\right) \in SU(N_c)$. And the fields are in the Lie algebra $A_\mu\left(x + a\frac{\hat{\mu}}{2}\right) \in \mathfrak{su}(N_c)$. The gauge fields are usually periodic in Euclidean space-time, $A_\mu(L_\mu + a\frac{\hat{\mu}}{2}) = A_\mu(a\frac{\hat{\mu}}{2})$.

The gauge fields, as Lie matrices, can be decomposed as $A_\mu\left(x + a\frac{\hat{\mu}}{2}\right) = T^a A_\mu\left(x + a\frac{\hat{\mu}}{2}\right)^a$, where the T's are the $N_c^2 - 1$ generators of the group. Throughout this work we use the following conventions for generic $SU(N_c)$ matrices in the fundamental representation,

$$\begin{aligned} A &= A^a T^a, \\ \mathrm{Tr}\left[T^a T^b\right] &= \frac{1}{2}\delta^{ab}, \\ \left[T^a, T^b\right] &= i f^{abc} T^c, \\ \left\{T^a, T^b\right\} &= d^{abc} T^c + \frac{1}{N_c}\delta^{ab}. \end{aligned} \tag{2.11}$$

Following these rules, if one wishes to compute the antisymmetric structure function f^{abc} or the symmetric d^{abc}, one uses,

$$\begin{aligned} f^{abc} &= -2i\mathrm{Tr}\left[[T^a, T^b]T^c\right], \\ d^{abc} &= 2\mathrm{Tr}\left[\{T^a, T^b\}T^c\right]. \end{aligned} \tag{2.12}$$

Following the discussion on importance sampling for the path integral, we wish to weight our gauge fields exponentially by the gauge action. The simplest gauge action $S(A_\mu)$, first introduced in lattice gauge theories by Wilson [156] is defined by,

$$S(A_\mu) = \frac{\beta}{2N_c}\sum_{x,\nu\neq\mu} 1 - \Re\left(\mathrm{Tr}\left[P_{\mu\nu}(x)\right]\right). \tag{2.13}$$

The parameter β is the bare coupling strength $\beta = \frac{2N_c}{g_0^2}$, and the plaquette term $(P_{\mu\nu}(x))$ [1] being defined as the 1×1 reverse-oriented Wilson loop,

$$P_{\mu\nu}(x)^\dagger = U_\mu(x + a\hat{\mu}/2)U_\nu(x + a\hat{\mu} + a\hat{\nu}/2)U_\mu(x + a\hat{\nu} + a\hat{\mu}/2)^\dagger U_\nu(x + a\hat{\nu}/2)^\dagger. \tag{2.14}$$

The plaquette is the smallest gauge invariant quantity measurable on the lattice.

[1] I have used the notation of Chapter 4 (i.e. labelling the reverse oriented plaquette as $P_{\mu\nu}(x)$) for consistency.

Upon expansion of the exponential in powers of a and using the Baker Campbell Hausdorff (BCH) [104] relation (and ignoring any higher order commutators/powers of ag_0 beyond leading order) we find,

$$e^b e^c e^d e^e = \exp\left(b + c + d + e + \frac{1}{2}\left\{[b,c] + [d,e] + [b,d] + [c,d] + [b,e] + [c,e]\right\}\right). \tag{2.15}$$

We perform a shift $x' = x - a\frac{\hat{\mu}}{2} - a\frac{\hat{\nu}}{2}$, to define the variables,

$$\begin{aligned} b &= iag_0 A_\mu\left(x' - a\frac{\hat{\nu}}{2}\right), \qquad c = iag_0 A_\nu\left(x' + a\frac{\hat{\mu}}{2}\right), \\ d &= -iag_0 A_\mu\left(x' + a\frac{\hat{\nu}}{2}\right), \qquad e = -iag_0 A_\nu\left(x' - a\frac{\hat{\mu}}{2}\right). \end{aligned} \tag{2.16}$$

Upon defining the symmetric finite difference,

$$a\Delta_\mu A_\mu(x') = A_\mu\left(x' + a\frac{\hat{\mu}}{2}\right) - A_\mu\left(x' - a\frac{\hat{\mu}}{2}\right), \tag{2.17}$$

we obtain the expansion of the plaquette,

$$P_{\mu\nu}(x)^\dagger = 1 + ia^2 g_0\left(\Delta_\mu A_\nu(x') - \Delta_\nu A_\mu(x')\right) - a^2 g_0^2\left[A_\mu(x'), A_\nu(x')\right] + O(a^3). \tag{2.18}$$

The relation between the plaquette and the field strength tensor is (where we have re-shifted the x),

$$P_{\mu\nu}(x)^\dagger = e^{ia^2 g_0\left(F_{\mu\nu}\left(x + a\frac{\hat{\mu}}{2} + a\frac{\hat{\nu}}{2}\right) + O(a)\right)}. \tag{2.19}$$

The field strength tensor in some sense lives in the centre of the plaquette. To lowest order, we have the famous connection between the Wilson gauge action and the continuum gauge field action [156],

$$S(A_\mu) = -\frac{\beta}{2N_c} a^4 g_0^2 \sum_{x',\nu\neq\mu} \mathrm{Tr}\left[F_{\mu\nu}(x')F_{\mu\nu}(x')\right]. \tag{2.20}$$

The Wilson plaquette gauge action is not the only possibility, various others have been suggested that add an extra 2×1 rectangular term to cancel or mitigate higher order contributions in Eq.2.19. Some of the available options are the tree level improved Symanzik[60], the Iwasaki [132] and the DBW2 [152]. These will be discussed in Chapter 4 in the context of link smearing.

It is often the best idea to describe lattice objects in terms of their dimensionless counterparts which are the variables in computer programs, e.g. $A_\mu\left(x + a\frac{\hat{\mu}}{2}\right) = ag_0 A_\mu\left(x + a\frac{\hat{\mu}}{2}\right)$, $U_\mu\left(x + a\frac{\hat{\mu}}{2}\right) = e^{iA_\mu\left(x + a\frac{\hat{\mu}}{2}\right)}$. This is the notation we will use from now on.

2.2 Lattice fermions

The continuum fermionic contribution of one fermion, to the action is (in $N_d = 4$ dimensions) $S_f = \int d^4x \bar{\Psi}(x)(\gamma_\mu \partial_\mu + m)\Psi(x)$. Naïvely this can be put into a discretised theory by turning the derivative into a symmetric finite difference and thus defining the Dirac matrix M [63].

2.2.1 Naïve fermions

The naïve fermionic discretised action can be written for a single fermion of mass m, as (where roman indices are site indexes and Greek indices are spin),

$$\begin{aligned} S_f &= \sum_{xy;\alpha\beta} \bar{\Psi}^\alpha(x) M^{\alpha\beta}(x,y) \Psi^\beta(y), \\ M^{\alpha\beta}(x,y) &= \frac{1}{2a} \sum_\mu \left((\gamma_\mu)^{\alpha\beta} \delta_{x+a\mu,y} - (\gamma_\mu)^{\alpha\beta} \delta_{x-a\mu,y} \right) + m\delta_{x,y}\delta_{\alpha,\beta} \end{aligned} \tag{2.21}$$

The fermions hereon considered, will be periodic in the spatial directions and anti-periodic in the temporal direction.

Upon taking the Fourier transform, we have,

$$\begin{aligned} \tilde{M}(p,q) &= \frac{1}{V} \sum_{x,y} e^{ip_\mu x_\mu} M(x,y) e^{iq_\mu y_\mu} = \delta_{p,q} \tilde{M}(p), \\ \tilde{M}(p,q) &= \frac{1}{V} \sum_{x,y} e^{ip_\mu x_\mu} e^{iq_\mu y_\mu} \left(m + \frac{1}{a} \sum_\mu \gamma_\mu \sin(p_\mu) \right), \\ \tilde{M}(p) &= \left(m + \frac{1}{a} \sum_\mu \gamma_\mu \sin(p_\mu) \right). \end{aligned} \tag{2.22}$$

$\tilde{M}(p)$ is our inverse propagator. Dropping the mass term for simplicity, we associate poles in the propagator (i.e. times when $\sum_\mu \gamma_\mu \sin(p_\mu) = 0$) as on shell states and have the unavoidable conclusion that there is the physical pole at p=(0,0,0,0) and 15 others[2], these come from all of the corners of the first Brillouin zone (BZ). These states can be pair produced in an interacting theory and so will affect the dynamics.

The continuum Lagrangian for fermions is invariant under the local gauge transformations (where $g(x) \in SU(N_c)$),

$$\Psi(x) = g(x)\Psi(x) \qquad \bar{\Psi}(x) = \bar{\Psi}(x) g(x)^\dagger. \tag{2.23}$$

[2]For example the $(-\Pi, 0, 0, 0)$ and its four Bose-symmetry equivalents will contribute.

This has to be preserved in our discretised theory and the derivatives in the discrete fermion action have terms $\bar{\Psi}(x)\Psi(x+\mu)$, which are not gauge invariant. To make it so, we must insert the parallel transport matrices between the quark sites. The combination $\bar{\Psi}(x)U_\mu\left(x+a\frac{\hat{\mu}}{2}\right)\Psi(x+a\hat{\mu})$ is now the correct, gauge invariant quantity. Inserting this into the naïve fermion action gives the interacting, naïve fermion action,

$$\begin{aligned} S_f = \sum_x m\bar{\Psi}(x)\Psi(x)+ \\ \frac{1}{2a}\sum_{x,\mu}\left(\bar{\Psi}(x)\gamma_\mu U_\mu\left(x+a\frac{\hat{\mu}}{2}\right)\Psi(x+a\hat{\mu}) - \bar{\Psi}(x)\gamma_\mu U_\mu\left(x-a\frac{\hat{\mu}}{2}\right)^\dagger\Psi(x-a\hat{\mu})\right). \end{aligned} \tag{2.24}$$

2.2.2 Wilson fermions

One way to eliminate the unphysical modes in the naïve action is by using the Wilson action [156], whereby an irrelevant operator is added so that the extra zeros of the naïve prescription pick up an additional factor proportional to a^{-1}. The modification to our naïve action is to add the term,

$$S_W = -\frac{1}{2a}\sum_{x,\mu}\bar{\Psi}(x)\left(U_\mu\left(x+a\frac{\hat{\mu}}{2}\right)\Psi(x+a\hat{\mu}) - 2\Psi(x) + U_\mu\left(x-a\frac{\hat{\mu}}{2}\right)^\dagger\Psi(x-a\hat{\mu})\right). \tag{2.25}$$

The fermionic matrix to invert for the updating of gauge fields using the Wilson action (i.e. incorporating the naïve discretisation and the Wilson term) is (omitting spin indices),

$$\begin{aligned} M(x,y) = (4+m)\delta_{x,y} - \frac{1}{2a}\sum_{\mu=1}^{4}\Bigg((1-\gamma_\mu)U_\mu\left(x+a\frac{\hat{\mu}}{2}\right)\delta_{x+a\hat{\mu},y} \\ + (1+\gamma_\mu)U_\mu\left(x-a\frac{\hat{\mu}}{2}\right)^\dagger\delta_{x-a\hat{\mu},y}\Bigg). \end{aligned} \tag{2.26}$$

The addition of the Wilson term means that chiral symmetry is explicitly broken for this action [63, 127]. This is a serious problem for the computation of weak matrix elements where the couplings to weak gauge bosons are chirally symmetric, and for other objects that depend on chirality. For the case of weak matrix elements, which can have additional operator mixings that do not arise in the continuum calculation due to the discretisation of the fermion action.

One of the aspects of this work is to compute matrix elements, for this we should use a chirally-symmetric action (or a very good approximation to one). We now introduce the Domain Wall Fermion action, which will be used throughout this thesis and which has good chiral symmetry properties. As an aside, "twisted mass" [83] simulations are

performed by adding a term to the Wilson action which is a rotation in the flavour space of the theory i.e. $S_{tm} = S_f + S_W + \sum_{x,\mu} \bar{\Psi}(x) i\mu\gamma_5\sigma^3\Psi(x)$ where σ^3 is a Pauli matrix, this extra term acts on the u, d doublet. This action does not preserve chiral symmetry but does remove most of the difficulty in renormalising chiral matrix elements such as those for B_K.

2.2.3 Domain Wall Fermions

To reproduce the continuum, chiral behaviour, our action must satisfy the Ginsparg-Wilson relation [91],

$$\gamma_5 D + D\gamma_5 = aD\gamma_5 D. \tag{2.27}$$

Where D is the lattice Dirac operator. This is then associated with the lattice variant of the continuum local chiral symmetry transformation,

$$\Psi(x)' = \exp\left\{i\alpha\left(1 - a\frac{D}{2}\right)\right\}\Psi(x). \tag{2.28}$$

The Domain Wall Fermion (DWF)[3] action utilises the idea that a chiral four dimensional lattice gauge theory could exist as the low energy effective limit of a five dimensional gauge theory [111] with index s and five-dimensional length L_s, coupled to five dimensional fermions. The corresponding 4D effective theory has been proven to satisfy the Ginsparg-Wilson relation (Eq.2.27), after the subtraction of the Pauli-Villars fields the usual DWF propagator is chirally symmetric in the $L_s \to \infty$ limit.

The non-interacting (infinite L_s) Euclidean continuum fermionic Lagrangian for such a theory can be written (after separating the 4D and 5D components),

$$\mathfrak{L}(x) = \bar{\Psi}(x,s)\left(\gamma_\mu\partial_\mu + \gamma_5\frac{\partial}{\partial s} - M(s)\right)\Psi(x,s). \tag{2.29}$$

Where $M(s)$ is a 5 dimensional mass term, whose value varies with extent of the fifth dimension as a step function such that $M(s>0) = M$, $M(s<0) = -M$.

Assuming our fermions can be described as $\Psi(x,s) = e^{ip_\mu x_\mu}\Psi(s)$, we have the solution to the 5D Dirac equation with a zero mass chiral mode,

$$\left(\gamma_5\partial_5 - M(s) + i\gamma_\mu p_\mu\right)\Psi(s) = 0. \tag{2.30}$$

We can split the positive and negative chiralities of $\Psi(s) = \frac{1\pm\gamma_5}{2}u_\pm$, if $i\gamma_\mu p_\mu\Psi(s) = 0$,

[3]There is also another more computationally expensive chiral fermion action, that of the overlap [131].

we have the equation for the positive chirality fermion,

$$(\gamma_5 \partial_5 - M(s)) \frac{1+\gamma_5}{2} e^{ip_\mu x_\mu} u_+ = 0. \tag{2.31}$$

Eq.2.31 has the solution,

$$\Psi(x,s) = e^{ip_\mu x_\mu} e^{-M|x_5|} u_+. \tag{2.32}$$

This is in essence a single fermion of positive chirality stuck to the wall at s=0, with exponential decay in the fifth dimension direction, this is the Callan-Harvey argument [49]. Kaplan [111] proposed placing this model on a discrete lattice with a 5D Wilson term. With periodic fifth dimension we have two domain walls with chiral modes of opposite chirality attached to each and exponentially decaying in the fifth dimensional direction.

In implementing the Domain Wall action for a finite lattice volume it can be split into its chiral 4D bulk theory and its five dimensional contribution [85]. The Dirac matrix for this theory is [90] (suppressing color and spin indices and using x and y to indicate 4D indices and s,r to indicate 5D)

$$M(x,y;s,r) = \delta_{s,r} M^{\text{bulk}}(x,y) + \delta_{x,y} M^{(5)}(s,r). \tag{2.33}$$

The bulk 4D Dirac matrix looks like the Wilson action with the inclusion of the (negative) 5D mass term M,

$$\begin{aligned} M^{\text{bulk}}(x,y) = (4-M)\delta_{x,y} - \frac{1}{2a}\sum_{\mu=1}^{4} \Bigg(& (1-\gamma_\mu) U_\mu \left(x + a\tfrac{\hat{\mu}}{2}\right) \delta_{x+a\hat{\mu},y} \\ & + (1+\gamma_\mu) U_\mu \left(x - a\tfrac{\hat{\mu}}{2}\right)^\dagger \delta_{x-a\hat{\mu},y} \Bigg). \end{aligned} \tag{2.34}$$

The gauge field is the same for every four dimensional discrete "slice" in the fifth dimension. The contribution from the fifth dimension is [63, 90]

$$\begin{aligned} M^{(5)}(s,r) = & \delta_{s,r} - (1-\delta_{s,L_s-1}) P_- \delta_{s+1,r} - (1-\delta_{s,0}) P_+ \delta_{s-1,r} \\ & + m(P_- \delta_{s,L_s-1} \delta_{0,r} + P_+ \delta_{s,0} \delta_{L_s-1,r}). \end{aligned}$$

The parameter m is the simulated quark mass of the 4D theory. The projectors $P_\pm$ are the usual chiral projection operators $P_\pm = (1 \pm \gamma_5)/2$.

The 4D fermion fields are obtained from the 5D fermions at the boundaries $s = 0, L_s - 1$ of the five-dimensional theory by (x is the 4D lattice index) [32],

$$\begin{aligned} \Psi(x) &= P_- \Psi(x,0) + P_+ \Psi(x, L_s - 1), \\ \bar{\Psi}(x) &= \bar{\Psi}(x, L_s - 1) P_+ + \bar{\Psi}(x, L_s - 1) P_-. \end{aligned} \tag{2.35}$$

2.3 Chiral symmetry and m_{res}

The Domain Wall action has a global vector flavour symmetry, $\Psi(x,s)' = e^{i\alpha^a T^a}\Psi(x,s)$ where T^a is a generator of the $SU(N_f)$ flavour group, which gives rise to the five-dimensional currents [30],

$$\begin{aligned} j^a_\mu(x,s) = \Big(& \Psi(x+a\hat{\mu},s)(1+\gamma_\mu)U_\mu\left(x+a\tfrac{\hat{\mu}}{2}\right)^\dagger T^a\Psi(x,s) \\ & - \bar{\Psi}(x,s)(1-\gamma_\mu)U_\mu\left(x+a\tfrac{\hat{\mu}}{2}\right)T^a\Psi(x+a\hat{\mu},s)\Big), \\ j^a_5(x,s) = \Big(& \Psi(x,s+1)(1+\gamma_5)T^a\Psi(x,s) \\ & - \bar{\Psi}(x,s)(1-\gamma_5)T^a\Psi(x,s+1)\Big). \end{aligned} \tag{2.36}$$

Which act upon the nf-let of fermion flavours. There is a unique vector transformation yielding a conserved 4D vector current,

$$\mathfrak{V}^a_\mu(x) = \sum_{s=0}^{L_s-1} j^a_\mu(x,s). \tag{2.37}$$

We can define a local vector current using the 4D quarks defined in Eq.2.35,

$$V^a_\mu(x) = 2\Psi(x)T^a\gamma_\mu\Psi(x). \tag{2.38}$$

The connection between the two is the vector renormalisation factor $Z_V V^a_\mu(x) = \mathfrak{V}^a_\mu(x)$.

The 5D conserved axial current can be defined as [10],

$$\mathfrak{A}^a_\mu(x) = \sum_{s=0}^{L_s-1} \text{sign}\left(1-\frac{Ls-1}{2}\right) j_5. \tag{2.39}$$

Finite L_s, and the introduction of fermion masses breaks chiral symmetry, and so we now have a Partially Conserved Axial Current (PCAC), which has a non-zero derivative,

$$\delta_\mu\mathfrak{A}^a_\mu(x) = 2\left(m_f j^a_\mu(x,L_s-1) + j^a_5\left(x,\frac{L_s}{2}-1\right)\right). \tag{2.40}$$

$j^a_5(x,s)$ is exponentially suppressed so that in practice the axial current renormalises multiplicatively, $Z_A A^a_\mu(x) = \mathfrak{A}^a_\mu$. The 4D local axial current (A^a_μ) is defined,

$$A^a_\mu(x) = 2\bar{\Psi}(x)\gamma_\mu\gamma_5 T^a\Psi(x). \tag{2.41}$$

In the continuum limit, the Ward identities must be restored, resulting in,

$$Z_{\mathfrak{A}}\delta_{\mu}\mathfrak{A}^{a}_{\mu}(x) = 2j^{a}_{\mu}(x)\left(m_{f} + m_{\mathrm{res}}\right). \tag{2.42}$$

$Z_{\mathfrak{A}}$ is the renormalisation factor for the PCAC (which is practically 1). The term m_{res} is so-called Domain Wall residual mass generated from the small breaking of chiral symmetry due to the finite value of L_s we must use. Naturally, this can be measured and allows for the definition of the chiral limit for Domain Wall Fermions to be $m_f = -m_{res}$. As L_s is increased, or as the field strength coupling is increased the residual mass shrinks [8].

2.4 Correlation functions

Considering Eq.2.7, with the operator $\mathcal{O} = \bar{\Psi}(x)\Psi(y)$, and using Eq.2.4 we have,

$$\langle\bar{\Psi}(x)\Psi(y)\rangle = \int \mathcal{D}A_{\mu}\det(M)M^{-1}(x,y)e^{-S(A_{\mu})}. \tag{2.43}$$

Defining S as the (Green's) function that is the solution of,

$$M(x,z)S(z,y) = \delta_{x,y}. \tag{2.44}$$

We immediately recognise $S(z,y) = M(y,z)^{-1}$, is the fermion propagator. A contraction of $\bar{\Psi}(x)\Psi(y)$ yields the propagator $S(x,y)$. Rows of S may be calculated using standard sparse matrix inversion techniques.

Defining the local correlator $c(t)$ at zero momenta as (with Γ_1 and Γ_2 being Dirac matrices),

$$c_{\Gamma_1,\Gamma_2}(t) = \sum_{x}\mathrm{Tr}\left[\bar{\Psi}(x,t)\Gamma_1\Psi(x,t)\bar{\Psi}(0,0)\Gamma_2\Psi(0,0)\right]. \tag{2.45}$$

Where the Fourier Transform has been performed over the spatial directions of x only. Performing the Wick contractions on the correlator, we find

$$\begin{aligned} c_{\Gamma_1,\Gamma_2}(t) = \sum_{x} &\mathrm{Tr}\left[S(x,t;0,0)\Gamma_1 S(0,0;x,t)\Gamma_2\right] \\ &- \mathrm{Tr}\left[S(x,t;x,t)\Gamma_1\right]\mathrm{Tr}\left[S(0,0;0,0)\Gamma_2\right]. \end{aligned} \tag{2.46}$$

The second term is the disconnected piece, which is 0 for all flavour non-singlet correlators. The expression in Eq.2.46 gives the measurement of a quark being created at the source (0,0) and being annihilated at the sink (x,t), and a quark propagating in the opposite direction. As a quark propagating in the opposite time direction is the same as an anti-quark propagating from (0,0) to (x,t), we can use the equation (for

fermions with γ_5 Hermiticity, which is all we will consider in this work),

$$S(0,0;x,t) = \gamma_5 S(x,t;0,0)^\dagger \gamma_5. \tag{2.47}$$

And only require one matrix inversion. Correlators of the form in Eq.2.46 are called point-source (or local source to local sink) propagators, where a local source/sink is an individual site.

Considering a correlator that has a non-local source, $\phi(y,z;x,t)$ for the position x on the time slice t, we have the correlator,

$$c_{\Gamma_1,\Gamma_2}(t) = \sum_x \sum_{y,z,y',z'} \mathrm{Tr}\left[\phi(y,z;x,t)\phi(y',z';0,0)S(y,t;y',0)\Gamma_1\gamma_5 S(z,t;z',0)^\dagger\gamma_5\Gamma_2\right]. \tag{2.48}$$

This is not manifestly gauge invariant [63], however if we fix to some smooth covariant gauge (the use of Coulomb gauge is argued to be the best as it does not constrain the temporally polarised links)[4] and take ϕ to be a smooth function in x and y good overlap with the hadronic ground state can be achieved. If we take the path ϕ to be the whole gauge field on that slice, these correlation functions are called wall propagators.

It is common in Lattice QCD to label the different fermion flavours with their corresponding quarks, e.g. for $N_f = 2{+}1$, DWF u, d and s. Meson correlation functions are computed using Eq.2.46, with choice of Dirac matrices (Γ_1, Γ_2) such that the the interpolating operator has the same quantum numbers as the physical particle. For instance the pseudoscalar (P) mesons the Pion and the Kaon are computed from the operators,

$$\begin{aligned} \mathcal{O}_\pi(x) &= \bar{u}(x)\gamma_5 d(x), \\ \mathcal{O}_K(x) &= \bar{s}(x)\gamma_5 d(x). \end{aligned} \tag{2.49}$$

The large time behaviour of the zero momentum correlation function allows us to compute the masses (m) and amplitudes (N) of the particles,

$$c_{\Gamma_1,\Gamma_2}(t) = \sum_x \mathrm{Tr}\left[S(x,t;0,0)\Gamma_1\gamma_5 S(x,t;0,0)^\dagger\gamma_5\Gamma_2\right] = Ne^{-mt}|_{t>>0} \tag{2.50}$$

[4]The methods to do so will be introduced in Chapter 6.

Masses and decay constants

To obtain the relation in Eq.2.50, we use the fact that two interpolating operators at large Euclidean time have the form [90] (where the summation is over energy levels n),

$$\lim_{t\to\infty}\langle\mathcal{O}(t)\mathcal{O}(0)^\dagger\rangle = \sum_n \langle 0|\mathcal{O}|n\rangle\langle n|\mathcal{O}^\dagger|0\rangle e^{-tE_n}. \tag{2.51}$$

Expanding the sum, and only keeping the first term and using the identity $\langle 0|\mathcal{O}|n\rangle = \langle n|\mathcal{O}^\dagger|0\rangle^*$ we have,

$$\lim_{t\to\infty}\langle O(t)\mathcal{O}(0)^\dagger\rangle = \frac{|\langle 0|\mathcal{O}|n\rangle|^2}{2mL^3}e^{-mt}. \tag{2.52}$$

The factor L^3 is the spatial hypercube volume $L_xL_yL_z = L^3$. Upon fitting the correlation function to an exponential at large enough times, and if there is sufficient overlap between the interpolating fields and the required particle's ground state the particle's mass in lattice units can be deduced, as well as its amplitude. From Eq.2.52 we can define the effective mass,

$$m_{\text{eff}} = \log\left(\frac{c_{\Gamma_1,\Gamma_2}(t)}{c_{\Gamma_1,\Gamma_2}(t+1)}\right). \tag{2.53}$$

When this function displays a plateau, we have an estimate for both when the correlation function is describing the intended ground state particle, and what the particle's mass is in lattice units. In practice the effective mass is not used for an accurate measurement of the particle's mass. Instead (often simultaneous) fits to the exponential in Eq.2.52 are used.

As our simulation is in a finite box, there will also be a propagator propagating backwards in time from the other end of the temporal separation of the lattice. The correlator's large time behaviour is hence,

$$c_{\Gamma,\Gamma}(t) = |\langle 0|\mathcal{O}|n\rangle|^2\left(e^{-mt} \pm e^{-m(L_t-1-t)}\right). \tag{2.54}$$

Where the $\pm$ depends on the eigenvalue of the interpolating operator under time reversal symmetry. For a pseudoscalar the two propagators are summed and the function behaves like a cosh, for an pseudoscalar-axial (P,A) interpolator the functions are subtracted and behaves like a sinh.

The hadronic current between a pseudoscalar meson and the vacuum is defined by,

$$\langle 0|A_\mu(0)|PS(p)\rangle = iZ_A p_\mu f_{PS} e^{ip_\mu x_\mu}. \tag{2.55}$$

Where f is called the pseudoscalar decay constant. We have to include the axial renormalisation factor Z_A because we are not using the conserved 5D current.

Defining the correlator in terms of the amplitude $N^{s_1,s_2}_{\mathcal{O}_1,\mathcal{O}_2}$ where s_1 and s_2 are the sources (Wall (W) or Point/Local (L)), we have,

$$c^{s_1,s_2}_{\mathcal{O}_1,\mathcal{O}_2}(t) = \frac{\langle 0|{\mathcal{O}_1}^{s_1}|PS\rangle\langle PS|{\mathcal{O}_2}^{s_2}|0\rangle}{2m_{PS}L^3}e^{-m_{PS}t} = N^{s_1,s_2}_{O_1,O_2}e^{-m_{PS}t}. \tag{2.56}$$

And the correlator for the local axial A_μ ($\Gamma_1 = \Gamma_2 = \gamma_\mu$) current and the pseudoscalar P ($\Gamma_1 = \Gamma_2 = \gamma_5$) can give us the pseudoscalar decay constant via the formula,

$$f_{PS} = Z_A\sqrt{\frac{1}{2L^3m_{PS}}\frac{N^{W,L}_{A_0,P}N^{W,L}_{A_0,P}}{N^{W,W}_{P,P}}}. \tag{2.57}$$

The pseudoscalar masses and the pseudoscalar decay constants for the Pion and Kaon are well measured experimentally, and we can use these measurements to set our lattice scale, i.e. the lattice spacing is the value where the lattice measured values in the chiral limit take the experimentally measured values.

2.4.1 Four Quark operators

One of the studies presented in this thesis is to calculate Kaon mixing in and beyond the standard model. This is achieved by computing the four quark operator matrix element,

$$\langle \bar{K}^0(t_i)|\mathcal{O}(t)|K^0(t_f)\rangle. \tag{2.58}$$

This describes a neutral Kaon created at time t_i oscillating to an neutral anti-Kaon, and then annihilating at time t_f. This is known as a matrix element and a one loop contribution to this oscillation can be viewed diagrammatically for the standard model by Diagram.1.

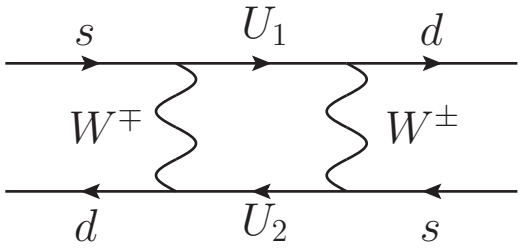

Diagram 1: One of the standard model one loop contributions to neutral Kaon mixing, mediated by the Weak force. U_1 and U_2 are standard model quarks the Charm and Top.

No known method exists for the inclusion of weak bosons with QCD on the lattice. Instead we consider the Operator Product Expansion (OPE) whereby the box diagram

becomes effectively pinched into a point and a local four quark operator with the desired symmetry properties can be used to effectively describe the interaction.

From now on I drop the ^{0} on the Kaon notation as it is implicit in the rest of this work that they are neutral. The zero momentum correlator for such an object (using point source propagators "L") is,

$$c^{(\mathcal{O})}(t_i,0,t_f)^{LLL} = \sum_{x_i,x_f} \langle \bar{d}(x_f,t_f)\gamma_5 s(x_f,t_f)\mathcal{O}(0)\bar{d}(x_i,t_i)\gamma_5 s(x_i,t_i)\rangle. \tag{2.59}$$

For the Standard model, the neutral Kaon mixing four quark operator is the vector-axial (V-A),

$$\mathcal{O}_{V-A,V-A}(x,t) = \bar{s}(x,t)\gamma_\mu(1-\gamma_5)d(x,t)\bar{s}(x,t)\gamma_\mu(1-\gamma_5)d(x,t). \tag{2.60}$$

Upon Wick contraction, we have the "trace-trace" and the "trace" constituent parts,

$$\begin{aligned} c^{(V-A,V-A)}(t_i,0,t_f)^{LLL} = \sum_{x_i,x_f} & \mathrm{Tr}\left[S(x_f,t_f;0,0)\gamma_\mu(1-\gamma_5)S(0,0;x_f,t_f)\right] \\ & \times \mathrm{Tr}\left[S(x_i,t_i;0,0)\gamma_\mu(1-\gamma_5)S(0,0;x_i,t_i)\right] \\ & -\mathrm{Tr}\Big[S(x_f,t_f;0,0)\gamma_\mu(1-\gamma_5)S(0,0;x_i,t_i) \\ & \quad \times S(x_i,t_i;0,0)\gamma_\mu(1-\gamma_5)S(0,0;x_f,t_f)\Big]. \end{aligned} \tag{2.61}$$

In practice the original method in Eq.2.61 (point-source contractions to the t=0 point) is not a good way to measure the four quark correlation function, due to its poor statistical resolution. Instead, wall sources are used (at t_i and t_f) for the two Kaons and the vertex position (t) is varied, giving much higher statistical resolution for the matrix element (a factor of L^3 better sampling). The two separate traces are due to the summation over spin indices which have been suppressed in the notation.

If we consider the quantity in Eq.2.59 in the limit of large correlation times, and ignoring backwards propagation we have (where $P = \bar{d}\gamma_5 s$),

$$\begin{aligned} \lim_{t_f>t>t_i} c^{(V-A,V-A)}(t_i,t,t_f)^{WLW} = \\ \langle 0|P^W|\bar{K}\rangle\langle\bar{K}|\mathcal{O}_{V-A,V-A}(t)|K\rangle\langle K|P^W|0\rangle \frac{1}{4m_k^2L^6}e^{-m_k(t_f-t_i)}. \end{aligned} \tag{2.62}$$

The desired matrix element is the piece sandwiched in the middle of Eq.2.62. As seen earlier, we can compute the matrix elements of the pseudoscalar Kaons from their

correlation functions at large times,

$$\begin{aligned} c(t_i,t)^{W,L}_{P,A_0} &= \frac{\langle 0|P^W|\bar{K}\rangle\langle\bar{K}|A_0^L|0\rangle}{2m_K L^3} e^{-m_K(t-t_i)}, \\ c(t,t_f)^{L,W}_{A_0,P} &= \frac{\langle 0|A_0^L|K\rangle\langle K|P^W|0\rangle}{2m_K L^3} e^{-m_K(t_f-t)}. \end{aligned} \tag{2.63}$$

Upon taking the ratio (and only considering the parity even part so that $(V-A)(V-A) \to VV+AA$),

$$\frac{c^{(VV+AA)}(t_i,t,t_f)^{WLW}}{c(t_i,t)^{WL}_{P,A_0} c(t,t_f)^{LW}_{A_0,P}} = \frac{\langle\bar{K}|\mathcal{O}_{VV+AA}(t)|K\rangle}{\langle\bar{K}|A_0|0\rangle\langle 0|A_0|K\rangle}. \tag{2.64}$$

This is the lattice evaluation of the quantity B_k. With appropriate normalisation factor $\frac{8}{3}$,

$$B_k(a) = \frac{c^{(VV+AA)}(t_i,t,t_f)^{WLW}}{\frac{8}{3} c(t_i,t)^{WL}_{P,A_0}\ c(t,t_f)^{LW}_{A_0,P}}. \tag{2.65}$$

Where the "a" is there to illustrate that at the moment this is a lattice measure, and needs to be renormalised for comparing to continuum theory.

The full basis of (dimension-6) irrelevant operators that contribute to neutral Kaon mixing are (with a and b being color indices and I illustrate only the color unmixed, the color mixed swaps an a with a b in the indices.),

$$\begin{aligned} O_1 &= (\bar{s}\gamma_\mu(1-\gamma_5)d)(\bar{s}\gamma_\mu(1-\gamma_5)d), \\ O_{2,3} &= (\bar{s}_a(1-\gamma_5)d_a)(\bar{s}_b(1-\gamma_5)d_b), \qquad \text{(unmixed,mixed)} \\ O_{4,5} &= (\bar{s}_a(1+\gamma_5)d_a)(\bar{s}_b(1+\gamma_5)d_b). \qquad \text{(unmixed,mixed)} \end{aligned} \tag{2.66}$$

The unmixed and mixed refer to the color indices that are being contracted, unmixed means the quarks color indices within the parentheses are contracted and mixed means the color contractions are performed across the two parentheses. The mixed and unmixed cases are the same for the O_1 operator. This basis is the so-called "SUSY-basis" [45, 87], which is not what we measure directly, as will be discussed in Chapter 5.

The dimension-6 irrelevant operators $O_{2,3}, O_{4,5}$ allow for neutral Kaon mixing via a non-SM i.e. a non left handed current, this would be seen in Diagram 1 but with the W-boson replaced by another heavier particle such as a SUSY gluino. Although the basis of BSM operators is called the SUSY basis, these operators are model independent. They can be used to parameterise the low-energy QCD corrections of a particular model, and can then be used to constrain the minimum allowed energy scale of new physics.

2.5 Monte Carlo statistical analysis

Say we have a thermalised, finite set of N measurements of O computed from our simulations at different, equally spaced Monte Carlo times t. Assuming such measurements are uncorrelated, we have the sample average,

$$\bar{\mathcal{O}} = \frac{1}{N}\sum_{t=1}^{N}\mathcal{O}(t). \tag{2.67}$$

And the unbiased sample variance,

$$\sigma^2(\mathcal{O}) = \frac{1}{N-1}\sum_{t=1}^{N}(\mathcal{O}(t)-\bar{\mathcal{O}})^2. \tag{2.68}$$

For more sophisticated methods for the estimation of the variance, we consider now the jackknife and bootstrap techniques.

2.5.1 Jackknife and Bootstrap error Analysis

The jackknife technique reuses elements in its series as a method of eliminating bias. Considering again our N equally spaced measurements. We generate the jackknifed distribution [113],

$$\theta(i) = \frac{1}{N-1}\sum_{j\neq i}^{N}\mathcal{O}(j). \tag{2.69}$$

Where we eliminate each i'th element from each combined average, the variance is computed from the θ's and the jackknifed average $\bar{\theta}$ and sample average $\bar{O}$ are the same,

$$\sigma^2(\theta) = \frac{N-1}{N}\sum_{i=1}^{N}\left(\theta(i)-\bar{\mathcal{O}}\right)^2. \tag{2.70}$$

The bootstrap analysis method is similar to the jackknife [78], in that it is a technique for using the sample distribution as an estimator for the population probability distribution. Unlike the jackknife, the bootstrap procedure is a random sampling with replacement procedure, whereas the jackknife is a resampling without replacement. For bootstrap resampling a length N subset of the original sample is generated by randomly picking out (denoted rand) of all t measurements and averaging data from the original sample. This is performed N_{boots} times,

$$\phi(i) = \frac{1}{N}\sum_{j=1}^{N}\mathcal{O}(\text{rand}(j)). \tag{2.71}$$

The estimate of the error can be computed with $\sigma^2(\phi)$ deduced from all of the bootstraps, assuming the distribution is normal, but it is a better idea to sort the data and take confidence levels from above and below as a more robust error estimation.

Monte Carlo simulations are often correlated between successive updates. Such a correlation between measurements must be measured and accounted for when quoting results, where possible. One can cater for this error by the process of binning, whereby at some finite bin length successive bins are uncorrelated. It is simple to tell whether enough binning has been performed, because the errors for larger and larger bins stay approximately the same. The procedure of binning is simple, we average within a local subset of our time series into N_b individual bins of length t',

$$\eta(b) = \frac{1}{t'} \sum_{i=bt'}^{(b+1)t'} \mathcal{O}(i). \tag{2.72}$$

Jackknife and bootstrap analysis is then performed on the binned data. Even though the binning method is effective, the correlation between successive measurements can also be measured directly.

2.5.2 Autocorrelations

The autocorrelation function $\rho(t)$ is measured by the quantity,

$$\rho(t) = \frac{1}{N-1} \sum_{t'=1}^{N-t} \left(\mathcal{O}(t) - \bar{\mathcal{O}}\right) \left(\mathcal{O}(t+t') - \bar{\mathcal{O}}\right). \tag{2.73}$$

At t=0, this function is the sample variance. This function is expected to decay exponentially with measurement separation time t $\rho(t) \approx e^{-t/\tau_{\text{int}}}$. The factor τ_{int} is called the integrated autocorrelation time and can be computed using the formula,

$$\tau_{\text{int}}(t') = \frac{1}{2} + \frac{1}{\rho(0)} \sum_{t=1}^{t'} \rho(t'). \tag{2.74}$$

Where we have defined a windowed measurement so that the function can be plotted against the maximal measurement time t'. The first time this function plateaus gives the value of the integrated autocorrelation time.

Chapter 3

The strong coupling α_s

The strong coupling $\alpha_s = \frac{g^2}{4\pi}$ (where "g" is the coupling strength of our theory) of QCD is one of the very few free parameters of the Standard Model of particle physics, it is a fundamental *constant* of nature, and in the limit of massless fermions is the only free parameter for the theory of QCD. The renormalised running coupling between gluons, ghosts and quarks determines many facets of the rich dynamics of QCD. Its renormalised value at some scale must be determined accurately by experiment, either numerical or physical, and by as many different avenues as possible as it should be the same no matter which measurement choice is made.

In general, an evaluation of some QCD object, be it a cross-section or lattice measurement $\sigma(\mu)$ at scale μ has the perturbative expansion,

$$\sigma(\mu) = a_0 + a_1\alpha_s(\mu) + a_2\alpha_s(\mu)^2 + ... \tag{3.1}$$

The coefficients $a_0, a_1...$ can be non-perturbative coefficients evaluated using lattice perturbation theory. Or one can (if applicable) use continuum perturbation theory for these coefficients, which are often evaluated at higher order (power of α_s) [126]. If matching lattice measurements to continuum perturbation theory, the continuum limit must be taken first. Accurate evaluation of the coupling directly affects all theoretical predictions.

The strong coupling (in scheme M) changes value (runs) with the scale via the equation [52, 101, 137, 157],

$$\frac{d\left(\alpha^{(M)}(\mu^2)\right)}{d\ln(\mu^2)} = \beta^{(M)}\left(\alpha(\mu^2)\right) = -4\pi\sum_{i\geq 0}\beta_{(i)}^{(M)}\left(h^{(M)}\left(\mu^2\right)\right)^{i+2}. \tag{3.2}$$

Where the coefficients $\beta_{(i)}$ have to be computed, at the first two orders of perturbation theory they are the same in all schemes. The parameter h is $\frac{\alpha^{(M)}(\mu^2)}{4\pi}$.

As a test of QCD, separate measurements of the coupling should agree, in the same renormalisation scheme at the same renormalisation scale. It is common practice to determine the coupling in the Modified Minimal Subtraction scheme $\overline{\text{MS}}$, and because the value of the coupling varies with the scale according to Eq.3.2 a specific scale for comparison should also be chosen. As such, the Z-boson mass μ=M_z (91.1876 GeV) [24], is commonly used and will be the scale at which we quote our results.

We will be performing our measurement at the available scale to our simulation $\mu \approx a^{-1}$, and so numerical integration of Eq.3.2 will have to be used to attain a result at M_z. The scheme $\overline{\text{MS}}$ is not directly applicable to many lattice calculations, and so conversion (matching) in the continuum limit using continuum perturbation theory between schemes attenable for lattice measurements and $\overline{\text{MS}}$ will have to be performed, these topics will be discussed in Sec.3.6. For the matching of vertex function evaluations, Landau gauge must be implemented on our lattice configurations and a technique to do so is discussed in Chapter 6.

The strong coupling of QCD can be determined directly by experiment or numerically by lattice QCD measurements [6, 27, 136]. Experimentally, the coupling can be taken from Hadronic Tau decays, whose scale is comparable to that of lattice measurements. Or by evaluations of deep inelastic scattering (DIS), e^+e^- scattering or Z boson width fits. Considering the world average in Fig.3.1 from [27], we see that the evaluations are roughly equivalent and that lattice determinations contribute with the smallest error. The author of [6] removes several evaluations (including those using lattice techniques) from their average and finds a compatible result.

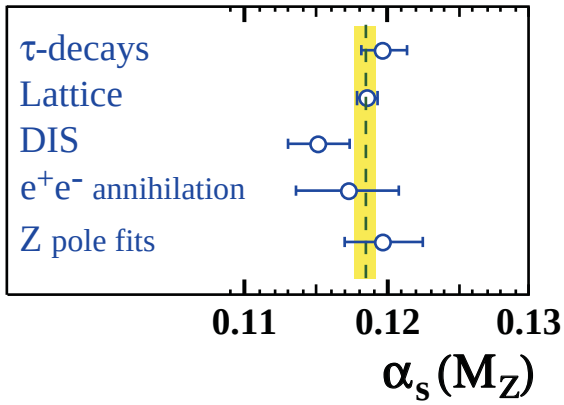

Figure 3.1 *$\alpha^{\overline{\text{MS}}}_{N_f=5}(M_z)$ world average from various determinations, taken from [27]. The yellow band is the combined world average $\alpha^{\overline{\text{MS}}}_{N_f=5}(M_z)$ =* 0.1184(7).

Several techniques exist to compute the strong coupling using lattice methods, currently the most accurate evaluation is found in [125], which uses lattice perturbation theory to match the average of 22 different Wilson loop evaluations to obtain $\alpha^{\overline{\text{MS}}}_{N_f=5}(M_z) = 0.1184(6)$ and uses an $N_f = 2 + 1$, staggered fermion discretisation. Another, very different approach has been taken in [65] using the $N_f = 2$ Schrödinger functional scheme [121] to evaluate the coupling which runs with $\mu = 1/L$ where L is the lattice length, this scheme allows for large perturbative-scale lattice evaluations at the cost of poor granularity of scale in their measurement, this method also requires dedicated and costly simulations.

Another, very accurate determination of the coupling can be obtained by fitting the hadronic vaccuum polarisation to its continuum OPE expression with free fit parameter α_s [143]. The authors obtain a result of $\alpha^{\overline{\text{MS}}}_{N_f=5}(M_z) = 0.1181(3)^{(+14)}_{(-12)}$ (with the first error statistical and the second systematic) using an $N_f = 2+1$ fermionic discretisation with excellent chirality (the overlap prescription) with high-order continuum OPE expressions and have detailed systematics, their measurement procedure does require fermion propagator inversions which are computationally expensive.

One can also perform direct field-theoretic measurements of the strong coupling by evaluating amputated vertex functions. The ghost-gluon vertex has been measured recently with $N_f = 2+1+1$ Twisted Mass fermions, with result $\alpha^{\overline{\text{MS}}}_{N_f=5}(M_z) = 0.1200(14)$ [29]. This measurement requires the costly computation of the ghost propagator, which is evaluated by inverting the Faddeev-Popov matrix [108], but because it only requires the evaluation of gluon and ghost two point functions it has good statistical resolution. Attempts have also been made at evaluating the quark-gluon vertex [146].

We intend to measure the Landau gauge-fixed amputated triple gluon vertex definition of the coupling as was performed in [3, 41, 134], this has the benefit of being numerically cheap to perform as it requires no costly matrix inversions and new ensembles do not need to be generated, although fixing to Landau gauge has to be performed and a statistically large sample size is required. The triple gluon vertex evaluation also has the benefit of high-order (three and two loop) matching coefficients between (exceptional and non-exceptional) renormalisation schemes and $\overline{\text{MS}}$ in continuum perturbation theory. For our analysis, we will be using the following $N_f = 2 + 1$ DWF ensembles [1],

In this study we also intend to illustrate the applicability of the triple gluon vertex measurement of the coupling, as well as that of vertex functions in general for coupling evaluations in candidate Beyond the Standard Model (BSM) theories. In particular the theory of Minimal Walking Technicolor which has a candidate theory of SU(2)

[1] The lattice spacings for the $\beta = 2.13$ and $\beta = 2.25$ ensembles were taken from [14] and that of the $\beta = 2.23$ was estimated from the Wilson flow analysis of Chapter.4. am_l is the simulated degenerate light quark mass and am_s the simulated strange quark mass

	$16^3 \times 32$					$24^3 \times 64$			$32^3 \times 64$		
am_l	0.01	0.02	0.03	0.01	0.02	0.005	0.01	0.02	0.004	0.006	0.008
Configurations	738	750	1463	774	774	1555	802	572	519	746	450
am_s	0.04			0.031		0.04			0.03		
a^{-1} (GeV)	1.73(3)			2.19(6)		1.73(3)			2.28(3)		

Table 3.1 *SU(3) $N_f = 2 + 1$ Domain Wall Fermion ensembles used throughout this thesis. The two $16^3 \times 32$ and $32^3 \times 64$ ensembles were used for the non-exceptional (*MOMggg*) analysis and the larger $24^3 \times 64$ and $32^3 \times 64$ for the exceptional (*$\widetilde{\text{MOMgg}}$*) determination. We use the Iwasaki gauge action and fifth dimension length 16.*

gauge group with 2 fermions in the Adjoint representation. This analysis shall be seen in Sec.3.9. We begin this chapter with a discussion of the techniques required for a determination of the coupling for $SU(N_c)$ theories.

3.1 On momentum space gluon fields

As discussed in greater detail in 6.2.1, we represent our gluon fields as,

$$\begin{aligned} A_\mu\left(x + a\frac{\hat{\mu}}{2}\right) &= \frac{1}{i}\log\left(U_\mu\left(x + a\frac{\hat{\mu}}{2}\right)\right), \\ A_\mu(p) &= e^{i\frac{p_\mu}{2}} \sum_x e^{ip_\mu x_\mu} A_\mu\left(x + a\frac{\hat{\mu}}{2}\right) \end{aligned} \tag{3.3}$$

With the logarithm being either the Hermitian projection (Log-A A.1.1) or the exact Hermitian projection (Log-C A.1.3), using the definitions of Appendix A.

The fields $A_\mu(p)$ are traceless, but the spatial fields' Hermiticity is translated to $p, -p$ conjugacy. This can be seen by,

$$\begin{aligned} A_\mu(p) &= A_\mu(-p)^\dagger, \\ e^{i\frac{p_\mu}{2}} \sum_x e^{ip_\mu x_\mu} A_\mu\left(x + a\frac{\hat{\mu}}{2}\right) &= \left(e^{-i\frac{p_\mu}{2}}\right)^* \sum_x \left(e^{-ip_\mu x_\mu}\right)^* A_\mu\left(x + a\frac{\hat{\mu}}{2}\right)^\dagger. \end{aligned} \tag{3.4}$$

where, $A_\mu\left(x + a\frac{\hat{\mu}}{2}\right)^\dagger = A_\mu\left(x + a\frac{\hat{\mu}}{2}\right)$.

If one wishes to obtain the different Lie elements of the field itself (we choose to use trace identities of the fields in this work, but the following will provide a useful check for our identities). It is common to use [2, 41],

$$A^a_\mu(p) = e^{i\frac{p_\mu}{2}} \text{Tr}\left[\sum_x e^{ip_\mu x_\mu} A_\mu\left(x + a\frac{\hat{\mu}}{2}\right) T^a\right]. \tag{3.5}$$

Where the T^a's are the generators for $SU(N_c)$ (and satisfy the relations 2.11). As the Fourier transform is performed element by element, the matrix multiplication of the generator can be performed outside of the Fourier transform,

$$A^a_\mu(p) = e^{i\frac{p_\mu}{2}} \mathrm{Tr}\left[\left(\sum_x e^{ip_\mu x_\mu} A_\mu\left(x + a\frac{\hat{\mu}}{2}\right)\right) T^a\right]. \tag{3.6}$$

For SU(3) the matrix form of $A_\mu(p)$ can be expressed in terms of its constituent Lie elements as,

$$A_\mu(p) = \frac{e^{ip_\mu/2}}{2} \begin{pmatrix} A^3_\mu(p) + \frac{A^8_\mu(p)}{\sqrt{3}} & A^1_\mu(p) + iA^2_\mu(p) & A^4_\mu(p) + iA^5_\mu(p) \\ A^1_\mu(p) - iA^2_\mu(p) & -A^3_\mu(p) + \frac{A^8_\mu(p)}{\sqrt{3}} & A^6_\mu(p) + iA^7_\mu(p) \\ A^4_\mu(p) - iA^5_\mu(p) & A^6_\mu(p) - iA^7_\mu(p) & -2\frac{A^8_\mu(p)}{\sqrt{3}} \end{pmatrix}$$

And specific Lie components can be taken by linear combinations, e.g

$$A^1_\mu(p) = (A_\mu(p)[1] + A_\mu(p)[3]). \tag{3.7}$$

Instead of performing unnecessary matrix multiplications with the generators that have numerous exact zero elements as in Eq.3.5. Computations based upon the Lie elements will perform a part of a useful check on the correctness of the identities we use to compute Green's functions.

Computationally, for generic N_c we use the matrix operation in Eq.3.5 to pick out Lie elements. To compute the generators, one embeds the $N_c - 1 \times N_c - 1$ generator matrices into the top left of the $N_c \times N_c$ matrices, and then fills in the final row and final column using the fact that the generators are Hermitian. The final generator is the diagonal $\frac{1}{\sqrt{N_c(N_c-1)}}(1, 1, 1, ..., -N_c)$. To compute the structure functions for $SU(N_c)$ one should create a table of the non-zero values, indexing the color indices and use,

$$\begin{aligned} f^{abc} &= -2i\left(\mathrm{Tr}\left[T^aT^bT^c\right] - \mathrm{Tr}\left[T^bT^aT^c\right]\right), \\ d^{abc} &= 2\left(\mathrm{Tr}\left[T^aT^bT^c\right] + \mathrm{Tr}\left[T^bT^aT^c\right]\right). \end{aligned} \tag{3.8}$$

With explicit form for the trace of the product of three matrices (as is written in Alg.1). This saves on unnecessary matrix multiplications, providing computational speedup by eliminating the need for temporary matrices and by not performing operations that do not contribute to the final result, and means f and d can be computed at the same time.

3.2 Lattice Green's functions

Non-perturbative lattice Green's functions are defined in position space as,

$$G^{(n)\ a_1 a_2 \cdots a_n}_{\mu_1 \mu_2 \cdots \mu_n}(x_1, x_2 \cdots x_n) = \langle A^{a_1}_{\mu_1}(x_1) A^{a_2}_{\mu_2}(x_2) \cdots A^{a_n}_{\mu_n}(x_n) \rangle. \tag{3.9}$$

Where index "a" represents one of the color charges, μ the Lorentz polarisation and $\langle \cdots \rangle$ a Monte-Carlo average. This has momentum-space counterpart,

$$G^{(n)\ a_1 a_2 \cdots a_n}_{\mu_1 \mu_2 \cdots \mu_n}(p_1, p_2 \cdots p_n) \delta^{Nd}(p_1 + p_2 + \cdots p_n). \tag{3.10}$$

With some abuse of notation I have used the Dirac delta function, which is related to the discrete Kronecker delta by,

$$\int d^{N_d} x e^{i p_\mu x_\mu} = (2\pi)^{N_d}\, \delta^{\text{dirac}}(p) = V \delta^{\text{Kronecker}}_p = a^{N_d} \sum_x e^{i p_\mu x_\mu}. \tag{3.11}$$

One can form correlation functions of the Fourier transformed fields,

$$G^{(n)\ a_1 a_2 \cdots a_n}_{\mu_1 \mu_2 \cdots \mu_n}\left(p_1, p_2, \cdots, -\left(\sum_{i=1}^{n-1} p_i\right)\right) = \frac{1}{V} \langle A^{a_1}_{\mu_1}(p_1) A^{a_2}_{\mu_2}(p_2) \cdots A^{a_n}_{\mu_n}\left(-\sum_{i=1}^{n-1} p_i\right) \rangle. \tag{3.12}$$

3.3 The momentum space gluon propagator

I now begin to specialise to areas of interest, first the lattice Landau-gauge gluon propagator. As the two point function of Eq.3.12,

$$G^{(2)\ ab}_{\mu\nu}(p, -p) = \frac{1}{V} \langle A^a_\mu(p) A^b_\nu(-p) \rangle. \tag{3.13}$$

This defines the gluon correlator, it has the following Lorentz structure and may be decomposed to scalar functions, the transverse G and longitudinal F (where F is proportional to ϵ our gauge fixing parameter, in Landau gauge this is 0),

$$G^{(2)\ ab}_{\mu\nu}(p, -p) = \delta^{ab} \left(g_{\mu\nu} - \frac{p_\mu p_\nu}{p^2} \right) G^{(2)}(p^2) + \frac{p_\mu p_\nu}{p^2} F(p^2). \tag{3.14}$$

We can project out the scalar form factor $G^{(2)}(p^2)$, with

$$G^{(2)}(p^2) = \frac{1}{(N_d - 1)(N_c^2 - 1)} \delta^{ab} \left(g_{\mu\nu} - \frac{p_\mu p_\nu}{p^2} \right) G^{(2)\ ab}_{\mu\nu}(p, -p). \tag{3.15}$$

Where we have used the fact that $\delta^{ab}\delta_{ab} = N_c^2 - 1$. In Landau gauge, the longitudinal term $\frac{p_\mu p_\nu}{p^2} G^{ab}_{\mu\nu}(p,-p)$ is zero. If we were considering a propagator in a gauge with gauge parameter $\epsilon \neq 0$, then there would be a longitudinal contribution. To extract this the projection,

$$\frac{1}{N_c^2 - 1} \frac{p_\mu p_\nu}{p^2} \delta^{ab} G^{ab}_{\mu\nu}(p^2) = F\left(p^2\right), \tag{3.16}$$

can be used. The form factor F will be proportional to the gauge parameter ϵ.

There exists an issue with the derivation of Eq.3.15, as we have projected the term $\frac{p_\mu p_\nu}{p^2}$, without considering the case for $p = 0$. It is convention within the community to use the normalisation $\frac{1}{Nd}$ for Landau gauge instead of $\frac{1}{N_d - 1}$ for the zero momentum component. The argument is that the Landau condition is trivially satisfied for p=0, and there is an unconstrained degree of freedom in the system [35, 58, 133]. This factor will be of considerable interest for our study.

We do not project out the Lie components of our fields, instead if we consider the usual group-theoretic definitions for fundamental $SU(N_c)$ matrices. The T's are the generators of the group,

$$\begin{aligned} T^a T^b &= \frac{1}{2}\left(\left[T^a, T^b\right] + \left\{T^a, T^b\right\}\right), \\ &= \frac{1}{2}\left(\left(if^{abc} + d^{abc}\right) T^c + \frac{1}{N_c}\delta^{ab} I\right). \end{aligned} \tag{3.17}$$

Considering the trace of the product $A_\mu(p)A_\nu(-p)$, we have in terms of Lie elements,

$$\begin{aligned} \mathrm{Tr}\left(A_\mu(p)A_\nu(-p)\right) &= \mathrm{Tr}\left(A^a_\mu(p) T^a A^b_\nu(-p) T^b\right), \\ &= A^a_\mu(p) A^b_\nu(-p) \mathrm{Tr}\left(T^a T^b\right), \\ &= \frac{1}{2} A^a_\mu(p) A^b_\nu(-p) \delta^{ab}. \end{aligned} \tag{3.18}$$

Specialising to Landau gauge ($\epsilon = 0$) and using the result in Eq.3.18, we associate the non-perturbative lattice gluon propagator with the quantity,

$$G^{(2)}(p^2) = \frac{1}{V} \frac{2}{\left(N_c^2 - 1\right)\ \left(N_d - 1\right)} \langle \mathrm{Tr}\left[A_\mu(p) A_\mu(-p)\right] \rangle. \tag{3.19}$$

We know there is a $p, -p$ symmetry from Eq.3.4, we can write the propagator as,

$$G^{(2)}(p^2) = \frac{1}{V} \frac{2}{\left(N_c^2 - 1\right)\ \left(N_d - 1\right)} \langle \mathrm{Tr}\left[A_\mu(p) A_\mu(p)^\dagger\right] \rangle. \tag{3.20}$$

Which is guaranteed to be real, and is simply, (in terms of a linearised matrix element

index "a")

$$\mathrm{Tr}\left[A_\mu(p)A_\mu(p)^\dagger\right] = \sum_{a=0}^{N_c^2-1} A_\mu(p)[a]A_\mu(p)[a]^*. \tag{3.21}$$

It should also be noted that although we perform the multiplicative $e^{i\frac{p_\mu}{2}}$ correction on the fields to ensure the correct momentum space evaluation of the Landau condition ($p_\mu A_\mu(p) = 0$) for our fields, as discussed in Sec.6.2.1. This is not necessary for the computation of the gluon propagator as this factor explicitly cancels.

If we wish to extract the longitudinal factor $F(q^2)$ one can use the relation,

$$\mathrm{Tr}\left[q_\mu A_\mu(q) q_\nu A_\nu(-q)\right] = \mathrm{Tr}\left[\left(q_\mu A_\mu(q)\right)\left(q_\nu A_\nu(q)\right)^\dagger\right]. \tag{3.22}$$

Computationally, one only has to compute the object $T = q_\mu A_\mu(q)$, and then compute $\mathrm{Tr}\left[TT^\dagger\right]$. Where Eq.3.21 can be used.

3.3.1 The gluon field renormalisation

To connect with continuum physics and continuum perturbation theory, renormalisation of bare quantities in some scheme and at some scale must be performed. The gluon field renormalisation $Z_{A_\mu}(p^2)$ is defined by ensuring that the non-perturbative gluon propagator at very large momenta tends to the tree level continuum propagator, i.e. as $\frac{1}{p^2}$.

We define the renormalisation factor as follows,

$$Z_{A_\mu}(\mu^2) = G^{(2)}(p^2)p^2|_{p^2=\mu^2}. \tag{3.23}$$

Upon renormalisation, this is the same as a renormalising the gauge field $A_\mu^R(p) = \sqrt{Z_A}A_\mu^{(0)}$, where the R stands for the renormalised field and the (0) indicates the bare measurement.

3.3.2 Momentum cuts

One expects simulations to only be justifiably comparable to continuum physics when renormalisation scales within the Rome Southampton window are used (where a is the lattice spacing of our simulation and Λ is the "Landau pole" of the theory)[17], this is defined by the window,

$$\Lambda^2 << \mu^2 << \left(\frac{\pi}{a}\right)^2. \tag{3.24}$$

The degree to which this inequality must be satisfied is subjective, but does provide a rough guide for where one could realistically match their lattice theory to continuum physics if applicable.

The upper bound is sensible as this is around the region that large differences between momentum definitions matter, i.e $p_\mu \not\approx 2\sin(p_\mu/2)$. In practice, with current technology, this is not an easy condition to satisfy. To minimise errors in the matching to continuum perturbation theory often it is advisable to sit as close to the high end of the Rome-Southampton window as one can afford while not believing lattice artifacts dominate.

We perform an FFT over the entire configuration space lattice gluon fields $A_\mu\left(x + a\frac{\hat{\mu}}{2}\right)$ to obtain our momentum-space gluon fields. We therefore have an abundance of momentum space fields, and a filtering method should be utilised to ensure we are using only momentum modes we believe are least affected by lattice artifacts. The simplest filter being a spherical cut in momenta, whereby only momenta (Fourier modes) lying within a hypersphere (perhaps with a cavity neglecting small momenta).

Special care must be taken if there is asymmetry ($L_{x,y,z...} \neq L_t$) in the lattice volume to make sure that roughly equivalent in magnitude momenta are taken. If performing the cut with Fourier modes, this is ensured by computing the anisotropy ratios $S_\mu = \frac{L_\mu}{L_{sm}}$, where L_{sm} is the smallest direction in lattice units. Then the spherical cut becomes $(n_\mu S_\mu)^2 < n^2_{max}$. Another possible cut is the "hyper-cubic" cut, which one specifies a maximum on-axis momentum (e.g $(p, 0, \cdots, 0) = p_{max}$ and its hyper-cubic rotations), this allows the inclusion of more diagonal momenta, and fewer on-axis contributions compared to the spherical cut.

Both of these cuts allow for the inclusion of momenta which are particularly "hard" in one direction, in the free field case this would not be wise since the lattice momentum $2\sin\left(\frac{p_\mu}{2}\right)$ is more deviant from the continuum propagator for this orientation. It is therefore understood that the largest errors from gluon propagator measures are in the regime when there are zero-momentum Fourier transforms. A popular method to alleviate this difficulty is to perform a cylinder cut [114, 115] in momenta. This entails the inclusion of momenta that only lie within a cylinder along the body-diagonals of the momentum-space lattice, and is argued to reduce the $O(N_d)$ rotational symmetry breaking by the lattice and have the smallest lattice artefacts.

Following [2], we create a reference direction $\hat{n} = \frac{1}{\sqrt{N_d}}(1, 1, 1, ..., 1)$ (or one of its $2^{(N_d-1)}$ symmetrisation) and compute the variation away from this body diagonal,

$$\Delta\hat{q} = (\hat{q} - (q \cdot n)\hat{n})\,. \tag{3.25}$$

Where $q = \frac{2\pi n_\mu}{L_\mu}$. We then reject any momenta where $|\Delta\hat{q}| < \frac{2\pi}{L_{sm}}$. This definition has

the quality that it incorporates any lattice asymmetry into the definition, because we are using the lattice momentum directly.

3.4 α_s from the triple gluon vertex

Following from the gluon propagator measurements we can also define three point correlation functions,

$$G^{(3)\ abc}_{\mu\nu\rho}(p,q,r) = \frac{1}{V}\langle A^a_\mu(p)A^b_\nu(q)A^c_\rho(r)\rangle. \tag{3.26}$$

Analogously to the two point function, and using the relations from Eq.2.11 we have the trace identity for generic $SU(N_c)$ matrices in the fundamental representation,

$$\begin{aligned} \mathrm{Tr}\left[ABC\right] &= A^aB^bC^c\mathrm{Tr}\left[T^aT^bT^c\right], \\ T^aT^bT^c &= \frac{1}{2}\left(\left(if^{abc}+d^{abc}\right)T^cT^c + \frac{1}{2N_c}\delta^{ab}T^c\right). \end{aligned} \tag{3.27}$$

And so, in terms of our fields,

$$\begin{aligned} \mathrm{Tr}\left[A_\mu(p)A_\nu(q)A_\rho(r)\right] &= A^a_\mu(p)A^b_\nu(r)A^c_\rho(q)\mathrm{Tr}\left[T^aT^bT^c\right], \\ &= A^a_\mu(p)A^b_\nu(r)A^c_\rho(q)\frac{1}{2}\left(if^{abc}+d^{abc}\right)\mathrm{Tr}\left[T^cT^c\right], \\ &= A^a_\mu(p)A^b_\nu(r)A^c_\rho(q)\frac{1}{4}\left(if^{abc}+d^{abc}\right). \end{aligned} \tag{3.28}$$

The method to calculate the coupling is straightforward, and follows the standard textbook field-theoretic approach. We pick a momentum configuration satisfying a specific kinematic and compute the vertex function Γ, this is related to the three point Green's function thusly,

$$\begin{aligned} G^{(3)\ abc}_{\mu\nu\rho}(p,q,-(p+q)) = G^{(2)\ ad}_{\mu\mu'}(p,-p)G^{(2)\ be}_{\nu\nu'}(q,-q)G^{(2)\ cf}_{\rho\rho'}(-(p+q),p+q) \\ \Gamma^{def}_{\mu'\nu'\rho'}(p,q,-(p+q)). \end{aligned} \tag{3.29}$$

The three point Green's function is the vertex function contracted with three external gluon propagator legs.

We work in a momentum subtraction (MOM) scheme, the one particle irreducible (1PI) vertex function can be decomposed as,

$$\Gamma^{abc}_{\mu\nu\rho}(p,q,r) = -igf^{abc}\sum_i T^i_{\mu\nu\rho}(p,q,r), \tag{3.30}$$

where the T's are tensors of the polarisation and momentum, and one of these can be set to the standard tree level vertex,

$$\Gamma_{\mu\nu\rho}(p,q,r) = -igf^{abc}\left(g_{\mu\nu}(p-q)_\rho + g_{\nu\rho}(q-r)_\nu + g_{\rho\mu}(r-p)_\mu\right), \tag{3.31}$$

but the others will be dependent on the kinematic we use to define our scheme.

The method for determining the running coupling $g(\mu^2)$, requires the non-perturbative lattice calculation of the amputated renormalised vertex function at the scale μ to take its tree level continuum perturbative value at the renormalisation point $\mu^2 = p^2 = q^2 = r^2$.

We now discuss the exceptional or "asymmetric" scheme and the non-exceptional or "symmetric" scheme.

3.4.1 The exceptional scheme

The exceptional scheme we use is called the $\widetilde{\text{MOM}}$gg, and was first used in lattice studies in [134], and is defined at the renormalisation point μ as $p^2 = \mu^2, q = -p, r = 0$, with zero-momentum gluon polarised parallel to the direction of the momenta, and the two gluons polarised perpendicular to their momenta.

The 1PI vertex (from Eq.3.30) for an exceptional gluon configuration has Lorentz structure,

$$\begin{aligned}\Gamma^{abc}_{\mu\nu\rho}(p,-p,0) = -igf^{abc}\Big((2g_{\mu\nu}p_\rho - g_{\mu\rho}p_\nu - g_{\rho\nu}p_\mu)T_1(p^2) \\ (g_{\mu\nu} - \frac{p_\mu p_\nu}{p^2})p_\rho T_2(p^2)\Big).\end{aligned} \tag{3.32}$$

The $\widetilde{\text{MOM}}$gg scheme is defined by the renormalisation condition [51],

$$T_1(\mu^2) - \frac{1}{2}T_2(\mu^2) = 1. \tag{3.33}$$

The projector required to act upon the vertex in Eq.3.32 to pick out the scalar T's is [3, 38],

$$P^{abc}_{\mu\nu\rho}(p,-p,0) = \frac{if^{abc}}{2(D-1)N_c(N_c^2-1)}\left(\delta_{\mu\nu} - \frac{p_\mu p_\nu}{p^2}\right)\frac{p_\rho}{p^2}. \tag{3.34}$$

Continuum perturbative expressions for the matching of this scheme to the modified minimal subtraction ($\overline{\text{MS}}$) in Landau gauge up to three loops exist [51]. As the projector in Eq.3.34 is projecting onto the gluonic three point function in Landau gauge the term $\frac{p_\mu p_\nu p_\rho}{p^4}$ is proportional to the Ward identity and is zero, and so can be dropped. In

analogy to the gluon propagator we define the exceptional scalar three point function,

$$G^{(3)\ \widetilde{MOMgg}}(p^2) = \frac{1}{V}\frac{4}{2(N_d-1)N_c(N_c^2-1)}\delta_{\mu\nu}\frac{p_\rho}{p^2}\langle\Re\left(\mathrm{Tr}\left[A_\mu(p)A_\nu(-p)A_\rho(0)\right]\right)\rangle. \quad (3.35)$$

Where we have used the trace identity from Eq.3.28 to absorb the factor of $\frac{1}{4}if^{abc}$, and noting that the contribution from d^{abc} will be 0 because the vertex is antisymmetric. And so we need only take the real part of the vertex function.

Once we have the computed the exceptional scalar three point function, we extract the coupling by first amputating the gluon propagator legs to leave the 1PI vertex function, and performing the gluon field renormalisation at the momentum scale μ to obtain our $\widetilde{\mathrm{MOMgg}}$ coupling. We define the coupling as,

$$g(\mu^2) = Z_{A_\mu}^{3/2}\left(p^2\right)\frac{G^{(3)\ \widetilde{MOMgg}}(p^2)}{\left(G^{(2)}(p^2)\right)^2 G^{(2)}(0)}\Big|_{p^2=\mu^2}. \quad (3.36)$$

Which, when considering the definition of $Z_{A_\mu}\left(p^2\right)$ from Eq.3.23, can be more succinctly written as,

$$g(\mu^2) = p^3\frac{G^{(3)\ \widetilde{MOMgg}}(p^2)}{\sqrt{G^{(2)}(p^2)}G^{(2)}(0)}\Big|_{p^2=\mu^2}. \quad (3.37)$$

3.4.2 The non-exceptional scheme

The scheme defined in Sec.3.4.1, is not the only one possible for defining the lattice triple gluon vertex function. There is another combination of momenta that can be used, a triplet of non-exceptional momenta defined as,

$$p^2 = q^2 = r^2 = \mu^2, \qquad p+q+r = 0. \quad (3.38)$$

This has the benefit that no one momentum is zero, and hence evades the thorny issue of normalising by a zero momentum propagator (Sec.3.5.3).

In terms of lattice Fourier modes, this combination is not trivial to achieve. And only lattice simulations with an integer aspect ratio $L_t/L_{x,y,z...}$ can provide statistically significant data.

The first attempt to compute the non-exceptional triple gluon vertex was [41]. We disagree with this prescription however. We instead follow [98], which provides the matching from this scheme, the MOMggg to $\overline{\mathrm{MS}}$ at two loop order in continuum perturbation theory and has a projector for the vertex we agree with. The number of independent Lorentz form factors (3) identified in [98] is greater than that of [41], and we have concluded that the projection of [41] was incorrect as discussed in the

appendices of [99].

The scalar vertex function in the MOMggg scheme is defined through the projection,

$$f^{abc}G^{(3)}(p,q)^j = M^{k,l}\left(P^{l,j}_{\mu\nu\rho}G^{abc}_{\mu\nu\rho}(p,q,p-q)\right). \tag{3.39}$$

The matrix "M" is a normalisation matrix and "P" is one of the 14 Tensor structures allowed by the scheme. I define the quantity,

$$\tilde{P}^j_{\mu\nu\rho} = M^{j,k}P^k_{\mu\nu\rho}. \tag{3.40}$$

As the projector that picks out the "j$^{\text{th}}$" scalar vertex function.

The projection matrix is defined as the inverse of the matrix,

$$M^{-1}_{k,l} = N_{k,l} = \left(P^k_{\mu_1\ldots\mu_D}P^l_{\mu_1\ldots\mu_D}\right). \tag{3.41}$$

With the projectors,

$$\begin{gathered}
P^1_{\mu\nu\rho}(p,q) = \delta_{\mu\nu}p_\rho,\ P^2_{\mu\nu\rho}(p,q) = \delta_{\nu\rho}p_\mu,\ P^3_{\mu\nu\rho}(p,q) = \delta_{\rho\mu}p_\nu,\\
P^4_{\mu\nu\rho}(p,q) = \delta_{\mu\nu}q_\rho,\ P^5_{\mu\nu\rho}(p,q) = \delta_{\nu\rho}q_\mu,\ P^6_{\mu\nu\rho}(p,q) = \delta_{\rho\mu}q_\nu,\\
P^7_{\mu\nu\rho}(p,q) = \frac{p_\mu p_\nu p_\rho}{p^2},\ P^8_{\mu\nu\rho}(p,q) = \frac{p_\mu p_\nu q_\rho}{p^2},\ P^9_{\mu\nu\rho}(p,q) = \frac{p_\mu q_\nu p_\rho}{p^2},\ P^{10}_{\mu\nu\rho}(p,q) = \frac{q_\mu p_\nu p_\rho}{p^2},\\
P^{11}_{\mu\nu\rho}(p,q) = \frac{p_\mu q_\nu q_\rho}{p^2},\ P^{12}_{\mu\nu\rho}(p,q) = \frac{q_\mu p_\nu q_\rho}{p^2},\ P^{13}_{\mu\nu\rho}(p,q) = \frac{q_\mu q_\nu p_\rho}{p^2},\ P^{14}_{\mu\nu\rho}(p,q) = \frac{q_\mu q_\nu q_\rho}{p^2}.
\end{gathered} \tag{3.42}$$

The first six tensor structures appear in the tree-level Feynman rule. The normalisation matrix for generic N_d is, defined in block matrix order,

$$M = \frac{1}{27(N_d-2)p^2}\begin{pmatrix} M_{11} & M_{12} & M_{13}\\ M_{21} & M_{22} & M_{23}\\ M_{31} & M_{32} & M_{33}\end{pmatrix} \tag{3.43}$$

which is real and symmetric. The sub-matrices are,

$$M_{11} = \begin{pmatrix} 36 & 0 & 0 & 18 & 0 & 0\\ 0 & 36 & 0 & 0 & 18 & 0\\ 0 & 0 & 36 & 0 & 0 & 18\\ 18 & 0 & 0 & 36 & 0 & 0\\ 0 & 18 & 0 & 0 & 36 & 0\\ 0 & 0 & 18 & 0 & 0 & 36\end{pmatrix}, M_{12} = -\begin{pmatrix} 48 & 24 & 24 & 24\\ 48 & 24 & 24 & 24\\ 48 & 24 & 12 & 12\\ 24 & 48 & 12 & 12\\ 24 & 12 & 12 & 48\\ 24 & 12 & 48 & 12\end{pmatrix}, \tag{3.44}$$

$$M_{13} = -\begin{pmatrix} 12 & 12 & 48 & 24 \\ 48 & 12 & 12 & 24 \\ 12 & 48 & 12 & 24 \\ 24 & 24 & 24 & 48 \\ 24 & 24 & 24 & 48 \\ 24 & 24 & 24 & 48 \end{pmatrix}, \tag{3.45}$$

$$M_{22} = \begin{pmatrix} 64(N_d+1) & 32(N_d+1) & 32(N_d+1) & 32(N_d+1) \\ 32(N_d+1) & 32(2N_d-1) & 16(N_d+1) & 16(N_d+1) \\ 32(N_d+1) & 16(N_d+1) & 32(2N_d-1) & 16(N_d+1) \\ 32(N_d+1) & 16(N_d+1) & 16(N_d+1) & 32(2N_d-1) \end{pmatrix}, \tag{3.46}$$

$$M_{23} = -\begin{pmatrix} 16(N_d+4) & 16(N_d+4) & 16(N_d+4) & 8(N_d+10) \\ 8(4N_d+4) & 8(4N_d+1) & 8(N_d+4) & 16(N_d+4) \\ 8(4N_d+4) & 8(N_d+4) & 8(4N_d+1) & 16(N_d+4) \\ 8(N_d+4) & 8(4N_d+1) & 8(4N_d+1) & 16(N_d+4) \end{pmatrix}, \tag{3.47}$$

$$M_{33} = \begin{pmatrix} 32(2N_d-1) & 16(N_d+1) & 16(N_d+1) & 32(N_d+1) \\ 16(N_d+1) & 32(2N_d-1) & 16(N_d+1) & 32(N_d+1) \\ 16(N_d+1) & 16(N_d+1) & 32(2N_d-1) & 32(N_d+1) \\ 32(N_d+1) & 32(N_d+1) & 32(N_d+1) & 64(N_d+1) \end{pmatrix}. \tag{3.48}$$

And the M_{21}, M_{31}, M_{32} can be obtained from the transpose of the M_{12}, M_{13}, M_{23} matrices.

Our normalisation matrix (Matrix.3.43) has for the off-diagonal block matrices the opposite sign than that in [98] because their renormalisation condition is $p^2 = -\mu^2$. We also have the extra factor of $\frac{1}{p^2}$ in our normalisation, which comes from each $P^l P^k$ term producing the normalisation factor p^2.

We have defined the projection matrix M which allows us to generate a projector for any of the 14 scalar parts of the gluonic three point function, i.e to project out the renormalisation condition of our vertex and allow for a direct computation of the coupling in complete analogy to the exceptional kinematic Eq.3.34. Of course this is with the exception that we no longer have to perform a zero momentum gluon propagator amputation.

The projector used to match from the MOMggg to $\overline{\text{MS}}$ in [98] was $\tilde{P}^1_{\mu\nu\rho}(p,q)$. The first six projectors are numerically related, and we check this by computing the ratio,

$$R_i = \frac{G^{(3)}(p,q)^1}{G^{(3)}(p,q)^i}. \tag{3.49}$$

For the first five scalar three point functions ($i = 2, 3, 4, 5, 6$), the ratios should equal $1, -\frac{1}{2}, -1, \frac{1}{2}, -1$.

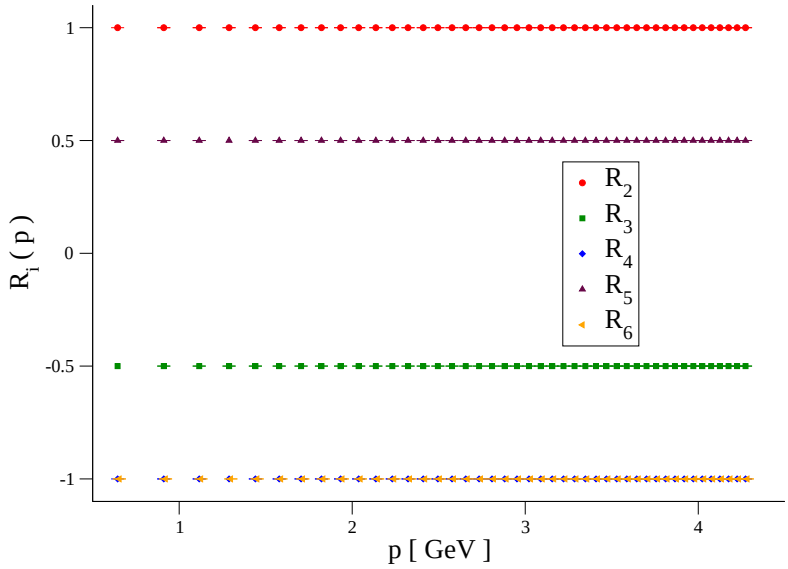

Figure 3.2 *Ratios of the respective non-exceptional projectors from Eq.3.49, from a* $32^3 \times 64, am = 0.004, ams = 0.3, \beta = 2.25$ *Iwasaki gauge ensemble. Errors are from a Jackknife analysis,* R_4 *and* R_6 *have been shifted in momentum slightly for clarity.*

Fig.3.2 shows the ratios of projectors from a Jackknife analysis, allowing for direct cancellation of the underlying field content and yielding the projector ratios. We obtain the expected ratios from [98], and so have confidence in the procedure.

These numerical relations allow us to define the projector,

$$\begin{aligned}\tilde{P}_{\mu\nu\rho}(p,q) = \frac{1}{6}\Big(& \tilde{P}^1_{\mu\nu\rho}(p,q) + \tilde{P}^2_{\mu\nu\rho}(p,q) \\ & - \frac{1}{2}\tilde{P}^3_{\mu\nu\rho}(p,q) - \tilde{P}^4_{\mu\nu\rho}(p,q) \\ & + \frac{1}{2}\tilde{P}^5_{\mu\nu\rho}(p,q) - \tilde{P}^6_{\mu\nu\rho}(p,q)\Big).\end{aligned} \tag{3.50}$$

which is,

$$\begin{aligned}\tilde{P}_{\mu\nu\rho}(p,q) = \frac{1}{18(N_d-2)p^2}\Big(& (2\delta_{\mu\nu}(q_\rho - p_\rho) - \delta_{\nu\rho}(4q_\mu + 5p_\mu) + \delta_{\rho\mu}(5q_\nu + 4p_\nu)) \\ & + \frac{2}{p^2}\left(p_\mu q_\rho(q_\nu - p_\nu) + q_\nu p_\rho(q_\mu - p_\mu)\right) \\ & + \frac{4}{p^2}\left(p_\nu p_\rho(q_\mu - p_\mu) - q_\mu q_\rho(q_\nu + p_\nu)\right)\Big).\end{aligned} \tag{3.51}$$

It should be noted that this is a different projector than the one defined in [40, 41], even though they are supposedly describing the same scheme. We have tested this projector

by contracting it with the tree level vertex function and it gives a value of 1.

And in complete analogy with the exceptional $\widetilde{\text{MOMgg}}$ case, we define the non-exceptional scalar three point function,

$$G^{(3)\ MOMggg}(p^2) = \frac{1}{V}\frac{4}{N_c(N_c^2-1)}\langle \tilde{P}_{\mu\nu\rho}(p,q)\Re\left(\text{Tr}\left[A_\mu(p)A_\nu(q)A_\rho(-(p+q))\right]\right)\rangle. \tag{3.52}$$

To check our calculation, we perform a test with four $16^3 \times 32$ configurations fixed to Landau gauge. With which, we check the color structure and antisymmetric nature of the vertex function. This is performed via the Lie elements of our gauge fields and using either the symmetric or antisymmetric structure functions. From Fig.3.3 we note

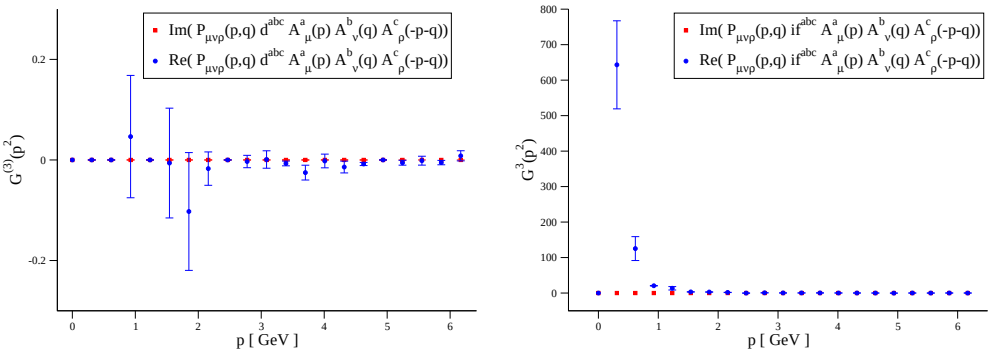

(a) *The symmetric part.* **(b)** *The antisymmetric part.*

Figure 3.3 *The color symmetric and antisymmetric parts of our unrenormalised, non-exceptional gluonic three point correlation function calculation. From four Landau gauge-fixed* $16^3 \times 32, \beta = 2.13$ $N_f = 2+1$ *Domain Wall configurations. The errors are from a jackknife procedure.*

that the symmetric contribution is zero within statistical errors, and only the real part of the if^{abc} color projection contributes.

Eq.3.52 allows us to directly write the coupling for this scheme,

$$g(\mu^2)^{MOMggg} = Z_{A_\mu}^{3/2}\left(p^2\right)\left.\frac{G^{(3)\ MOMggg}(p^2)}{\left(G^{(2)}(p^2)\right)^3}\right|_{p^2=\mu^2}. \tag{3.53}$$

Once we have computed the renormalised gauge coupling $g(\mu^2)$ from our lattice simulation in our desired scheme, we convert it to the more commonly used measure the strong coupling $\alpha_s(\mu)$,

$$\alpha_s\left(\mu^2\right) = \frac{g\left(\mu^2\right)^2}{4\pi}. \tag{3.54}$$

We then must match to continuum perturbation theory and perform the running of the coupling defined by that scheme's β-function to obtain our result at the oft-quoted Z-boson mass scale.

3.4.3 Technical remarks

Picking the relevant momenta that satisfy the momentum condition $p+q+r=0, p^2 = q^2 = (p+q)^2$ is difficult. Our implementation requires several steps, first a spherical cut to remove the high p^2 edge effects from the Brillouin zone and then a recursive iteration through momenta checking the momentum conservation at the vertex, we do this recursively so that the routine can be N_d-generic. At every p^2 we generate a list of the triplets that satisfy the momentum condition, we then compute the N_d^3 projectors (one for each polarisation combination $\mu\nu\rho$), and store these as well. These two caching techniques are invaluable in this analysis.

For both the $\widetilde{\text{MOM}}$gg and the MOMggg schemes, we require the computation of the trace of the product of three matrices $\text{Tr}\left[A_\mu(p)A_\nu(q)A_\rho(r)\right]$. And up to N_d^3 times per triplet for the MOMggg. We have a general expression for the trace of the product of three generic matrices, which is shown in Alg.1 and provides significant ($O(3\times)$ for SU(3)) speed-up over performing the product and then taking the trace.

Algorithm 1 *Generic trace of the product of three (ABC) lexicographically-ordered row-major $N_c \times N_c$ matrices.*

$tr \leftarrow 0$
for $i = 0 \rightarrow N_c^2$ **do**
  $Prod \leftarrow 0$
  for $j = 0 \rightarrow N_c$ **do**
    $Prod \leftarrow Prod + A[j + N_c(i\%N_c)]B[jN_c + \lfloor i/N_c \rfloor]$
  end for
  $tr \leftarrow tr + C[i] * Prod$
end for

3.5 Gluonic correlator measurements

In this section we measure the two building blocks for our strong coupling evaluation. The gluon propagator and the gluonic three point function. We use the ensembles introduced in Tab.3.1 and define our physical momenta $p_\mu = \frac{2}{a}\sin\left(\frac{p_\mu}{2}\right)$. Labels of momenta p in GeV are $\sqrt{p_\mu p_\mu}$.

3.5.1 The exact log propagator

We have investigated the renormalised Landau gauge gluon propagators in four dimensions (renormalised at 2.5 GeV) of the same fields with the four gauge fixings

discussed in Sec.6.8 and their field renormalisation $Z_{A_\mu}(p^2)$ (Eq.3.23). With the intention of understanding whether there was any statistical reduction or other benefit in using an exact field definition, or using a derivative with more terms in the gauge fixing procedure.

Fixing $-\alpha$ is the standard Fourier-Accelerated Cornell approach with symmetric finite difference of Hermitian projected (Log-A in the notation of Appendix A) fields and reunitarisation in its exponential. Fixing $-\beta$ is the same as Fixing $-\alpha$ but uses the nearest neighbour derivative. Fixing $-\chi$ uses the symmetric finite difference of exact Hermitian projected (Log-C) fields and exact exponentiation as described in Sec.A.2.3 of Appendix A and Fixing $-\delta$ is the same but with the nearest neighbour derivative. For consistency, we use the same field definition for the gluon propagator as was used in the derivative for the gauge fixing.

For this investigation we used 24, $16^3 \times 32$, $\beta = 2.13$, $am_l = 0.01$ configurations separated by Monte Carlo time of 100. The results are shown in Fig.3.4.

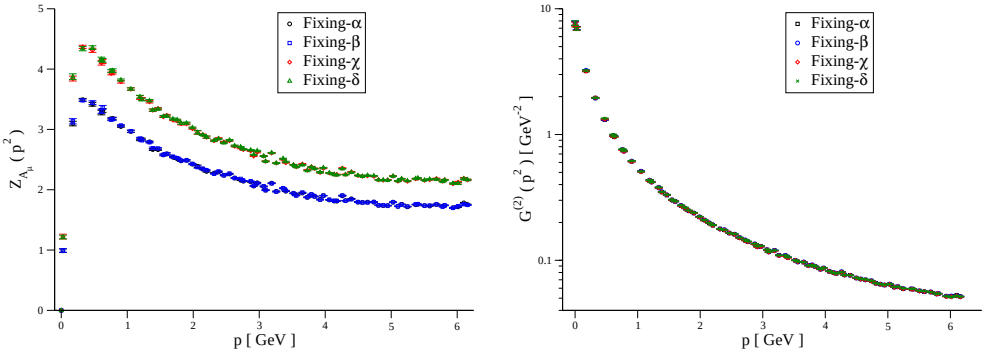

(a) *The gluon field renormalisation* $Z_{A_\mu}(p^2)$

(b) *The renormalised gluon propagator*

Figure 3.4 *The Landau gauge gluon field renormalisation* $Z_{A_\mu}(p^2)$ *is shown in (a) for the Landau gauge fixing methods detailed in Sec.6.8. Their propagators renormalised at* $\mu = 2.5$ *GeV are shown in (b). A cylinder cut was applied and the momentum definition used in the scale was the sine definition. Some O(4)-breaking scatter is evident in the renormalisation constants, due to the small volume.*

Although the field renormalisation factors of Fig.3.4 are different for the logarithmic definition (Log-C A.1.3) of the gauge fields compared to the linear definition (Log-A A.1.1) (fixings α and χ), we see that after renormalisation all of the gluon propagators from all the fixing types are comparable within error. This is evidence to suggest that renormalised quantities are not affected by the field definition and the gauge fixing functional definition. There appears to be no reduction in the statistical error by using any of the improved fixing methods and derivatives, and so we continue our study with the computationally cheapest (as seen in Tab.6.1) standard method of [62], that of Fixing-α i.e. The linear (Log-A) definition of the fields and the symmetric finite

difference derivative with reunitarisation in the exponentiation (A.2.2).

3.5.2 Gribov copies

To assess the impact of Gribov copies in our work, we computed the so called worst and best copies for a set of thermalised $16^3 \times 32$ configurations. The worst copy being the copy that gave the largest gauge fixing functional from 150 randomly gauge transformed copies of each configuration, and the best copy being the one that minimised the gauge fixing functional. The best copies were attained using the smeared-preconditioned method, described in Chapter 1, Sec.6.7.3.

Once this had been performed for an appreciable number of configurations (30 with separation 100 in Monte Carlo time), we measured the unrenormalised gluon propagator $G^{(2)}(p^2)$.

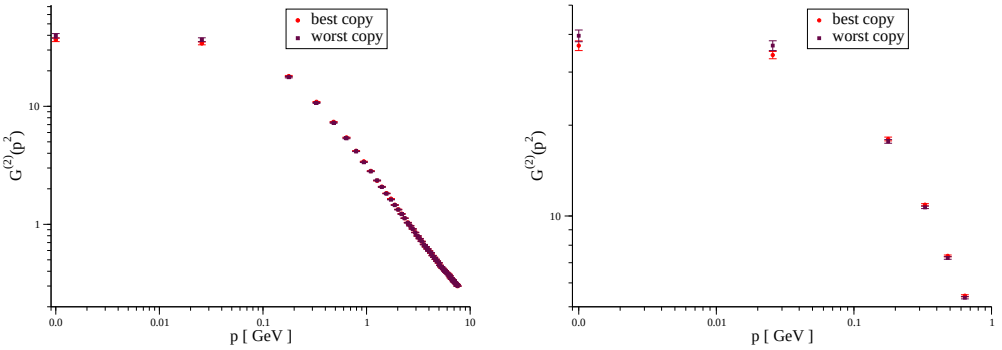

(a) *Log-Log plot of the propagator.* **(b)** *A zoom into the IR.*

Figure 3.5 *The unrenormalised gluon propagator for the best and worst from 150 random gauge transformations per 30 well-separated* $16^3 \times 32$*, $N_f = 2+1$ Domain Wall configurations. The zero momentum mode has been shifted so that it can be included in the log-log plot.*

Fig.3.5 illustrates a measurement of the Landau gauge gluon propagator using the worst and best from 150 Gribov copies of 30 configurations. It seems that whatever effect Gribov copies play for this measure it is slight (as long as we are properly sampling the space of copies effectively and the gauge fixing functional is the best measure for Gribov effects) as also seen in [148] and exists in the low momentum region (IR), with only one mode (the (0,0,0,1)) not overlapping between copies within statistical errors.

As in Fig.3.4, we see the expected $\frac{1}{p^2}$ behaviour, but in the low momentum IR region we see a change from this. This is widely construed as the gluon having an effective dynamically-generated mass [123]. A form for the gluon propagator of $G^{(2)} = \frac{1}{p^2+m^2}$ would cause this, however phenomenology of the IR limit of QCD is difficult in a finite volume (as we will see in Sec.3.5.3) and not the subject of this thesis.

There appears to be little distinction from the zero momentum mode and the first Fourier mode, but both require different normalsation (Sec.3.3). There appears to be a trend in the IR for the best copy having a lower-valued gluon propagator compared to the worst copy, although this could just be due to statistical fluctuations, similar effects have been seen in previous studies [33, 149]. In an earlier study on smaller 12^4 quenched ($N_f = 0$) lattices [144] with the unimproved Wilson plaquette action, slightly more significant deviation between copies was found, perhaps due to less precise gauge fixing than that used here.

Ultimately, apart from the very lowest modes, Gribov copies play a seemingly negligible rôle in the high renormalisation scale gluon phenomenology we are interested in at the level of statistical resolution we have available. However, our exceptional scheme evaluation of the amputated Landau gauge triple gluon vertex does require the amputation of a zero momentum propagator. So one could worry that Gribov effects will be manifest, but this is not the only issue with amputation of a maximally infra-red propagator.

3.5.3 The zero momentum propagator

The definitions of the gluon propagator thus far hold for an isotropic lattice. Our configurations are asymmetric, with larger temporal extent than spatial. It is assumed that this does not, and should not affect the physics of obsevables dependent only on shorter length scales than this volume and does not change quantities such as the lattice spacing. We intend to follow previous work and compute the renormalised strong coupling $\alpha_s(\mu)$ using the Landau gauge triple gluon vertex, and one of the schemes we use (the exceptional kinematic Sec.3.4.1) requires amputation by a zero momentum gluon propagator. One might suspect (with hindsight) that the propagator at zero momentum will be the most sensitive to the lattice geometry as any deviation between polarisations should only be a finite volume affect and the zero momentum propagator is clearly the most susceptible to finite volume corrections.

For asymmetric lattices, studies have found that the polarisations of the zero momentum gluon are in general distinct [114]. We study whether this is the case for our ensembles via the ratios at some high-scale reference point p_0 (where i is the spatial polarisation index and t is the temporal, we average over the spatial indices i hence the $N_d - 1$ norm),

$$\frac{\sum_{i \neq t} G_{ii}(0)}{(N_d - 1)G^{(2)}(p_0^2)}, \qquad \frac{G_{tt}(0)}{G^{(2)}(p_0^2)}. \tag{3.55}$$

If the zero momentum gluon propagator is a well motivated observable for matching to

infinte volume perturbation theory then any asymmetry induced in the zero momentum propagator should disappear in the infinite volume limit. Since this ratio is the field being renormalised at the point p_0 multiplied by p_0^2, if we fix the reference scale p_0, direct comparison between all of our available ensembles can be made, up to lattice artifacts that are mild because both the zero momentum mode and the reference scale p_0 are well below the cut-off scale.

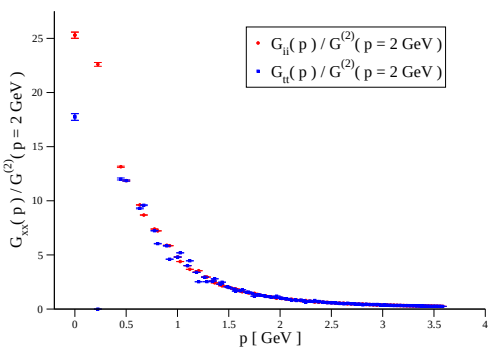

(a) *Spatial and temporal polarised gluon propagators.*

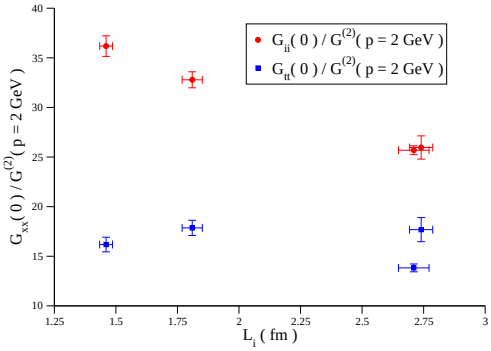

(b) *Chiral limit polarisation ratios vs. spatial lattice extent.*

Figure 3.6 *Normalised Landau gauge gluon propagators. Fig.(a) shows the self-normalised at 2 GeV temporally and spatially polarised gluon propagators. We see large finite volume effects at low momentum. Fig.(b) shows that this effect is present for different physical spatial volumes. The aspect ratio induces a breaking of Euclidean symmetry at zero momentum even for our largest volume.*

Fig.3.6 shows that in the infra-red region there is a very large discrepancy between the temporally and spatially polarised zero momentum gluon propagator normalised at a reference scale that should be available to all of the configurations. Furthermore, by plotting this ratio versus the physical spatial lattice length L_i, we see that no coherent infinite volume limit is reached for our ensembles. We conclude that the asymmetry in our lattice volume is influencing the zero momentum gluon propagator and we do not see any theoretically correct way for one to match the exceptional three gluon vertex with a zero momentum propagator leg, to infinite volume perturbation theory.

Attempts have been made to normalise the zero momentum gluon propagator in such a way to account for this difference between polarisations [145] but it is not obvious this has any theoretical control. As one can ask, which polarisation (the asymmetric or the symmetric) direction's propagator is the more physical? This discussion makes prescriptions such as the $\frac{1}{N_d}$ norm for the 0-momentum propagator seem ad-hoc.

Our study casts large doubt on the computation of the QCD strong coupling using an exceptional kinematic triple gluon vertex measurement as it is unclear how we normalise the zero-momentum gluon leg appropriately. Although it appears that in the infra red of our theory the gluon propagator suffers from large finite volume errors, at higher

momenta ($> 1GeV$) from Fig.3.6(a) we see that the gluon polarisations all behave similarly. We take this as motivation to study a kinematic which requires gluon legs to retain $p^2 = \mu^2$, and therefore we need perform no zero-momentum gluon amputation. This is why we chose to investigate the non-exceptional kinematic.

3.5.4 Investigation of the gauge fixing accuracy

In [134] it was noted that high gauge fixing accuracy was necessary for reliable measurement of the gluonic three point function, where the author worked with fixed number of gauge fixing iterations rather than overall accuracy, and saw a large discrepancy for a $24^3 \times 48$ quenched lattice ensemble for the $\widetilde{\text{MOMgg}}$ scheme gluonic three point function. The author compared the results of the scalar three point function on a single configuration with 500,1400 and 1600 iterations of their Landau gauge fixing code. As we have seen in the previous chapter, a fixed number of iterations does not provide a fixed accuracy and while the steepest descent's algorithm is still integrating out Fourier modes the gauge fixing accuracy fluctuates quite wildly. This can be seen in Fig.6.1. In later publications the author uses fixed accuracy of 10^{-11}[3], which was the best they could do as they were working in single precision.

To investigate the level of Landau gauge fixing accuracy required for the computation of the gluon propagator and three point function we measured 80 $16^3 \times 32$ configurations' gluonic two and $\widetilde{\text{MOMgg}}$ three point functions at fixed accuracies of $\Theta = 10^{-5},\ 10^{-8},\ 10^{-11},\ 10^{-14}$ and 10^{-20}, the three point function was the most illustrative in this study, as the gluon propagator fluctuated far less with varied gauge fixing accuracy, and so is not shown. A cylinder cut in momenta has been taken, as well as a fuzzy momentum average where momenta within a range $\left|(ap)^2 - (ap')^2\right| < 0.05$ are considered indistinct and averaged for visual clarity.

From Fig.3.7 we can see that there is sensitivity to the gauge fixing accuracy for a single configuration, although we must note that the scatter of data is large. For this single example configuration the discrepancy between 10^{-8} and 10^{-11} can be large for many momenta, and that after 10^{-11} it appears we have converged. If we consider the zoom, we see that we are still converging even between accuracies of 10^{-14} and 10^{-20}, although the correction here is very small. The correction for this example configuration from accuracy 10^{-11} to 10^{-14} is 0.007% and between 10^{-14} to 10^{-20} is 0.0002%.

If we then consider Fig.3.7(c), we can see that for 80 configurations there are only a few momenta that disagree within statistical errors over the range of accuracies measured. Illustrating that for this measure statistical error appears to dominate, this can be seen by the scatter of the data in (a). Considering the error of the point at 2 GeV in (c),

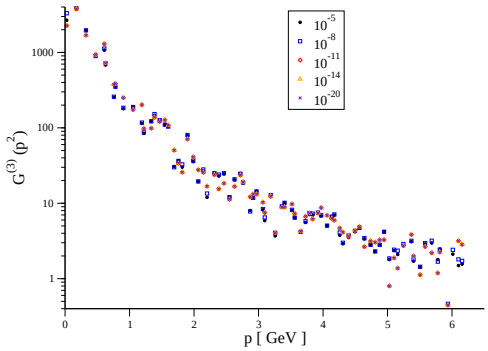

(a) *$G^{(3)}(p^2)$ for an individual configuration.*

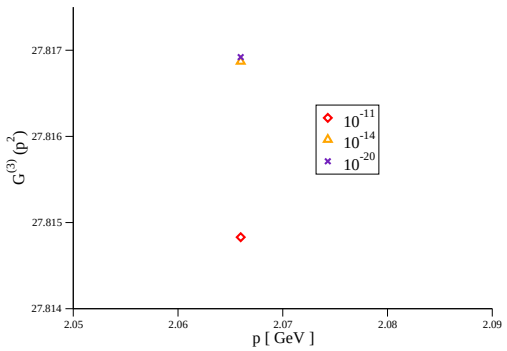

(b) *Zoom for higher accuracies.*

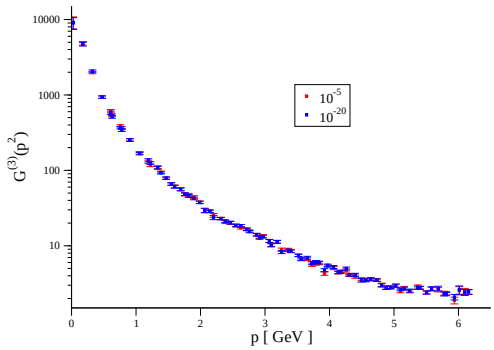

(c) *Average over 80 configurations.*

Figure 3.7 *(a) and (b) show an individual* $16^3 \times 32$ *configuration's* $G^{(3)}(p^2)$ *using the exceptional kinematic for various gauge fixing accuracies* $\Theta = 10^{-5}$, 10^{-8}, 10^{-11}, 10^{-14} *and* 10^{-20} *against physical momenta, with (b) being a zoom around the closest momentum point to 2 GeV to illustrate convergence. (c) is an average over the 80 configurations with Jackknife errors for accuracies* 10^{-5} *and* 10^{-20}.

which is measured to be 6.7%, and assuming the usual Monte-Carlo error reduction of $\frac{1}{\sqrt{N}}$, to be able to see a correction of 0.007% we would need $O(10^6)$ configurations, which is unfeasible.

This does not entirely mean we should not fix to an accuracy of $\Theta = 10^{-14}$ or higher, as for individual configurations the point at which all Fourier modes have converged in the gauge fixing is difficult to ascertain apriori, although it appears that for this coupling and volume, fixing to around 10^{-11} suffices. To make sure corrections due to the accuracy of the fixing in the procedure are as small as possible it does make sense to converge to as high an accuracy if the resources and particularly fast routines are available. This argument applies as well for the non-exceptional kinematic which suffers from larger statistical fluctuations.

The gluon propagator is even better behaved, with all momenta overlapping statistically between 10^{-5} and 10^{-20} gauge fixing accuracy for the average over the 80 configurations and is not shown for this reason. It is common in the field to err on the side of caution

and fix to $\approx 10^{-15}$ accuracy, and then justifiably remove this effect from the systematic error estimation.

3.6 Matching and running

Ideally we wish to match our lattice result to continuum physics. To do so, we must use continuum perturbation theory. Expressions for the scheme-dependent β functions in the exceptional and non-exceptional schemes for the coupling, are known at four and three loop order respectively in continuum perturbation theory. And so, matching coefficients from these schemes to $\overline{\text{MS}}$ are known at the three and two loop order respectively.

If the coupling is calculated for our MOM schemes $\left(h^{MOM}\left(\mu^2\right) = \frac{\alpha^{MOM}\left(\mu^2\right)}{4\pi}\right)$ in terms of the $\overline{\text{MS}}$ coupling $\left(h\left(\mu^2\right) = \frac{\alpha^{\overline{\text{MS}}}\left(\mu^2\right)}{4\pi}\right)$. In Landau gauge the following relation holds [51],

$$\beta^{MOM}(h^{MOM}\left(\mu^2\right)) = \frac{\partial h^{MOM}\left(\mu^2\right)}{\partial h^{\overline{\text{MS}}}\left(\mu^2\right)}\beta^{\overline{\text{MS}}}\left(\mu^2\right). \tag{3.56}$$

Where the coefficients of the $\overline{\text{MS}}$ β function are known to five loop order from [140].

The following expressions relating the couplings in our scheme's to those of $\overline{\text{MS}}$ below are valid for any generic $SU(N_c)$, 4D gauge theory with number of fermions N_f, fermion representation T_f and group theoretical Casimirs CF and CA and coupling h in the Landau gauge.

Factor	Fundamental	Adjoint	2 S	2 AS
C_A	N_c	N_c	N_c	N_c
T_f	$\frac{1}{2}$	N_c	$\frac{N_c+2}{2}$	$\frac{N_c-2}{2}$
C_F	$\frac{N_c^2-1}{2N_c}$	N_c	$\frac{N_c^2-1}{2N_c}$ $\frac{2(N_c+2)}{N_c+1}$	$\frac{N_c^2-1}{2N_c}$ $\frac{2(N_c-2)}{N_c-1}$

Table 3.2 *Table of the group theoretical factors for several different fermion representations, the Fundamental, the Adjoint, the Two Index Symmetric and the Two Index Antisymmetric. For an $SU(N_c)$ gauge theory.*

$$
\begin{aligned}
h^{\widetilde{MOM}gg} = h &+ h^2(7.777777778\ C_A - 4.888888889\ N_f T_f) \\
&+ h^3(+94.47015477\ C_A^2 - 98.22139350\ C_A N_f T_f \\
&\quad - 7.100422883\ C_F N_f T_f + 18.56790123\ N_f^2 T_f^2) \\
&+ h^4(+1395.382550\ C_A^3 - 46.29934612\ C_A^2 C_F \\
&\quad - 2022.356053\ C_A^2 N_f T_f - 133.0854651\ C_A C_F N_f T_f \\
&\quad - 11.52771527\ C_F^2 N_f T_f + 778.9761348\ C_A N_f^2\ T_f^2 \\
&\quad + 54.98235669\ C_F N_f^2 T_f^2 - 62.33196159\ N_f^3 T_f^3).
\end{aligned}
\tag{3.57}
$$

The coupling in the non-exceptional scheme in terms of the $\overline{\rm MS}$ one (h) is known to one fewer order in perturbation theory, [98],

$$
\begin{aligned}
h^{MOMggg} = h &+ h^2(+8.830829625\ C_A - 6.833612869\ N_f T_f) \\
&+ h^3(+106.7180798\ C_A^2 - 130.1598169\ C_A N_f T_f \\
&\quad - 10.26792816\ C_F N_f T_f + 30.74957207\ N_f^2 T_f^2).
\end{aligned}
\tag{3.58}
$$

$$
\begin{aligned}
\beta^{\widetilde{MOM}_{gg}} = &-h^2(+3.666666667\ C_A - 1.333333333\ N_f T_f) \\
&-h^3(+11.33333333\ C_A^2 - 6.666666667\ C_A N_f T_f - 4.0\ C_F N_f T_f) \\
&-h^4(+89.33912715\ C_A^3 - 71.74729115\ C_A^2 N_f T_f \\
&\quad - 17.70155057\ C_A C_F N_f T_f + 2.000000000\ C_F^2 N_f T_f \\
&\quad - 16.73361526\ C_A N_f^2 T_f^2 - 5.199436156\ C_F N_f^2 T_f^2 \\
&\quad + 7.111111111\ N_f^3 T_f^3) \\
&-h^5(+1135.391008\ C_A^4 - 339.5285382\ C_A^3\ C_F + 409.7906966\ N_c^2 \\
&\quad + 11.38307490\ N_c^4 - 76.23150084\ N_c N_f - 12.70525014\ N_c^3 N_f \\
&\quad - 7.933051411 N_f^2 + \frac{23.79915423\ N_f^2}{N_c^2} + 1.322175235\ N_c^2 N_f^2 \\
&\quad - 1589.590058\ C_A^3 N_f T_f + 416.3021772\ C_A^2 C_F N_f T_f \\
&\quad - 224.3376123\ C_A\ C_F^2 N_f T_f + 46.00000000\ C_F^3 N_f T_f \\
&\quad + 771.3583269\ C_A^2 N_f^2 T_f^2 - 371.3790348\ C_A C_F N_f^2 T_f^2 \\
&\quad + 6.342641472\ C_F^2 N_f^2 T_f^2 - 328.9674000\ C_A N_f^3 T_f^3 \\
&\quad + 88.35330018\ C_F N_f^3\ T_f^3 + 63.20987654\ N_f^4 T_f^4 \\
&\quad + 59.83572140\ C_A C_F N_f^2 T_f^2).
\end{aligned}
\tag{3.59}
$$

By comparing term by term the expansion of the MOM-scheme couplings in terms of the $\overline{\rm MS}$, we can readily see that the two schemes are similar in magnitude and sign of their

respective N_f, C_F and C_A terms. Suggestive of the two schemes behaving similarly and having similar perturbative errors. The generic β functions for the $\widetilde{\text{MOMgg}}$ and the MOMggg schemes in Landau gauge are written in numerical form in Eqs.3.59 and 3.60.

The β-function is scheme independent until $O(h^4)$ terms and higher. For the non-exceptional $\widetilde{\text{MOMgg}}$ scheme for generic $SU(N_c)$ and representation of fermions, and only including the scheme dependent part of the β-function, we have,

$$\begin{aligned}\beta^{MOMggg} = \beta^{\widetilde{MOM}_{gg}}&(2 \text{ loops}) \\ -h^4(&- 58.18460726\, C_A^3 - 10.88782370\, C_A^2 N_f T_f \\ &+ 25.10352918\, C_A C_F N_f T_f - 2.000000000\, C_F^2 N_f T_f \\ &+ 85.56160742\, C_A N_f^2 T_f^2 + 8.754991712\, C_F N_f^2 T_f^2 \\ &- 21.26492370\, N_f^3 T_f^3).\end{aligned} \tag{3.60}$$

The simulations we use are $\beta = 2.13,\ 2.25$, $N_f = 2{+}1$ Domain Wall Fermion simulations with inverse lattice spacings $a^{-1} = 1.73(3),\ 2.28(3)\ GeV$ respectively. We intend to match to continuum perturbation theory near the edge of our Rome Southampton window, where the perturbative errors are smallest and we still have control over our discretisation errors. This suggests that we intend on matching our simulation to theory at a scale above that of the Charm quark threshold. As our simulated theory is $N_f = 3$ in a region where physically there are four active quark flavours at accessible momenta. We need to perform perturbative running to the charm threshold using $N_f = 3$ running and match to $N_f = 4$ running. To quote our result at M_z we also have to run our coupling numerically.

3.6.1 Running the coupling

To run the perturbative coupling in some scheme M to some scale μ, we must integrate Eq.3.2. This is performed numerically, and it is pertinent to consider the running in logarithmic scale, consider the Taylor expansion,

$$\alpha\left(\ln(\mu) + \frac{h}{2}\right) = \alpha(\ln(\mu)) + \frac{h}{2}\frac{d\alpha(\mu)}{d\ln(\mu)} + O(h^2). \tag{3.61}$$

The derivative term is the β-function, and so the prescription for numerically integrating the coupling is the evaluation,

$$\begin{aligned} \alpha\left(\ln(\mu)+\frac{h}{2}\right) &= \alpha(\ln(\mu)) + h\beta(\mu) + O(h^2), \\ \mu &= \mu\, e^{\frac{h}{2}}. \end{aligned} \tag{3.62}$$

This defines a typical Euler integration step, extension to an RK4 procedure is simple and it is common to use an adaptive RK4 procedure [142], we use the embedded Cash-Karp adaptive RK4[138]. If we have a fixed step size integrator we can precompute the exponential and the method only requires computation of the β-function and the updating of the scale. If we overstep past our target scale μ' to some scale μ, we must perform the adjustment step in the procedure (by a single RK4 step),

$$h = \ln\left(\frac{\mu}{\mu'}\right). \tag{3.63}$$

To illustrate the differences between our two MOM-schemes and the $\overline{\text{MS}}$, we compute the running of $\alpha^{\overline{MS}}(\mu)$ using Eq.3.62 with fixed step-size RK4 integration procedure and step $h = 0.001$ for fixed $N_f = 3$, for SU(3) gauge theory with fermions in the fundamental representation. We choose a value $\alpha^{(\overline{MS})}(M_z) = 0.106$[2], and run it to $\mu = 2\ GeV$, we also compute the couplings in Eqs.3.57, 3.57 from the $\overline{\text{MS}}$ coupling for comparison. We fix the number of flavours so that we do not have to incorporate threshold matching for the $\overline{\text{MS}}$ scheme.

Fig.3.8 shows the magnitude of the couplings as they approach a low energy scale from a frozen-in $N_f = 3$ high scale. We see there is little difference between the two MOM-schemes and both have significantly larger couplings than the $\overline{\text{MS}}$ scheme, and both seem to diverge at low scales. This is a surprise as it is quite often the case that non-exceptional schemes are much better behaved than their exceptional counterparts for fermionic quantities, for example in the renormalisation of fermionic bilinears large reductions in the next leading order term were seen [150], and one may have hoped this would translate to gluonic Green's functions. As a rough estimate for the next-order correction to the coupling in the MOMggg scheme we might take the correction between two and three loops in the $\widetilde{\text{MOM}}$gg scheme.

There are some causes for concern from Fig.3.8, because we see that the perturbative series is not particularly well-behaved for the MOM-schemes at matching scales available to current lattice simulations as we can see from our ensembles in Tab.3.1. We

[2]This value was obtained by running the $N_f = 5$ world average value $\alpha(M_z) = 0.1184$ down to the charm mass, through thresholds and run up to 3 GeV in the three flavour theory. We then run this value to M_z in the fixed three flavour theory.

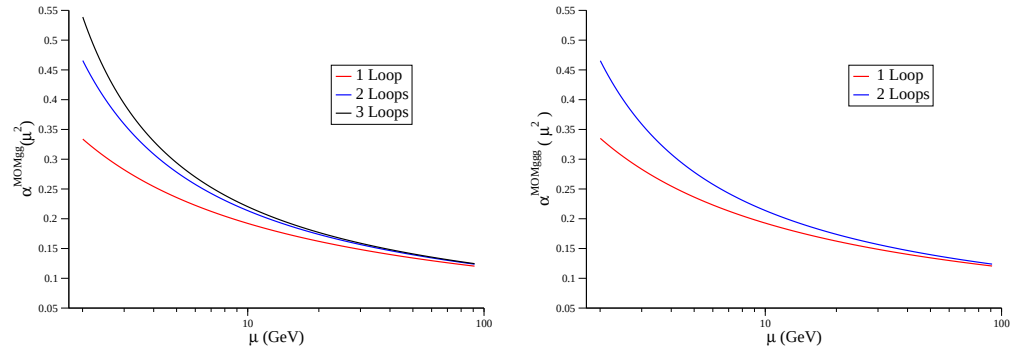

(a) *$\widetilde{MOMgg}$ scheme (exceptional).* **(b)** *MOMggg scheme (non-exceptional).*

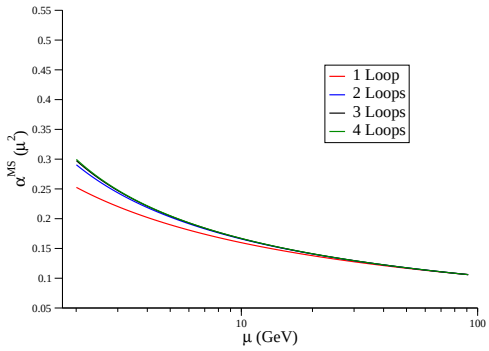

(c) *$\overline{MS}$ scheme.*

Figure 3.8 *The convergence at different loop orders for frozen $N_f = 3$ QCD.*

note that there is a 5% correction between two and three loop order for the $\widetilde{\text{MOMgg}}$ scheme even at 10 GeV! Suggestive of the series converging very slowly. It is also of great concern that the MOM-scheme couplings are diverging at around 2 GeV, in practice for QCD this means we cannot run to the Charm mass threshold and match to the physical $N_f = 4$ theory in either of the MOM-schemes. Instead, we must match directly to $\overline{\text{MS}}$ at our lattice scale, and run in that scheme. For this theory, $\overline{\text{MS}}$ is a much better behaved scheme at the scales we currently have available, a similar argument was made in [122] where running in the $\overline{\text{MS}}$ was used instead of a MOM-scheme to alleviate higher order perturbative truncation errors.

If there are two perturbative schemes with known matching between them, one of which is perturbatively benign around the Charm mass and one which is sick in the IR around the Charm mass, one could convert between the sick and benign schemes at a high scale where both schemes are convergent, and run down to Charm mass in the benign scheme to match to the correct N_f. It would clearly be better to repeat the calculation with a fine lattice spacing and $N_f = 2+1+1$ (i.e. a dynamical Charm quark), but this option is not available.

To determine the coupling in $\overline{\text{MS}}$ for QCD we use a Newton-Raphson method (Halley's) with initial guess for the coupling as that of the MOM-scheme, and solve for the real

root of Eqs.3.58 and 3.57 in terms of the $\overline{\text{MS}}$ coupling h. We then run to the on-shell Charm quark mass (1.6 GeV) to match to the physical $N_f = 4$ theory at that scale. A successive matching to $N_f = 5$ theory through the Bottom quark mass (4.7GeV) threshold is also required for quoting our results at M_z.

3.6.2 Threshold matching

We will be performing the running in $\overline{\text{MS}}$, we must match through quark mass thresholds from a theory with $N_f - 1$ to N_f active quark flavours, or vice versa. This is performed explicitly using the language of effective field theories, whereby we have a heavy quark mass m_h much above our scale μ which does not interact with our light flavours. It is said to have decoupled from the theory.

At some scale $\mu \approx m_h$ the heavy quark interactions are turned on by hand explicitly, and we go from a $N_f - 1$ to an N_f theory. There is some arbitrary-ness in the precise scale at which one performs the matching between the two theories. Fortunately in $\overline{\text{MS}}$ threshold matching is an $O(\alpha^2)$ effect, so at leading order and next leading order $\alpha^{(N_f-1)} = \alpha^{(N_f)}$. To perform the matching consistently, threshold matching at the order of one loop less than the running should be used [52, 53].

As we wish to perform the running and flavour matching for QCD, we express the threshold matching coefficients in terms of the on-shell scheme, and turn on the threshold matching at the point where $\mu = M_h$, the physical on shell mass. This choice benefits us by cancelling any $\log\left(\frac{\mu^2}{M_h^2}\right)$ terms in the series.

We are left with the following numerical form for the matching down from N_f to $N_f - 1$,

$$\alpha^{(N_f-1)}(\mu) = \zeta^2(\mu)\alpha^{(N_f)}(\mu), \tag{3.64}$$

where $\zeta^2(\mu)$ for 4 loop running of the β-function for QCD in the on-shell scheme is,

$$\begin{aligned}\zeta^2(\mu = m_h) =& 1 - 0.02955201190(\alpha^{(N_f)})^2 + \\ & (- 0.1717036285 + (N_f - 1)0.008465086429)(\alpha^{(N_f)})^3.\end{aligned} \tag{3.65}$$

Although it is quite common to use an inverse series for the upward ($N_f - 1 \to N_f$) threshold matching [52, 53, 142], we instead solve Eq.3.64 for the real root of $\alpha^{(N_f-1)}$ using a Newton-Raphson method, so that if we run forward through a threshold and then backward through the same threshold to the same starting point we have the same initial coupling that we started with up to the accuracy of the integrator, this behaviour is not guaranteed by using the inverse series.

To illustrate the contribution threshold matching makes, we run the perturbative coupling in $\overline{\text{MS}}$ from $\alpha^{N_f=5}(M_z) = 0.118$ down to the on-shell Bottom quark mass threshold $M_b = 4.7\ GeV$, perform the matching from Eq.3.65 and then run down to the on-shell Charm quark mass $M_c = 1.6\ GeV$. At successive perturbative orders, with and without threshold matching.

Perturbative order	$\alpha^{\overline{\text{MS}}}_{N_f=4}(M_c)$ (with decoupling)	$\alpha^{\overline{\text{MS}}}_{N_f=4}(M_c)$ (without)
1	0.291790	0.291790
2	0.331858	0.331858
3	0.336412	0.337191
4	0.337862	0.339470

Table 3.3 *Table illustrating the effect threshold matching (decoupling) has, when running through the Bottom mass threshold.*

Tab.3.3 shows that the inclusion of threshold matching in our region of interest is small, of the order of half a percent or so with the four loop expression for the β-function.

3.7 Numerical results

Our numerical procedure is as follows, where the final bullet only applies to QCD,

- Configuration space gauge fix to Landau gauge to an acceptably high accuracy.
- Take the logarithm of all of our gauge fields, using the same field definition as was used in the gauge fixing.
- (Fast) Fourier transform our gauge fields to momentum space.
- Filter our momentum so that only theoretically acceptable momenta are included.
- Perform the $e^{i\frac{p_\mu}{2}}$ correction on our cut fields, test the momentum space Landau condition.
- Compute the normalised gluon propagators and normalised and projected three point functions in either kinematic.
- Compute the renormalised lattice coupling using Eqs.3.36 and 3.53.
- Fit our data to a reasonable ansatz.
- Match our fitted data to continuum $\overline{\text{MS}}$, run down to the Charm threshold (1.6 GeV) using the $N_f = 3$ β-function, threshold match to $N_f = 4$ theory, run to the

Bottom mass threshold (4.7 GeV) using the $N_f = 4$ β-function threshold match to $N_f = 5$ theory. Run using $N_f = 5$ β-function to M_z (91.1876 GeV)[24].

I will go over each step in a little more detail now. We fix our configurations to the accuracy of $\Theta = 10^{-25}$, to ensure that the gauge fixing accuracy plays no part in our systematics. We fix to such a high level because it is cheap with an effective algorithm (and after a certain albeit high accuracy Θ behaves linearly with the number of iterations) and we can fix to such a high level because we work solely in double precision.

FFT-ing all of our configuration space fields allows us to easily select many momenta, and for large lattices is a much cheaper alternative than Discrete Fourier transforming (DFT) every momenta you want. For the exceptional scheme we always use a cylinder cut, because of its removal of hard, on axis propagators with the exception of the 0-mode. The $e^{ip_\mu/2}$ correction and computation of the momentum space Landau condition is a vital sanity check.

We compute the gluon correlation functions using extensive use of the identities previously discussed (e.g Eq.3.21 and Alg.1) to speed up numerical efficiency. We write the gluon propagator and the three point function to a file for later analysis.

In the analysis part of the method the renormalised coupling is computed and the result is bootstrapped (2.5.1), so that we can extrapolate between different ensembles with differing number of configurations while still including as much statistical information as possible. We then perform a fit of the form,

$$\alpha(p^2) = a + b\log\left(\frac{p^2}{p_0^2}\right) + c\log^2\left(\frac{p^2}{p_0^2}\right), \tag{3.66}$$

where p_0 is a reference momentum at the middle of our fit range, and hence a is the value of α at p_0.

The fit ansatz we use is theoretically motivated by the Taylor expansion of the explicit solution of Eq.3.2. By having explicit forms for the fit function and values computed between a specific range $\mu \to \mu'$ we can continuum extrapolate the results of our lattice spacings which we could not with just their physical momenta. For our analysis it is easier to continuum extrapolate our fitted data, match to $\overline{\text{MS}}$ by solving numerically for h in Eq.3.58 or 3.57 and running to M_z numerically using Eq.3.62.

Our analysis is different from previous attempts [38, 42], where an explicit fit to the perturbative form of the coupling was used to compute the Landau pole (Λ_{QCD}) of the theory, and corrections of $O\left(\frac{1}{p^2}\right)$ (justified by the gluon condensate term in the OPE) were required to reconcile the result with evaluations of (Λ_{QCD}) in $\overline{\text{MS}}$. Or by an explicit

conversion of the coupling to $\Lambda_{\rm QCD}$ as in [3]. We instead follow a simpler route and expect that any discretisation effects to the physics will not survive the extrapolation of $a^2 \to 0$ within our Rome-Southampton window.

3.8 The QCD strong coupling

In this section we detail the coupling evaluations from the exceptional Sec.3.4.1 and the non-exceptional Sec.3.4.2 schemes. The ensembles used in these measurements are detailed in Tab.3.1. First, the measurements of our couplings for various lattice spacings from Tab.3.1 are made. We then linearly extrapolate to $a^2 \to 0$, before matching to $\overline{\rm MS}$ and running the coupling to $\rm M_z$.

3.8.1 The exceptional scheme

We have seen from Fig.3.7 that the gluonic three point function is a statistically noisy observable, and so we really have to use as many configurations as we can. Fortunately, the objects we are measuring, the gluon propagator and the gluon three point function are ultra-local having integrated autocorrelation time of no greater than 5 Monte Carlo time steps, so we have no qualms in using every configuration available after thermalisation. We must first extrapolate our result to the chiral limit, and then a^2 extrapolate to the infinite volume limit.

Our first plot (Fig.3.9) is of the coupling determined using the exceptional kinematic for the three 32^3 masses available. The data is taken from a cylinder cut of large width $\frac{3\pi}{L_{sm}}$, so that we can average over more equivalent p^2 modes. To this end we also average over neighbouring momenta using the criteria $|(ap)^2 - (ap')^2| < 0.05$, for clarity. We use a subset of the configurations listed in 3.1. We use 165 of the $am = 0.004$, 558 of the $am = 0.006$ and 170 of the $am = 0.008$ configurations.

Fig.3.9 shows the mass dependence of the strong coupling in the $\widetilde{\rm MOMgg}$ scheme. We observe no mass dependence beyond the statistical resolution of the measure. The observation that the coupling for different masses is oscillating around a central value and the coupling for different masses swaps over in magnitude is indicative of the statistical noise in the measurement being much larger than any chiral behaviour. We therefore must assume the approach to the chiral limit is flat, which allows us to average the contributions from the masses. The exact same behaviour is seen for the 24^3 ensembles, where no chiral limit can be resolved above statistical noise. This then allows us to compute the coupling in what we infer is the chiral limit with 2929

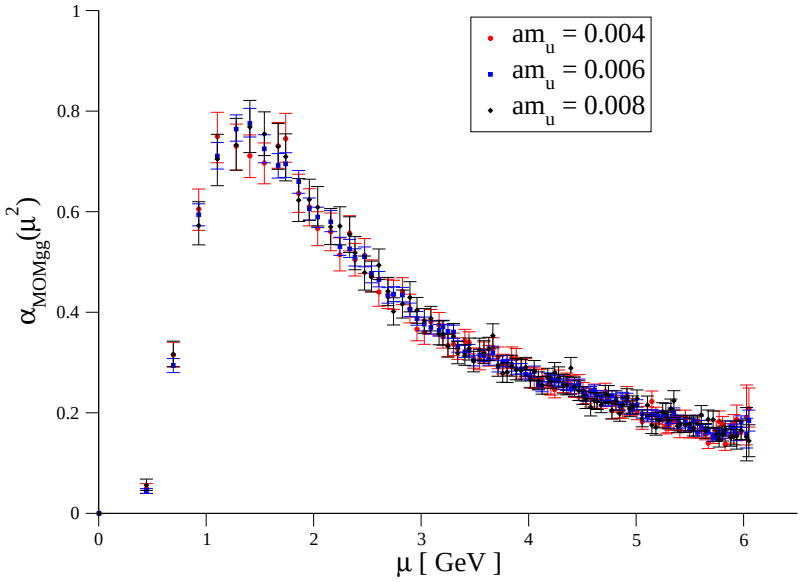

Figure 3.9 *The strong coupling for three different masses for the* 32^3 *ensemble.*

configurations for the $\beta = 2.13$ ensemble and 1715 configurations for the $\beta = 2.25$ ensemble. This will give us the statistical resolution to determine the strong coupling with great accuracy.

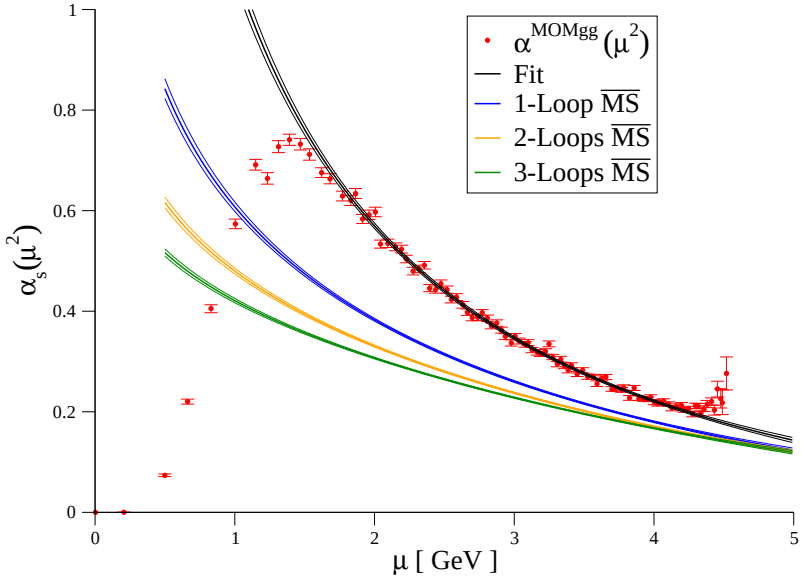

Figure 3.10 *The QCD strong coupling for the* 24^3*,* $\beta = 2.13$ *ensemble using the exceptional kinematic. We have performed an average over the three available masses and a fuzzy momentum average of* $0.05(a^{-2})$*. The* $\overline{\text{MS}}$ *coupling is obtained by numerically solving Eq.3.57 for h.*

From the two figures 3.11 and 3.10 we see that this is a viable way to calculate the QCD strong coupling, and the fit over the whole perturbative range is possible. One interesting point is the turnover at momenta less than $\approx 1.5GeV$, this is an IR effect that could be due to instantons [39] and is not the subject of this study. It is only

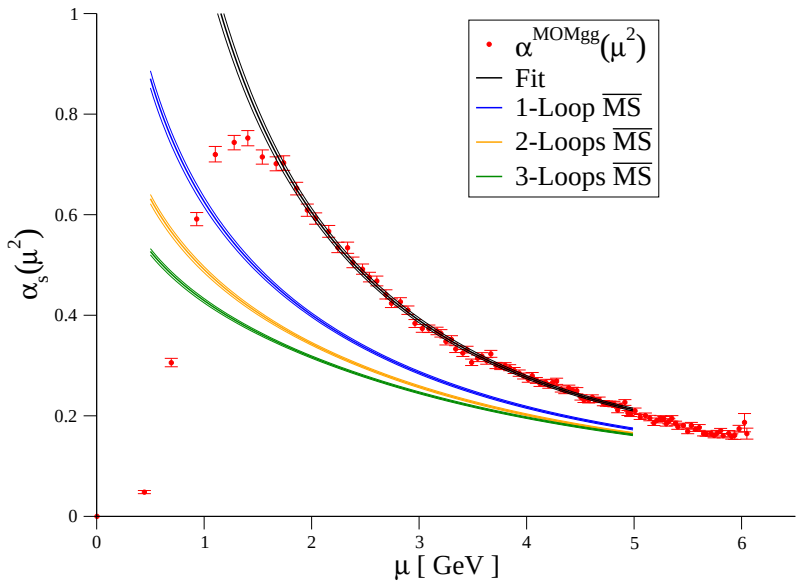

Figure 3.11 *The QCD strong coupling for the* 32^3*,* $\beta = 2.25$ *ensemble using the exceptional kinematic. Using an average over the three available masses and a fuzzy momentum average of* $0.05(a^{-2})$*. The* $\overline{\text{MS}}$ *coupling has been obtained by numerically solving Eq.3.57 for h.*

the UV range of the simulation we are interested in as that is where the perturbative comparison can occur.

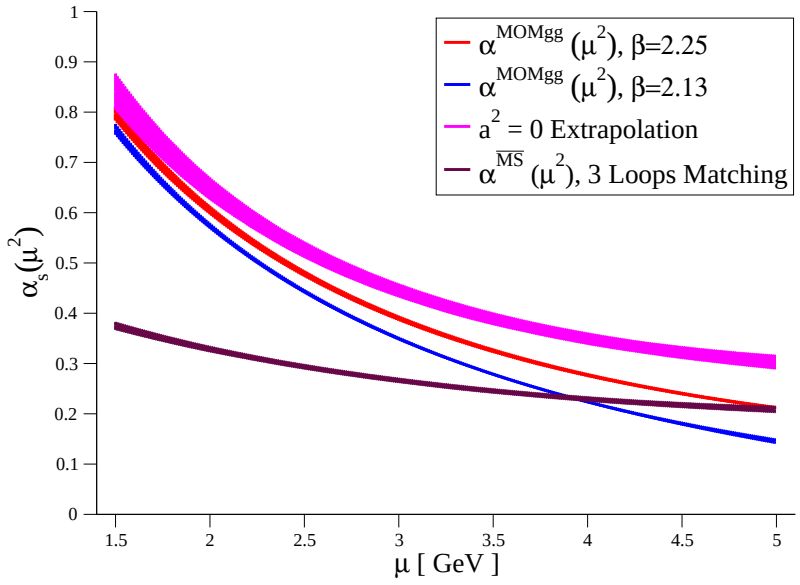

Figure 3.12 *Linear* $a^2 \to 0$ *continuum extrapolations of the fits to the* $\beta = 2.13$ *and* $\beta = 2.25$ *ensembles in the* $\widetilde{\text{MOMgg}}$ *scheme, and its subsequent matching to* $\overline{MS}$*by solving Eq.3.57.*

Fig.3.12 shows the continuum extrapolations of the two fits in Figs.3.11 and 3.10, where the fit parameters have been used to extrapolate the fit down to 0.5 GeV and up to 5 GeV. We see significant scaling violation (i.e. large a^2 defects) between the $\beta = 2.13$

and $\beta = 2.25$ ensembles. Particularly at high momentum, where both ensembles are suspected to be outside of their Rome-Southampton window. In this plot we see that there are significant scaling violations between the two ensembles that are growing with the scale, this is probably due to the exceptional nature of the kinematic.

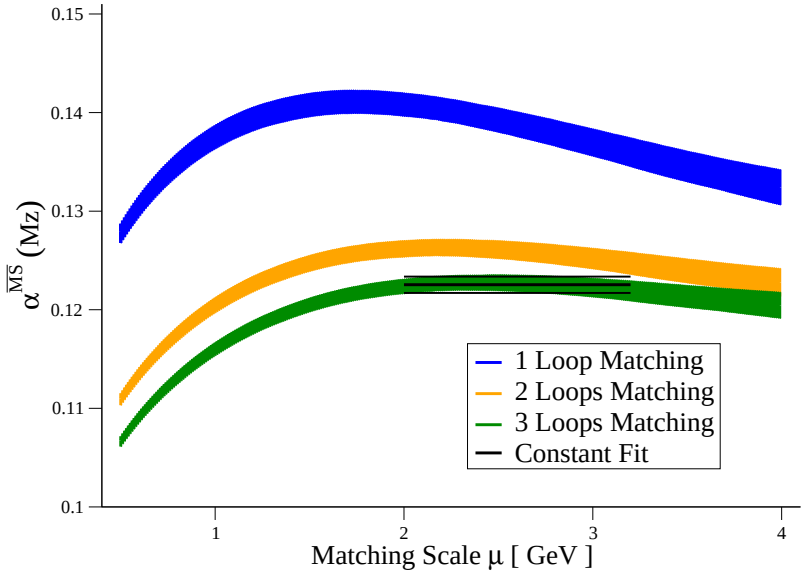

Figure 3.13 *The QCD strong coupling in* $\overline{\text{MS}}$ *at* M_z *for varied loop order of matching and running for renormalisation matching scale* μ*, after a linear fit and* $a^2 \to 0$ *extrapolation. For the* $\widetilde{\text{MOM}}$gg *scheme determination.*

Fig.3.13 shows $\widetilde{\text{MOM}}$gg evaluated and matched perturbative $N_f = 5$ $\overline{\text{MS}}$ QCD coupling at the Z-boson mass M_z, for different loop orders of matching and running. We run the coupling at the order we match between the schemes, and at a plateau we perform a constant fit to obtain our final result.

We see large corrections between successive loop orders even at M_z, illustrative of the poor convergence of the scheme at the matching scale available. We also note that at higher orders of perturbation theory the coupling in $\overline{\text{MS}}$ at M_z is flatter for a larger range of the matching scale μ. It is tempting to infer from this data that we are slowly converging from above to the coupling at M_z as we increase the order of the matching and running, but we have no idea what the fourth order term in the series in Eq.3.57 will do to the conversion to $\overline{\text{MS}}$. Going from two loop order to three loops in the matching and running at 3 GeV gave a 2.4% correction. A conservative estimate on the perturbative error could be to use this as an estimate for the contribution of all of the remaining orders.

The results in Tab.3.4 show that a statistically precise determination of the strong coupling can be made using this technique, with both coupling evaluations in the $\widetilde{\text{MOM}}$gg scheme having $O(1\%)$ statistical error for reasonable fits. The extrapolations

$a^2(GeV^{-2})$	$\frac{\chi^2}{dof}$ [Fit Range (GeV)]	$\alpha^{\widetilde{\mathrm{MOMgg}}}_{N_f=3}(3\ GeV)$	$\alpha^{\overline{\mathrm{MS}}}_{N_f=3}(3\ GeV)$	$\alpha^{\overline{\mathrm{MS}}}_{N_f=5}(\mathrm{M_z})$
0.334(4)	2.17 [2 $\rightarrow$ 4]	0.3493(31)	0.2293(13)	0.11433(32)
0.192(2)	1.13 [2 $\rightarrow$ 5]	0.3898(48)	0.2458(19)	0.11815(42)
0	-	0.445(13)	0.2663(48)	0.1224(83)

Table 3.4 *The statistical results from the* $\widetilde{\mathrm{MOMgg}}$ *scheme computation at fixed matching scale 3 GeV at each stage of the analysis.*

to the continuum have been performed incorporating the error in the lattice spacings.

As discussed in Sec.3.5.3, the zero momentum gluon's normalisation as seen from the difference in polarisations has not been taken into account. It is our understanding that amputation with such a propagator is an incorrect procedure because it introduces out of control finite volume systematics to the measurement. To estimate the error, we consider Fig.3.6 and the difference between the temporally-polarised and spatially polarised gluon. The worst difference from their average comes from the 24^3 ensemble and is a factor of 0.82 and 1.53 for the spatial and temporal respectively. Using the temporal polarisation for the norm induces a multiplicative factor of 1.5 and the spatial a factor of 0.5 on the value of the $\widetilde{\mathrm{MOMgg}}$ α. After running to $\mathrm{M_z}$ these translate to couplings 0.128 and 0.087, symmetrising the difference from the average these yield gives us an estimate on our finite volume systematic of 0.02. Our final result for $\alpha_s(M_z)$ in $\overline{\mathrm{MS}}$ is,

$$\alpha^{\overline{\mathrm{MS}}}_{N_f=5}(M_z) = 0.1224(8)_{\mathrm{stat}}(29)_{\mathrm{pert}}(200)_{\text{finite volume}}. \tag{3.67}$$

3.8.2 The non exceptional scheme

The non-exceptional scheme uses a kinematic that is theoretically sound, and use of this scheme is well motivated by its absence of a zero-momentum gluon propagator amputation.

Its difficulty in measurement lies in the task of locating sufficient triplets of external momenta, statistics is one of the largest hurdles to overcome in this measure. As stated at the introduction to the scheme in Sec.3.4.2 we cannot use the $24^3 \times 64$ data as in the previous exceptional kinematic study. Also, this scheme defines the momentum conservation using the Fourier mode definition for the momentum ($p_\mu = \frac{2\pi n_\mu}{L_\mu}$), although we have argued that the sin definition of momentum $p_\mu = 2\sin(p_\mu/2)$ is the correct one to use, if we do use the sin definition of momentum then the triplets we have selected no longer necessarily conserve momenta.

It is much more difficult to incorporate triplets that conserve momenta using the sin

definition, and for this study we only use the Fourier mode definition. And use it consistently both in the projectors and for the scale. Of course the choice of momentum is just a choice and after taking the continuum limit ($a^2 \to 0$) the two should give the same results up to higher order corrections.

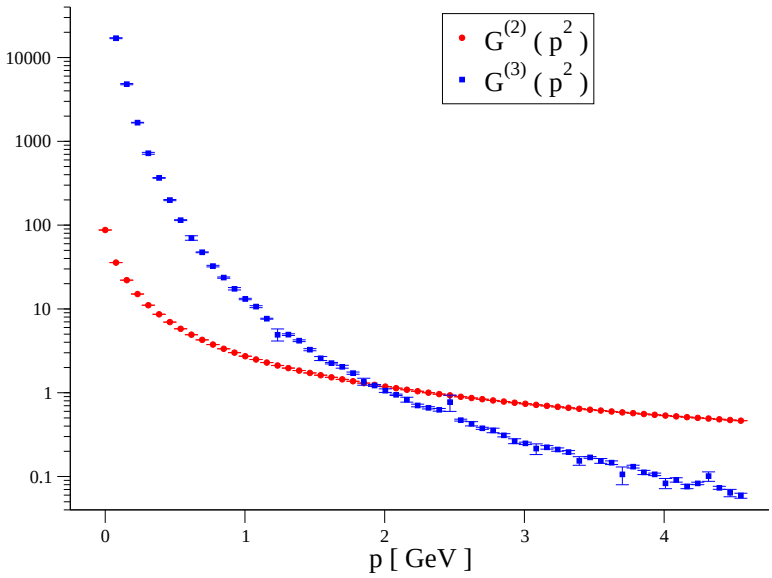

Figure 3.14 *The unrenormalised gluon propagator and non-exceptional kinematic three point function for the $\beta = 2.25$, $32^3 \times 64$ ensemble, where an average over the three available masses has been made.*

Fig.3.14 shows the lattice-units, unrenormalised, gluon propagator and the MOMggg scheme three point function, for the $\beta = 2.25$ ensemble. An average over the three masses has been made and no momentum binning (fuzzy averaging) has been performed. This plot is meant to illustrate that there are fewer momenta available for this kinematic and that the three point function is statistically noisy, with large fluctuations on p^2-modes that do not have many momenta available to average over. Again, much as in the case of the $\widetilde{\text{MOM}}$gg scheme, no discernible chiral limit was available and so an average over the measurement at all available masses was made. This was also the case for the two $16^3 \times 32$ ensembles investigated in this section.

The three plots in Fig.3.15 show our measurement of the QCD strong coupling using the MOMggg scheme. The $\beta = 2.25$, 32^3 ensemble has had a cut whereby the points that have a greater than 10% error on their value are discarded. This can be performed because the 32^3 configuration has enough data points that the outliers are irrelevant. Within statistical error this cut makes no difference on the result of the fit and is mostly for clarity. We note that this measure is statistically noisy and that the coupling takes a higher value in the IR compared to the exceptional scheme, similar behaviour was seen in [41], although we do disagree with the projector they used to determine the coupling. As in the previous evaluation using the exceptional scheme, we use the fit to

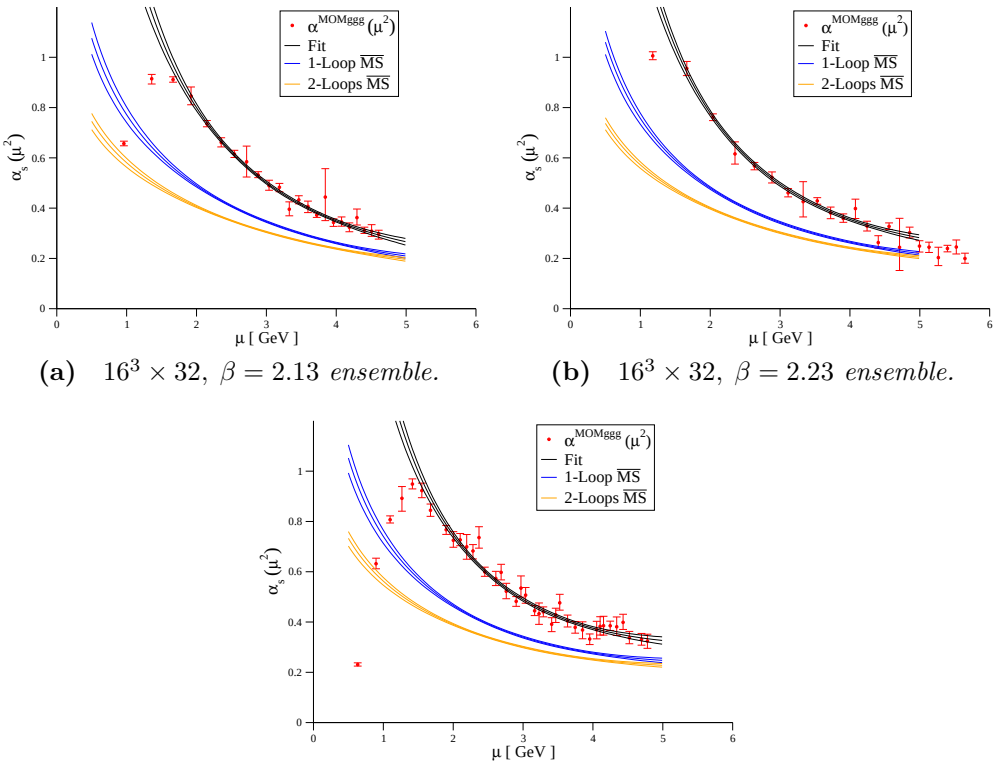

(a) $16^3 \times 32$, $\beta = 2.13$ *ensemble.* **(b)** $16^3 \times 32$, $\beta = 2.23$ *ensemble.*

(c) $32^3 \times 64$, $\beta = 2.25$ *ensemble.*

Figure 3.15 *The strong coupling evaluation for the* MOMggg *coupling. The* $\beta = 2.25$ *measurement has had a cut applied where only the lowest error points contribute.*

our data to continuum extrapolate.

From Fig.3.16, we see that the scaling violations in this measure are large, and there is crossover between the determinations as one approaches a higher scale. We see that unlike the exceptional kinematic it appears there are smaller extrapolations in the approach to the continuum. We had to omit the $\beta = 2.23$ ensemble as it was spoiling the continuum extrapolation due to its lattice spacing being too close to the 32^3 data's, this was seen from very high $\frac{\chi^2}{dof}$ (> 10) for the $a^2 \to 0$ extrapolations and is probably due to the simulation having too small a physical volume.

In Fig.3.16 large scaling violations in the determination of the coupling from the triple gluon vertex exist even using the more theoretically sound non-exceptional kinematic, we attribute this violation to large $(ap)^2$ corrections and only obtain flat logarithmic running of the continuum after $a^2 \to 0$ extrapolation. We proceed to run our coupling to M_z, as we only have matching coefficients at the two loop level threshold matching does not play a rôle.

Our final result for this scheme is based on the graph Fig.3.17 and the table Tab.3.5, where we again see a large correction from the one-loop matching to the two-loop

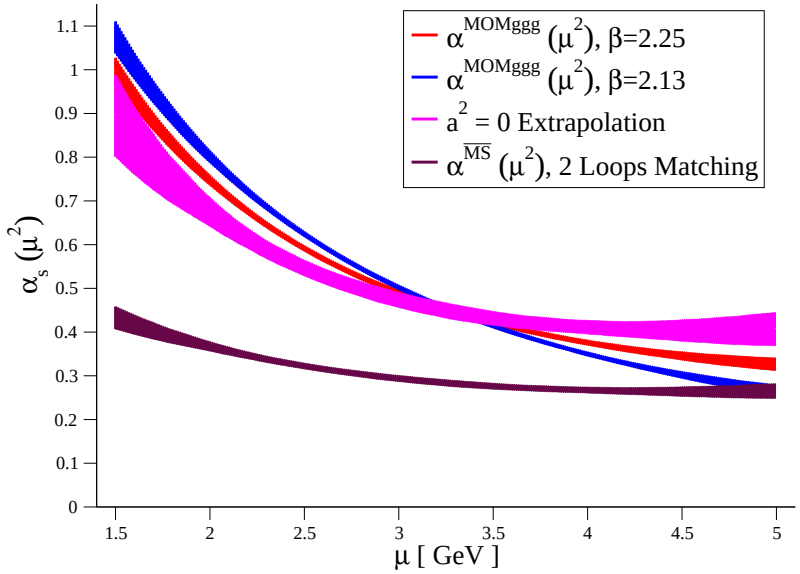

Figure 3.16 *Linear $a^2 \to 0$ continuum extrapolations of the fits of the coupling from the $\beta = 2.13$ and $\beta = 2.25$ ensembles in the* MOMggg *scheme and its subsequent matching at two loop order in continuum perturbation theory to* $\overline{\text{MS}}$ *by solving Eq.3.58 for h.*

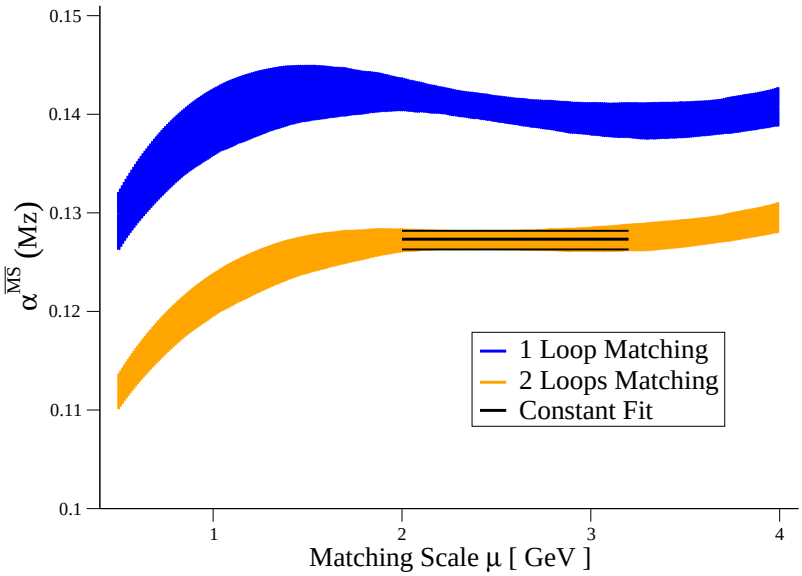

Figure 3.17 *The QCD strong coupling in* $\overline{\text{MS}}$ *at M_z for varied loop order of matching and running for renormalisation matching scale μ, after $a^2 \to 0$ extrapolation. For the* MOMggg *scheme determination.*

matching in $\overline{\text{MS}}$ at M_z as in the exceptional scheme of about 8.7% on the central value. Very conservatively we use this as an estimate for all other higher order corrections for this scheme. Our final result for the non-perturbatively renormalised coupling in the MOMggg scheme at 3 GeV and its matched and run, $N_f = 5$ $\alpha_s(\mu)$ in $\overline{\text{MS}}$ at M_z is,

$$\alpha^{\text{MOMggg}}_{N_f=3}(3\ GeV) = 0.476(16)_{\text{stat}}, \qquad \alpha^{\overline{\text{MS}}}_{N_f=5}(M_z) = 0.1273(9)_{\text{stat}}(110)_{\text{pert}}. \tag{3.68}$$

$a^2(GeV^{-2})$	$\frac{\chi^2}{dof}$ [Fit Range (GeV)]	$\alpha^{MOMggg}_{N_f=3}(3\ GeV)$	$\alpha^{MS}_{N_f=3}(3\ GeV)$	$\alpha^{MS}_{N_f=5}(\mathrm{M_z})$
0.334(4)	0.57 [1.92 → 4.61]	0.5012(57)	0.3050(22)	0.12994(40)
0.192(2)	1.17 [1.90 → 4.78]	0.4893(66)	0.3002(26)	0.12910(48)
0	-	0.476(16)	0.2947(66)	0.1275(12)

Table 3.5 *The statistical results from the* MOMggg *scheme computation at fixed matching scale 3 GeV at each stage of the analysis.*

This is the first measurement of the QCD strong coupling using the non-exceptional matching and projectors of [98], and the first evaluation of the QCD strong coupling using the $N_f = 2 + 1$ DWF configurations generated by UKQCD and RBC [14]. The accuracy of the measurement is good, and this translates to a statistical accuracy at $\mathrm{M_z}$ in $\overline{\mathrm{MS}}$ of under 1%, unfortunately at matching scales computationally available and with current perturbative calculations available in the literature we are almost completely dominated by perturbative truncation errors. Circumventing this issue will require much smaller lattice spacings, and more likely higher orders of perturbative corrections, both of which are daunting tasks. Although a step-scaling scheme to take us to higher scales could be used [16], this would require a dedicated configuration generation programme which is beyond the scope of this work. Also, considering the plots in Fig.3.8 we do not see spectacular convergence at 10 GeV or higher, even at this scale we still might be dominated by perturbative error.

We now turn our attention to theories where a non-perturbative coupling measurement in any scheme is of interest.

3.9 SU(2) gauge theory with $N_f = 2$ Adjoint fermions

I now introduce a different non-abelian gauge theory, that has been implemented on the lattice. That of SU(2) gauge theory with nf=2 dynamical fermions in the Adjoint representation. It is tantamount to the versatility of our procedure that very little in terms of analysis is required to change, in order to perform this measurement. This lattice theory has been of interest as a possible Beyond the Standard Model (BSM) theory for dynamical Electroweak Symmetry Breaking (dEWSB). This theory is part of the family of Technicolor models (strong dynamics at the Tera electron-Volt TeV scale), where the lightest hadronic states are the Standard Model Higgs boson.

Many versions of Technicolor are ruled out by the s-parameter [68, 135], apart from exotic higher representations of fermions or perhaps theories with a large number of

fermions [68][3]. Many of these new models display the behaviour of so-called walking, where there is a cancellation at some value of the coupling between the leading order and next leading order of the perturbative β-function, making the coupling run slowly, this can be created using higher representations of fermions, different gauge groups and large number of fermion flavours. We can investigate what walking behaviour of the coupling beyond perturbation theory exists using the techniques of the lattice.

Our evaluation is the first measurement of the non-perturbatively renormalised coupling of this theory using the triple gluon vertex. By virtue of using vertex functions one can fit continuous $(ap)^2$, allowing for a continuous β-function calculation, for comparing to the walking ansatz.

We have two ensembles for this theory, both simulated using the Wilson action for fermions and the Wilson gauge action using the HiRep code [64], both with $\beta = 2.25,\ am_l = -1.15$.

	$32^3 \times 64$	$48^3 \times 80$
am_l	-1.15	-1.15
Configurations	750	500
β	2.25	2.25

Table 3.6 *The SU(2) ensembles, with nf=2 Adjoint fermions used for this analysis. The configurations were generated using the Wilson plaquette gauge action and the Wilson fermion discretisation.*

3.9.1 Gluon field renormalisation

Our first computation is of the gluon field renormalisation $Z_{A_\mu}\left(p^2\right)$, defined by Eq.3.23. By plotting this function we can attempt to infer where the perturbative behaviour of our theory is by seeing where this function flattens out. This is then a clear indication that the gluon propagator is behaving in its free field $\frac{1}{p^2}$ form.

From Fig.3.18, we can see that the expected $\frac{1}{p^2}$ behaviour sets in early for these configurations. This is indicative of perturbative behaviour. It is very surprising just how large the field renormalisation needs to be in the IR and how quick the onset of perturbative behaviour occurs. This is very different behaviour to QCD (Fig.3.4), where the transition from non-perturbative physics to perturbative is slow. It appears that in the deep IR of this theory at this bare coupling ($\beta = 2.25$) lies the strong dynamics.

[3] Although the perturbative evaluation of the S-parameter grows with nf.

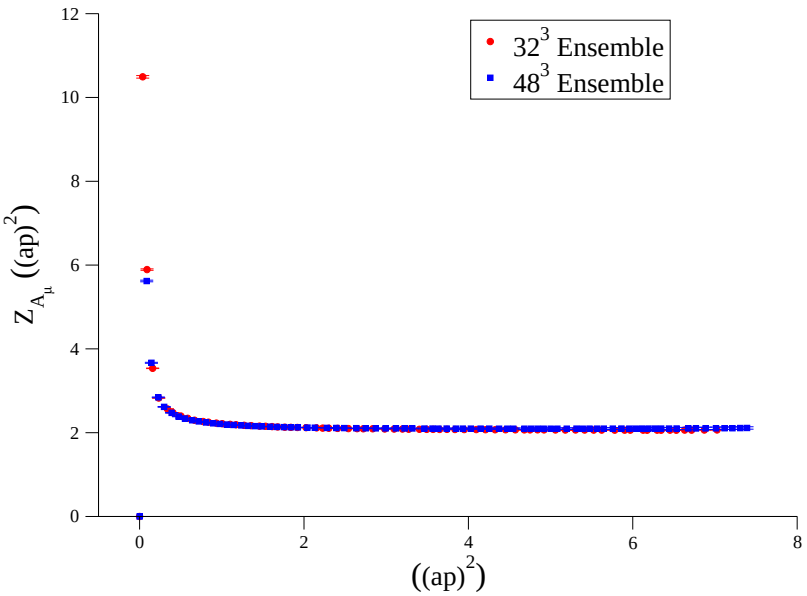

Figure 3.18 *The gluon field renormalisation factor $Z_{A_\mu}((ap)^2)$, for both the 32^3 and 48^3 ensembles.*

3.9.2 Matching coefficients

The matching coefficients for our MOM-couplings for SU(2), nf=2 gauge theory with two Fermions in the Adjoint representation to $\overline{\text{MS}}$ are, for the exceptional kinematic,

$$h^{\widetilde{MOMgg}} = h\,(1.0 + h(-4.0 + h(-167.6074922 - 1181.415908h))\,. \tag{3.69}$$

And for the non-exceptional,

$$h^{MOMggg} = h\,(1.0 + h(-9.672792226 - 204.5564887h)\,. \tag{3.70}$$

This is already a noticeably different result to QCD, where the MOM-scheme couplings were larger than the $\overline{\text{MS}}$. In this case the sign of the corrections is negative, meaning the perturbative coupling in the MOM schemes will almost always lie lower than the $\overline{\text{MS}}$. Solving the matching to $\overline{\text{MS}}$ for the coupling using a Newton Raphson method became unstable at low momentum indicating a very sharp rise in the MOM-scheme couplings, we choose instead to use the inverse series for the $\overline{\text{MS}}$ couplings.

$$\begin{aligned} h =& h^{\widetilde{MOMgg}}\Big(1.0 + h^{\widetilde{MOMgg}}\big(4.0 \\ &+ h^{\widetilde{MOMgg}}(199.6074922 + 4853.565753h^{\widetilde{MOMgg}})\big)\Big). \end{aligned} \tag{3.71}$$

$$h = h^{MOMggg}\big(1.0 + h^{MOMggg}(9.672792226 + 391.6823076h^{MOMggg})\big). \tag{3.72}$$

The scheme-independent parts of the β functions read,

$$\beta = -h^2(2.0) - h^3(-40.0). \tag{3.73}$$

And the scheme-dependent parts for the exceptional kinematic are,

$$\beta^{\widetilde{MOMgg}} = \beta - h^4(-931.2149844) - h^5(-13974.69900). \tag{3.74}$$

And for the non-exceptional,

$$\beta^{MOMggg} = \beta - h^4(+1387.150485). \tag{3.75}$$

The two schemes are quite different from one another, in terms of their higher order corrections.

3.9.3 The strong coupling

We perform the same analysis as previously, comparing both schemes' evaluations of the coupling and their evaluation in $\overline{\text{MS}}$. We can only use the smaller ensemble (the $32^3 \times 64$) for the evaluation of the MOMggg coupling because, as was the case with the $24^3 \times 64$ SU(3) ensemble the aspect ratio makes it very difficult to locate momenta that satisfy the kinematic.

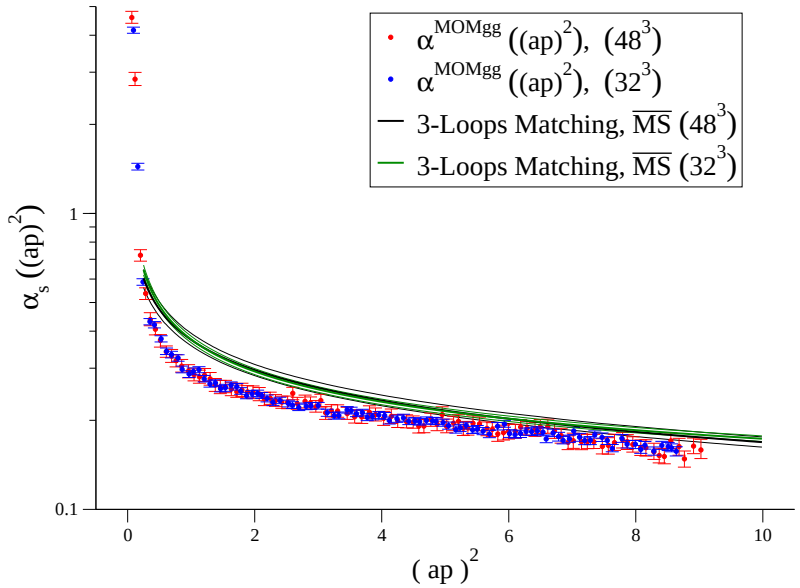

Figure 3.19 *The strong coupling $\alpha_s\left((ap)^2\right)$ from the exceptional kinematic and its subsequent matching to $\overline{MS}$ at 3 loop order for the $32^3 \times 64$ and $48^3 \times 80$ ensembles. Large cylinder radii of 3 and four lattice spacings were used for this computation and a fuzzy momentum average of 0.075 was also used.*

The evaluation of $\alpha_s(\mu)$ for this theory differs dramatically from our previous QCD evaluations of the coupling. As seen in Fig.3.19 there is no visible turnover at low momentum for these ensembles, and the coupling is running very slowly with lattice momentum. The evaluations from the two lattice sizes are in good agreement, suggestive of having finite volume lattice artifacts under control. We plot the data close to what we would expect to be the upper edge of our Rome-Southampton Window ($(ap)^2 << \pi^2$) to try and illustrate the evolution of the coupling over as large a range as possible. We see a very sharp non-perturbative peak with slow running afterwards, suggestive of being in the theory's confining region.

The non-exceptional coupling is shown in Fig.3.20. As in the QCD case, this measure is statistically noisier, both schemes, however show a very sharp peak and very slow running as a function of $(ap)^2$. We do not see a complete flattening of the coupling, which would be expected for a zero of the non-perturbative β-function, instead we see slow but probably logarithmic running of the coupling, this could well be due to large $O\left((ap)^2\right)$ terms, as we saw from calculation of the QCD running coupling in Figs.3.12 and 3.16.

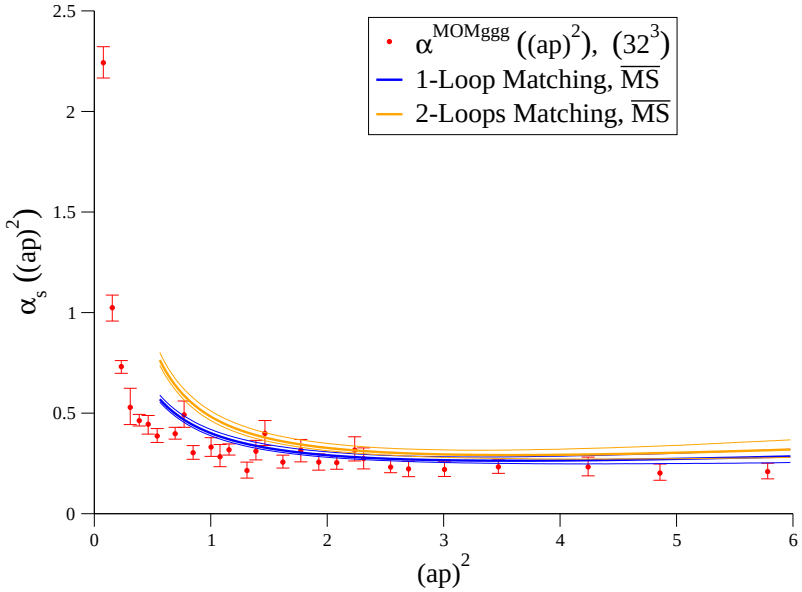

Figure 3.20 *The strong coupling $\alpha_s\left((ap)^2\right)$ from the non exceptional kinematic and its subsequent matching to $\overline{\text{MS}}$ at 1 and 2 loop order for the $32^3 \times 64$ ensembles.*

3.9.4 Renormalised β function

From our results it is straightforward to compute the renormalised β-function for our two MOM schemes and in $\overline{\text{MS}}$. We do this by differentiating our fit ansatz with respect

to $\log(\mu^2)$, yielding,

$$\begin{aligned} \beta(\mu^2) &= b + 2c \log\left(\frac{\mu^2}{\mu_0^2}\right), \\ \beta(\mu^2) &= \pm\sqrt{b^2 + 4c(\alpha(\mu^2) - a)}. \end{aligned} \tag{3.76}$$

Where the second coupling is found by solving for $\log\left(\frac{\mu^2}{\mu_0^2}\right)$. For the $\overline{\text{MS}}$ β-function, we numerically differentiate the matched, fitted coupling using the Euler version of the finite difference. We can only use the fitted, exceptional scheme's data due to the noise in the statistical fluctuations of the data not providing a smooth enough function to resolve the numerical derivative. The non-perturbative $\widetilde{\text{MOMgg}}$ and the matched to three loop perturbative order $\overline{\text{MS}}$ β functions are shown in Fig.3.21.

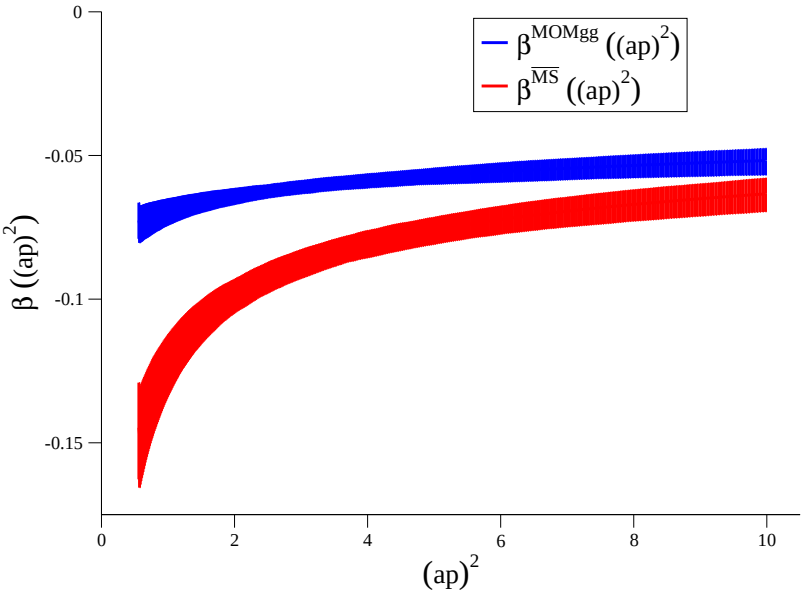

Figure 3.21 *The SU(2) nf=2 Adjoint representation β functions for the exceptional scheme and its 3 loop matched $\overline{\text{MS}}$ evaluation for our 32^3 dataset.*

From Fig.3.21, it is interesting to note that our $\widetilde{\text{MOMgg}}$ evaluation of the coupling yields a small, but still negative β function. Caution must be taken in stating whether this theory is apparently walking in this regime or not, because we only have results from one lattice spacing and do not have $(ap)^2$ errors under control, although there is evidence from the non-exceptional scheme (Fig.3.20) that may suggest a very slow if not stopped running and greater statistics could be beneficial in determining whether this is the case, but due to large p^2 errors in the SU(3) case and without a second β we do not have a continuum evaluation.

As an investigative tool, evaluations of the strong coupling of various non-abelian field theories via vertex functions can give lots of fine detail on the low energy fundamental behaviour of a particular theory. As a method for determining the running coupling of QCD $\alpha_s(\mu)$, the triple gluon vertex evaluation on the lattice can produce statistical

errors of the order of 1%. Unfortunately, if one wishes to match this evaluation to continuum perturbation theory large systematics due to the truncation of the perturbative series spoils the measurement.

If we compare our result of $\alpha^{\overline{\text{MS}}}_{N_f=5} = 0.1273(9)_{\text{stat}}(110)_{\text{pert}}$ to the world average of $\alpha^{\overline{\text{MS}}}_{N_f=5} = 0.1184(7)$, we are far from it. This must be from the perturbative truncation errors, and only higher order perturbative matching and an increased lattice matching scale (with the former being more important) will this technique be competetive with other determinations.

We have cast doubt on the theoretical validity of the previously used exceptional scheme, noting that amputation by a maximally infrared object suffers from large unknown systematic errors due to the finite volume, we have also seen large p^2 effects in the continuum extrapolation. We are the first to compute the coupling using the MOMggg scheme of [98], which we believe provides the correct projection of the triple gluon vertex in the non-exceptional kinematic (compared to the one used in [40, 41]), and is theoretically sound due to its lack of amputation by a finite-volume sensitive object. Although we do find the non-exceptional scheme evaluation to be technically challenging.

As a probe for new models of strong dynamics, the triple gluon vertex is a useful tool as it can be measured on existing configurations and is computationally cheap to perform the analysis if a fast enough Landau gauge fixing method is available, and there are enough configurations available. We have seen that Gribov copies do not appear to play a strong rôle in the dynamics of the gluon propagator, especially in the regime where continuum perturbative matching is considered possible.

Chapter 4

Link smearing and the Wilson flow

In this Chapter I will discuss several smearing methods and techniques used by the community. Smearing is the method of smoothing out gauge fields by successive averages over the original field, which can reduce UV fluctuations in the gauge field. It is often used to reduce chiral symmetry breaking [73], and "taste" [80] (when using staggered fermions) breaking when incorporating fermions in the simulation.

The Wilson flow is a new method in the arsenal of lattice gauge theorists to compute several important quantities, such as the lattice spacing. It is very closely related to the technique of smearing.

I intend to illustrate the connection between the link smearing transformation and the Wilson flow update. I then attempt to elucidate the connection between several popular smearing techniques; those of APE, STOUT and LOG. Showing that they are different levels of approximation to the intended smearing transformation and that they are all equivalent at the tree level order in a weak field expansion.

From the weak field analysis we derive the effective smearing radius $f(r)$, and perform a measurement of this quantity using the momentum-space Landau gauge-fixed gluon propagator machinery of Chapter 3. The effective smearing radius weak-field prediction is often used as an argument for using certain smearing techniques [103] and performing a certain number of smearing iterations, a measurement of this quantity using strongly-coupled configurations should show whether the weak-field prediction has any predictive power for realistic gauge configurations.

We attempt to illustrate that smearing can be used for determining the topological charge of a configuration using the gauge field definition, and also provide a warning that too much (Wilsonian) smearing can result in inconsistent topological charge definitions,

as it is seen to destabilise instanton solutions. We introduce a proposed panacea for this, that of (over)improved smearing. We investigate a wealth of different possible smearing types within this extension to the standard smearing procedure, determination of the topological charge can indicate whether the simulation is sampling all possibilities of the fields (ergodicity).

We move on to discuss the Wilson flow determination of the lattice spacing, and our determination of the parameter W_0 that can be used to set the physical scale of simulations (i.e. determine the lattice spacing) in a computationally cheap manner, with good statistical accuracy. For percent-level error of physical predictions from lattice measurements, percent-level and below evaluations of the lattice spacing are required. And the Wilson flow allows for such a level of precision.

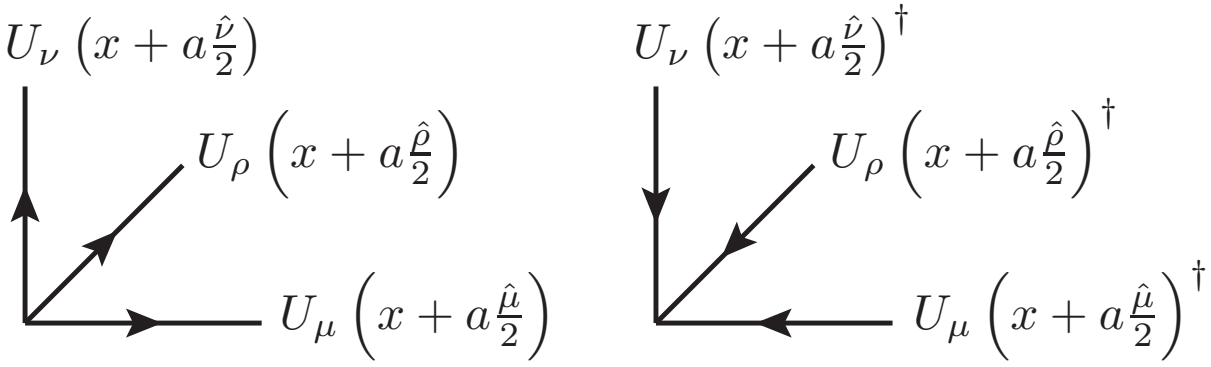

Figure 4.1 *Pictorial representation of link matrices from a point "x" to a point $x+a\hat{\mu}, x+a\hat{\nu}, x+a\hat{\rho}$ on our lattice for orthogonal directions μ, ν and ρ.*

4.1 Smearing types

The basic smearing recipe is the replacement of a gauge link by the (weighted by some tuning parameter) average of its surrounding staples, and is meant to suppress high energy fluctuations. The method is a steepest descent method of moving the configuration to the nearest local solution of the classical equations of motion, this is essentially the same as performing a forward Euler integration of the Wilson flow. We

first define,

$$\begin{aligned} P_{\mu\nu}(x) &= \left(U_\nu(x+a\hat{\nu}/2)U_\mu(x+a\hat{\nu}+a\hat{\mu}/2)U_\nu(x+a\hat{\mu}+a\hat{\nu}/2)^\dagger U_\mu(x+a\hat{\mu}/2)^\dagger\right), \\ O_{\mu\nu}(x) &= \left(U_\nu(x-a\hat{\nu}/2)^\dagger U_\mu(x-a\hat{\nu}+a\hat{\mu}/2)U_\nu(x+a\hat{\mu}-a\hat{\nu}/2)U_\mu(x+a\hat{\mu}/2)^\dagger\right), \\ Q_{\mu\nu}(x) &= \log(O_{\mu\nu}(x)) + \log(P_{\mu\nu}(x)). \end{aligned} \tag{4.1}$$

Which are then used to define the replacement,

$$U_\mu\left(x+a\tfrac{\hat{\mu}}{2}\right) = \exp\left[\frac{\alpha}{2(N_d-1)}\sum_{\nu\neq\mu} Q_{\mu\nu}(x)\right] U_\mu\left(x+a\tfrac{\hat{\mu}}{2}\right). \tag{4.2}$$

It is clear that the recipe in 4.2 is gauge covariant, as the argument of the logarithms form a closed loop, which is manifestly a gauge covariant quantity. The parameter α is a tuning parameter dictating how aggressively we smooth our link, if it is too large the smearing roughens the configurations introducing noise into the smearing.

Recalling from Eq.2.19, the link between the plaquette and the field strength tensor, $P_{\mu\nu}(x)^\dagger = e^{iF_{\mu\nu}\left(x+a\frac{\hat{\mu}}{2}+a\frac{\hat{\nu}}{2}\right)}$ and the fact that the term that contributes below the link is $O_{\mu\nu}(x) = e^{iF_{\mu\nu}\left(x+a\frac{\hat{\mu}}{2}-a\frac{\hat{\nu}}{2}\right)}$, we see that for Hermitian F,

$$Q_{\mu\nu}(x) = -iF_{\mu\nu}\left(x+a\frac{\mu}{2}+a\frac{\nu}{2}\right) + iF_{\mu\nu}\left(x+a\frac{\hat{\mu}}{2}-a\frac{\hat{\nu}}{2}\right) = -ia\Delta_\nu F_{\mu\nu}\left(x+a\frac{\hat{\mu}}{2}\right). \tag{4.3}$$

Which is the lattice variant of the classical equation of motion for the field $\frac{\partial S}{\partial U}$. Performing a small expansion in α, we have the update,

$$U_\mu\left(x+a\tfrac{\hat{\mu}}{2}\right) = U_\mu\left(x+a\tfrac{\hat{\mu}}{2}\right) - i\alpha a\Delta_\nu F_{\mu\nu}\left(x+a\frac{\hat{\mu}}{2}\right) U_\mu\left(x+a\tfrac{\hat{\mu}}{2}\right). \tag{4.4}$$

This is a steepest descent step along the gradient of the gauge action. If we consider the update in Eq.4.4 as a step in some fictitious time $t = \alpha$, then we immediately see that it is the Euler solution to the gradient equation (the dot denotes differentiation in fictitious time),

$$\dot{U_\mu}\left(x+a\frac{\hat{\mu}}{2}\right) = -ia\Delta_\nu F_{\mu\nu}\left(x+a\frac{\hat{\mu}}{2}\right) U_\mu\left(x+a\tfrac{\hat{\mu}}{2}\right). \tag{4.5}$$

Integration of this is called the gradient flow. In this description, the Wilson plaquette action has been used to define the field strength tensor and hence Q, its gradient flow is called the Wilson flow. If a different gauge action is used to alter or refine the definition of the field strength tensor, then the gradient flow changes as the local minima of the classical equations of motion are different.

I now consider three different types of smearing, the first two (APE and STOUT) are approximations to Eq.4.2 and the final (LOG) is the exact reproduction of Eq.4.2.

4.1.1 APE

APE smearing is the oldest smearing technique, it was used to smooth configurations for the measurement of glueball spectra (color bound states) [1, 79]. Again, we define the combination,

$$\begin{aligned} L_{\mu\nu}(x) &= \left(U_\nu(x+a\hat{\nu}/2)U_\mu(x+a\hat{\nu}+a\hat{\mu}/2)U_\nu(x+a\hat{\mu}+a\hat{\nu}/2)^\dagger\right), \\ M_{\mu\nu}(x) &= \left(U_\nu(x-a\hat{\nu}/2)^\dagger U_\mu(x-a\hat{\nu}+a\hat{\mu}/2)U_\nu(x+a\hat{\mu}-a\hat{\nu}/2)\right), \\ N_{\mu\nu}(x) &= L_{\mu\nu}(x)+M_{\mu\nu}(x). \end{aligned} \tag{4.6}$$

The update step proposed was,

$$U_\mu\left(x+a\tfrac{\hat{\mu}}{2}\right)' = P_{SU(N)}\left((1-\alpha)U_\mu\left(x+a\tfrac{\hat{\mu}}{2}\right)+\frac{\alpha}{2(N_d-1)}\sum_{\nu\neq\mu}N_{\mu\nu}(x)\right). \tag{4.7}$$

Where $P_{SU(N)}$ is a projection back into $SU(N)$ which is often performed by trace maximisation (A.2.1) such as in our implementation, but can also be performed by using a rational approximation [116]. In Eq.4.7 $N_{\mu\nu}(x)$ are the so-called staples and is represented pictorially in Fig.4.2. These are the link contributions to the plaquette action under the alteration of the link $U_\mu\left(x+a\frac{\hat{\mu}}{2}\right)$.

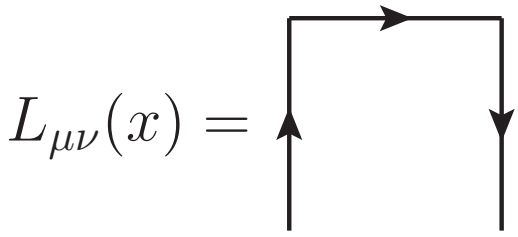

Figure 4.2 *Pictorial representation of the positive-ν staple $L_{\mu\nu}(x)$ from point "x" to a point $x+a\hat{\mu}$ in the $\mu-\nu$ plane.*

The relation between Eq.4.2 and Eq.4.7, is as follows; Eq.4.7 can be rewritten as,

$$P_{SU(N)}\left((1-\alpha)+\frac{\alpha}{2(N_d-1)}\sum_{\nu\neq\mu}N_{\mu\nu}(x)U_\mu\left(x+a\tfrac{\hat{\mu}}{2}\right)^\dagger\right)U_\mu\left(x+a\tfrac{\hat{\mu}}{2}\right). \tag{4.8}$$

This operation is legal because the projection $P_{SU(N)}(XU) = P_{SU(N)}(X)U$ for any arbitrary matrix X and any $SU(N_c)$ matrix U, this also means that the projection is

gauge invariant. We now expand Eq.4.2 in the weak field approximation to $O((ag_0)^2)$ in the logarithm and the exponential.

$$\begin{aligned}
\log(P_{\mu\nu}(x)) &= \log\left(1 - iF_{\mu\nu}\left(x + a\frac{\hat{\mu}}{2} + a\frac{\hat{\nu}}{2}\right)\right), \qquad \log(P_{\mu\nu}(x)) = -iF_{\mu\nu}\left(x + a\frac{\hat{\mu}}{2} + a\frac{\hat{\nu}}{2}\right), \\
\log(O_{\mu\nu}(x)) &= \log\left(1 + iF_{\mu\nu}\left(x + a\frac{\hat{\mu}}{2} - a\frac{\hat{\nu}}{2}\right)\right), \qquad \log(O_{\mu\nu}(x)) = +iF_{\mu\nu}\left(x + a\frac{\hat{\mu}}{2} - a\frac{\hat{\nu}}{2}\right), \\
-ia\Delta_\nu F_{\mu\nu}\left(x + a\frac{\hat{\mu}}{2}\right) &= -iF_{\mu\nu}\left(x + a\frac{\hat{\mu}}{2} + a\frac{\hat{\nu}}{2}\right) + iF_{\mu\nu}\left(x + a\frac{\hat{\mu}}{2} - a\frac{\hat{\nu}}{2}\right).
\end{aligned} \tag{4.9}$$

Expanding the exponential, we get the result,

$$U_\mu\left(x + a\tfrac{\hat{\mu}}{2}\right)' = \left(1 + \frac{\alpha}{2(N_d - 1)}\sum_{\nu\neq\mu} -ia\Delta_\nu F_{\mu\nu}\left(x + a\frac{\hat{\mu}}{2}\right)\right) U_\mu\left(x + a\tfrac{\hat{\mu}}{2}\right). \tag{4.10}$$

Expanding Eq.4.8 to the same order, we get,

$$\begin{aligned}
N_{\mu\nu}(x)U_\mu\left(x + a\tfrac{\hat{\mu}}{2}\right)^\dagger &= 1 - iF_{\mu\nu}\left(x + a\frac{\hat{\mu}}{2} + a\frac{\hat{\nu}}{2}\right) + iF_{\mu\nu}\left(x + a\frac{\hat{\mu}}{2} - a\frac{\hat{\nu}}{2}\right), \\
U_\mu\left(x + a\tfrac{\hat{\mu}}{2}\right)' &= \left(1 + \frac{\alpha}{2(N_d - 1)}\sum_{\pm\nu\neq\mu} -ia\Delta_\nu F_{\mu\nu}\left(x + a\frac{\hat{\mu}}{2}\right)\right) U_\mu\left(x + a\tfrac{\hat{\mu}}{2}\right).
\end{aligned} \tag{4.11}$$

The term "$1 - \alpha$" exists in the projection to explicitly cancel the $\left(\frac{\alpha}{2(N_d-1)}\sum_{\pm\nu\neq\mu} 1\right)$ term in the weak field expansion of the exponential of the plaquette.

If we consider the weak field expansion of the APE smearing procedure again, ignoring the projection step for simplicity, and this time expanding the previous link on the right hand side of Eq.4.11 we obtain,

$$\begin{aligned}
U_\mu\left(x + a\tfrac{\hat{\mu}}{2}\right)' = \Bigg(1 + iA_\mu\left(x + a\tfrac{\hat{\mu}}{2}\right) + \frac{i\alpha}{2(N_d - 1)}\sum_\nu \\
+ A_\nu(x + a\hat{\nu}/2) + A_\mu(x + a\hat{\nu} + a\hat{\mu}/2) - A_\nu(x + a\hat{\mu} + a\hat{\nu}/2) - A_\mu(x + a\hat{\mu}/2) \\
- A_\nu(x - a\hat{\nu}/2) + A_\mu(x - a\hat{\nu} + a\hat{\mu}/2) + A_\nu(x + a\hat{\mu} - a\hat{\nu}/2) - A_\mu(x + a\hat{\mu}/2)\Bigg).
\end{aligned} \tag{4.12}$$

The sum has changed to be over all positive ν, because at $\mu = \nu$ all of the terms in the sum at this order cancel. We can then pick out the finite differences,

$$\begin{aligned}
a\Delta_\nu A_\nu(x) &= A_\nu(x + a\hat{\nu}/2) - A_\nu(x - a\hat{\nu}/2), \\
a^2\Delta_\nu\Delta_\nu A_\mu(x + a\hat{\mu}/2) &= A_\mu(x + a\hat{\nu} + a\hat{\mu}/2) + A_\mu(x - a\hat{\nu} + a\hat{\mu}/2) - 2A_\mu(x + a\hat{\mu}/2).
\end{aligned} \tag{4.13}$$

We obtain upon a change of variables $\tilde{x} = x - a\frac{\hat{\mu}}{2}$,

$$U_\mu(\tilde{x}) = \left(1 + iA_\mu(\tilde{x}) + \frac{ia^2\alpha}{2(N_d-1)}\sum_\nu \Delta_\nu\Delta_\nu A_\mu(\tilde{x}) - \Delta_\mu\Delta_\nu A_\nu(\tilde{x})\right). \tag{4.14}$$

In terms of the updated (primed) gluon field, we have the expression,

$$A_\mu(\tilde{x})' = \left(1 + \frac{a^2\alpha}{2(N_d-1)}\Delta_\nu\Delta_\nu\right)\delta_{\mu\nu}A_\nu(\tilde{x}) - \frac{a^2\alpha}{2(N_d-1)}\Delta_\mu\Delta_\nu A_\nu(\tilde{x}). \tag{4.15}$$

Under Fourier transform and noting that every derivative yields a factor $a\Delta_\nu A_\mu(\tilde{x}) = iaq_\nu A_\mu(q)$, we obtain for one smearing iteration the update to the gluon field in momentum space,

$$A_\mu(q) = \left(\delta_{\mu\nu} - \frac{a^2\alpha}{2(N_d-1)}\left\{q^2\delta_{\mu\nu} - q_\mu q_\nu\right\}\right)A_\nu(q). \tag{4.16}$$

For iterated smearing (n-smearing iterations), the form

$$A_\mu^{(n)}(q) = \left\{\left(1 - \frac{a^2\alpha}{2(N_d-1)}q^2\right)^n\left(\delta_{\mu\nu} - \frac{q_\mu q_\nu}{q^2}\right) + \frac{q_\mu q_\nu}{q^2}\right\}A_\nu^{(0)}(q). \tag{4.17}$$

Can be used [25, 50], where the index 0 means the completely unsmeared (original) gauge field and the q's are the usual sine-definition of momentum (Sec.6.2.1).

Eq.4.17 defines the smearing transformation in momentum space for fields in the weak field approximation. Due to the link between our standard recipe (Eq.4.2) and APE smearing at the linear order in this approximation, the expression for the momentum-space transformation holds for the following two smearing prescriptions STOUT and LOG.

4.1.2 STOUT

The STOUT smearing procedure was first introduced in [129] as a method to include smeared links in the HMC update, because it is an analytic and differentiable projection. It is based on Eq.4.2, and uses the Hermitian projection (Log-A of Sec.A.1.1) of the logarithm in the exponential and an exact exponential based upon Cayley-Hamilton theorem (Sec.A.2.3).

The relation to Eq.4.2 is,

$$\begin{aligned} U_\mu\left(x+a\tfrac{\hat{\mu}}{2}\right) &= \exp\left[\frac{\alpha}{2(N_d-1)}\sum_{\nu\neq\mu}Q_{\mu\nu}(x)\right]U_\mu\left(x+a\tfrac{\hat{\mu}}{2}\right), \\ &= \exp\left[\frac{\alpha}{2(N_d-1)}Pr\left\{\sum_{\nu\neq\mu}P_{\mu\nu}(x)+O_{\mu\nu}(x)\right\}\right]U_\mu\left(x+a\tfrac{\hat{\mu}}{2}\right), \\ &= \exp\left[\frac{\alpha}{2(N_d-1)}Pr\left\{\left(\sum_{\nu\neq\mu}N_{\mu\nu}(x)\right)U_\mu\left(x+a\tfrac{\hat{\mu}}{2}\right)^\dagger\right\}\right]U_\mu\left(x+a\tfrac{\hat{\mu}}{2}\right). \end{aligned} \tag{4.18}$$

where I have denoted $Pr\{\}$ as the Log-A projection, and used its distributivity (Eq.A.2) to pull the projection outside of the sum, and to pull the multiplication by $U_\mu\left(x+a\frac{\hat{\mu}}{2}\right)^\dagger$ outside of the sum and to the right of the expression, hence eliminating $2(N_d-1)$ matrix multiplications for smearing in all N_d dimensions. As mentioned before, the logarithm is a gauge invariant quantity and is traceless and Hermitian by definition. If we can guarantee that the exponential can be performed directly to $SU(N_c)$ we have no need for cumbersome projections back into the group, that are only correct up to a particular accuracy and are comparatively slow.

4.1.3 LOG

Logarithmic link smearing and direct computation of of the quantity Eq.4.2 is probably the most obvious smearing method and the least complicated conceptually, so it is no surprise that the method was implemented last out of all the procedures [75]. The computation of the logarithm in Eq.4.2 must be performed for every staple because the exact log (Log-B, C or D) does not adhere to distributivity in its arguments as Log-A does, this means there are $2(N_d-1)$ extra matrix multiplies and $2(N_d-1)$ logarithms that must be taken for every update of a single link.

The exact logarithm method (Log-B, C or D) has been outlined already in Sec.A.1.3 for SU(3) and SU(2). For generic N_c out of the two methods we have available Log-D is clearly the only viable option, this requires computation of the eigenvalues of the link matrix $U_\mu\left(x+a\frac{\hat{\mu}}{2}\right)$, possibly by some library. Otherwise rational approximation [86] or brute-force Taylor expansions [75] could be used, but are computationally expensive to perform and their accuracy needs to be controlled carefully.

For our Log-smearing, for SU(2) and SU(3) we use the Log-C method for determining the $Q_{\mu\nu}(x)$ because it was seen to be the fastest of the stable varieties. We then use the exact exponential technique from STOUT smearing to ensure we are projecting back to the group correctly (Tab.A.1). It is clear that because of the extra work

we are doing and the cost of taking the logarithm, this method will be the most expensive computationally out of all the smearing procedures. A cost-comparison of our implementation of the three techniques for SU(2), SU(3), SU(5) and SU(8) is below in Tab.4.1. The Log-C method was used for Log smearing for SU(2) and SU(3) and brute-force Taylor expansions for SU(5) and SU(8).

The data in Tab.4.1 shows the ratio of the time taken for that method of smearing divided by the STOUT method which is expected to be the fastest. For SU(2) however, APE is cheaper than STOUT because it only ever requires one rotation in the trace maximisation and requires one fewer matrix multiply per link update than STOUT. For SU(3), STOUT is the cheapest to perform due to the fixed cost per iteration compared to the variable cost per APE update. It is also over twice as fast as LOG smearing because one extra matrix multiply and logarithm must be made for each (positive and negative) staple per link update.

For large N_c I offer two solutions for the exponentiation of the STOUT projection. The first being a brute force Taylor expansion of the exponential based on the one detailed in the appendices of [75]. The second using the eigenvalues of the Log-A projected logarithm computed using the GSL library, and using these as input for the solution of the generic Vandermonde system for the f's and the exponential using Eq.A.5. The ratio for the APE smearing time for different $SU(N_c)$ links is shown in 4.1, where the value on the left of the comma is the Taylor expansion and on the right the time taken for the Vandermonde solution.

We see that as N_c increases, the Taylor expansion method becomes incredibly costly to perform due to its reliance on many matrix multiplications and error checking for the converged solution. The Vandermonde solution is the fastest as N_c increases, but only by a small amount compared to APE because we have sped up the APE smearing dramatically with the two cheaper matrix multiplication routines discussed in Sec.A.2.1.

Smearing	SU(2)	SU(3)	SU(5)	SU(8)
APE	0.95	1.73	0.44, 1.03	0.39, 1.05
LOG	1.80	2.54	32.7, 75.5	152, 404

Table 4.1 *The time taken per iteration of our implementation of the two smearing types APE and LOG normalised by the time taken per iteration of the STOUT procedure. For SU(2), SU(3), SU(5) and SU(8) gauge group. For SU(5) and SU(8) the first measure is from the brute force Taylor expansion for the exponential and the other is from using the generic Vandermonde solver for the f-constants in the exponential. A number greater than 1 indicates worse performance compared to STOUT.*

4.2 Hypercubic Blocking

A hypercubic blocking or nesting, requires each link in the staple to be smeared with staples orthogonal to that link's polarisation and the polarisation of the link we are attempting to hypercubically-block and smear. The procedure recurses down the list of free polarisations to construct orthogonal staples with. It was introduced as an attempt to reduce the smearing radius whilst providing maximal smoothing of the gauge field per iteration [103]. For 4D hypercubically blocked smearing we have the 3 updating steps per iteration,

$$\begin{aligned} V_{\mu,\nu\rho}(x) &= \exp\left\{\frac{\alpha_3}{2(N_d-3)}\sum_{\sigma\neq\mu\nu\rho} Q_{\mu\sigma}(U(x))\right\} U_\mu\left(x+a\tfrac{\hat{\mu}}{2}\right), \\ W_{\mu,\nu}(x) &= \exp\left\{\frac{\alpha_2}{2(N_d-2)}\sum_{\rho\neq\mu\nu} Q_{\mu\rho}(V(x))\right\} U_\mu\left(x+a\tfrac{\hat{\mu}}{2}\right), \\ U_\mu\left(x+a\tfrac{\hat{\mu}}{2}\right)' &= \exp\left\{\frac{\alpha_1}{2(N_d-1)}\sum_{\nu\neq\mu} Q_{\mu\nu}(W(x))\right\} U_\mu\left(x+a\tfrac{\hat{\mu}}{2}\right). \end{aligned} \tag{4.19}$$

Originally only considered for the APE projection, the technique was called HYP [103]. As we have seen in the previous sections, extension to STOUT (HEX) [73] and LOG (HYL) [75] only require the change in projection. The different α's can be tuned for the greatest reduction of noise per iteration. Originally, the parameters for SU(3) $(\alpha_1,\alpha_2,\alpha_3)$ $\alpha = (0.75, 0.6, 0.3)$ were found to be optimal and are sometimes called HYP-1.

Upon successive smearing iterations, the Hypercubic-blocking transformation in the weak field approximation is supposed to behave in momentum space for n-smearing iterations to lowest order in q^2 as [50],

$$A_\mu^{(n)}(q) = \left\{\left(1-\frac{\alpha_1(1+\alpha_2(1+\alpha_3))}{2(N_d-1)}(aq)^2\right)^n\left(\delta_{\mu\nu}-\frac{q_\mu q_\nu}{q^2}\right)+\frac{q_\mu q_\nu}{q^2}\right\}A_\nu^{(0)}(q). \tag{4.20}$$

It is clear that the parameters $(\alpha,0,0)$ would describe the original, non-hypercubically nested smearing. Again, at this order of approximation there is no difference in the three projections.

4.3 Smearing radii

Considering the two weak field approximations for the behaviour of our fields under the smearing transformations described above (Eqs.4.17 and 4.20) we can test to what extent this approximation holds in the strong coupling regime that our simulations reside in.

We relabel the previous equations (4.17 and 4.20) to include the smearing form factor $f(q^2)$,

$$A_\mu^{(n)}(q) = \left\{ f^{(n)}(q^2) \left(\delta_{\mu\nu} - \frac{q_\mu q_\nu}{q^2} \right) + \frac{q_\mu q_\nu}{q^2} \right\} A_\nu^{(0)}(q). \tag{4.21}$$

For large number of smearing iterations, and small smearing parameter α, we can rewrite the smearing form factor as,

$$f^{(n)}(q^2) = \exp\left(-\frac{n\alpha_1(1+\alpha_2(1+\alpha_3))}{2(N_d-1)}(aq)^2 \right). \tag{4.22}$$

Upon Fourier Transformation and defining the width to be $f(r) = e^{-1/2} f(x)$, we obtain the effective smearing radius,

$$r^2 = n\frac{\alpha_1(1+\alpha_2(1+\alpha_3))}{N_d-1}. \tag{4.23}$$

In our attempt to measure various smearing radii, we consider the smearing transformation equation acting upon a Landau gauge-fixed gluon field,

$$A_\mu^{(n)}(q) = f^{(n)}(q^2)\,(\delta_{\mu\nu})\,A_\nu^{(0)}(q). \tag{4.24}$$

We then consider the gluon correlator in Landau gauge (Sec.3.3),

$$A_\mu^{(n)}(q) A_\mu^{(n)}(-q) = f^{(2n)}(q^2) A_\mu^{(0)}(q) A_\mu^{(0)}(-q). \tag{4.25}$$

Upon taking the trace, we have a measure for the smearing form factor that we can calculate non-perturbatively,

$$f^{(n)}(q^2) = \left(\frac{\mathrm{Tr}\left[A_\mu^{(n)}(q) A_\mu^{(n)}(-q) \right]}{\mathrm{Tr}\left[A_\mu^{(0)}(q) A_\mu^{(0)}(-q) \right]} \right)^{1/2}. \tag{4.26}$$

To compute the effective smearing radius we used 20 configurations at several masses with two β's. We use the $24^3 \times 64$, $\beta = 2.13$ $N_f = 2+1$ DWF configurations with light quark masses $am = 0.005,\ 0.01,\ 0.02$ and 0.03 which we call the coarse ensemble, and the $32^3, \beta = 2.25$ with light quark masses $am = 0.004,\ 0.006,\ 0.008$ which we call

the fine ensemble. We compute the gluon correlators of Landau gauge fixed, smeared and unsmeared configurations, using a cylinder cut in momentum with radius $2\pi/L_{sm}$ to reduce O(4) breaking induced by the lattice, as was performed in Chapter 3.

As a check for our procedure we also produced artificially weak configurations by taking the Logarithm of the fixed link in configuration space, multiplying the lie elements by a small value (10^{-3}) and then exact exponentiating the Lie matrices back to their links before smearing. The gluon field definition used in the gauge fixing functional was that of the Hermitian projection (Log-A) definition, and so to produce the weak fields we must take the Log-A logarithm, we note that by doing this there was a slight decrease in the accuracy of our gauge fixing in momentum-space, equivalent to a drop from $\Theta = 10^{-25}$ to $\Theta = 10^{-14}$.

We consider three N_d-dimensional smearing recipes, one and two iterations of HYP-1 smearing (0.75,0.6,0.3), two iterations of HEX smearing (0.95,0.76,0.38) [73] and three iterations of STOUT smearing (0.6,0.0,0.0). We compare both the artificial weak field results and our configurations' determinations of the smearing form factor f(q). We see that on our strongly coupled configurations the zero momentum gluon propagator for our smeared configurations does not equal the unsmeared gluon propagator at zero momentum. Treating this as a multiplicative field renormalisation factor induced by the smearing, we divide our computed $f(q^2)$ by f(0), to ensure that f(0)=1 allowing direct comparison to the perturbative result.

From Fig.4.3 and Fig.4.4 we can clearly see that this technique does in fact yield the smearing form factor as predicted by the weak field approximation on toy weak fields. As seen from the graphs in the left column, especially that of STOUT smearing where the overlap between prediction and our test is miniscule. For the hypercubically-nested smearing techniques our artificial weak field measurement agrees with theory only at low momentum. This is because we plot,

$$f^{(n)}(q^2)_{\text{tree}} = \left(1 - \frac{\alpha_1(1+\alpha_2(1+\alpha 3))}{2(N_d-1)}(aq)^2\right)^n. \tag{4.27}$$

We are neglecting terms of order q^4 at this order in the expansion of small ag_0.

For the physical, strong coupling results we see large deviation from the weak coupling prediction. The non-perturbative smearing form factor we compute is larger than expected, and deviates less with momenta corresponding to a lower than predicted smearing radius. From our data, 1 iteration of HYP-1 and 3 iterations of STOUT smearing represent comparable degrees of smearing.

We choose to evaluate our effective smearing radius using two different measurements; a fit to our data and an approach assuming gaussianity. Our fit is based on the leading

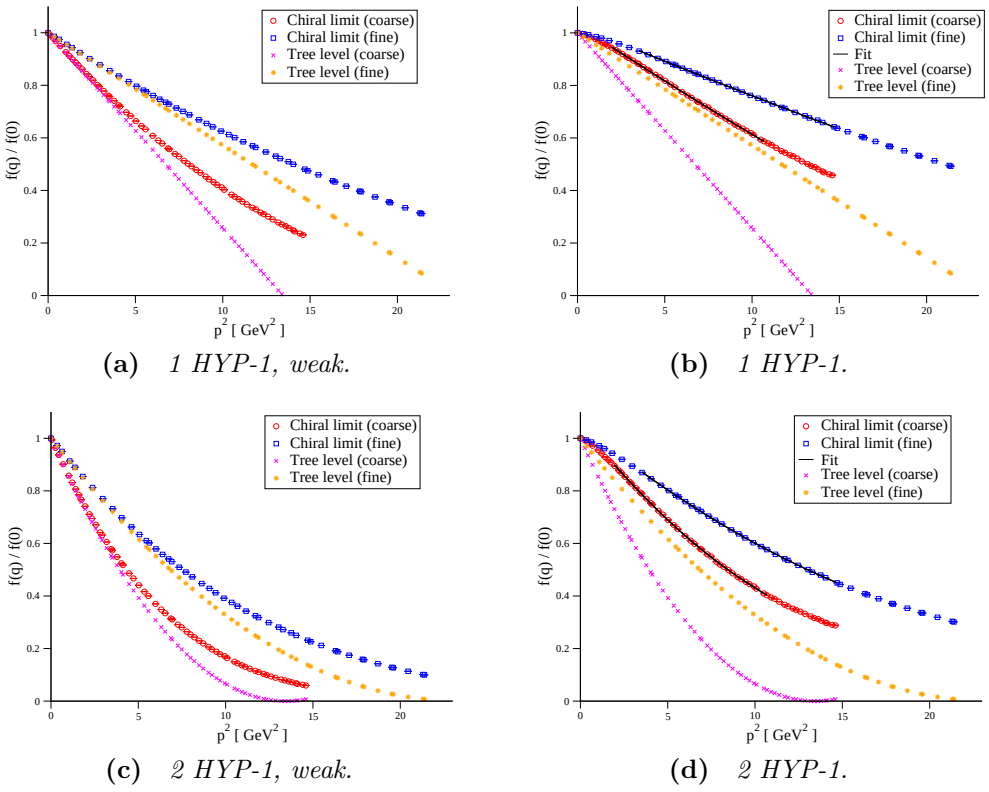

(a) *1 HYP-1, weak.* **(b)** *1 HYP-1.*

(c) *2 HYP-1, weak.* **(d)** *2 HYP-1.*

Figure 4.3 *Comparison plots between the artificial weak field and our configurations for the quantity $f(q)/f(0)$ in the chiral limit, and their comparison to the tree level perturbative form.*

order expansion of $f^{(n)}(q^2)$, namely

$$f^{(n)}(q^2) = 1 - \frac{r^2}{2}q^2 + O(q^4). \tag{4.28}$$

We chose to fit our data to the quadratic form, $f^{(n)}(q^2) = a + bq^2 + cq^4$. The fit is shown in the graphs on the right column of Figs.4.4 and 4.3, and we equate our fit parameter b to be $\frac{r^2}{2}$. As we are trying to resolve the behaviour that is roughly linear in q^2 we do not fit from $q^2 = 0$ as this constrained the fit too much. We call this "r-fit".

The second technique for evaluating our effective smearing radius comes from the definition of the radius. If we consider our data to be Gaussian we have,

$$f^{(n)}(q^2) = e^{-\frac{r^2}{2}q^2}. \tag{4.29}$$

If we find the point where [1],

$$\frac{f^{(n)}(q^2)}{f(0)} = e^{-\frac{1}{2}}. \tag{4.30}$$

[1] We are bound by Fourier modes for our momenta so a linear interpolation is used to match exactly.

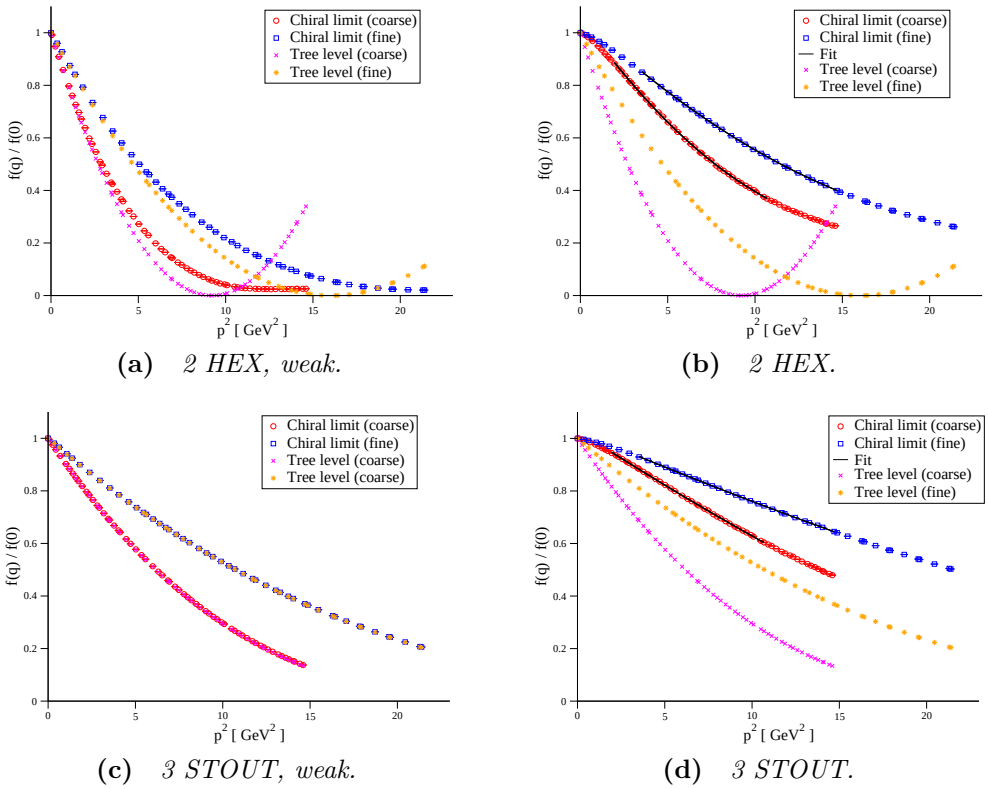

(a) *2 HEX, weak.* **(b)** *2 HEX.*

(c) *3 STOUT, weak.* **(d)** *3 STOUT.*

Figure 4.4 *Same as Fig.4.3 but for the HEX and STOUT smearings.*

Then we can compute the smearing radius with,

$$r^2 = \frac{1}{q^2}\Big|_{f^{(n)}(q^2)=f(0)e^{-1/2}}. \tag{4.31}$$

This measure will be called "r-exp".

A table of the two measures for the effective smearing radii is shown in Tab.4.2 with their comparison to the perturbative prediction "r-pert". We see some tension between the exponential measure of the radius and the measure from the fit. This is because the data is not well described by a Gaussian.

Smearing	r-fit (coarse)	χ^2/dof	r-exp	r-fit (fine)	χ^2/dof	r-exp	r-pert
1 HYP	0.514(2)	1.3	0.5418(3)	0.539(1)	1.9	0.5663(1)	0.775
2 HYP	0.706(1)	1.3	0.6847(5)	0.747(1)	1.4	0.7271(2)	0.943
2 HEX	0.746(2)	1.2	0.7165(4)	0.802(1)	1.3	0.7730(3)	1.139
3 STOUT	0.509(2)	1.1	0.5307(4)	0.543(1)	1.3	0.5625(2)	0.667

Table 4.2 *Smearing radius of our ensembles measured using the exponential method or by a quadratic fit in q^2, and a comparison with the tree-level perturbative prediction.*

Our data shows that on strongly coupled non-perturbative configurations the effective smearing radius is lower than the perturbative prediction, indicating that link smearing

is *more local* than expected on typical configurations. This is quite surprising and could be used to argue that link smearing for the fermionic determinant in the HMC can be used more aggressively than first thought. This is not wise though, as we found that for amputated fermionic vertex functions computed on a smeared background, continuum scaling behaviour was seen to break at scales quite low in the Rome-Southampton Window. For more aggressive smearing methods such as the parameters used for HEX the breaking scale was very low [18].

4.4 Field strength tensor and naïve Topological Charge

As indicated in Eq.4.9, to leading order in a, the gauge field strength tensor at site x ($F_{\mu\nu}\left(x + a\frac{\hat{\mu}}{2} + a\frac{\hat{\nu}}{2}\right)$) is the logarithm of the oriented plaquette in the $\mu - \nu$ plane, $P_{\mu\nu}(x)^{\dagger}$. It is common to use the symmetric "clover" term for $F_{\mu\nu}(x)$. Which, pictorially is shown in Fig.4.5, where an average over the four oriented 1x1 Wilson loops (plaquettes) is made after they have had their logarithm taken, although if using the Hermitian projection (Log-A), because of its distributivity the logarithm can be taken after the matrix sum of the Wilson loops.

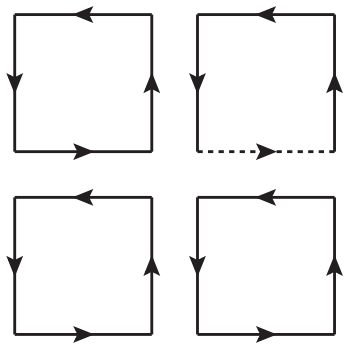

Figure 4.5 *The clover definition of the lattice field strength tensor in the $\mu - \nu$ plane, $F_{\mu\nu}(x)$. Where the individual Wilson loops are averaged and the dashed line is the link $U_{\mu}\left(x + a\frac{\hat{\mu}}{2}\right)$.*

A much higher-order approximation [2] to the continuum field strength tensor using lattice links is available [28, 81] and uses combinations of $1 \times 1(k_1)$, $1 \times 2(k_3)$, $1 \times 3(k_4)$, $2 \times 2(k_2)$ and $3 \times 3(k_5)$ Wilson loops. For the 1×2 and 1×3 rectangles an average over the vertical and horizontal contributions is made as they should be equivalent for an isotropic gauge field.

[2] Classically correct to $O(a^4)$, although this could depend on the order of the logarithm of the Wilson loops

The various contributions to the field strength tensor for the top right corner of the clover is pictorially represented in Fig.4.6.

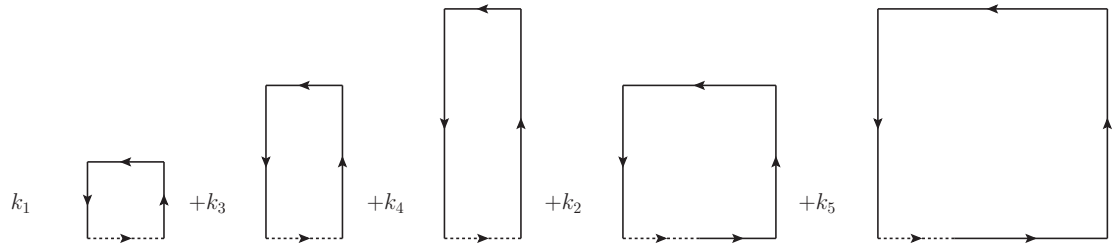

Figure 4.6 *Highly improved gauge field strength measure in the $\mu - \nu$ plane for the top right hand contribution to the symmetric field strength tensor. The dashed line is the link $U_\mu\left(x + a\frac{\hat{\mu}}{2}\right)$.*

The multiplicative factors for each Wilson loop are,

$$\begin{aligned} k_1 &= \left(\frac{19}{9} - 55k_5\right) \qquad k_2 = \left(\frac{1}{36} - 16k_5\right), \\ k_3 &= \left(64k_5 - \frac{32}{45}\right) \qquad k_4 = \left(\frac{1}{15} - 6k_5\right). \end{aligned} \tag{4.32}$$

The parameter k_5 is free and we set it to 0, eliminating the most expensive Wilson loop computation. By smearing our gauge field (and with a good choice of smearing parameter α) we can approach the classical limit where UV fluctuations in our gauge field play no rôle and the lattice field strength tensor is, to a very good approximation the classical one.

The continuum topological charge in four dimensions is defined as,

$$Q_{\text{top}}^{\text{Cont}} = \frac{1}{64\pi^2}\int d^4x\, \epsilon_{\mu\nu\rho\sigma} F^a_{\mu\nu}(x) F^a_{\rho\sigma}(x). \tag{4.33}$$

With direct lattice analog,

$$Q_{\text{top}}^{\text{Latt}} = \frac{1}{32\pi^2}\sum_x \epsilon_{\mu\nu\rho\sigma}\,\text{Tr}\left[F^{\text{Latt}}_{\mu\nu}(x) F^{\text{Latt}}_{\rho\sigma}(x)\right]. \tag{4.34}$$

Where we have used the trace identity from Eq.3.18 to absorb the factor of 1/2 between the two definitions. In practice the field strength tensors F_{tx}, F_{ty}, F_{tz}, F_{xy}, F_{xz} and F_{yz} are the only ones needed.

Lattice measurements of the topological charge $Q_{\text{top}}^{\text{Latt}}$ from the gauge field strength tensor (due to the discrete approximation of the integral) in general will not provide an integer value of the topological charge. As is expected from the continuum theory and the index theorem, although under well chosen smearing parameters the background can

be smoothed in such a way that the lattice topological charge measurement approaches an integer, it was noted in [118] at small effective coupling, near the edge of the classical limit the lattice topological charge is best measured. A non-zero integer value of the topological charge is identified with an instanton which is a field configuration that satisfies the classical equations of motion [107].

The topological charge is of great interest to the lattice community, topological tunnelling is an indicator of ergodicity in our Monte Carlo update and of the autocorrelations in our procedure.

4.4.1 Topological Charge under Hypercubic blocking

We investigated the gauge field definition of the topological charge under the three different smearing methods with hypercubic blocking. We use the classically highly improved field strength tensor with $k_5 = 0.0$ on a single $16^3 \times 32, SU(3)$ configuration simulated with Iwasaki gauge action $\beta = 2.13$ and with known topological charge 1 [15].

The topological charge for this configuration has been determined from the exact zero eigenvalues of the chirally symmetric Dirac operator, via the Atiyah-Singer index theorem [20]. We perform 1000 iterations of HYP, HEX and HYL measuring the naïve gauge definition of the topological charge. I choose the parameters $(0.74, 0.49, 0.24)$ for all of the smearings as this translates to the maximally convergent α for all of the methods for the unimproved smearing (Tab.4.5) for each stage of the blocking.

From Fig.4.7 we see that the HYL smearing only reaches the index theorem's evaluation of the topological charge at very large number of smearing iterations for this configuration $O(360)$, and it takes up to $O(500)$ for the three methods to agree at the per-thousand level. Considering there is a bump for the HYP and HEX smearing it seems likely there is some defect being smoothed out and universal behaviour between the smearings is only achieved at very large number of smearing iterations. This behaviour is unexpected and we believe warrants investigation using a different procedure.

Comparing the computational cost for our implementations of the hypercubically blocked routines for SU(3) HEX smearing is the cheapest, HYP took approximately 2.3 times as long to run and HYL 2.5 times.

We see that under hypercubic blocking, the gauge definition of the topological charge depends on the number of smearing iterations. We also note that computationally this measurement is quite costly, requiring computation and storage of the "dressed links"

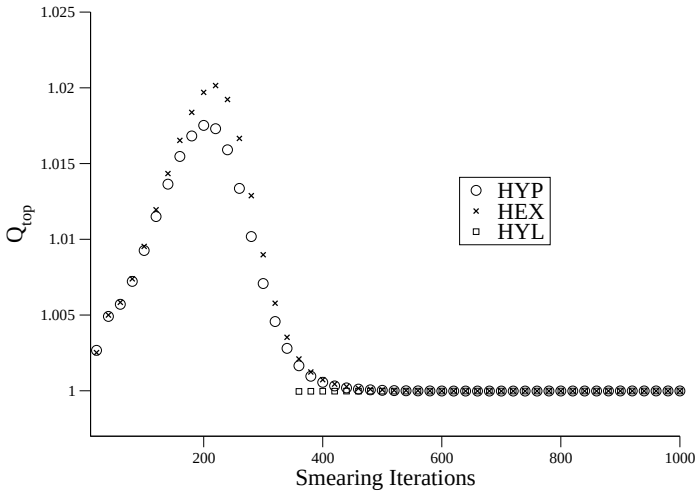

Figure 4.7 *The naïve, highly improved topological charge from hypercubically blocked smearing routines HYP, HEX and HYL for a large number of smearing iterations with* $\alpha = (0.74, 0.49, 0.24)$*. For iterations less than 360, the HYL evaluation is* $Q_{top} = 0$*.*

[103] (V and W in Eq.4.19). We investigate another procedure which should be cheaper to implement and is argued able to provide stable classical instanton solutions.

4.5 (Over)improved smearing

Smearing procedures have been proposed that follow a similar recipe to improving the gauge action [36]. Adding rectangle terms with varied coefficients to the smearing iteration. i.e. altering the description of the gauge action we use to move toward the classical solution of. The general smearing recipe changes to,

$$U_\mu\left(x + a\frac{\hat{\mu}}{2}\right)' = \exp\left\{\frac{\alpha}{2(N_d-1)}\sum_{\nu\neq\mu}\left(c_0 Q_{\mu\nu}(x) + c_1\sum_{i=1}^{6} R^{(i)}_{\mu\nu}\right)\right\} U_\mu\left(x + a\frac{\hat{\mu}}{2}\right). \quad (4.35)$$

Where the c's are values that describe different improved actions. We investigate the Symanzik tree level improved [60], the Iwasaki [132] and the DBW2 [152] whose parameters are shown in Tab.4.3.

There are six 2×1 rectangular terms $R^{(i)}$ that contribute to the smearing, 3 different rectangles and contributions from $\pm\nu$ I have written the positive ν terms below in

Improved smearing	c_0	c_1
Symanzik	$1-8c_1$	$-\frac{1}{12}$
Iwasaki	$1-8c_1$	-0.331
DBW2	$1-8c_1$	-1.4069

Table 4.3 *Table of the parameters c_0 and c_1 used for different improved smearing techniques.*

Eq.4.36 and the full smearing update can be deduced from Fig.4.8,

$$\begin{aligned}
R^{(1)}_{\mu\nu} = & \log\left(U_\nu\left(x+a\frac{\hat{\nu}}{2}\right)U_\nu\left(x+a\frac{3\hat{\nu}}{2}\right)U_\mu\left(x+2a\hat{\nu}+a\frac{\hat{\mu}}{2}\right)U_\nu\left(x+a\hat{\mu}+a\frac{\hat{3\nu}}{2}\right)^\dagger\right. \\
& \left. U_\nu\left(x+a\hat{\mu}+a\frac{\hat{\nu}}{2}\right)^\dagger U_\mu\left(x+a\frac{\hat{\mu}}{2}\right)^\dagger\right). \\
R^{(2)}_{\mu\nu} = & \log\left(U_\mu\left(x-a\frac{\hat{\mu}}{2}\right)^\dagger U_\nu\left(x-a\hat{\mu}+a\frac{\hat{\nu}}{2}\right)U_\mu\left(x+a\hat{\nu}-a\frac{\hat{\mu}}{2}\right)U_\mu\left(x+a\hat{\nu}+a\frac{\hat{\mu}}{2}\right)\right. \\
& \left. U_\nu\left(x+a\hat{\mu}+a\frac{\hat{\nu}}{2}\right)^\dagger U_\mu\left(x+a\frac{\hat{\mu}}{2}\right)^\dagger\right). \\
R^{(3)} = & \log\left(U_\nu\left(x+a\frac{\hat{\nu}}{2}\right)U_\mu\left(x+a\hat{\nu}+a\frac{\hat{\mu}}{2}\right)U_\mu\left(x+a\hat{\nu}+a\frac{3\hat{\nu}}{2}\right)U_\nu\left(x+2a\hat{\mu}+a\frac{\hat{\nu}}{2}\right)^\dagger\right. \\
& \left. U_\mu\left(x+a\frac{3\hat{\mu}}{2}\right)^\dagger U_\mu\left(x+a\frac{\hat{\nu}}{2}\right)^\dagger\right).
\end{aligned} \tag{4.36}$$

Pictorially, the contributions in the $\mu-\nu$ plane are shown in Fig.4.8, the rectangle terms are to be read from left to right as $R^{(1)}$, $R^{(2)}$, $R^{(3)}$, the negative ν contributions $R^{(4)}$, $R^{(5)}$, $R^{(6)}$ have also been shown.

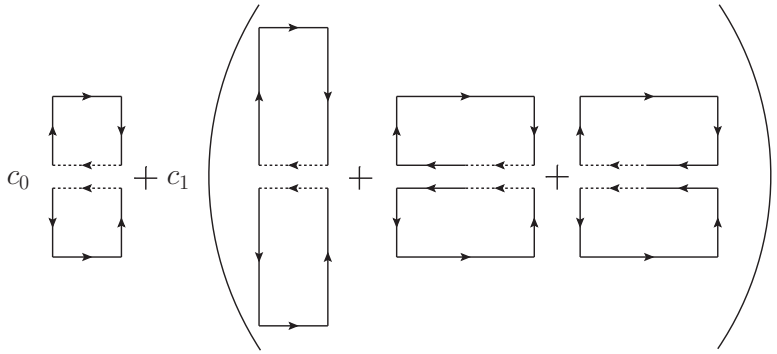

Figure 4.8 *A pictorial representation of the staples contributing to improved link smearing in the $\mu-\nu$ plane. The dashed line is the link $U_\mu\left(x+a\frac{\hat{\mu}}{2}\right)^\dagger$, and the terms above and below it are assumed to have their projection specific Logarithm taken and added.*

We can clearly use any of the projections APE, STOUT or LOG with this method as

they are just different levels of the approximation of the logarithm and exponential in the smearing recipe.

The authors of [128], based on the previous work of [89], suggest an empirical "over-improved" algorithm with a free parameter ϵ that can be tuned so that classical instantons are stable (i.e. Q_{top} is constant) under a large range of successive smearing (cooling in the earlier work) steps when measuring the naïve gauge definition of the topological charge.

We shall see that not all smearing methods stabilise instanton solutions. The idea of the free parameter ϵ is to tune the smearing parameters to lie somewhere in the space where a value of 0 would include the staple and the rectangle term (values in the table 4.3) and a value of 1 would return the standard staple term. A table of the parameters used in this study is shown in Tab.4.4.

Improved smearing	c_0	c_1
Symanzik	$1 + \frac{2}{3}(1-\epsilon)$	$-\frac{1}{12}(1-\epsilon)$
Iwasaki	$1 + 2.648(1-\epsilon)$	$-0.331(1-\epsilon)$
DBW2	$1 + 11.2536(1-\epsilon)$	$-1.4069(1-\epsilon)$

Table 4.4 *Table of the over improved smearing parameters used in this study.*

4.5.1 The $\alpha - \epsilon$ plane

The authors in [128] identify the value of $\epsilon = -0.25$ and smearing parameter $\alpha = 0.36$ as their best parameters for Symanzik "over-improvement", we choose to investigate the plane in $\alpha - \epsilon$ where this technique can be applied.

Stability of classical instantons under smearing is a necessary condition for smeared topological charge measurements to genuinely be determining physical quantities. Furthermore, the gauge field strength measure should agree with the index of a chiral Dirac operator, if we are successfully describing the physics of the vacuum. We propose to use these criteria to determine the range of α and ϵ which can be used for gauge field determinations of topological charge.

Link smearing provides a method to reduce the UV components of the field strength $F_{\mu\nu}(x)$ and approach the closest classical solution of the equations of motion of the field, as we remove the pure UV quantum lattice portion of the gauge field.

For any ϵ there appears to be an α above which the plaquette does not converge to a stable value. We call this $\alpha_{\text{Max}}(\epsilon)$. Non-convergence of the plaquette is certainly a

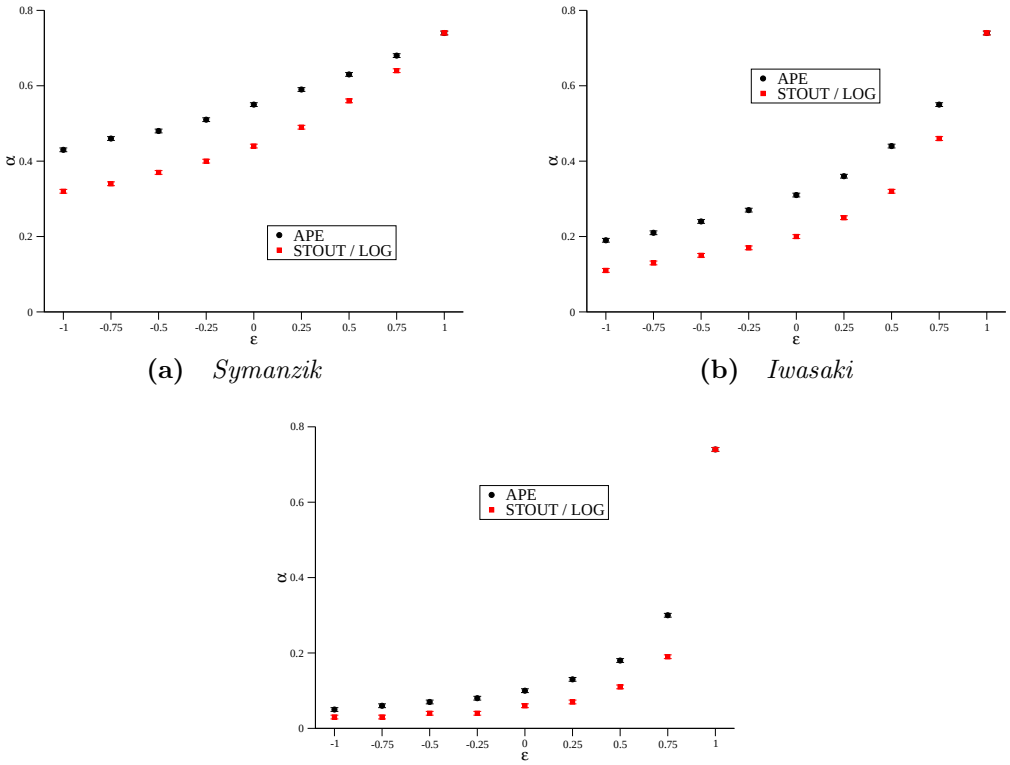

(a) *Symanzik* **(b)** *Iwasaki*

(c) *DBW2*

Figure 4.9 *The line of α_{Max} for each ϵ for three different improvement programs, the Symanzik, Iwasaki and DBW2. Error bars are a constant ± 0.005, the resolution of our search.*

clear sign that we are not obtaining physical results and is indicative of ill convergence in the smearing procedure.

As ϵ is reduced from 1, the contribution from the rectangle term increases and so smaller α would be required. Any α below α_{Max} and above zero will converge to the closest classical solution of the field equations albeit in a slower fashion, and will therefore converge on the same instanton solution as that of α_{Max}.

For smearing parameter $\alpha < \alpha_{\mathrm{Max}}(\epsilon)$ we may have physical predictions, we test this by comparing to the index of a chiral Dirac operator and the stability of the naïve gauge topological charge as a function of the number of smearing iterations. When the gauge field definition of the topological charge is stable and agrees with the Dirac operator index definition on a test configuration we deem these parameters of α and ϵ acceptable for extracting genuine topological charge measurements.

ϵ	Symanzik		Iwaski		DBW2	
	APE	STOUT	APE	STOUT	APE	STOUT
-1.0	0.43	0.32	0.19	0.11	0.05	0.03
-0.75	0.46	0.34	0.21	0.13	0.06	0.03
-0.5	0.48	0.37	0.24	0.15	0.07	0.04
-0.25	0.51	0.40	0.27	0.17	0.08	0.04
0.0	0.55	0.44	0.31	0.20	0.10	0.06
0.25	0.59	0.49	0.36	0.25	0.13	0.07
0.5	0.63	0.56	0.44	0.32	0.18	0.11
0.75	0.68	0.64	0.55	0.46	0.30	0.19
1.0	0.74	0.74	0.74	0.74	0.74	0.74

Table 4.5 *The maximal smearing parameter α that gives convergence to unity for the plaquette, for different improvement factors c_0 and c_1 and for different smearing methods APE and STOUT. LOG smearing evaluations are not shown because its α_{Max} is the same as STOUT.*

4.5.2 Evaluation of the ideal ϵ

We investigate the topological charge history under 1000 APE, STOUT and LOG smearing iterations at $\epsilon = -1.0$, -0.75, -0.5, -0.25, 0.0, 0.25, 0.5, 0.75 and 1.0 for the Symanzik, Iwasaki and DBW2 over-improvement measures on the same configuration which has chiral Dirac operator index 1 as used in 4.4.1. A factor of $\epsilon = 1.0$ is the usual un-improved smearing procedure, and a factor of $\epsilon = 0.0$ is the choice of parameters that gives the standard improvement terms.

We see many interesting results from the two figures 4.10, and 4.11. First is that the topological charge measurement does not reproduce the index measure of the topological charge under any version of unimproved smearing at large number of smearing iterations. $\epsilon = 1$ consistently provides an inaccurate measure of the topological charge, and use of many unimproved smearing iterations to perform a topological charge measurement [14] should be avoided.

For greater than $O(120)$ iterations the topological charge measurement yields a value different from the chiral Dirac index, illustrating the smearing procedure is altering the size of the instanton background. We see that although they have the same $\alpha_{\mathrm{MAX}}(\epsilon)$ probably due to the common exponentiation, the STOUT and LOG smearing methods are very different in practice, with the LOG smearing being effective over a great range of ϵ's for the different rectangle coefficient strategies.

We see that although $\epsilon = -0.25$ Symanzik over-improvement with STOUT links does appear to converge to the Dirac operator's topological index, the convergence is poor for this configuration. We note that the LOG DBW2 method fairs much better with a

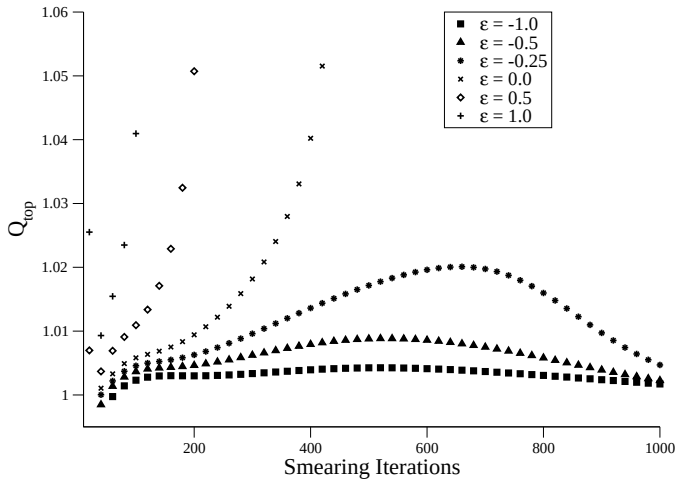

Figure 4.10 *The topological charge evolution for 1000 smearing iterations for varied ϵ using Symanzik over improvement with STOUT link smearing.*

greater range of ϵ seemingly yielding the same physical prediction.

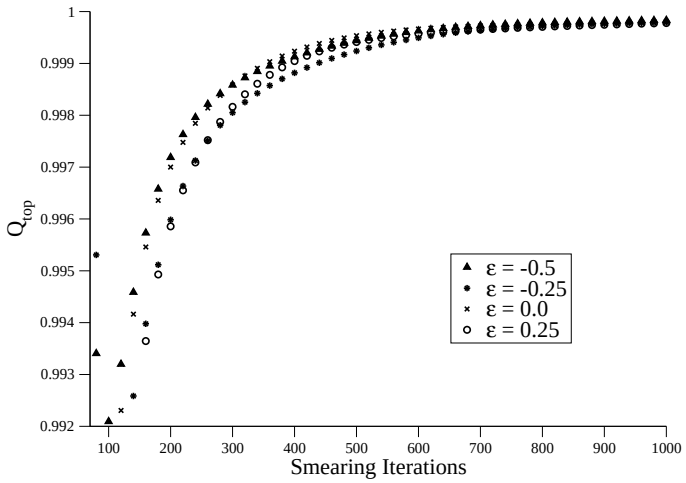

Figure 4.11 *The topological charge evolution for 1000 smearing iterations for varied ϵ using DBW2 over improvement with LOG link smearing.*

From Tab.4.6 we see that the smearing methods behave very differently, and the LOG seems to stabilise the topological charge over the largest range of over improving ϵ. As was seen previously in [128] an ϵ of -0.25 and STOUT smearing does stabilise the instanton, as it does for both APE and LOG. We also note that many smearing iterations $O(> 80)$ or so are required for the procedure to stabilise to approximately its topological charge as described by the index.

Improvement	STOUT	LOG	APE
Symanzik	-1.0,-0.75,-0.5,-0.25	-0.25,0.0,0.25,0.5	-1.0,-0.75,-0.5,-0.25
Iwasaki	0.5,0.75	-0.75,-0.5,-0.25,0.0	0.25,0.5
DBW2	0.0	-1.0,-0.5,-0.25,0.0,0.25,0.75	0.0

Table 4.6 *The values for ϵ which gave the expected topological charge, for varied smearing methods and improvement factors.*

4.6 Wilson flow

The Wilson flow was first introduced in [120] as a technique for improving the convergence and speed of the HMC by mapping the gauge fields to a smoother region to do the integration and then mapping back, requiring the mapping to be invertible. This is performed by integrating the flow equation, for generic fields U at fictitious flow time t,

$$\dot{U}_t = Z(U_t)U_t. \tag{4.37}$$

Considering an Euler integration of Eq.4.37, we have,

$$U_{t+\epsilon} = U_t + \epsilon \frac{d}{dt} U_t. \tag{4.38}$$

And upon plugging Eq.4.37 in and approximating an exponential for small integration step ϵ we have,

$$U_{t+\epsilon} = \exp\left\{\epsilon Z(U_t)\right\} U_t. \tag{4.39}$$

This is exactly the same as the smearing recipe in Eq.4.2. Standard link smearing is a steepest descent method, which is the same as an Euler integration of the gradient flow, when the choice of the generator of the flow Z is the same as that of the smearing procedure (Eq.4.2).

We will only consider smearing recipes which are differentiable and invertible i.e. STOUT and LOG. For the standard smearing recipe the integration of the flow equation is called the Wilson flow, for the improved smearing methods we have the Symanzik, Iwasaki and DBW2 flow.

Accurate, reversible Euler integration (Eq.4.38) of the flow is costly, with a large number of very small smearing steps required for consistent accuracy. One would wonder if higher order integration schemes are applicable, and in fact they are. The RK4

integration scheme is defined by the steps [119],

$$\begin{aligned} W_0 &= U_t, \\ W_1 &= \exp\left\{\frac{\epsilon}{4}Z(W_0)\right\} W_0, \\ W_2 &= \exp\left\{\epsilon\left(\frac{8}{9}Z(W_1) - \frac{17}{36}Z(W_0)\right)\right\} W_1, \\ U_{t+\epsilon} &= \exp\left\{\epsilon\left(\frac{3}{4}Z(W_2) - \frac{8}{9}Z(W_1) + \frac{17}{36}Z(W_0)\right)\right\} W_2. \end{aligned} \tag{4.40}$$

It is important to note that the update in this procedure is happening over all of the lattice fields for each step in the integration. The temporary field, Z, is lattice-wide and so for each step the memory should be rewritten following the prescription,

$$\begin{aligned} &\text{Step 1} : Z = -\frac{17}{36}Z(W_0), \qquad W_1 = \exp\left\{-\epsilon\frac{9}{17}Z\right\} W_0, \\ &\text{Step 2} : Z = \frac{8}{9}Z(W_1) + Z, \qquad W_2 = \exp\left\{\epsilon Z\right\} W_1, \\ &\text{Step 3} : Z = -\frac{3}{4}Z(W_2) + Z, \qquad U_{t+\epsilon} = \exp\left\{-\epsilon Z\right\} W_2. \end{aligned} \tag{4.41}$$

We know that $Z \in \mathfrak{su}(N_c)$, and so we only need store the upper or lower triangular $(N_c(N_c+1)/2 - 1$ elements as was discussed in Sec.6.7.1. Taking the same idea from Sec.6.7.1, for SU(3) we store the fields Z as a complex type, but we know that its diagonal elements are purely real, so we put the real part of Z[4] in the imaginary part of Z[0], saving on storing another complex element.

One may think that the temporaries W_i also need to be stored lattice-wide. This is not the case. As the smearing procedure in all directions has its most non-local contributions coming from the staples for which $\nu = \pm t$, only knowledge of the links one time-slice above and below the time-slice we are operating on (and two for the improved smearing methods to incorporate the 2×1 vertical rectangle) are ever needed. One may think, therefore, that only two temporaries (above and below the time slice being smeared) spanning the $N_d - 1$-dimensional lattice hypercube are necessary but this is not the case, in fact we require three time-slice-wide temporaries.

The memory saving smearing method we use is outlined in Alg.2. We need an extra temporary for the last iteration of the procedure, because we have already over-written the fields that contribute to the smearing in the t=0 time-slice and so the $L_t - 1$ time-slice smeared fields need to be stored. It should be understood that index [t] means all of the matrices on the time-slice t being copied over and smear is one of the link smearing recipes with replacement of the links they are acting upon.

Inclusion of this memory saving technique means we only need to store 3 time slice-wide

temporaries (for unimproved and 5 for improved) compared to storing 1 lattice wide temporary. We use this technique for all N_d-wide smearing procedures including the final level of the hypercubically-blocked smearing method. For the Wilson flow, and for our largest available lattice ($64^3 \times 128$) the difference between naïvely performing the flow and including the memory saving methods outlined in this section is just over a saving of half the computer memory required. Including the storage of the full lattice-wide gauge fields in both cases.

Algorithm 2 *Memory saving smearing iterations.*

```
lat4 ← Smear(lat[Lt − 1])
for t = 0 → L_t − 2 do
    lat2 ← Smear(lat[t])
    if t ≠ 0 then
        lat[t − 1] ← lat3
    end if
    lat3 ← lat2
end for
lat[L_t − 2] ← lat3
lat[L_t − 1] ← lat4
```

4.6.1 Invariants and scale setting

It was first suggested in [119] that by picking some reference scale for the dimensionless quantity,

$$G(t) = t^2 \langle \bar{F}_{\mu\nu} \bar{F}_{\mu\nu} \rangle|_{t=t_0^2} = 0.3, \tag{4.42}$$

where the F's are the lattice gauge field strength tensors (Sec.4.4) averaged over the lattice volume (denoted by the bar). One can very accurately measure the lattice spacing once the continuum value t_0 in physical units is calibrated using some other, more physical input. As t_0 has units of the lattice spacing we can measure $a = \frac{t_0^{\text{cont}}}{t_0}$ from our measured t_0. Where t_0^{cont} is the continuum evaluated value, and is evaluated by some other physical measure to set the scale.

In principle, any measure with lattice units can be used to determine the scale, such as the Pion, Kaon or Omega masses or the Sommer scales [147] r_0 or r_1 [76]. One of the benefits of using the Wilson flow is that it is cheap to perform, requiring no fermion propagator calculations and is insensitive to the lattice volume. Unlike the Sommer scale, it does not require fitting to a potential, and has been argued to be even more statistically precise [37].

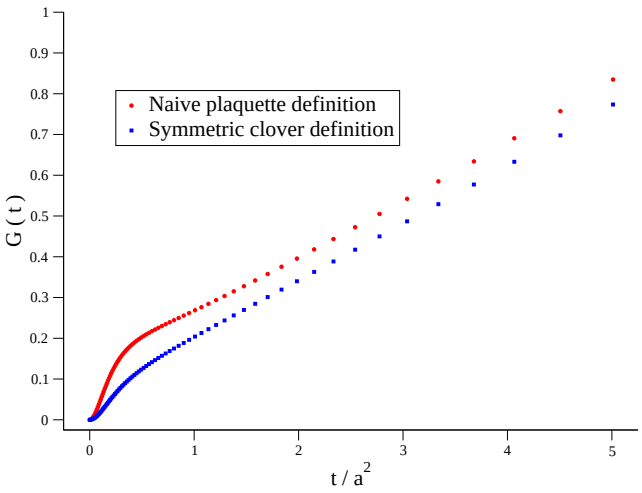

(a) *G(t) for STOUT smearing*

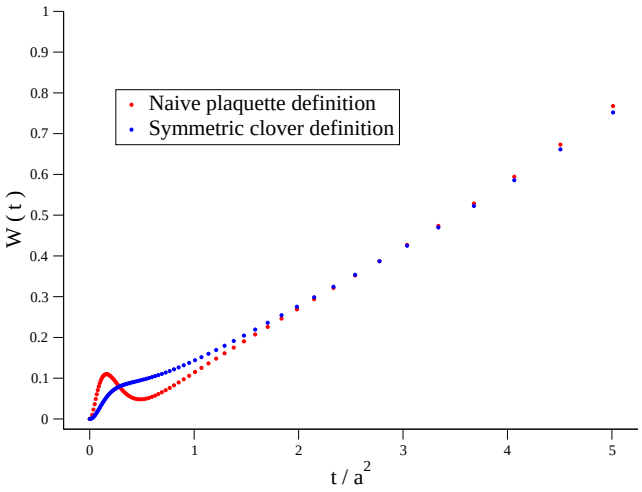

(b) *W(t) for STOUT smearing*

Figure 4.12 *The measures G(t) (Eq.4.42) and W(t) (Eq.4.42) for STOUT smearing using the adaptive integration procedure for an example* $16^3 \times 32$, $\beta = 2.13$ *Iwasaki gauge configuration. Where the field strength tensor's definition was either the naive plaquette definition or the symmetric clover, large lattice artifacts are seen for* $G(t)$*, by using* $W(t)$ *we see these discrepancies are reduced.*

It has been advocated in [37], that the related dimensionless parameter,

$$W(t) = t\frac{d}{dt}t^2\langle \bar{F}_{\mu\nu}\bar{F}_{\mu\nu}\rangle|_{t=W_0^2} = 0.3. \tag{4.43}$$

Was better for the determination of the coupling, as it was argued to be less sensitive to discretisation effects, as was seen in [66], due to it being the evaluation of the slope of the energy density with fictitious time rather than the absolute value. This can be seen in Fig.4.12, where the difference between two descriptions of the field strength tensor are shown for the quantities $G(t)$ and $W(t)$. The description of the field strength

tensor being the naive plaquette definition of Eq.2.19 vs the symmetric clover definition of Fig.4.5 and the flows were integrated using the two-step adaptive routine of Sec.4.6.2. We see that lattice artifacts are quite large for the definition $G(t)$ but its gradient is much better behaved at the flow times of interest in this study.

The value W_0 becomes our reference scale in exactly the same way as t_0 did, and the derivative of the field strength is performed using a finite difference method. We explicitly compute both G(t) and W(t) in our implementation, using a leapfrog determination of the derivative in Eq.4.43 as a guide for when to stop. To a very good approximation, we have found $G(t)$ behaves approximately linearly with t for small steps of t around W_0^2. We perform at least 8 fine ($\epsilon \approx 0.01$) measures of G(t) around W_0^2 and fit linearly. Determining W_0 from the fit parameters,

$$W_0^2 = \frac{0.3}{\frac{dG(t)}{dt}}. \tag{4.44}$$

We could equivalently fit the leapfrog values of $W(t)$ linearly to interpolate to $t = W_0^2$, and saw no difference between these two evaluations.

4.6.2 Improvement for Wilson flow measures

Apart from the memory-wise improvements mentioned in the previous section (Alg.2), we can imagine other technical improvements to the Wilson flow integration. The integration scheme in Eq.4.41 is considered to have error of $O(\epsilon^4)$ for the Wilson flow. And was seen to behave similarly for the Symanzik flow [37], assuming scaling behaviour of $O(\epsilon^3)$ [119] one would expect the error of the integration procedure with step size 0.01 to be of the order 10^{-6}.

As an improvement method, we have implemented a two-step adaptive RK4 method, based on the update in Eq.4.41. This was to test the error of our fixed ϵ implementation for different flow regimes and to provide a fixed-error computation. The two step adaptive integration scheme is one of the simplest adaptive algorithms, it requires the calculation of one step with some size ϵ and the same integration with two half steps and compares the error between the two evaluations and adjusts the integration step accordingly[3].

Our error term is the difference between the lattice average plaquette traces ($\bar{U_p}$) of the single and two half-step evaluations (effectively measuring the error in the most naïve evaluation of $G(t)$). If they are equivalent to within some tolerable accuracy we increase the integration step-size ϵ, otherwise we decrease it. The parameters for increasing and

[3]We overwrite our temporary lattice with the two half-step evaluation to save space.

decreasing the step size are a dark art and we found it acceptable to use [138] (S is the "safety factor" 0.9),

$$\epsilon = \begin{cases} \epsilon\, S\, \left(\frac{\delta(\bar{U}_p)}{\mathrm{Tol}}\right)^{1/5}; & \bar{U}_p > \mathrm{Tol} \\ \epsilon\, S\, \left(\frac{\delta(\bar{U}_p)}{\mathrm{Tol}}\right)^{1/4}; & \bar{U}_p < \mathrm{Tol}. \end{cases}$$

To check the validity of our adaptive routine, we compute the Wilson flow on a single configuration with the adaptive integration (with tolerance 10^{-7}) and the fixed step-size routine (with $\epsilon = 0.01$). For this choice of parameters the error in the integration is considered to be roughly equivalent for both of these procedures. We measure the quantity G(t) for a single $16^3 \times 32$, $\beta = 2.13$ configuration up to $t \approx W_0^2$. The graph of the results is Fig.4.13, we see fantastic agreement between the two methods. We also note that it is only at very early flow times that a small integration step is required, and at large flow times, linear behaviour is seen in $G(t)$ with the fictitious flow time t.

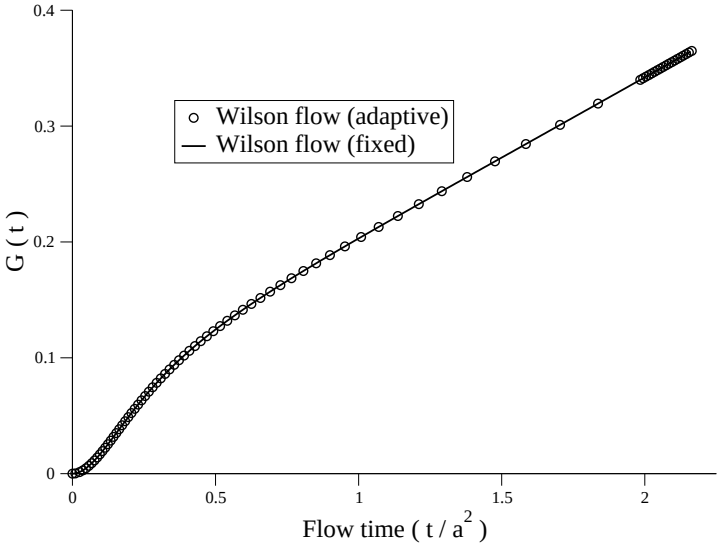

Figure 4.13 *A test of the adaptive integration procedure for the Wilson flow with the comparable fixed-ϵ integration procedure for an example $16^3 \times 32$ configuration.*

The authors in [37] investigated two STOUT smeared flows, the Wilson and the Symanzik. With fixed step size $\epsilon = 0.01 \rightarrow 0.02$. We investigate the Symanzik, Iwasaki, DBW2 and Wilson flows with STOUT and LOG smearing on an example $16^3 \times 32, \beta = 2.13$, $N_f = 2+1$, Iwasaki gauge configuration using the two-step adaptive procedure with tolerance 10^{-7} (except for the LOG-Iwasaki and LOG-DBW2 which have tolerance 10^{-5}) the parameters $G(t)$ and $W(t)$ are shown in Fig.4.14. This investigation was intended to understand the the best fixed ϵ's for each method.

We note that to ensure an accuracy of 10^{-7} is attained, for the Symanzik, Iwasaki and DBW2 at low flow times require an integration step much less than 0.01. A table of the minimum step size required for the different smearing procedures is shown in

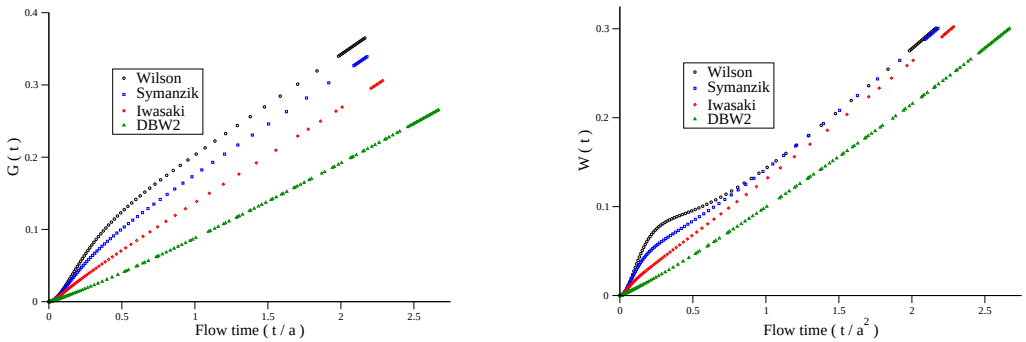

(a) *G(t) for STOUT smearing* **(b)** *W(t) for STOUT smearing*

(c) *G(t) for LOG smearing* **(d)** *W(t) for LOG smearing*

Figure 4.14 *The measures G(t) (Eq.4.42) and W(t) (Eq.4.42) for STOUT and LOG smearing for the Wilson, Symanzik, Iwasaki and DBW2 flows for an example* $16^3 \times 32$ *configuration. We used the adaptive algorithm with Tolerance* 10^{-7} *for all but the LOG-Iwasaki and LOG-DBW2 where a Tolerance of* 10^{-5} *was used. We used the* $O(a^2)$ *symmetric clover term for the field strength tensor.*

Tab.4.7 for this tolerance. We see that the step-size has to be altered to accommodate for the various c_0's, upon adjusting for these large values (i.e. multiplying by c_0) we have roughly the same magnitude step-size for each recipe which ensure fixed accuracy. We also note that due to the aggressive manner that LOG smearing smooths out configurations, a much smaller integration step size in general is required. This can be best seen in Fig.4.14 where the LOG smeared Wilson flow G(t) is much closer to the Symanzik flow's. For LOG smearing all of the improved flows lie closer together for both the parameters $G(t)$ and $W(t)$.

4.6.3 Large time evaluations

We have seen that the adaptive integration procedure for the flow equation increases the integration step at larger positive flow times. This makes heuristic sense as the flow smooths the gauge field the difference between small time steps in the plaquette will be smaller as the average plaquette trace converges to the identity. This allows for

Flow	STOUT	LOG
Wilson	0.00929	0.00346
Symanzik	0.00571	0.00147
Iwasaki	0.00263	0.00031
DBW2	0.00080	-

Table 4.7 *The minimum step-size from the adaptive integration of the flow equation 4.37 for several flow types with STOUT and LOG smearing to achieve an error in the average plaquette of less than* 10^{-7} *from an example* $16^3 \times 32$ *configuration. The step-size for the Log-DBW2 flow was seen to not be converging in a reasonable time, different tuning of the adaptation parameters is needed for this flow.*

larger steps in the integration scheme.

We have chosen to test the effectiveness of the adaptive algorithm for large flow time evaluations (which are sometimes used to measure the topological charge)[4] by measuring the computation time taken for the fixed ϵ integration to reach a certain flow time, divided by the computation time for the adaptive algorithm to reach the same flow time (including a correction step to the exact time).

We choose to investigate the Wilson flow with $\epsilon = 0.01$ and adaptive tolerance 10^{-7} for flow times $t/a = 1,\ 2,\ 4,\ 6,\ 8$ and 10 for an example $16^3 \times 32$ configuration. We found that after $t \approx 10$ the adaptive algorithm suffered from numerical instabilities and would require a lower tolerance for flow times above 10.

From Fig.4.15 we see up to 3.3× speed up using the adaptive algorithm for large time separations. The break-even point for the adaptive algorithm is at roughly $\frac{t}{a} = 2$, any flow time higher than this we would be better off using the adaptive algorithm. As the adaptive procedure is fixed-error instead of fixed step size and is a cheaper method at large flow times, it is the recommended method. Also, if one were to use an improved action such as Symanzik or one of the others and assumed their fixed step-size error was the same as the Wilson flow's then significant errors could accumulate (particularly for the DBW2 or Iwasaki and especially for the LOG smearing method).

When measuring the parameter W_0 using the adaptive procedure, once $W(t)$ is within 10% of the reference value (0.3 in our case), we switch to fixed-ϵ=0.01, fine measurements for accurate determination of $t = W_0^2$. We stop our integration once we have moved past the reference value and at least 8 fine measurements have been made.

The derivative in the definition of $W(t)$ using the adaptive procedure has to be the

[4]We found that only the Wilson and Symanzik provided the chiral Dirac index definition topological charge on our test configuration for STOUT smearing, and only the Wilson flow did for LOG smearing.

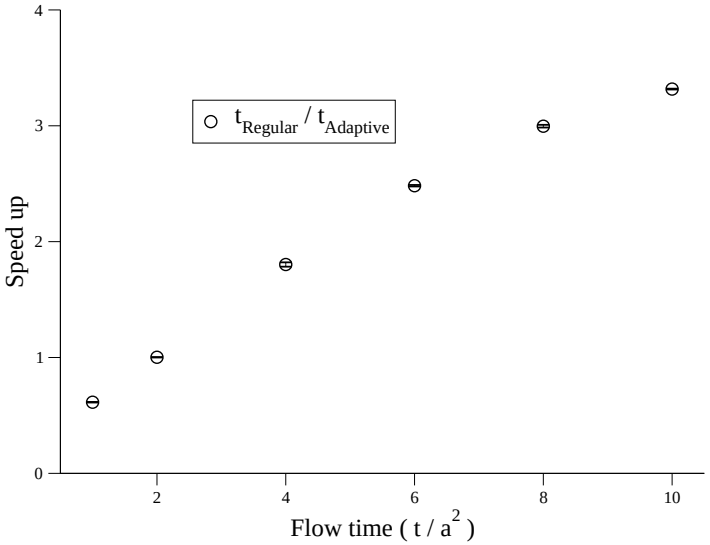

Figure 4.15 *The large flow time speed up with the adaptive routine. Evaluated from the computation time taken to flow to a specific time using the fixed ϵ integration divided by the computation time for the two step adaptive routine. The errors are from a Jackknife analysis over 5 runs.*

Euler, because the step-size is not fixed for successive steps. For our determination of W_0 using the adaptive algorithm we prefer to fit the 8 fine measurements of $G(t)$ linearly and use Eq.4.44.

4.6.4 Continuum W_0 scale evaluations

We chose to determine the physical continuum W_0 by using our coarse $24^3 \times 64$ and fine $32^3 \times 64$ $N_f = 2 + 1$ DWF ensembles, with inverse lattice spacings $a^{-1} = 1.73(3)$ GeV and $a^{-1} = 2.28(3)$ GeV respectively. The lattice spacings have been determined by a global fit to the Pion, Kaon Mesons and the Omega Baryon in [14].

We use the same approach as [37] for determining the parameter W_0, i.e. using the Wilson flow integration and STOUT smearing (Eq.4.41) with fixed step-size $\epsilon = 0.01$ and integrating until $W(t) > 0.3$. The rationalé for using the fixed step-size approach was based on the estimate of our $\beta = 2.13$ ensemble having $W_0^2 \approx 2$, i.e. the break even point of the adaptive algorithm. Using the fixed step-size evaluation allows for a direct comparison to the result in [37]. We use a linear interpolation to obtain $W(W_0^2) = 0.3$ from the final 8 integration steps of W(t).[5]

[5] As a check of our results, our fixed step-size Wilson flow integration code has been directly checked against the BMW implementation [37] and another implementation in HiRep [139].

4.6.5 Autocorrelations

It was seen in [37] that the Wilson flow suffers from fairly large autocorrelations of the order 50 or so HMC trajectories. We have investigated the autocorrelations of our data using the windowing method for determining the integrated autocorrelation time $\tau_{\rm int}(t)$. Where the time of the first plateau indicates $\tau_{\rm int}(t)$.

Coarse		Fine	
mass	$\tau_{\rm int}$	mass	$\tau_{\rm int}$
0.005	80	0.004	80
0.010	100	0.006	40
0.020	60	0.008	60
0.030	50	-	-

Table 4.8 *The estimates for the integrated autocorrelation times for the parameter W_0 for our coarse and fine lattices.*

4.6.6 Chiral and Continuum limits

In Fig.4.16, we have the chiral extrapolation of W_0 for the coarse data. Extrapolated in the simulated light quark mass to the physical degenerate light quark mass, as our chiral limit. And in Fig.4.17 we have the chiral extrapolation for the fine ensemble.

For the coarse ensemble we use the degenerate simulated light quark masses $am_l = 0.005,\ 0.01,\ 0.02$ and 0.03, with strange quark mass $am_s = 0.04$. For the fine ($\beta = 2.25$), we have $am_l = 0.004,\ 0.006,\ 0.008$ with strange quark mass $am_s = 0.03$. We have binned our evaluations up to the estimate of the integrated autocorrelation time in our Monte-Carlo times to obtain our final results to account for any autocorrelation. For both extrapolations we have performed an uncorrelated linear fit and obtained $\chi^2/dof = 4.15, 0.83$ for the coarse and fine extrapolations respectively.

The $a^2 \to 0$ data for our evaluation of the parameter W_0 (Fig.4.18) shows some scaling with the lattice spacing, with the difference from our coarse ensemble's chiral W_0 to the continuum extrapolation being a correction of around 4%. Our continuum limit evaluation of the W_0 parameter in fm is (with the term on the right being the result of the fit),

$$W_0 = 0.1806(14)(fm), \qquad W_0(a) = 0.1806(14) - 0.0209(44)a^2. \tag{4.45}$$

There is some tension between our value and that of [37], which was 0.1755(18)(04). And slightly less between ours and the preliminary result of [66]'s value of 0.1782 fm

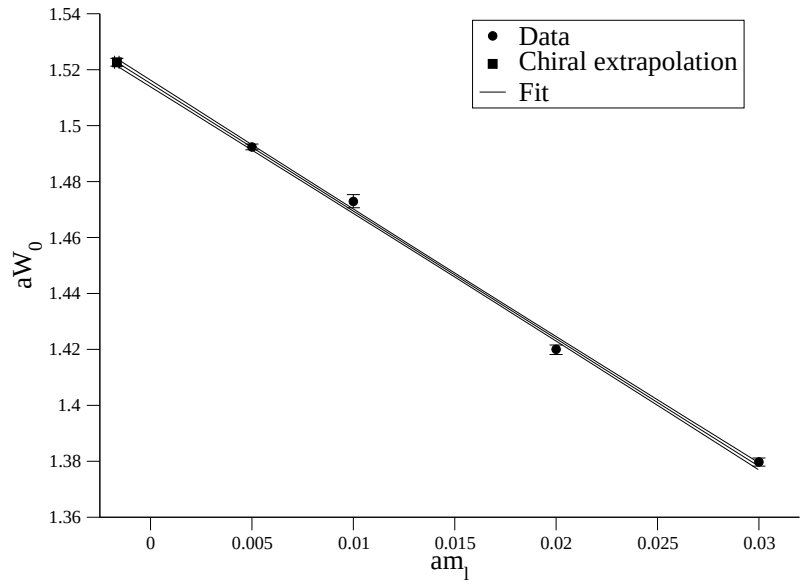

Figure 4.16 *Chiral extrapolation of aW_0 for the coarse data to the physical degenerate light quark mass.*

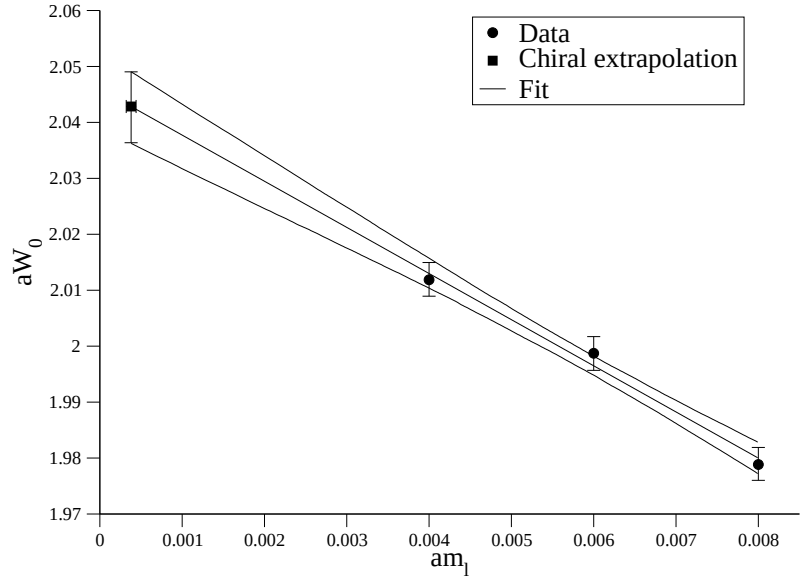

Figure 4.17 *Chiral extrapolation of aW_0 for the fine data to the physical degenerate light quark mass.*

where no error was quoted, but the same gauge action in the generation of configurations as our study was used. The discrepancy could be due to the $a^2 \to 0$ extrapolation not being fully under control and a third lattice spacing would be very useful for further studies, it is intriguing to note that if the a^2 extrapolation were flat we would recover [37]'s result within error.

We have a value for the physical W_0, which we can then use to predict lattice spacings,

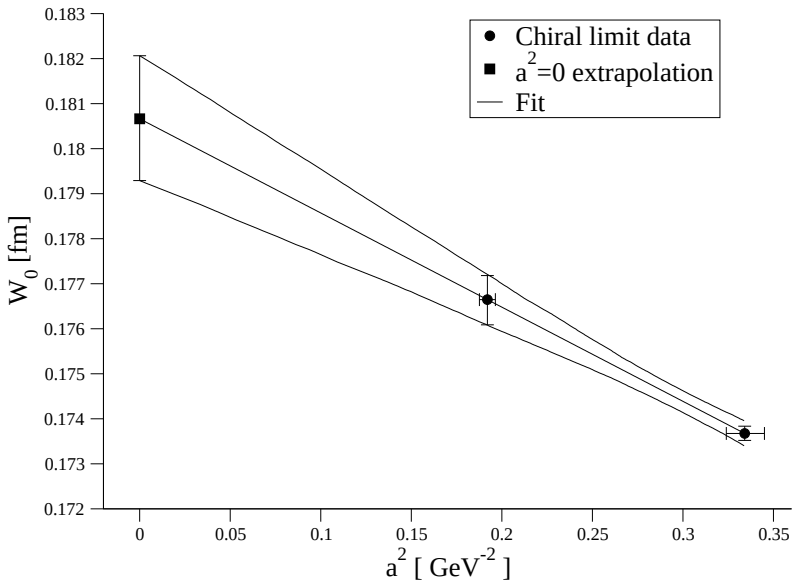

Figure 4.18 *The $a^2 \to 0$ extrapolation of our chiral limit data, for W_0 in fm.*

if the continuum extrapolation were flat we would use,

$$a^{-1}(GeV) = 0.1975269 \left(\frac{aW_0}{0.1806(14)} \right). \tag{4.46}$$

It is not, instead we have to solve,

$$a^{-1}(GeV) = 0.1975269 \left(\frac{aW_0}{0.1806(14) - 0.0209(44)a^2} \right). \tag{4.47}$$

Which has positive solution (in terms of the lattice-measured parameter aW_0),

$$a^{-1}(GeV) = \frac{aW_0 + \sqrt{(aW_0)^2 + 0.387(20)}}{1.830(14)}. \tag{4.48}$$

And should define the value we would obtain if we measured our lattice spacing using the physical Pion, Kaon and Omega which we usually use to set the lattice scale for our scaling trajectory.

We have an $N_f = 2 + 1$ $16^3 \times 32$, $\beta = 2.23$ ensemble with two degenerate light quark masses $am_l = 0.01,\ 0.02$, with undetermined lattice spacing. We estimate the residual mass for this configuration to lie between that of the coarse and fine ensembles' (1.6×10^{-3}), and we linearly fit the evaluations of aW_0 to $-m_{\text{res}}$ to obtain the chiral limit value of 1.957(59). This gives inverse lattice spacing $a^{-1}(\beta = 2.23) = 2.192(63)GeV$ using our evaluation from Eq.4.48, or $a^{-1}(\beta = 2.23) = 2.203(69)GeV$ using [37] and assuming a flat continuum extrapolation. With both evaluations errors are added in quadrature. We found that we needed to bin 60 and 40 configurations for the $am = 0.01$ and $am = 0.02$ ensembles respectively to cope with the autocorrelation

errors. The statistical error evaluation is quite large, because we don't get much of an error reduction from the self-average over the volume and the configurations not being adequately separated in Monte Carlo time.

As we found non-flat behaviour in the extrapolation to the continuum limit, we include the fit parameters and their errors into the computation of the lattice spacing, but evaluations of the lattice spacing with this method should allow for $O(1\%)$ errors. The Wilson flow also allows for very fast searches of parameter space as it is computationally cheap to perform and for large volumes provides very accurate lattice spacing determinations. As a by-product topological charge measurements are almost free to perform as the flow increases, which can then be used to investigate the topological tunnelling of the simulation. This is to what we now turn.

4.6.7 Exploration using the Wilson flow

As an exploration into changing our simulation program's gauge action to the tree level Symanzik rather than Iwasaki in the attempt to retain ergodicity whilst also being able to decrease the physical lattice spacing, we investigated a short run of $32^3 \times 64,\ N_f = 2+1,\ SU(3)$ DWF ensembles with $\beta = 4.17,\ 4.22,\ 4.25$ and $am_l = 0.01,\ am_s = 0.03$ using the adaptive Wilson flow procedure with tolerance 10^{-7} and with the symmetric unimproved clover definition of the gauge field strength tensor (Fig.4.5).

	$\beta = 4.17$	$\beta = 4.22$	$\beta = 4.25$
Configurations	$330 \rightarrow 570$	$345 \rightarrow 605$	$390 \rightarrow 510$
Measurement step	5	5	5
Binning	4	4	4
$a^{-1}GeV$	2.576(21)	2.958(21)	3.223(21)

Table 4.9 *The exploratory configurations used for this study, we have binned every 20th Monte Carlo time, and for the estimate of the lattice spacing we have used [37] as we do not know the scaling behaviour with a of the lattice spacing to the continuum, so we have to use the flat assumption.*

Tab.4.9 shows the configurations we worked with for this quick study. The lower bound is taken from an estimate of thermalisation, the number of $\beta = 4.25$ configurations measured was small. Fitting linearly the lattice spacings for each bare coupling β we obtain for this scaling trajectory,

$$a^{-1}(GeV) = -31.0(1.3) + 8.04(32)\beta. \tag{4.49}$$

As we are measuring the field strength tensor for the calculation of G(t) and the flow stopping time, it is computationally almost free to compute the naïve gauge definition of the topological charge. We plot the topological charge for the three β's at $t \approx W_0^2$ to investigate the tunnelling properties. This is shown in the plots in Fig.4.19.

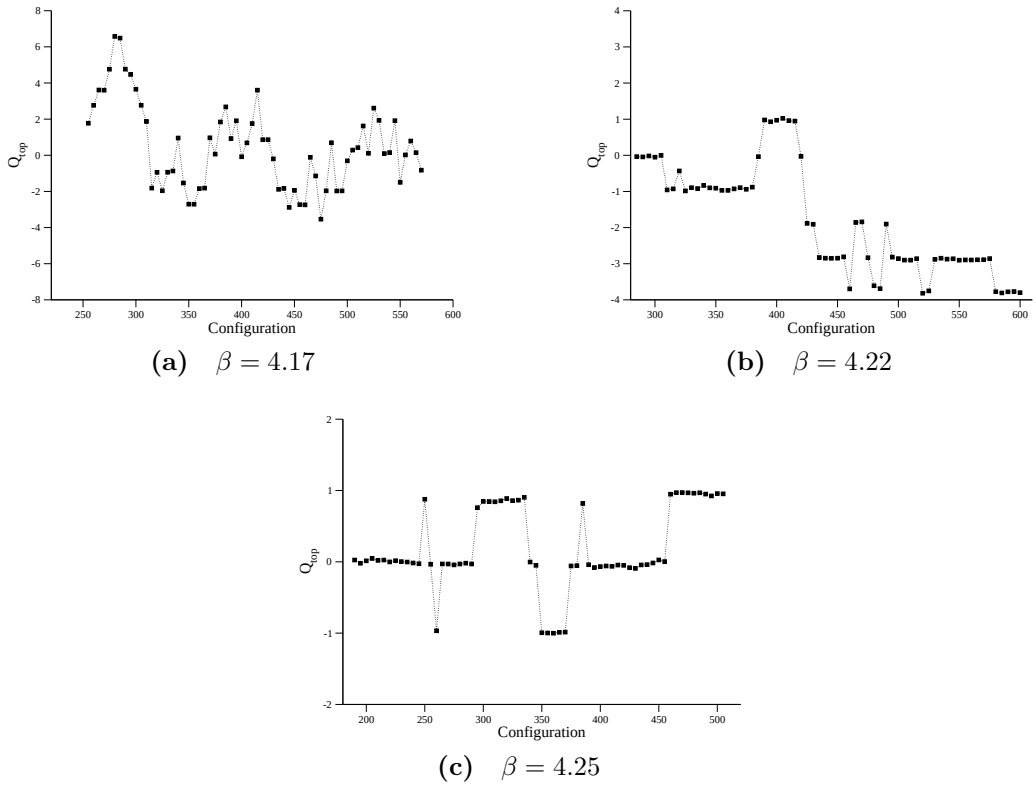

(a) $\beta = 4.17$ **(b)** $\beta = 4.22$

(c) $\beta = 4.25$

Figure 4.19 *The topological charge evaluated at $t \approx W_0^2$ from the adaptive Wilson flow procedure. The dashed line is to guide the eye.*

Fig.4.19 shows the worrying issue that plagues many modern lattice simulations [9]. As the lattice spacing decreases, the topological charge changes very slowly in Monte Carlo time. At our largest inverse bare coupling $\beta = 4.25$ the topological charge barely fluctuates from 0, this raises concerns about our algorithm's ability to sample the parameter space adequately and calls into question whether we remain ergodic as the lattice spacing is reduced with this gauge action and with periodic boundary conditions on the fields. The situation has been seen to be more dire for the Iwasaki action, and we could not hope to have topological tunnelling around $a^{-1} \approx 3GeV$ [9], in this respect it appears that switching to the tree level Symanzik action does allow for slightly smaller lattice spacings whilst retaining tunnelling. Conversely, this will increase the quantity m_{res} [12].

As a tool for investigating future, large-scale simulation programs. Small, Wilson flow studies can be invaluable in mapping out the available parameter space quickly and effectively. With the ability to measure accurately the lattice spacing (we attained a sub percent statistical error for the lattice spacing from 48 configurations with binning

factor of four) and to investigate the topological sampling simultaneously this method is a must for investigations into new simulation parameters, gauge actions and alike.

Due to improvements in accurately determining renormalisation constants with very few configurations via step-scaling, and in conjunction with the Wilson flow. We propose a fast and accurate way to compute step-scaling functions that determine the running of renormalisation constants between scales by determining the scale using the Wilson flow. With accurate determination of the lattice spacing over a handful of well separated configurations and accurate measurement of renormalisation constants perturbative matching errors can be greatly reduced by matching our data non-perturbatively up to a high scale where continuum perturbation theory matching can be performed with limited perturbative series truncation error. Such a technique could be invaluable for measurements of the strong coupling where in Chapter 3 we have seen large systematic errors in matching to continuum perturbation theory.

Chapter 5

$K^0 - \bar{K}^0$ mixing in and beyond the Standard Model

Our simulations are performed using Domain Wall Fermions, which have the luxury of very small chiral symmetry breaking and should be considered as a great playground for Flavour Physics calculations. Early investigations of K^0-$\bar{K}^0$mixing using the Wilson action [5] or the overlap operator [131] on quenched gauge configurations [21] were performed. As well as a recent $N_f = 2$ dynamical Twisted Mass calculation [26]. We present our continuum limit evaluations of the higher dimensional operators that constrain flavour violation in the Kaon sector Beyond the Standard Model (BSM) and produce an independent analysis of our collaboration's evaluation of the Standard Model (SM) bag parameter B_K.

The parameter B_K is directly related to CP violation. CP is the proposed symmetry that particles under a parity (P) transformation and charge (C) transformation should remain the same [1]. This is a symmetry of the QCD Lagrangian, but not a symmetry of the Standard Model, in particular the inclusion of the weak interaction allows for flavour changing interactions between quarks, this is seen by the mass eigenstates of the Kaons not being eigenstates of CP. The first measurement of CP violation in the Kaon sector resulted in a Nobel Prize in physics for Cronin and Fitch [54] in 1980.

The Cabbibo-Kobayashi-Maskawa (CKM) [48, 112] matrix describes the mixing between quark flavours due to the weak interaction, its discovery led to the Nobel

[1]Spin 1/2 particles themselves are not eigenstates of Parity, but certain bilinear structures are. Under charge conjugation (C) fermion fields transform as $C\Psi C \rightarrow -i\left(\gamma_0\gamma_2\bar{\Psi}\right)^T$.

prize in physics for Kobayashi and Maskawa in 2008. The matrix has the form,

$$\begin{bmatrix} d \\ s \\ b \end{bmatrix} = \begin{bmatrix} V_{ud} & V_{us} & V_{ub} \\ V_{cd} & V_{cs} & V_{cb} \\ V_{td} & V_{ts} & V_{tb} \end{bmatrix} \begin{bmatrix} d' \\ s' \\ b' \end{bmatrix} = V^{\mathrm{CKM}} \begin{bmatrix} d \\ s \\ b \end{bmatrix}. \tag{5.1}$$

The matrix is unitary and the elements V_{ij} are hence complex, the magnitude of the individual elements must be provided from experiment. The unitarity of the CKM matrix means,

$$\begin{aligned} \sum_{j=\{d,s,b\}} V_{ij}V_{kj}^* = 0, \qquad i \neq k, \qquad i,k = \{u,c,t\}, \\ \sum_{j=\{d,s,b\}} V_{ij}V_{kj}^* = 1. \qquad i = k, \qquad i,k = \{u,c,t\}. \end{aligned} \tag{5.2}$$

Therefore there are six relations yielding zero (the top summation in Eq.5.2), these are known as Unitary triangles. The six triangles will look different, but their area will be the same.

There are many choices for a reparameterisation of the CKM matrix, but the standard one is,

$$V^{\mathrm{CKM}} = \begin{bmatrix} c_{12}c_{13} & s_{12}c_{13} & s_{13}e^{-i\delta} \\ -s_{12}c_{23} - c_{12}s_{23}s_{13}e^{i\delta} & c_{12}c_{23} - s_{12}s_{23}s_{13}e^{i\delta} & s_{23}c_{13} \\ s_{12}s_{23} - c_{12}c_{23}s_{13}e^{i\delta} & -s_{23}c_{12} - s_{12}c_{23}s_{13}e^{i\delta} & c_{23}c_{13} \end{bmatrix}. \tag{5.3}$$

Where $c_{ij} = \cos(\theta_{ij})$, $s_{ij} = \sin(\theta_{ij})$, this parameterisation has three real angles θ_{ij} and one phase δ, the phase dictates the amount of CP violation. The CKM matrix can be expressed more simply in terms of the Wolfenstein parameters [158] which are (Next Leading Order (NLO)) numerical approximations to the exact parameterisation of Matrix 5.3,

$$\begin{gathered} s_{12} = \Lambda, \qquad s_{13} = e^{i\delta}A\Lambda^3(\rho - i\eta), \qquad s_{23} = A\Lambda^2, \\ c_{12} = 1 - \frac{\Lambda^2}{2} + \frac{\Lambda^4}{8}, \qquad c_{13} = 1 - \frac{1}{2}e^{i2\delta}A^2\Lambda^6(\rho - i\eta), \qquad c_{23} = 1 - \frac{A^2\Lambda^4}{2} \\ \rho = \frac{s_{13}}{s_{12}s_{23}}\cos(\delta), \qquad \eta = \frac{s_{13}}{s_{12}s_{23}}\sin(\delta). \end{gathered} \tag{5.4}$$

Which gives the form of the CKM matrix,

$$V^{\mathrm{CKM}} = \begin{bmatrix} 1 - \frac{\Lambda^2}{2} + \frac{\Lambda^4}{8} & \Lambda & A\Lambda^3(\rho - i\eta) \\ -\Lambda + \frac{A^2\Lambda^4}{2}\left(1 - 2(\rho + i\eta)\right) & 1 - \frac{\Lambda^2}{2} + \frac{\Lambda^4}{8}\left(1 - 4A^2\right) & A\Lambda^2 \\ A\Lambda^3\left(1 - (\rho + i\eta)\left(1 - \frac{\Lambda^2}{2}\right)\right) & -A\Lambda^2\left(1 - \frac{\Lambda^2}{2}\left(1 - 2(\rho + i\eta)\right) + \frac{\Lambda^4}{8}\right) & 1 - \frac{A^2\Lambda^4}{2}. \end{bmatrix}. \tag{5.5}$$

Where Λ is small (experimentally ≈ 0.22). If we define the two following quantities,

$$\bar{\rho} = \rho\left(1 - \frac{\Lambda^2}{2}\right) \qquad \bar{\eta} = \eta\left(1 - \frac{\Lambda^2}{2}\right). \tag{5.6}$$

And we also define $\lambda_i = V_{id}V_{is}^*$, we have the following neat relations [44],

$$\begin{aligned} \Im(\lambda_t) = \Im(\lambda_c) &= \eta A\Lambda^5, \\ \Re(\lambda_t) &= A\Lambda^5\left(1 - \rho\left(1 - \frac{\Lambda^2}{2}\right)\right), \\ \Re\left(\lambda_c\right) &= -\Lambda\left(1 - \frac{\lambda^2}{2}\right). \end{aligned} \tag{5.7}$$

These relations will allow us to quantify the amount of mixing between quarks and CP-violation in the Standard Model, by allowing for a determination of the mixing angle δ.

It is common to define *the* Unitarity triangle from Eq.5.2 as (where I have used the Wolfenstein parameters),

$$\begin{aligned} V_{ud}V_{ub}^* + V_{cd}V_{cb}^* + V_{td}V_{tb}^* &= 0. \\ V_{ud}V_{ub}^* &= A\Lambda^3(\bar{\rho} + i\bar{\eta}), \\ V_{cd}V_{cb}^* &= -A\Lambda^3, \\ V_{td}V_{tb}^* &= A\Lambda^3\left(1 - \bar{\rho} - i\bar{\eta}\right). \end{aligned} \tag{5.8}$$

We can see directly that these relations all have the same common factor $A\Lambda^3$, which we ignore. Writing the expressions as vectors in the complex plane gives us $(-1, 0)$, $(\bar{\rho}, \bar{\eta})$ and $(1 - \bar{\rho}, -\bar{\eta})$. This can be visualised in the cartoon of Diagram 2.

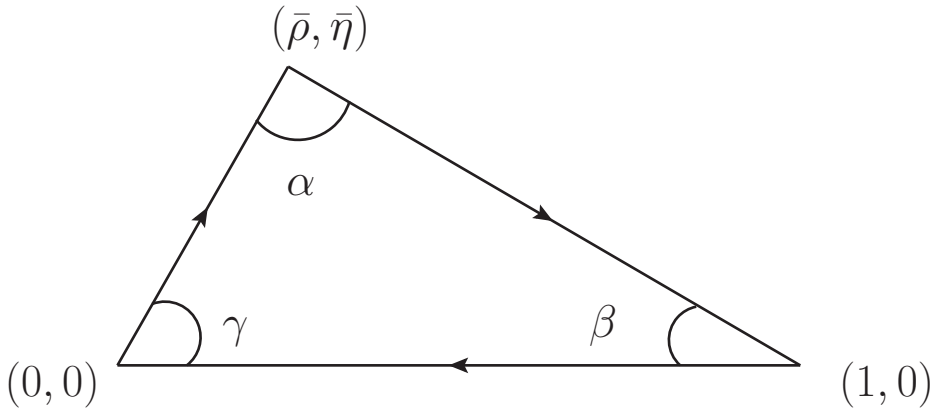

Diagram 2: A cartoon of the Unitarity triangle in the complex $\bar{\rho} - \bar{\eta}$ plane.

Our result for B_K along with some known factors can allow us to constrain the value of

the CP-violating phase δ, and hence $\bar{\rho}$ and $\bar{\eta}$ and the angle α in the unitarity triangle.

5.1 Flavour Changing and Kaon Oscillation

Kaon oscillation can only occur at the one-loop level and higher, mediated by box diagrams such as that in Diagram 3. Weak, heavy chiral bosons cannot be simulated on the lattice with present technology. Their contribution can be incorporated by integrating out their degrees of freedom and leaving an effective vertex which parameterises the interaction at a scale much less than the W-boson mass. This is called the Operator Product Expansion (OPE), and is represented diagrammatically for the SM in Diagram 3. Extension to BSM models follows similarly, where the necessarily heavier particles are integrated out to leave effective vertices only this time with a slightly larger possible basis of dirac structures.

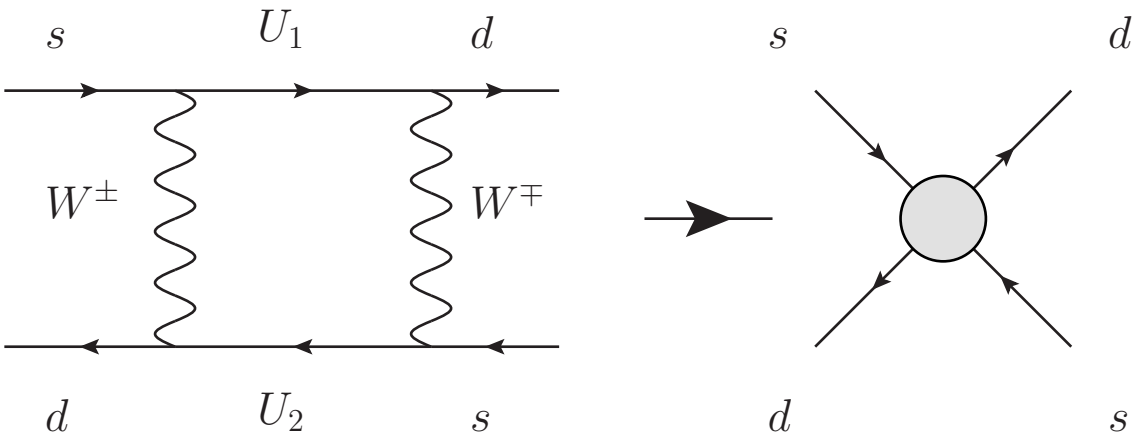

Diagram 3: Operator Product Expansion (OPE) pinch diagram illustrating how the integrating out of the heavy particles (W-bosons) leaves an effective vertex, which is the blob in the picture on the right of the box diagram. In this case, the SM one is the operator O_1.

Kaons mix their states, their time evolution equation is,

$$i\frac{d}{dt}\psi(t) = \hat{H}\psi(t), \qquad \psi(t) = \begin{pmatrix} |K^0(t)\rangle \\ |\bar{K}^0(t)\rangle \end{pmatrix}. \tag{5.9}$$

The (Hermitian) Hamiltonian parameterising their mixing is,

$$\hat{H} = \begin{bmatrix} M - \frac{i}{2}\Gamma & M_{12} - \frac{i}{2}\Gamma_{12} \\ M_{12}^* - \frac{i}{2}\Gamma_{12}^* & M - \frac{i}{2}\Gamma \end{bmatrix}. \tag{5.10}$$

Where M is the mass and Γ is the decay width of K^0. This matrix can be diagonalised to yield the eigenvalues,

$$\begin{aligned} q_{\pm} &= M - \frac{i}{2}\Gamma \pm Q, \\ Q &= \sqrt{\left(M_{12} - \frac{i}{2}\Gamma_{12}\right)\left(M_{12}^{*} - \frac{i}{2}\Gamma_{12}^{*}\right)}. \end{aligned} \tag{5.11}$$

And (mass) eigenstates,

$$\begin{aligned} K_{\pm} &= \frac{(1+\bar{\epsilon})\,K^0 \pm (1-\bar{\epsilon})\,\bar{K}^0}{\sqrt{2\,(1+|\bar{\epsilon}|^2)}}, \\ \frac{1+\bar{\epsilon}}{1-\bar{\epsilon}} &= \sqrt{\frac{M_{12}^{*} - \frac{i}{2}\Gamma_{12}^{*}}{M_{12} - \frac{i}{2}\Gamma_{12}}}. \end{aligned} \tag{5.12}$$

The parameter $\bar{\epsilon}$ is a small complex parameter that indicates the level of mixing between the Kaons.

We call the positive solution K-long (K_L), and the negative K-short (K_S), due to their difference in lifetime. As can be seen by K-long having a narrower decay width Γ and a greater mass M,

$$\begin{aligned} \Delta\Gamma_K &= \Gamma_L - \Gamma_S = -4\Im(Q), \\ \Delta M_K &= M_L - M_S = 2\Re(Q). \end{aligned} \tag{5.13}$$

The eigenstates of CP for the neutral Kaon system are [44],

$$K_1 = \frac{1}{\sqrt{2}}\left(K^0 - \bar{K}^0\right), \qquad K_2 = \frac{1}{\sqrt{2}}\left(K^0 - \bar{K}^0\right). \tag{5.14}$$

Using Eq.5.12, we see that the mass eigenstates differ from the CP eigenstates by the small amount $\bar{\epsilon}$,

$$K_L = \frac{K_2 + \bar{\epsilon}K_1}{\sqrt{1+|\bar{\epsilon}|^2}}, \qquad K_S = \frac{K_1 + \bar{\epsilon}K_2}{\sqrt{1+|\bar{\epsilon}|^2}}. \tag{5.15}$$

This is what we mean by neutral Kaon mixing. It is this slight difference between CP eigenstates and mass eigenstates that is known as *indirect* CP-violation, and is what was observed by Cronin and Fitch [54].

It can be shown that the parameter $\bar{\epsilon}$ can be written,

$$\bar{\epsilon} = \frac{1}{1+i}\frac{\Im(M_{12})}{\Delta M_K} + \frac{\zeta}{1+i}, \qquad \zeta = \frac{\Im(A_0)}{\Re\,(A_0)}. \tag{5.16}$$

The value of ζ is determined from I=0, $K \to \pi\pi$ decay rates and will later be discarded as it is small compared to the errors of other quantities. At the moment, $\bar{\epsilon}$ is convention dependent. The equation, $\epsilon = \bar{\epsilon} + i\zeta$ removes this, and allows us to write a convention-

free expression for the neutral Kaon mixing parameter ϵ that can also be measured experimentally.

$$\epsilon = \frac{e^{i\pi/4}}{\sqrt{2}\Delta M_K}\left(\Im\left(M_{12}\right) + 2\zeta\Re\left(M_{12}\right)\right). \tag{5.17}$$

The off-diagonal mass-mixing part of the Hamiltonian can be computed via the matrix element,

$$2m_K M_{12}^* = \langle \bar{K}^0 | \mathcal{H}_{eff} | K^0 \rangle. \tag{5.18}$$

The effective Hamiltonian after the OPE is,

$$\begin{aligned}\mathcal{H}_{eff} = \frac{G_F^2 M_w^2}{16\pi^2}\left({\lambda_c}^2\eta_1 S_0(x_c) + {\lambda_t}^2\eta_2 S_0(x_t) + \lambda_c\lambda_t\eta_3 S_0(x_t, c_t)\right) \times \\ \left(\alpha_{N_f=3}(\mu)\right)^{-2/9}\left(1 + \frac{\alpha_{N_f=3}(\mu)}{4\pi}J\right)O_1.\end{aligned} \tag{5.19}$$

Where J is scheme dependent and depends on the scheme of α. The multiplicative factors of α indicate we are using the Renormalisation Group Improved (RGI) variant of the definition of the effective Hamiltonian, which is assumed to have better perturbative convergence. The values of η_i have known NLO evaluations [105][2], and the values of $\lambda_{c/t}$ can be taken from Eq.5.7. The functions S_0 are the Inami-Lim functions [109].

The factor O_1 contains all of the low-energy, QCD corrections. This quantity is highly non-perturbative and can be computed using lattice techniques. The operator O_1 is (Eq.2.66),

$$O_1 = \left(\bar{s}\gamma_\mu\left(1-\gamma_5\right)d\right)\left(\bar{s}\gamma_\mu\left(1-\gamma_5\right)d\right).$$

We define the Kaon bag parameter, $B_1(\mu)$ (B_K) via the equation in the Vacuum Saturation Approximation (VSA) (where we have normalised the matrix element at the scale μ),

$$\frac{8}{3}f_K^2 m_K^2 B_K(\mu) = \langle \bar{K}^0 | O_1(\mu) | K^0 \rangle. \tag{5.20}$$

It is measured on the lattice by fitting to a constant the following correlation function in Euclidean time t (taking the results and definitions from Sec.2.4.1),

$$B_K(\mu) = \frac{c^{(1)}(t_i, t, t_f)(\mu)^{WLW}}{\frac{8}{3}c(t_i, t)^{WL}_{A_0,P}c(t, t_f)^{LW}_{P,A_0}}. \tag{5.21}$$

Where the correlator $(c^{(1)})$ has been renormalised non-perturbatively at the scale μ, as discussed below and in Appendix.B.

[2]Which are $\eta_1 = 1.38(20)$, $\eta_2 = 0.57(1)$ and $\eta_3 = 0.47(4)$

Defining the RGI quantity $\hat{B}_K(\mu)$ as,

$$\hat{B}_K(\mu) = \frac{1}{\frac{8}{3}m_K^2 f_K^2}\left(\alpha_{N_f=3}(\mu)\right)^{-2/9}\left(1+\frac{\alpha_{N_f=3}(\mu)}{4\pi}J\right)\langle \bar{K}^0|O_1(\mu)|K^0\rangle. \tag{5.22}$$

Where the quantity J is a scheme and N_f dependent quantity. We use the value quoted in [11] J=1.89506, for our evaluation of $\hat{B}_K(\mu)$ in the $\overline{\text{MS}} - NDR$ scheme.

Nneglecting the small correction of ζ in Eq.5.17, we have the following expression for the term ϵ,

$$\epsilon = \frac{G_F^2 M_W^2}{6\sqrt{2}\pi^2 \Delta M_K^2}\hat{B}_K(\mu)\Im\left(\lambda_t\right)\left[\Re\left(\lambda_c\right)\left\{\eta_1 S_0(x_c) - \eta_3 S_0(x_c,x_t)\right\} - \Re\left(\lambda_t\right)\eta_2 S_0(x_t)\right]e^{i\pi/4}. \tag{5.23}$$

The factor ϵ has been determined experimentally as $2.228(11)\times 10^{-3}$ [24]. Upon computation of the quantity in Eq.5.23 and inclusion of the terms in Eq.5.7 the CP-violating phase δ can be estimated, and used to constrain the angle α of the unitary triangle [45]. It is the error in the comuputation of $\hat{B}_K(\mu)$ that is the dominant factor in this estimation [24]. Accurate measurement of this quantity is very important and physically relevant for probing the CKM description of CP violation, and further constraining BSM physics.

The general effective four-quark Hamiltonian can be parameterised as,

$$\mathcal{H}_{eff} = C_i(\mu)O_i(\mu), \qquad i = 1,2,3,4,5. \tag{5.24}$$

The BSM calculation is the extension of the SM one to theories which may change the flavour of Kaons via some hitherto unknown mechanism which is not only "left handed" (not mediated by the W-boson), for instance super-symmetric (SUSY) theories. The long distance information for the Operator Product Expansion (OPE) is the same as the SM one but with the extension to a larger basis of four quark interpolating operators. The Wilson coefficients (denoted $C_i(\mu)$ in Eq.5.24) are dependent on the particular BSM model under consideration but the matrix element encoding the non-perturbative information remains the same.

The BSM operators in the SUSY basis are (Eq.2.66),

$$\begin{aligned} O_2 &= (\bar{s}_a(1-\gamma_5)d_a)(\bar{s}_b(1-\gamma_5)d_b), & O_3 &= (\bar{s}_a(1-\gamma_5)d_b)(\bar{s}_b(1-\gamma_5)d_a), \\ O_4 &= (\bar{s}_a(1+\gamma_5)d_a)(\bar{s}_b(1+\gamma_5)d_b), & O_5 &= (\bar{s}_a(1+\gamma_5)d_b)(\bar{s}_b(1+\gamma_5)d_a). \end{aligned} \tag{5.25}$$

The relation in the VSA for the Kaon bag parameters in the SUSY basis are,

$$\begin{aligned}
-\frac{5}{3}f_K^2 m_K^2 \left(\frac{m_K}{m_s(\mu)+m_d(\mu)}\right)^2 B_2(\mu) &= \langle \bar{K}^0|O_2(\mu)|K^0\rangle, \\
\frac{1}{3}f_K^2 m_K^2 \left(\frac{m_K}{m_s(\mu)+m_d(\mu)}\right)^2 B_3(\mu) &= \langle \bar{K}^0|O_3(\mu)|K^0\rangle, \\
2f_K^2 m_K^2 \left(\frac{m_K}{m_s(\mu)+m_d(\mu)}\right)^2 B_4(\mu) &= \langle \bar{K}^0|O_4(\mu)|K^0\rangle, \\
\frac{2}{3}f_K^2 m_K^2 \left(\frac{m_K}{m_s(\mu)+m_d(\mu)}\right)^2 B_5(\mu) &= \langle \bar{K}^0|O_5(\mu)|K^0\rangle.
\end{aligned} \tag{5.26}$$

These can be computed on the lattice as (where $c^{(i)}$ is the i'th operator's four point function in the SUSY basis, which have appropriate normalisations $N_i = \left(-\frac{5}{3}, \frac{1}{3}, 2, \frac{2}{3}\right)$),

$$B_i(\mu) = \frac{c^{(i)}(t_i, t, t_f)(\mu)^{WLW}}{N_i c(t_i, t)^{WL}_{P,P} c(t, t_f)^{LW}_{P,P}}. \tag{5.27}$$

The factor $\left(\frac{m_K}{m_s(\mu)+m_d(\mu)}\right)^2$ has been argued to introduce unnecessary systematics to the computation [70], and although the bag parameters are traditionally the object of measurement, the ratio (where "lattice" is the measurement of the quantities from the lattice, and experiment are the experimentally measured quantities taken from [24]),

$$R_i(\mu) = \left[\frac{f_K^2}{m_K^2}\right]_{\text{experiment}} \left[\frac{m_K^2}{f_K^2}\frac{c^{(i)}(t_i, t, t_f)(\mu)^{WLW}}{c^{(1)}(t_i, t, t_f)(\mu)^{WLW}}\right]_{\text{lattice}}, \tag{5.28}$$

is considered to be a more worthwhile measurement [21]. This is because systematic error cancellation may occur in the ratio of four point functions, and there is no need to introduce the renormalised quark masses which also introduce systematic error. Also, the dimensionless factor $\left(\frac{m_K^2}{f_K^2}\right)$ removes the leading chiral behaviour, making chiral extrapolations smoother (as can be seen in Fig.5.10). It should be noted that the physical point $m_{k,\text{lattice}} = m_{k,\text{experiment}}$ these ratios give directly the BSM to the SM contributions.

The matrix elements that contribute to neutral Kaon mixing are the parity even operators. As we cannot compute the color-mixed contributions of the operators in the SUSY basis, we instead compute the operators in the renormalisation basis (the non-perturbative renormalisation is performed in the renormalisation basis too). The SUSY basis color-mixed operators can then be computed by Fierz transformation, from the parity even renormalisation basis operators, which are,

$$\begin{aligned}
Q_{VV\pm AA} &= \bar{s}\gamma_\mu d \bar{s}\gamma_\mu d \pm \bar{s}\gamma_\mu\gamma_5 d \bar{s}\gamma_\mu\gamma_5 d, \\
Q_{SS\pm PP} &= \bar{s}d\bar{s}d \pm \bar{s}\gamma_5 d \bar{s}\gamma_5 d, \\
Q_{TT} &= \bar{s}\sigma_{\mu\nu} d \bar{s}\sigma_{\mu\nu} d.
\end{aligned}$$

Where $\sigma_{\mu\nu} = \frac{1}{2}[\gamma_\mu, \gamma_\nu]$ is the tensor operator. The relation between the color mixed (where a and b are color indices) $(\bar{s}_a \Gamma d_b)(\bar{s}_b \Gamma d_a)$ and the unmixed $(\bar{s}_a \Gamma d_a)(\bar{s}_b \Gamma d_b)$, lies in the matrix equation [110],

$$\begin{bmatrix} \Gamma = S \\ V \\ T \\ A \\ P \end{bmatrix}_{\text{Mixed}} = \frac{1}{4} \begin{bmatrix} -1 & -1 & 1 & 1 & -1 \\ -4 & 2 & 0 & 2 & 4 \\ 6 & 2 & 0 & 2 & 6 \\ 4 & 2 & 0 & 2 & -4 \\ -1 & 1 & 1 & -1 & -1 \end{bmatrix} \begin{bmatrix} S \\ V \\ T \\ A \\ P \end{bmatrix}_{\text{Unmixed}} . \tag{5.29}$$

The relation between the color mixed and unmixed operators in the renormalisation basis is,

$$\begin{bmatrix} V+A \\ V-A \\ S+P \\ S-P \\ T \end{bmatrix}_{\text{Mixed}} = \begin{bmatrix} 1 & 0 & 0 & 0 & 0 \\ 0 & 0 & -2 & 0 & 0 \\ 0 & -\frac{1}{2} & 0 & 0 & 0 \\ 0 & 0 & 0 & -\frac{1}{2} & \frac{1}{2} \\ 0 & 0 & 0 & \frac{3}{2} & \frac{1}{2} \end{bmatrix} \begin{bmatrix} V+A \\ V-A \\ S+P \\ S-P \\ T \end{bmatrix}_{\text{Unmixed}} . \tag{5.30}$$

Which gives us the following relations between the renormalisation basis operators Q_i and the SUSY basis quantities O_i.

$$\begin{aligned} O_1 &= Q_{VV+AA}, \\ O_2 &= Q_{SS+PP}, \\ O_3 &= -\frac{1}{2}\left(Q_{SS+PP} - Q_{TT}\right), \\ O_4 &= Q_{SS-PP}, \\ O_5 &= -\frac{1}{2}\left(Q_{VV-AA}\right). \end{aligned} \tag{5.31}$$

Where the indices could equally be understood as $1 = VV + AA$, $2/3 = SS + PP$(unmixed/mixed) and $4/5 = SS - PP$(unmixed/mixed).

The BSM bag parameters (Eq.5.26), or the ratios (Eq.5.28) can be used to roughly determine the scale of expected new physics. This is because the BSM Wilson coefficients are of the form (at the scale of new physics Λ and no summation over the index i)[3],

$$C_i(\Lambda) = \frac{F_i L_i}{\Lambda^2}, \qquad i = 2, 3, 4, 5. \tag{5.32}$$

The coefficient L_i is a loop factor depending on the interactions of the model considered and F_i is the new physics flavour coupling of such a model. The coefficients $C_i(\Lambda)$ are

[3]The operator is D=6, and thus irrelevant in a 4D theory. The factor of $\frac{1}{\Lambda^2}$ accounts for this.

computed in the RI-MOM scheme and renormalisation basis, via [34],

$$\langle \bar{K}^0|Q_i|K^0\rangle = \left(\sum_{j=1}^{5}\sum_{r=1}^{5}\left[\left\{b_j^{r,i} + Ac_j^{r,i}\right\} R_r A^{a_j}\right]\right) C_i(\Lambda)\langle \bar{K}^0|Q_1|K^0\rangle \tag{5.33}$$

Where the value A is the ratio of couplings $\frac{\alpha(\Lambda)}{\alpha(m_t)}$, R_r is the ratio of the BSM operators to the SM one. The coefficients b, c and a are so-called magic numbers and are available from [56]. The scale is deduced iteratively from varying A, and the measured ratio of the matrix elements. If we assume the coefficients $F_i, L_i \approx 1$, we can deduce the scale of new physics using $\Lambda = \sqrt{\frac{1}{C_i(\Lambda)}}$, as has been performed recently in [26], yielding constraints on the minimal scale of new physics with generic flavour structure of $O(10^4\ TeV)$.

5.2 Renormalisation

The non-perturbative matching coefficients in the RI-MOM scheme and their conversion to $\overline{\text{MS}}$, were computed by N.Garron and A.Lytle using Landau gauge fixed volume sources [95], and partially twisted fermionic boundary conditions [69, 141] (to reduce unwanted O(4) symmetry breaking due to the lattice). The use of non-exceptional momentum configurations is the state of the art for many procedures and has been used to compute B_K to very high precision [11], but cannot be used in this study due to unknown matching factors for the Q_3, Q_4 and Q_5 operators, this will lead to large systematic uncertainties from the non-perturbative renormalisation procedure. A discussion on some of the details of the renormalisation procedure can be found in Appendix.B.

We now reiterate the most salient points of the renormalisation procedure. We perform the $\overline{\text{MS}}$ scheme matching through the intermediate lattice RI-MOM scheme values of our operators (at some suitable scale μ) using,

$$r_i(\mu)_{\overline{\text{MS}}} = \left[\frac{Z_{ij}^{\overline{\text{MS}}}(\mu)\langle Q_j\rangle}{Z_{1j}^{\overline{\text{MS}}}(\mu)\langle Q_j\rangle}\right]_{\text{Lattice}}. \tag{5.34}$$

Although the perturbative matching is performed in the naïve dimensionally reduced (NDR)-$\overline{\text{MS}}$ [13, 55], with some abuse of notation we will just call $\overline{\text{MS}}$. After renormalisation, we use the relations in Eq.5.31 to convert to the SUSY basis. We then perform the mass correction in Eq.5.28 to remove the leading order chiral behaviour and to provide the renormalised ratios of the BSM contributions to the SM ones in our chosen scheme. The RI-MOM is an exceptional scheme, this allows zero-momentum transfer between legs which then allows for so-called Goldstone pole contamination,

this has to be subtracted explicitly from the renormalisation matrix $Z_{ij}(\mu)$ [94].

Considering the renormalisation of the bag parameters, we have the renormalisation basis's b's,

$$b_i(\mu)_{\overline{\rm MS}} = \frac{Z_{ij}^{\overline{\rm MS}}(\mu)}{Z_{\rm denom}(\mu)^2} \frac{\langle \bar{K}^0 | Q_j | K^0 \rangle}{\langle \bar{K}^0 | {\rm denom} | 0 \rangle \langle 0 | {\rm denom} | K \rangle}_{\rm Lattice}. \tag{5.35}$$

Where "denom"=P,A for i=1, and "denom"=P,P , otherwise. We then use the relations in Eq.5.31 to convert to the SUSY basis B_i's. Again incorporating the matching through the RI-MOM to $\overline{\rm MS}$ at 3 GeV to quote our results. The factors $Z_A(\mu)$ and $Z_P(\mu)$ have been computed for the datasets we use at our chosen renormalisation scale in [14, 19]. The renormalised bag parameters will be computed in this work alongside the more-favoured ratios. This will allow for direct comparison to previous efforts, and by comparing to the collaboration's measurement [14] of $B_K(3\,GeV)$ a vital check for the correctness of our analysis procedure.

5.3 The 24^3 dataset

For our analysis and eventual extrapolation to the continuum, we use the coarse ($\beta = 2.13$) and the fine ($\beta = 2.25$) $N_f = 2 + 1$ DWF datasets. A table of the relevant ensemble information is in Tab.5.1 for the coarse and Tab.5.4 for the fine.

Light sea mass (am_l)	0.005	0.01	0.02
configurations	155	152	146
MC time-step	40	20	20
Valence masses	0.005,0.03,0.035,0.04	0.01,0.03,0.035,0.04	0.02,0.03,0.035,0.04

Table 5.1 *The coarse ensembles used for this analysis. The simulated sea strange quark mass was $am_s = 0.04$. This ensemble is the 24^3 ensemble in Tab.3.1. This ensemble has renormalisation constants $Z_P^{\overline{MS}}(3\,GeV) = 0.69778(9)$, $Z_A = 0.71651(46)$, inverse lattice spacing $a^{-1} = 1.73(3)\,GeV$ and $m_{res} = 0.003076(58)$.*

We consider both **Unitary** (same valence quark masses $m(x, y)$ as strange (m_s) or degenerate light (m_l) sea quark masses) and **Partially Quenched** (PQ) (different valence quark masses compared to sea quark masses). This is performed by setting the bare quark mass in the Dirac operator to be different from the one used in the ensemble generation at the time of inversion and propagator computation, there is a small systematic error from including the partially quenched data. For the computation of the BSM ratios for K^0-$\bar{K}^0$mixing, we use Coulomb gauge fixed wall sources, where the Coulomb gauge fixing was performed using the techniques outlined in Sec.6.5 (i.e.

Fourier Acceleration on a slice by slice basis with random restarts upon failure to converge within a sufficient number of iterations). The gauge fixing accuracy was set to be $\Theta = 10^{-20}$. For this measurement, we set (in the language of Eq.5.27 and 2.59) walls at $t_i = 0,\ t_f = 32/a$. We have symmetry around $t = 32/a$ and we have another measurement of the operator in the range $t = 32/a \rightarrow t = 63/a$, this will be symmetrized to boost statistics.

5.3.1 2 point function analysis

To ensure the full statistical resolution when measuring amplitudes and masses of quark correlation functions, we also average or "fold" the forward and backward propagators together, and fit only the region decaying exponentially so as to not be fitting the contributions from the centre or the edges of the lattice where discretisation effects are most pronounced. Following [4, 14, 117] we use the definition of the pseudoscalar decay constant from Eq.2.57, where the amplitudes and masses ($N^{s_1,s_2}_{O_1,O_2}$ and m_{PS} from Eq.2.56) are computed from a simultaneous uncorrelated fit to the four amplitudes $N^{W,L}_{P,P}, N^{W,L}_{P,A}, N^{W,L}_{A,A}, N^{W,W}_{P,P}$, which constrains the common mass between the four correlators. Previously five channels were used but we consider the $N^{W,W}_{P,A}$ too noisy and found issues with our fit converging on a solution for the fine ensemble for this channel.

We begin by looking at the effective mass of our propagators using the simple definition in Eq.2.53. We use this measure to deduce the upper and lower fit ranges we can use for the exponential fit to compute the mass and amplitude, as this should be the range for which the effective mass plateaus.

As can be seen in Fig.5.1 the channels agree on the $am_l = 0.005$ Unitary Pion's mass being around $0.2a^{-1}[GeV]$. All of the channels plateau and agree between the $t/a = 7 \rightarrow 24$ (inclusive) region, for our final result we use the fit range $t/a = 9 \rightarrow 22$ based on the four point function analysis below. We note that at $t/a > 32$ we see the influence of the propagator travelling backwards in Euclidean time, as the correlator at $(t+1)/a$ is now greater than at t, the logarithm gives a negative effective mass.

Fig.5.2 shows the simultaneous fit to a cosh ((P,P),(A,A)) or sinh (P,A) for the lightest Unitary Pion data, whose effective mass plot was shown in Fig.5.1. As the correlation function is plotted on a logarithmic scale, the exponential decay of the correlation functions is nicely visible. The data for the masses as a function of the light,degenerate valence quarks used "x" and the (equal to or heavier) strange valence quarks used "y" for each of the datasets is shown in Tab.5.2.

The data presented in Tab.5.2 is consistent within error with the results published in

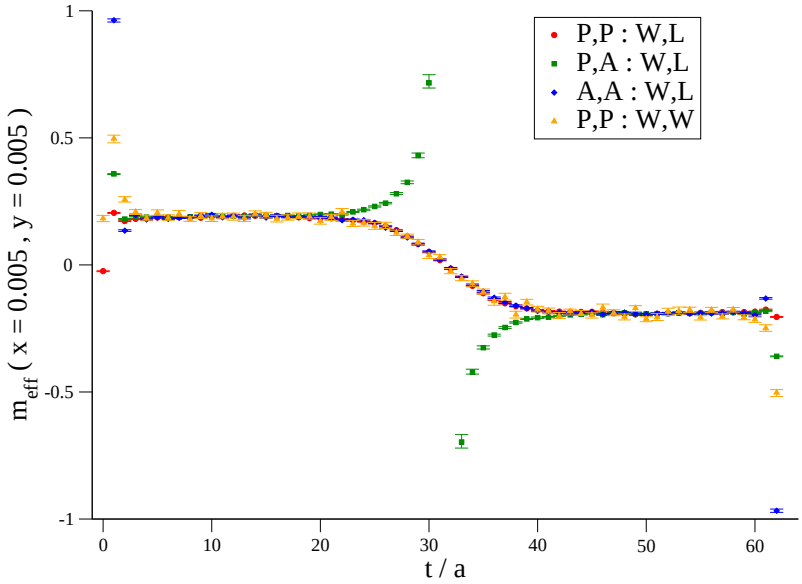

Figure 5.1 *The effective mass from Eq.2.53 for the lightest coarse ensemble's Unitary Pion ($am_l = 0.005$, $am_l^{Val} = 0.005$, $am_s^{Val} = 0.005$, where x and y are the valence light quark and valence strange quark respectively), for the four channels considered in this analysis. The terms on the left of the colon in the legend are the local operators used (O_1, O_2) and to the right of the colon the source types (s_1, s_2).*

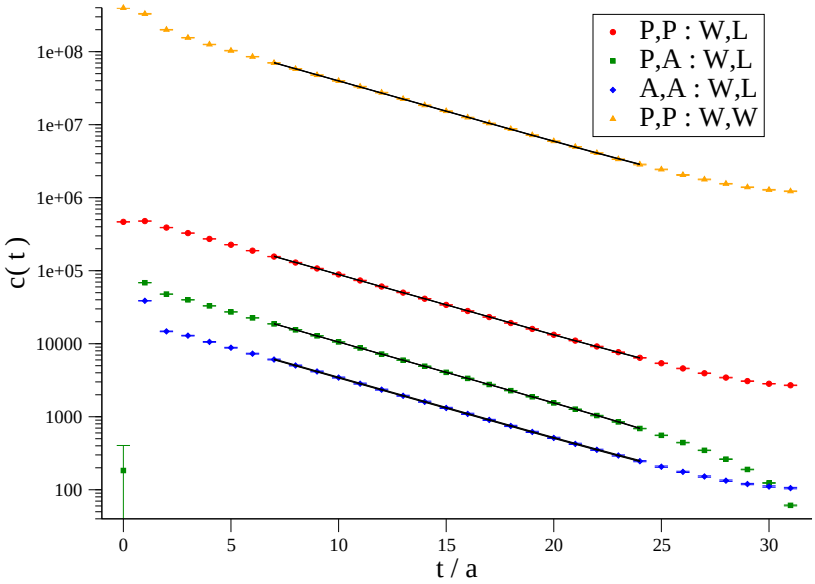

Figure 5.2 *The correlation function of the lightest coarse ensemble's Unitary Pion, for the four channels. As in Fig.5.1, the terms on the left of the colon are the local operators and on the right the source types. The data has been folded.*

[4, 14] which were obtained using periodic plus anti-periodic boundary conditions on the Fermions (effectively doubling the temporal extent of the lattice) when inverting the propagators and using $t_i = 5$, $t_f = 59$. We do not compute the axial current

m_l^{Val}	m_s^{Val}	$m_{ls}(0.005)$	$m_{ls}(0.010)$	$m_{ls}(0.020)$	$f_{ls}(0.005)$	$f_{ls}(0.010)$	$f_{ls}(0.020)$
0.0400	0.0400	0.4318(3)	0.4334(4)	0.4382(3)	0.1092(3)	0.1100(3)	0.1124(3)
0.0350	0.0350	0.4053(3)	0.4070(4)	0.4118(3)	0.1064(2)	0.1073(3)	0.1098(3)
0.0300	0.0300	0.3774(3)	0.3790(4)	0.3839(3)	0.1035(3)	0.1044(3)	0.1070(3)
0.0200	0.0400	-	-	0.3841(4)	-	-	0.1068(3)
0.0200	0.0350	-	-	0.3694(4)	-	-	0.1055(3)
0.0200	0.0300	-	-	0.3542(4)	-	-	0.1042(3)
0.0200	0.0200	-	-	0.3220(4)	-	-	0.1013(3)
0.0100	0.0400	-	0.3497(4)	-	-	0.1007(3)	-
0.0100	0.0350	-	0.3339(4)	-	-	0.0994(3)	-
0.0100	0.0300	-	0.3173(4)	-	-	0.0980(3)	-
0.0100	0.0100	-	0.2412(4)	-	-	0.0917(3)	-
0.0050	0.0400	0.3326(4)	-	-	0.0975(3)	-	-
0.0050	0.0350	0.3161(4)	-	-	0.0962(3)	-	-
0.0050	0.0300	0.2987(4)	-	-	0.0948(3)	-	-
0.0050	0.0050	0.1911(4)	-	-	0.0860(2)	-	-

Table 5.2 *The measured masses and decay constants for the coarse datasets used in this analysis. As we are only Partially-Quenching the valence sector in the strange quark masses for our measurements of Kaon quantities, many of the light quark data is not available. The argument of m_{ls} is the degenerate light sea quark mass. The results are from a simultaneous fit over four correlator channels using fit range $9 \to 22$ inclusive.*

renormalisation constant $Z_A(\mu)$ or the pseudoscalar current renormalisation constant $Z_P(\mu)$ or m_{res}, because now we know we are consistent with previous computations of masses and amplitudes we can use the previous results for these quantities. We now move on to discussing the computation of the three point function, renormalised ratios, bag parameters and our chiral extrapolations.

5.3.2 4 point function analysis

Our methodology for extracting the ratios of the BSM effective operators to the SM one is to fit to a constant at some applicable plateau the renormalisation basis ratio r_i, and for completeness and comparison with other previous studies the bag parameters b_i. We then renormalise to $\overline{\text{MS}}$ at μ=3 GeV using Eqs.5.34 or 5.34, and use the Fierz identities of Eq.5.31 to convert to the SUSY basis. We do not simulate our physics at the physical light or strange mass, so a chiral extrapolation to the physical Kaon is then performed (incorporating the known m_{res} for this ensemble).

We use fifth dimensional mass of 1.8 and walls at $t_i = 0$ and $t_f = 32$, this allows us to symmetrise our result between $t = 0 \to 32$ and $t = 32 \to 63$ to boost statistics.

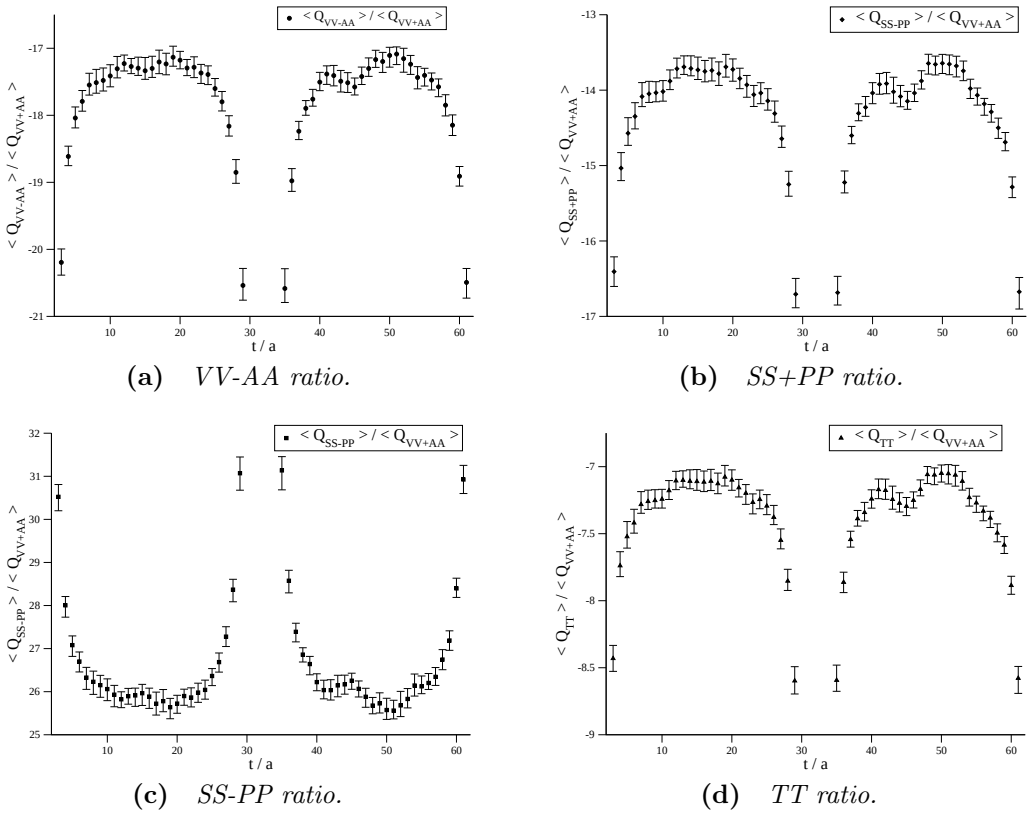

(a) *VV-AA ratio.* **(b)** *SS+PP ratio.*

(c) *SS-PP ratio.* **(d)** *TT ratio.*

Figure 5.3 *The renormalisation basis unrenormalised ratios (r_i's) for the lightest Unitary Kaon for the coarse ensemble.*

The unrenormalised, renormalisation basis ratios of the BSM effective operators against the SM operator for the lightest unitary Kaon $m_l^{\mathrm{Val}} = 0.005, m_s^{\mathrm{Val}} = 0.040$ are shown in Fig.5.3. We have not folded the data yet, but we can see that it is symmetric and we shall in later measurements. This will reduce statistical error if the data is uncorrelated, whilst also evening out some of the larger correlations in euclidean time that are clearly evident. We have shown the lightest Unitary Kaon's results because it is in some sense the worst behaved, its mass is the lightest and so the plateau length should be the shortest. Considering the plots, we deduce an acceptable fit range for the plateaus to be $t/a = 9 \rightarrow 22$ inclusive. The quoted results for the rest of this section and the proceeding ones will be from this range. Other, acceptable ranges, were tested and the agreement within measurement was always considerably better than the statistical resolution of the measurement.

The forced, block diagonal (i.e. omitting chirally forbidden mixing of operators) renormalisation matrix $Z_{ij}^{\overline{\mathrm{MS}}}(3\ GeV)$ for this ensemble is[4] (divided by the axial current

[4]Computed by both N.Garron and A.Lytle

renormalisation Z_A^2),

$$\frac{Z_{ij}^{\overline{\text{MS}}}}{Z_A^2}(3\ GeV) = \begin{bmatrix} 0.9051(13) & 0 & 0 & 0 & 0 \\ 0 & 1.0710(4) & 0.4402(12) & 0 & 0 \\ 0 & 0.0634(9) & 0.7212(61) & 0 & 0 \\ 0 & 0 & 0 & 0.7393(56) & -0.0277(10) \\ 0 & 0 & 0 & -0.4766(8) & 1.2517(24) \end{bmatrix}. \quad (5.36)$$

The renormalised ratios (Eq.5.28) for the $m_l = 0.01$ Unitary Kaon are shown in Fig.5.4. Upon renormalisation, a change of basis and the removal of the leading chiral behaviour, we see that the BSM effective operators are greatly enhanced compared to the SM one, as was seen in previous studies [5, 21, 26, 43].

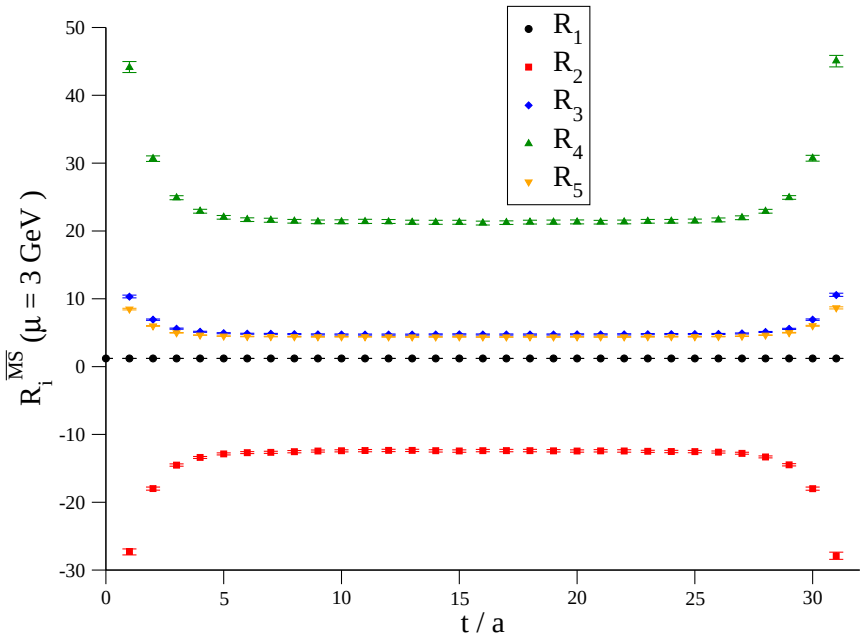

Figure 5.4 *The $m_l = 0.01$ Unitary Kaon's R_i's renormalised in $\overline{\text{MS}}$ at 3 GeV and folded at $t/a = 32$.*

5.3.3 Chiral results

We must extrapolate our results to the physical point $[m_K]_{\text{experiment}} = [m_K]_{\text{lattice}}$. We choose to do this by extrapolating to the Unitary Pion data to the physical Pion in the light quark sector, this will yield the value am_q^{chiral}. We then extrapolate to the value, $am_s + am_q^{\text{chiral}}$ for fixed, PQ and Unitary strange quark mass for the Kaons.

To match to the physical strange quark mass we interpolate (because we had PQ strange quark data lower than the physical strange quark mass and Unitary higher) to the physical strange quark mass for this ensemble which we set to be the point

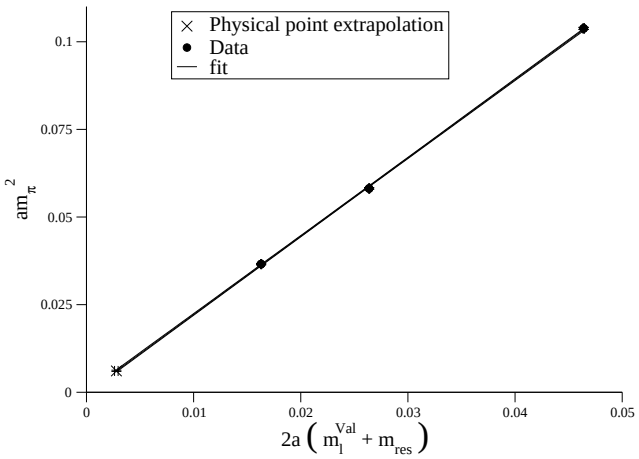

Figure 5.5 *Unitary light quark extrapolation to the physical Pion, with result* $a\,(m_l + m_{res}) = 0.00140(8)$.

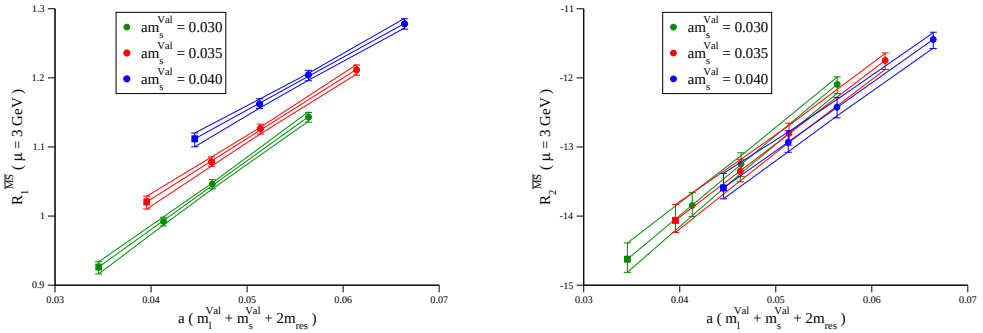

(a) R_1 **(b)** R_2

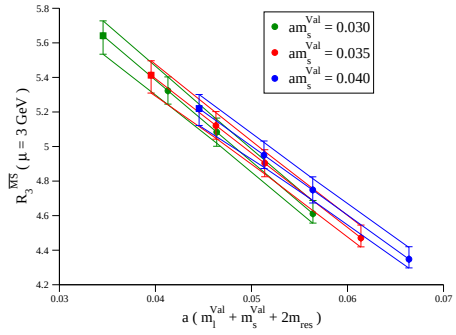

(c) R_3

Figure 5.6 *Chiral extrapolations in the light sector for the coarse ensemble for the renormalised ratios in* $\overline{\text{MS}}$ *at 3 GeV for the ratios* $R_{1,2,3}$. *Squares indicate the light quark extrapolated value and circles the data. The lines are a linear fit, and are used for the extrapolated result.*

where $R_1 = 1$, which should be very close if not exactly $am_s^{\text{phys}} = 0.0345$. This can be considered as the same as remeasuring the physical strange quark mass.

Fig.5.6 illustrates the extrapolations in the light quark sector for the renormalised ratios of Eq.5.28. The data was fit linearly in order to extrapolate to the physical

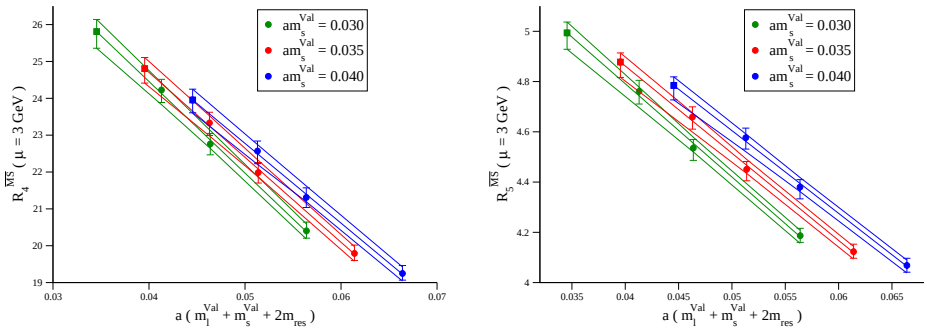

(a) R_4 **(b)** R_5

Figure 5.7 *The light quark extrapolations as shown in Fig.5.6 for the renormalised ratios R_4 and R_5.*

point (squares), defined by the value in Fig.5.5. We can see that the $am_s = 0.035$ extrapolated to the physical light quark, is almost directly at the physical Kaon. Its partially quenched strange mass was chosen to be so, as $am_s^{\text{phys}} = 0.0345$ [14]. Each fit was linear and had χ^2/dof of less than 1, we note that the mass dependence on the fits is very benign.

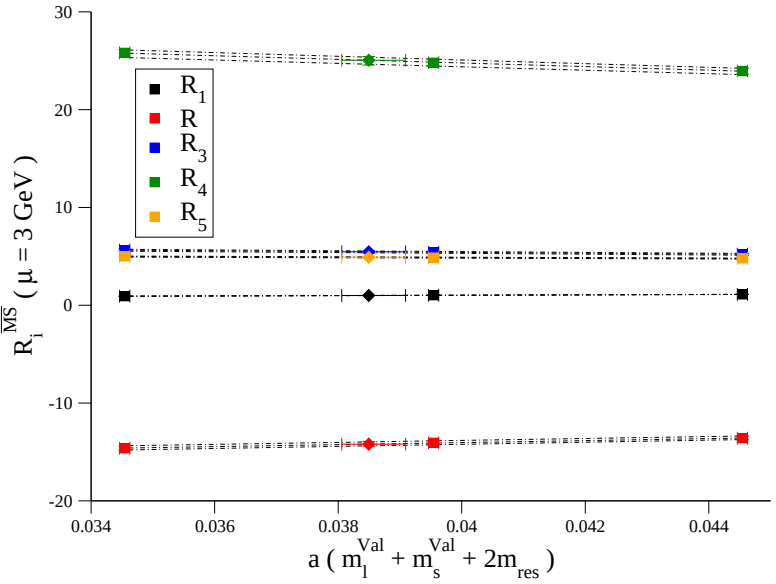

Figure 5.8 *Strange quark interpolation for the coarse lattice using the Unitary and partially quenched data. Squares represent the light sector chiral extrapolation and diamonds the physical strange quark interpolation, the dashed lines are a linear fit to the chirally extrapolated data. The results of the interpolation are presented in Tab.5.3.*

Once we have chirally extrapolated in the light quark sector, we must interpolate to the physical strange quark mass, which is shown in Fig.5.8. We do so by setting the physical point to be the point where the ratio $R_1 = 1$, this is very close to the physical strange quark mass quoted in [14]. From Fig.5.8 we can see that the mass dependence

is again very mild and under control in this interpolation.

Although the renormalised ratios R_i are the main result of this work, for completeness we have also computed the SM bag parameter B_K and the BSM B_i's, using Eq.5.21 for B_K, Eq.5.27 for the BSM contributions and renormalising using Eq.5.35. The same procedure for the chiral extrapolations of the B's has been made as with the R's, i.e. extrapolation in the light quark sector and interpolation using the partially quenched data in the strange quark sector to the physical point of $R_1 = 1$.

Our chirally extrapolated results at the physical point are shown in Tab.5.3, with statistical errors only as we save the systematic error estimation for the $a^2 \to 0$ extrapolation discussion. From this analysis we obtain results that are comparable in magnitude and sign to our results in [43] using the fine ensemble (discussed in Sec.5.4), suggestive of the $a^2 \to 0$ extrapolation being fairly mild.

i	$R_i^{\overline{\text{MS}}}(\mu = 3\ GeV)$	$B_i^{\overline{\text{MS}}}(\mu = 3\ GeV)$
1	1.0	0.508(15)
2	-14.19(20)	0.431(12)
3	5.46(9)	0.827(24)
4	25.07(41)	0.640(17)
5	4.91(6)	0.377(10)

Table 5.3 *Physical point, coarse ensemble ratios and bag parameters renormalised in* $\overline{\text{MS}}$ *at 3 GeV, errors are statistical only.*

We see from Tab.5.3 we obtain a reasonable evaluation of B_K, with 4% statistical error. The majority of the error comes from the RI-MOM non perturbative renormalisation procedure, which turns out to be one of the largest sources of systematic error of the whole procedure, as will be discussed when we produce our final $a^2 \to 0$ extrapolation in Sec.5.5.

5.4 The 32^3 dataset

The PQ and Unitary valence quark data available for the fine 32^3 ensemble was much larger than the coarse, it was generated using the CPS code and its evaluation of B_K was used in the analysis of [14]. Coulomb gauge fixed wall sources were used, with a gauge fixing accuracy of $\Theta = 10^{-14}$. The gauge fixing was not performed using our code. The available masses are shown in Tab.5.4. This data we analyse first formed a proceedings [155], but we found that some of the Fierz identities were not held due to some of the operators being incorrectly implemented. Forunately, there was enough information in the data to reconstruct the full renormalisation basis using Fierz identities, but it is unclear whether [155] was aware of this issue.

Light sea mass (am_l)	0.004	0.006	0.008
configurations	129	186	208
MC timestep	20	20	20
Valence masses	0.002,0.004,0.006	0.002,0.004,0.006	0.002,0.004,0.006
	0.008,0.025,0.03	0.008,0.025,0.03	0.008,0.025,0.03

Table 5.4 *The fine ensemble data used for this analysis, this is the same dataset that was used in the analysis for B_K in [14]. This ensemble has renormalisation constants $Z_P^{\overline{MS}}(3\ GeV) = 0.70572(9)$, $Z_A = 0.74469(13)$, inverse lattice spacing $a^{-1} = 2.28(3)\ GeV$ and $m_{res} = 0.0006643(82)$.*

For this ensemble we have a greater range of partially quenched light quark masses than the previous ensemble and only one partially quenched strange mass for the strange interpolation to the physical point. The data was generated using a single source at $t_i = t_f = 0$ and the inversion of the Dirac operator was performed twice, once with fermions that are periodic (p) in time and once for fermions that are anti-periodic (a) in time. The forward (fwd) and backward (bwd) propagating states are generated using the combinations fwd $= p + a$, bwd $= p - a$, this effectively doubles the temporal extent of the lattice, but should not improve the statistical resolution of the measurement. The analysis follows the previous, coarse measurement. First we investigate the two point correlation functions and compute the ratio $\left[\frac{m_K^2}{f_K^2}\right]_{\text{Lattice}}$, we follow [14] and use the fit range $t = 12 \to 52$ inclusive.

Comparing the order of the error from Tab.5.5 and Tab.5.2 we can see that the increased statistics and self averaging from the larger volume has decreased the statistical error. Our analysis is in good agreement with that of [14]. We proceed with the analysis of the four point functions for this ensemble, an example of the quality of the data is shown in Fig.5.9, which is of the lightest Unitary Kaon. Note how the periodic/anti-periodic data allows access to a much larger plateau compared to the coarse data (which has the same temporal extent) from Fig.5.3 and that the fit range $12 \to 52$ is clearly well within the plateau region. As we saw from the coarse data, our four point function result is quite correlated in Euclidean time, owing to the small lattice spacing between time-slices. As such, a fit over as large a temporal region as possible whilst still in plateau is hoped will even our temporal correlations and fluctuations.

To illustrate the mass dependence of the measure, we plot the ratios of the BSM operators to the SM with and without the multiplicative dimensionless factor $\left[\frac{f_k}{m_k}\right]^2_{\text{Experiment}} \left[\frac{m_{ls}}{f_{ls}}\right]^2_{\text{Lattice}}$ versus the ratio $\left[\frac{m_{ls}}{f_{ls}}\right]^2_{\text{Lattice}}$, shown in Fig.5.10. We see that without this multiplicative factor the ratios behave roughly as $\frac{1}{m_{ls}}$ and "blow up" as the mass goes to 0, upon applying the mass correction we see approximately linear behaviour over the entire

m_l^{Val}	m_s^{Val}	$m_{ls}(0.004)$	$m_{ls}(0.006)$	$m_{ls}(0.008)$	$f_{ls}(0.004)$	$f_{ls}(0.006)$	$f_{ls}(0.008)$
0.030	0.030	0.3217(1)	0.3215(1)	0.3226(1)	0.0812(1)	0.0809(1)	0.0816(1)
0.025	0.030	0.3079(1)	0.3077(1)	0.3088(1)	0.0797(2)	0.0794(1)	0.0802(1)
0.008	0.030	0.2565(1)	0.2565(1)	0.2582(1)	0.0734(2)	0.0733(1)	0.0744(1)
0.006	0.030	0.2500(1)	0.2501(1)	0.2518(1)	0.0726(2)	0.0725(1)	0.0733(1)
0.004	0.030	0.2434(1)	0.2436(1)	0.2455(1)	0.0717(2)	0.0717(1)	0.0732(2)
0.002	0.030	0.2367(1)	0.2371(1)	0.2391(1)	0.0711(2)	0.0713(2)	0.0729(2)
0.025	0.025	0.2935(1)	0.2933(1)	0.2944(1)	0.0781(2)	0.0779(1)	0.0787(1)
0.008	0.025	0.2395(1)	0.2396(1)	0.2412(1)	0.0719(2)	0.0719(1)	0.0730(1)
0.006	0.025	0.2326(1)	0.2327(1)	0.2344(1)	0.0711(1)	0.0711(2)	0.0723(1)
0.004	0.025	0.2255(1)	0.2258(1)	0.2275(1)	0.0703(2)	0.0703(1)	0.0717(1)
0.002	0.025	0.2183(1)	0.2188(1)	0.2206(1)	0.0697(2)	0.0699(1)	0.0714(2)
0.008	0.008	0.1711(1)	0.1714(1)	0.1728(1)	0.0660(1)	0.0660(1)	0.0671(1)
0.006	0.008	0.1612(1)	0.1617(1)	0.1631(1)	0.0651(1)	0.0652(1)	0.0664(1)
0.004	0.008	0.1509(1)	0.1514(1)	0.1527(1)	0.0642(2)	0.0643(1)	0.0656(1)
0.002	0.008	0.1398(1)	0.1406(1)	0.1418(1)	0.0634(2)	0.0637(2)	0.0651(1)
0.006	0.006	0.1508(1)	0.1513(1)	0.1526(1)	0.0642(2)	0.0643(1)	0.0655(1)
0.004	0.006	0.1395(1)	0.1402(1)	0.1414(1)	0.0633(1)	0.0635(1)	0.0647(1)
0.002	0.006	0.1274(1)	0.1283(1)	0.1294(1)	0.0624(2)	0.0627(1)	0.0641(1)
0.004	0.004	0.1272(1)	0.1280(1)	0.1292(1)	0.0623(1)	0.0625(1)	0.0639(1)
0.002	0.004	0.1136(1)	0.1147(1)	0.1157(1)	0.0613(2)	0.0616(2)	0.0631(1)
0.002	0.002	0.0979(1)	0.0992(1)	0.1001(1)	0.0602(2)	0.0605(2)	0.0621(1)

Table 5.5 *The measured masses and decay constants for the fine datasets used in this analysis. The fit range $t = 12 \rightarrow 52$ inclusive, was used throughout this study. The errors are computed from a Bootstrap analysis with 100 bootstraps. As in the coarse dataset analysis, an uncorrelated simultaneous fit to four channels was performed.*

range of masses except for the very lightest, and comparatively smoother chiral behaviour. The physical point for this data is 10.16, with m_K and f_K taken from [24].

N.Garron calculated the following renormalisation matrix to match our data to $\overline{\text{MS}}$ at 3 GeV for this ensemble,

$$\frac{Z_{ij}^{\overline{\text{MS}}}}{Z_A^2}(3\ GeV) = \begin{bmatrix} 0.9329(4) & 0 & 0 & 0 & 0 \\ 0 & 1.0562(9) & 0.3963(36) & 0 & 0 \\ 0 & 0.0484(6) & 0.6904(77) & 0 & 0 \\ 0 & 0 & 0 & 0.7135(70) & -0.0128(3) \\ 0 & 0 & 0 & -0.4303(32) & 1.2625(19) \end{bmatrix}. \quad (5.37)$$

The factors are quite similar to those of the coarse ensemble, i.e. large mixing between the VV-AA and SS-PP, and the SS+PP and TT. The error for the SS-PP channel's mixing with the TT is large compared to the coarse ensemble's. We use this matrix to compute the fine ensemble's analogue to the graph Fig.5.4 for the lightest Unitary

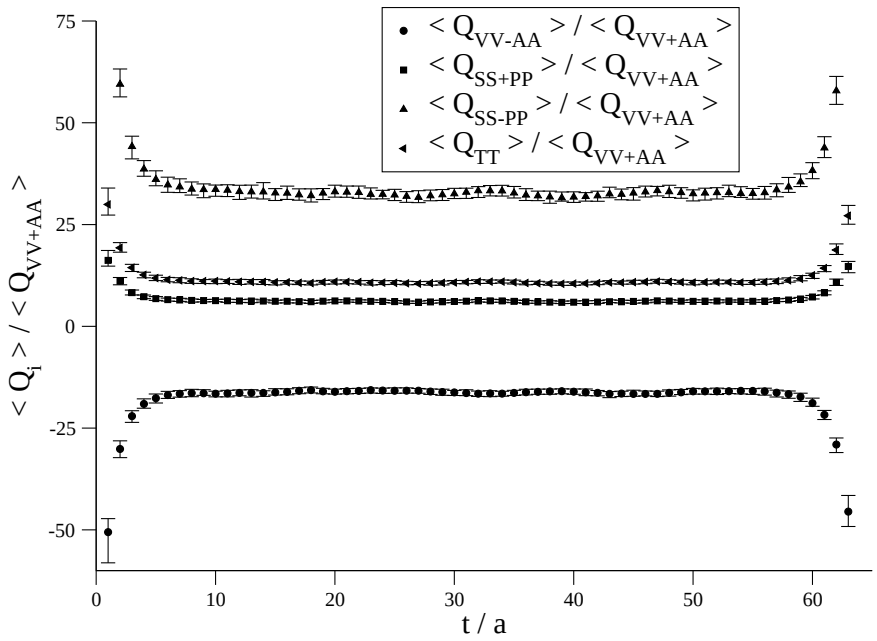

Figure 5.9 *Renormalisation basis four point function ratios for the lightest ($m_l = 0.004$) Unitary Kaon. This is to be compared with the coarse data analysis in Fig.5.3.*

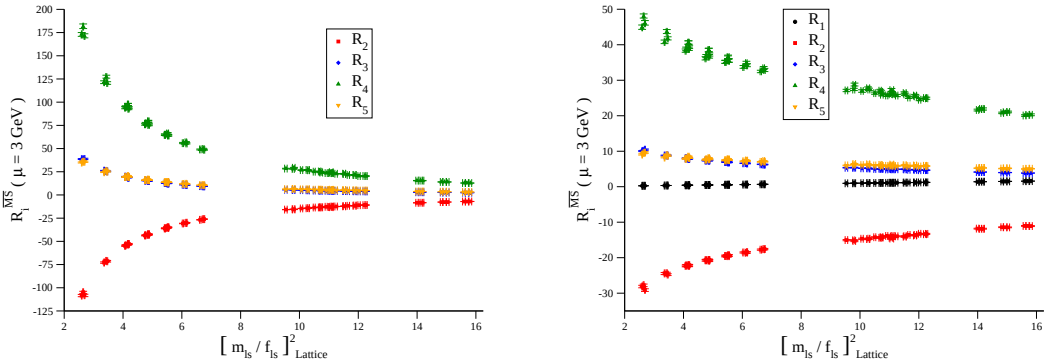

(a) *Without correction* **(b)** *With correction*

Figure 5.10 *The renormalised ratios of SUSY basis operators in* $\overline{\text{MS}}$ *at 3 GeV, with and without the multiplicative mass improvement of* $\left[\frac{m_{ls}}{f_{ls}}\right]^2_{Lattice}$ *for all of our fine ensemble data.*

Kaon data shown in Fig.5.9, this is shown in Fig.5.11.

Fig.5.11 shows the renormalised R_i's for the lightest Unitary Kaon. As previously noticed for the coarse ensemble, the ratios of the BSM to the SM effective operators are greatly enhanced, and appear larger for the fine ensemble compared to the coarse. As seen before, R_3 and R_5 are very similar in this scheme at this scale, and R_2 and R_4 are much larger than the SM contribution.

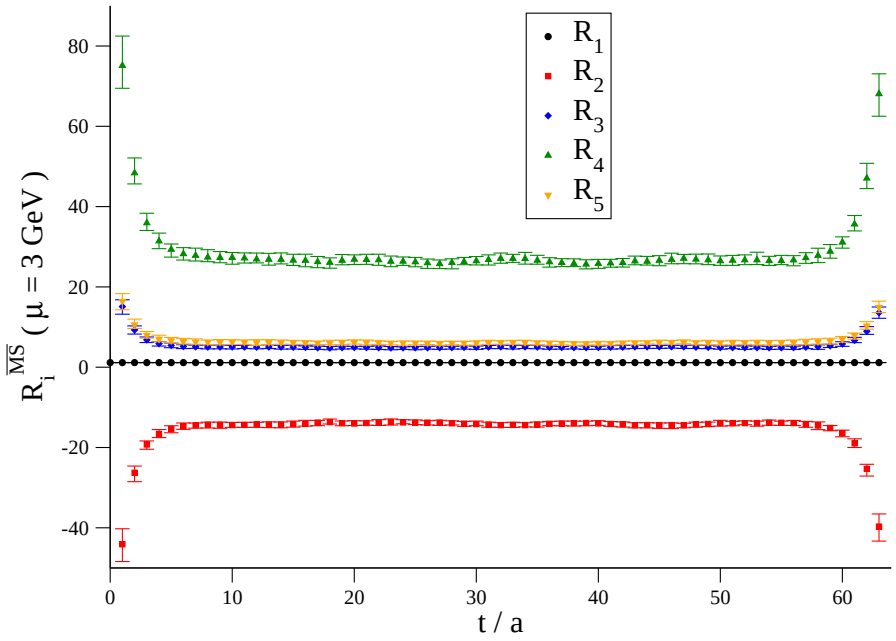

Figure 5.11 *The $m_l = 0.004$ fine ensemble, renormalised ratios of Eq.5.28 renormalised from the RI/MOM scheme to $\overline{\text{MS}}$ at 3 GeV, and converted to the SUSY basis.*

5.4.1 Chiral limit results

The approach to the chiral limit was performed in exactly the same manner as in the coarse ensemble analysis. Whereby extrapolation in the Unitary light quark sector to the physical Pion was made (with result $a\,(m_l + m_{\text{res}}) = 0.00097(3)$, and then interpolation in the heavy quark sector with the aid of a Partially Quenched strange quark valence data point to the physical strange defined as the point where $R_1 = 1$, which again lies very close to ($m_s^{\text{phys}} = 0.0273(7)$) [14]. The graph of this extrapolation and subsequent interpolation is shown in Fig.5.12.

Fig.5.12 attempts to illustrate the extrapolation and interpolation procedure of the coarse data all on one graph. The upward triangles are the Unitary Kaon data and the downward triangles are the PQ $am_s = 0.025$ data points. Each of which is extrapolated to the light quark physical point shown as the squares, and then the interpolated physical strange evaluation is measured (this is the diamond on the plot). Comparing the coarse and the fine chiral extrapolations to the physical point, we note that the extrapolation in mass is very benign for both. And the fine ensemble evaluations tend to be a little larger than the coarse evaluations for the ratios but otherwise similar in magnitude and sign. We also see that the ratios R_3 and R_5 for the fine ensemble have switched positions compared to the coarse ensemble. This is perhaps illustrative of some scaling violation (large $O(a^2)$ effect).

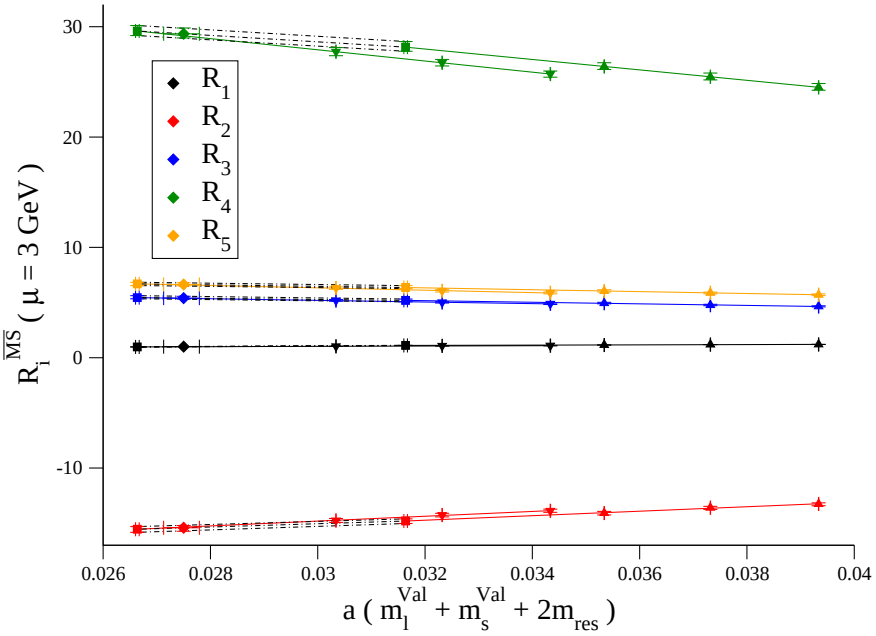

Figure 5.12 *Chiral extrapolations for the fine data. Results for the extrapolation in the light sector to the physical point ($R_1 = 1$) for the $m_s = 0.03$ (upward triangles) and the $m_s = 0.025$ (downward triangles) are shown as the squares at the end of their extrapolation lines, the lines are the midpoint of the fit. The dashed black line illustrates the interpolation to the physical strange quark mass which is shown as a diamond, as in the coarse data Fig.5.8. The results are presented in Tab.5.6.*

5.5 Continuum results

We now present the continuum evaluations of the R's and the B's from the previous two sections. We take as the lattice spacing of the coarse ensemble $a^{-1} = 1.73(3)\ GeV$ and the fine ensemble $a^{-1} = 2.28(3)\ GeV$, we fit our data linearly in a^2 and extrapolate to zero lattice spacing, this is taken as our naïve continuum limit evaluation.

i	$R_i^{\overline{\rm MS}}(\mu = 3\ GeV)$	$B_i^{\overline{\rm MS}}(\mu = 3\ GeV)$
1	1.0	0.518(4)
2	-15.46(46)	0.420(5)
3	5.47(18)	0.744(12)
4	29.40(90)	0.671(9)
5	6.56(20)	0.447(7)

Table 5.6 *Physical point, fine ensemble ratios and bag parameters renormalised in $\overline{\rm MS}$ at 3 GeV, errors are statistical only.*

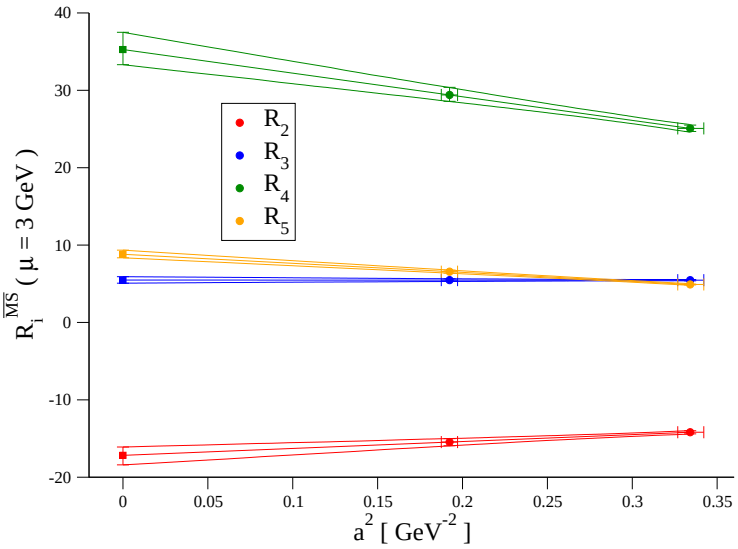

Figure 5.13 *The $a^2 \to 0$ extrapolated, ratios R_i's in $\overline{\text{MS}}$ at 3 GeV, (Eq.5.28) from the coarse and fine ensembles. The extrapolation was performed using a linear fit to the data, the final results are shown in Tab.5.8. The circles are the physical point data and the crosses are the extrapolated result. The ratio R_1 is not shown as it is defined to be 1.*

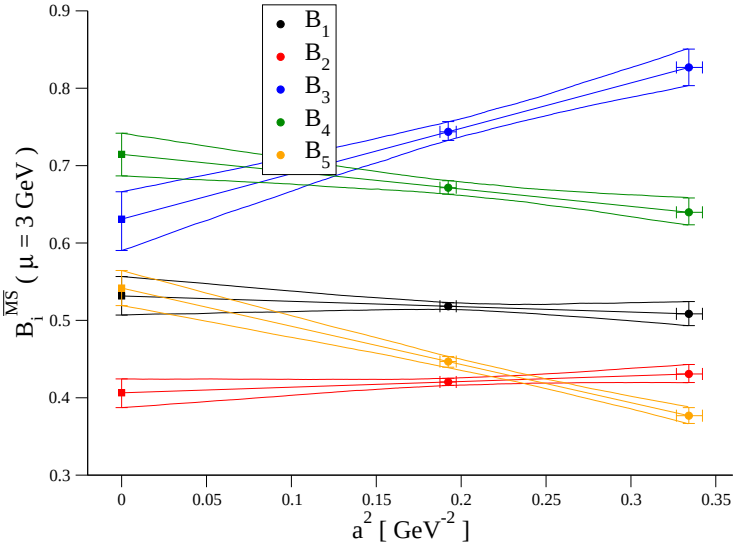

Figure 5.14 *The $a^2 \to 0$ extrapolated, RI/MOM renormalised and $\overline{\text{MS}}$ matched bag parameters (Eq.5.27) from the coarse and fine ensembles. The extrapolation was performed using a linear fit to the data, the final results are shown in Tab.5.8. The circles are the physical point data and the crosses are the extrapolated result.*

5.5.1 Systematic errors

We have postponed inclusion of systematic errors until our final $a^2 \to 0$ result. We identify three regions where errors are expected to contribute. These are considered to

be from the finite volume/measurement effects and the non perturbative and continuum perturbative renormalisation procedures.

To estimate the error of our measurement, we vary the fit range for the coarse data over a sensible range $(9, 10, 11, 12 \rightarrow 19, 20, 21, 22, 23)$, whilst keeping the fine data's evaluation fixed at $12 \rightarrow 52$ to obtain an estimate of the stability of the measurement and resulting continuum limit extrapolation for the ratios and bag parameters, we found that for all operators under consideration the variation of the fit range contributed a negligible ($< 0.1\%$) effect. Which was completely dwarfed by the final result's statistical error.

We are also confident in our chiral extrapolations, as the mass extrapolations and interpolations of the ratios and bag parameters are well described by a simple linear fit. We find a correction of the order of $< 1\%$ from our chiral extrapolation for the central value of R_1 away from 1, incorporating the error in the extrapolation point this error is effectively 0. We conclude that the dominant systematic errors arise from the non perturbative renormalisation and the perturbative matching.

Following the discussion in [43] we note that the use of the exceptional RI-MOM scheme is probably the dominant source of systematic uncertainty, as it introduces breaking of chiral symmetry and unphysical mixing of all the renormalisation basis operators. If we do not force the renormalisation matrix to be block-diagonal by incorporating chirally forbidden contributions and symmetry breaking effects and then renormalise with this non block-diagonal matrix and compare to our final (block diagonal) result, we get a handle on the systematic uncertainty emanating from the non perturbative renormalisation. This is the dominant error, and it should be noted that the use of non-exceptional schemes have been seen to suppress the chirally forbidden operator mixings for $B_K(\mu)$ [11]. We measure our block-diagonal and non continuum-extrapolated results and take half the difference on the central values as an estimate for the error.

The perturbative matching error from the RI-MOM scheme to $\overline{\text{MS}}$ is subjective, as one cannot estimate what the higher order terms in the series will be. The matching to $\overline{\text{MS}}$ in three flavour QCD at $\mu = 3\ GeV$ was is known at one-loop level [45, 55] with the coefficients of the perturbative mixing matrix given in Eq.B.16. The error estimate comes from taking half the difference between the leading order and the next to leading order result for the matching coefficients of each operator on an example dataset. For our analysis we choose the lightest Unitary Kaon from each ensemble and average the result for the two, to perform this analysis.

i	npr(R)	npr(B)	PT	Total(R)	Total(B)
1	-	0.10	0.85	-	0.86
2	6.21	4.25	4.4	7.61	6.12
3	4.99	4.56	1.6	5.24	4.83
4	2.27	1.37	8.0	8.32	8.12
5	2.51	1.92	10.4	10.70	10.58

Table 5.7 *The error budget for the two dominant sources of error, the non perturbative renormalisation in the RI-MOM scheme (npr) extrapolated to the continuum, and its subsequent matching to continuum perturbation theory (PT)* $\overline{\text{MS}}$ *as a percentage correction, errors are added in quadrature.*

5.5.2 Final results and discussion

Our final, continuum results for the ratios and bag parameters for K^0-$\bar{K}^0$mixing in and beyond the standard model are shown in Tab.5.8. It is pleasing to note that our evaluation of the continuum limit $B_K^{\overline{\text{MS}}}(3\ GeV)$ is consistent with a previous evaluation using these ensembles of $0.529(5)_{\text{stat}}(15)_{\text{syst}}$ [11] albeit with a larger statistical error, emanating from our use of the exceptional RI-MOM, rather than the theoretically more sound non-exceptional schemesh available for the computation of B_K, these being the $\text{SMOM}_{\gamma_\mu,\gamma_\mu}, \text{SMOM}_{\not{q},\not{q}}, \text{SMOM}_{\gamma_\mu,\not{q}}$ or $\text{SMOM}_{\not{q},\gamma_\mu}$. Renormalisation in these schemes is possible for the npr intermediate scheme, but the matching to $\overline{\text{MS}}$ is unknown for two of the operators.

i	$R_i^{\overline{\text{MS}}}(\mu = 3\ GeV)$	$B_i^{\overline{\text{MS}}}(\mu = 3\ GeV)$
1	1.0	0.532(25)(4)
2	-17.18(120)(130)	0.406(18)(25)
3	5.48(40)(28)	0.631(38)(33)
4	35.27(214)(293)	0.715(28)(59)
5	8.81(49)(96)	0.542(23)(59)

Table 5.8 *The* $a^2 \to 0$ *extrapolated ratios and bag parameters, renormalised in the RI-MOM scheme at 3 GeV and matched to* $\overline{\text{MS}}$ *and converted to the SUSY basis. The extrapolation was performed using a linear fit.*

Consulting Tab.5.8 we see that our our statistical error is between 5% and 9% for our operators, with R_3 having the largest percentage statistical error. The large systematics are due to our conservative estimate about the convergence of the perturbative matching to $\overline{\text{MS}}$ for these operators, as the matching is only at 1 loop order at a low matching scale μ. Moving to a non-exceptional scheme was very beneficial in reducing the errors in the non-perturbative renormalisation for B_K in previous studies. If perturbative matching coefficients were known for the final 3 operators in Tab.5.8 we could see a dramatic decrease in the error, both statistical and systematic.

Comparing the result from [43], we now know that the difference between the fine ensemble evaluation and the continuum is quite large, with ratios R_2 and R_4 increasing by $\approx$ 10% and R_5 increasing by $\approx$ 25% from the fine data to the continuum extrapolation point, with only R_3 being well within this estimate and consistent with a flat continuum extrapolation. The same behaviour is seen for the bag parameters, where the scaling violation of B_5 appears very large. Our continuum results are consistent in magnitude and sign with previous determinations [5, 21, 26] and a staggered fermion preliminary computation [22]. The most recent, comparable results to ours are from an $N_f = 2$ dynamical Twisted Mass calculation [26], we show a direct comparison of the two measurements in Tab.5.9. We see that our result is compatible with theirs within error for the ratios except for R_4 and for the bag parameters, except for B_2 and B_3.

i	$R_i^{\overline{\rm MS}}(\mu = 3\ GeV)$	[26]	$B_i^{\overline{\rm MS}}(\mu = 3\ GeV)$	[26]
1	1.0	1.0 (0)	0.53(3)	0.51(2)
2	-17.2(18)	-15.6(5)	0.41(3)	0.47(2)
3	5.5(4)	5.3(3)	0.63(5)	0.78(4)
4	35.3(36)	28.6(9)	0.72(7)	0.75(3)
5	8.8(11)	7.8(4)	0.54(6)	0.60(3)

Table 5.9 *A comparison of our continuum result and that of [26]. Statistical and systematic errors have been added in quadrature.*

We have calculated the renormalised matrix elements that can be used to constrain flavour physics beyond the standard model. We have performed the first computation with $N_f = 2 + 1$ dynamical Domain Wall Fermions, with the benefit of good chiral behaviour in the valence sector and in the sea. Our result is seen to be approximately compatible with another determination which used a different fermionic action. And with the addition of possible non-exceptional matching conditions for the non-perturbative renormalisation in the near future, we envisage a greater reduction in the error of our procedure. Using our combined error for $B_K(\mu = 3GeV)$ from Tab.5.9 we have the RGI bag parameter for $N_f = 3$, $\hat{B}_K(\mu = 3GeV) = 0.754(35)$.

Chapter 6

Fixing the gauge

Gauge invariant lattice measures do not, by definition, require one to fix the gauge. In perturbation theory however, the perturbative series is well defined only after this excess degree of freedom in the fields is removed [154]. Gauge fixing on the lattice is performed so that direct comparison to continuum perturbation theory can be made. It would be ideal to fix to a perturbatively simple gauge such as Feynman gauge, but the gauge fixing condition is difficult to implement on the lattice, apart from trivial cases such as non-compact QED [61, 72].

One must instead look at smooth gauge fixing regimes for which an iterative procedure can be followed to minimise a cost functional. Fixing to Landau gauge and Coulomb gauge are two of the most common procedures. We will discuss the procedure for Landau gauge as it completely fixes all the available degrees of freedom, and can be used to match continuum perturbative calculations. A brief discussion on our implementation for Coulomb gauge is also given, which will be useful in the context of gauge fixed wall source propagators used in Chapter 5.

The Landau gauge fixing condition in the continuum theory for QCD is,

$$\partial_\mu A^a_\mu(x) = 0. \tag{6.1}$$

If one were to restrict the summation range of μ, to one less than the dimension of our theory we would have the Coulomb gauge fixing procedure, which has uses in lattice simulations beyond matching to perturbation theory. I begin by discussing the case for continuum four-dimensional U(1) gauge theory and then extend to non-Abelian lattice gauge fixing.

The gauge fixing requirement in Eq.6.1, can be reexpressed in terms of the gauge fixing

functional,

$$F[A] = \int d^4x A_\mu(x) A_\mu(x). \tag{6.2}$$

Considering a gauge transformation,

$$A_\mu(x)^g = A_\mu(x) - \partial_\mu \Lambda(x). \tag{6.3}$$

We have the gauge-transformed functional,

$$F[A]^g = \int d^4x A_\mu(x) A_\mu(x) - 2A_\mu(x)\partial_\mu\Lambda(x) + (\partial_\mu \Lambda(x))^2. \tag{6.4}$$

Taking the functional derivative w.r.t the infinitesimal variation $\Lambda(x)$, yields,

$$\left.\frac{\delta F[A]^g}{\delta \Lambda}\right|_{\Lambda(x)=0} = 2\partial_\mu A_\mu(x). \tag{6.5}$$

At a stationary point of $F[A]^g$, i.e. a minimum of the functional, the Landau condition ($\partial_\mu A_\mu(x) = 0$) is satisfied. This allows us to turn the continuum gauge fixing condition into a minimisation problem, which is tractable on a computer.

If we set,

$$\Lambda(x) = \alpha \partial_\mu A_\mu(x). \tag{6.6}$$

We have the abelian gauge transformation,

$$A^g_\mu = A_\mu(x) - \alpha \partial_\mu \left(\partial_\nu A_\nu(x)\right). \tag{6.7}$$

This is a steepest descent step towards the minimum of the gauge fixing functional, as can be seen by considering the gauge transformed functional,

$$(A_\mu(x)^g)^2 = (A_\mu(x))^2 - 2\alpha \left(\partial_\mu A_\mu\right)^2 + \alpha^2 \left(\partial_\mu \partial_\nu A_\nu(x) \partial_\mu \partial_\gamma A_\gamma(x)\right). \tag{6.8}$$

For small α each gauge transformation decreases the functional. The idea being, that at every iteration of the routine we compute the gauge transormation matrices with Eq.6.6, and apply them. We and repeat until sufficient convergence.

The gauge transformation for non-abelian fields with $A_\mu(x) \in \mathfrak{su}(N_c)$ is (with $g(x) \in SU(N_c)$),

$$\begin{aligned} g(x) &= e^{i\Lambda(x)}, \\ A_\mu(x)^g &= g(x) A_\mu(x) g(x)^\dagger - i g(x) \partial_\mu g(x)^\dagger. \end{aligned} \tag{6.9}$$

The Landau condition is the same, and upon setting $\Lambda = \alpha \partial_\mu A_\mu(x)$ we obtain the non-Abelian continuum analog of Eq.6.7,

$$A_\mu(x)^g = g(x) A_\mu(x) g(x)^\dagger - i g(x) \left(\alpha \partial_\mu \partial_\nu A_\nu(x)\right) g(x)^\dagger. \tag{6.10}$$

6.0.3 Gribov copies

Unfortunately, as pointed out in [100] there are often many different solutions for the Landau gauge fixing condition Eq.6.1 for continuum, non-Abelian field theories. Smooth gauge-fixed lattice simulations also suffer from the Gribov ambiguity.

In lattice simulations, when fixing the gauge there can exist many independent local solutions to a smooth covariant gauge such that $a\Delta_\mu A_\mu(x) = 0$ and that are not related by a global gauge transformation. This can be illustrated on the lattice by gauge fixing our configuration, then performing local random gauge transformations over our original lattice links and running our gauge fixing algorithm again [92]. Ideally, this would provide us with the same result for the gauge fixing functionals (Eq.6.27), but in practice does not. The differing ensembles determined from such a procedure can be viewed as the lattice variant of the Gribov copies for that configuration.

One method to attempt to control the affect of having numerous local minima of the gauge fixing functional is to rerun the gauge fixing from random gauge transforms many times keeping the "best" configuration (the best copy "bc"), the one that does the best job of minimising the functional. However, no numerical minimisation heuristic can ever guarantee we have found the global minimum. A comparison between the best copy (bc) and the worst copy (wc) drawn from a sufficient number of copies should be able to illustrate whether Gribov copies play a systematically important rôle in gluonic observables.

6.1 Lattice gauge fixing

Gauge parallel transport matrices (links) are (Eq.2.10) defined to lie halfway between sites in the lattice theory,

$$U_\mu\left(x + a\frac{\hat{\mu}}{2}\right) = e^{iA_\mu\left(x + a\frac{\hat{\mu}}{2}\right)}.$$

Starting from the continuum definition of our gauge fixing procedure in Eq.6.10, we first note that the continuum gauge transformation is translated to the lattice by performing a Taylor expansion in small powers of the lattice spacing a (and including the factor

ag_0 to help with collecting equivalent orders of a),

$$\begin{aligned} U_\mu(x) &= e^{iag_0 A_\mu(x)}, \\ U_\mu(x)^g &= g(x)e^{iag_0 A_\mu(x)}g(x+a\hat{\mu})^\dagger, \\ &= g(x)(1+iag_0 A_\mu(x))(g(x)^\dagger + a\Delta_\mu g(x)^\dagger + O(a^2)), \\ &= 1 + iag_0 g(x)A_\mu(x)g(x)^\dagger + ag(x)\Delta_\mu g(x)^\dagger + O(a^2), \\ &= e^{iag_0 A_\mu(x)^g}, \end{aligned} \tag{6.11}$$

Within this expansion, and equating terms at the same order we recover the continuum definition of the gauge transformed fields,

$$A_\mu(x)^g = g(x)A_\mu(x)g(x)^\dagger - \frac{i}{g_0}g(x)\Delta_\mu g(x)^\dagger. \tag{6.12}$$

Under Taylor expansion to leading order in a, we can see that the definition,

$$g(x) = e^{i\alpha a\Delta_\mu A_\mu(x)}, \tag{6.13}$$

recreates the continuum Landau gauge fixing iteration from Eq.6.10 under the same small a expansion. Where we use the finite difference definition of the derivative (Eq.2.17),

$$a\Delta_\mu A_\mu(x) = \left(A_\mu\left(x + a\frac{\hat{\mu}}{2}\right) - A_\mu\left(x - a\frac{\hat{\mu}}{2}\right)\right) + O(a^3).$$

Pulling the definitions from Eq.6.11 and Eq.6.13, the procedure for iteratively fixing to a smooth gauge on the lattice is.

$$\begin{aligned} g(x) &= e^{ia\Delta_\mu A_\mu(x)}, \\ U_\mu\left(x + a\frac{\hat{\mu}}{2}\right) &= g(x)U_\mu\left(x + a\frac{\hat{\mu}}{2}\right)g\left(x + a\hat{\mu}\right)^\dagger. \end{aligned} \tag{6.14}$$

This method describes a local minimisation procedure.

6.1.1 Improved numerical derivative

The definition of the derivative we use for our fields is symmetric because the links lie halfway between the sites of our lattice, and hence automatically a^2-improved. We can take the neighbouring terms into consideration and push the error in the derivative to $O(a^4)$ in a weak field approximation and Taylor expansion in $A_\mu\left(x + a\frac{\hat{\mu}}{2}\right)$. The linear

combination,

$$
\begin{aligned}
a\Delta_\mu A_\mu(x) = &+ \frac{9}{8}\left(A_\mu\left(x + a\frac{\hat{\mu}}{2}\right) - A_\mu\left(x - a\frac{\hat{\mu}}{2}\right)\right), \\
&- \frac{1}{24}\left(A_\mu\left(x + a\frac{3\hat{\mu}}{2}\right) - A_\mu\left(x - a\frac{3\hat{\mu}}{2}\right)\right) + O(a^5\Delta_\mu^5 A(x)),
\end{aligned}
\tag{6.15}
$$

suffices. Although this definition of the derivative is accurate to $O(a^5)$ unless the fields are defined exactly, or the next term in the sine approximation is taken in the Hermitian projection (Log-A) the order of the error remains the same. As described later in Sec.6.2.1, this definition of the derivative leads to a slightly different definition of the lattice momentum.

One could eliminate the $O(a^5)$ errors by taking the combination,

$$
\begin{aligned}
a\Delta_\mu A_\mu(x) = &+ \frac{75}{64}\left(A_\mu\left(x + a\frac{\hat{\mu}}{2}\right) - A_\mu\left(x - a\frac{\hat{\mu}}{2}\right)\right), r \\
&- \frac{25}{384}\left(A_\mu\left(x + a\frac{3\hat{\mu}}{2}\right) - A_\mu\left(x - a\frac{3\hat{\mu}}{2}\right)\right), \\
&+ \frac{3}{640}\left(A_\mu\left(x + a\frac{5\hat{\mu}}{2}\right) - A_\mu\left(x - a\frac{5\hat{\mu}}{2}\right)\right) + O(a^7\Delta_\mu^7 A(x)).
\end{aligned}
\tag{6.16}
$$

In practice this is a poor idea, as often gauge actions with $O(a^2)$ errors are used, and to see the benefits of higher order improvements we need to control the other leading order errors in the procedure.

6.1.2 Exponentiation

Once we have computed the derivative using one of the definitions of the gauge field (Appendix A) and one of the definitions of the derivative (Sec.6.1.1), we can now perform one iteration of the steepest-descents step of Eq.6.14. We must exponentiate our calculated derivative to the gauge transformation matrices.

The authors in [62] suggest the Log-A definition of the fields and a Taylor expansion of the exponential up to the derivative term and a reunitarisation back into the group is acceptable (Sec.A.2.2), this one of the most common procedures and is often called the Cornell type [151]. When it comes to computing different Landau gauge fixing procedures we call it Fixing-α (Sec.6.8).

The leading error for the procedure is ambiguous because there is either a term proportional to $O(\alpha a^3 \Delta_\mu^{(3)} A_\mu(x))$ from the derivative or $O(\alpha A^3)$ from the Log-A definition of the fields. There is a also an error term of $O(\alpha^2 a \Delta_\mu A_\mu(x))$ from the truncated exponential. The term from the truncated exponential is expected to be

small as α must be small to ensure we are minimising $a\Delta_\mu A_\mu(x)$.

We can classically, systematically, remove errors from the procedure by improving the approximations in each sector. Although the reunitarisation procedure does suffice, we can do much better by utilising Cayley-Hamilton theorem allowing us to exponentiate $\alpha a \Delta_\mu A_\mu(x)$ exactly. The tools for doing so in the context of link variables have been known since the publication of the STOUT smearing technique [129] and are discussed in A.2.3. Even before the advent of the exact exponentiation technique, accurate exponentials (often by high order Taylor expansions of the matrix A) of Hermitian matrices have play a pivotal rôle in the Hybrid Monte Carlo (HMC) update [97].

Being an exact expression for the exponential we remove the terms $O(\alpha^2)$ and higher in the estimation of the error of our procedure coming from the exponential, which I have just argued is sub-leading. Exact exponentiation used in conjunction with the exact Hermitian projection (Log-C) of the fields should leave the error from the derivative as the only error term. We can then use the derivative form in 6.15 to obtain an $O(a^5)$ accurate and beyond algorithm, although we are then limited to the accuracy of our action and other discretisation errors.

6.2 Fourier acceleration

I switch back to the case of electromagnetism for simplicity for now. The steepest descents method in Eq.6.14 suffers from critical slowing down. This can be shown by taking the Fourier transform of the derivative of the updating procedure,

$$p_\mu A_\mu(p)^{(n+1)} = p_\mu A_\mu(p)^{(n)} - \alpha p^2 p_\mu A_\mu(p)^{(n)}. \tag{6.17}$$

Rearranging, we see that there is a recurrence (where the final step is correct for small α),

$$\begin{aligned} p_\mu A_\mu(p)^{(n+1)} &= p_\mu A_\mu(p)^{(n)} \left(1 - \alpha p^2\right), \\ &= p_\mu A_\mu(p)^{(n-1)} \left(1 - \alpha p^2\right)^2, \\ &= p_\mu A_\mu(p)^{(0)} \left(1 - \alpha p^2\right)^n, \\ &= p_\mu A_\mu(p)^{(0)} e^{-n\alpha p^2}. \end{aligned} \tag{6.18}$$

This illustrates that the momentum modes close to zero will take much longer to converge to $p_\mu A_\mu(p) = 0$ than the largest momentum modes. There is an exponential inequivalence in the convergence speed of the momentum modes.

Fourier acceleration [62] attempts to ameliorate this effect by forcing each mode at each iteration of the steepest descents to converge at the same rate. This is performed by

rescaling the p^2 dependence in momentum space, as illustrated below (where F and $\tilde{F}$ are forward and backward discrete Fourier transforms, and the factor of the volume (V) is to normalise the result),

$$a\Delta_\mu A_\mu(x)^{(n+1)} = a\Delta_\mu A_\mu(x)^{(n)} - \frac{\alpha}{V}\,\tilde{F}\,\frac{p^2_{\rm Max}}{p^2}\,F\,\left(a^2\Delta^{(2)}_\mu\right)a\Delta_\mu A_\mu(x)^{(n)}. \tag{6.19}$$

At the cost of two discrete Fourier transforms, critical slowing down is removed. For this to be a viable updating procedure, Fast Fourier Transforms (FFTs) need to be used, for our implementation the auto-tuning library FFTW has been used [84].

Considering the lattice analog of Eq.6.10, the derivative of the gauge field update is,

$$a\Delta_\mu A_\mu(x)^{(n+1)} = a\Delta_\mu A_\mu(x)^{(n)} - \alpha a\Delta_\mu D_\mu\left(a\Delta_\nu A_\nu(x)^{(n)}\right). \tag{6.20}$$

Where $D_\mu\Lambda(x) = a\Delta_\mu\Lambda(x) - i\,[A_\mu(x),\Lambda(x)]$, for $g(x) = e^{i\Lambda(x)}$. We see that for non-Abelian fields it is no longer the slow eigenvalues of $a^2\Delta^{(2)}_\mu$ that we wish to eliminate, but rather $a\Delta_\mu D_\mu$ which depend on the field. It was seen in [62] that in momentum space the difference between these two is seemingly small, and the Abelian Fourier acceleration technique for non-Abelian fields was still effective, and is what we shall use.

The Fourier accelerated algorithm for $SU(N_c)$ lattice gauge fields we use is,

$$\begin{aligned} g(x) &= \exp\left(i\frac{\alpha}{V}\,\tilde{F}\,\frac{p^2_{\rm Max}}{p^2}\,F\,a\Delta_\mu A_\mu(x)\right), \\ U_\mu\left(x + a\frac{\hat{\mu}}{2}\right) &= g(x)U_\mu\left(x + a\frac{\hat{\mu}}{2}\right)g(x + a\hat{\mu})^\dagger. \end{aligned} \tag{6.21}$$

6.2.1 Momentum space gluon fields

The Fourier transform of the gauge field $A_\mu\left(x + a\frac{\hat{\mu}}{2}\right)$ is performed element-by-element on the matrix, we define the momentum-space matrices,

$$A_\mu(p) = e^{ip_\mu/2}\sum_x e^{ip_\mu x_\mu}A_\mu\left(x + a\frac{\hat{\mu}}{2}\right). \tag{6.22}$$

The factor $e^{ip_\mu/2}$ must be present because we do not perform the Fourier transform over x's living halfway between the sites, but rather on the sites. And this needs to be corrected. The momenta p_μ are defined as,

$$p_\mu = \left(\frac{2\pi n_\mu}{L_\mu}\right). \tag{6.23}$$

where the n_μ's are the integer-valued Fourier modes which lie between $\frac{-L_\mu}{2}$ and $\frac{L_\mu - 1}{2}$ where the L_μ's are the length of the lattice in the μ direction.

If we consider the symmetric derivative Eq.2.17 of our fields again, but this time in momentum space,

$$\begin{aligned}
\sum_x e^{ip_\mu x_\mu} A_\mu \left(x + a\frac{\hat{\mu}}{2}\right) &= e^{ip_\mu/2} A_\mu(p), \\
\sum_x e^{ip_\mu x_\mu} A_\mu \left(x - a\frac{\hat{\mu}}{2}\right) &= e^{-ip_\mu/2} A_\mu(p), \\
\sum_x e^{ip_\mu x_\mu} \Delta_\mu A_\mu(x) &= 2i \sin(p_\mu/2) A_\mu(p).
\end{aligned} \tag{6.24}$$

This equation tells us that the minimisation condition $\partial_\mu A_\mu(x) = 0$ in momentum space is best described by $2\sin(p_\mu/2)A_\mu(p) = 0$, suggesting that the momentum definition for our gauge fields we should use is the so-called "sinus" definition [41].

Going back to the Fourier accelerated algorithm in Eq.6.21, we see that I did not define the values p^2 and p^2_{Max}, we define them as (for the unimproved derivative)

$$p^2 = 2\left(N_d - \sum_\mu \cos(p_\mu)\right). \tag{6.25}$$

where $p^2_{\text{Max}} = 4N_d$.

If we consider the nearest-neighbour improved numerical derivative, we obtain a slightly different Landau condition in momentum space,

$$2i\left(\frac{9}{8}\sin\left(p_\mu/2\right) - \frac{1}{24}\sin\left(3p_\mu/2\right)\right) A_\mu(p) = 0. \tag{6.26}$$

Again we associate our momentum with this quantity, $p_\mu = 2\left(\frac{9}{8}\sin\left(p_\mu/2\right) - \frac{1}{24}\sin\left(3p_\mu/2\right)\right)$, and similarly for the $O(a^7)$ derivative, $p_\mu = 2\left(\frac{75}{64}\sin\left(p_\mu/2\right) - \frac{25}{384}\sin\left(3p_\mu/2\right) + \frac{3}{640}\sin\left(5p_\mu/2\right)\right)$. This then, similarly affects p^2_{MAX}, which are included as $\frac{7}{6}4N_d$ and $\frac{1170}{960}4N_d$.

6.3 Linear and Logarithmic fields

The gauge fixing procedure fixes the description of the gauge fields and if using a different description of the derivative, the momentum definition. If one were to check the momentum space Landau or Coulomb condition one would need to use the respective field definition used in the gauge fixing procedure. This has been seen in [108] and not in terms of the logarithm of links but links of gauge fields defined as $A_\mu\left(x + a\frac{\hat{\mu}}{2}\right) = \frac{U_\mu\left(x+\frac{\hat{\mu}}{2}\right)^2 - U_\mu\left(x-\frac{\hat{\mu}}{2}\right)^2}{4i}\Big|_{\text{traceless}}$ in [93]. This is because the two functionals that we fix to are different.

Denoting the Hermitian projected (Log-A) links with a superscript "lin" and the logarithmic with a superscript "log", the logarithmic functional is just the lattice analog of the continuum one (Eq.6.1),

$$F^{log}(U) = \frac{1}{N_c N_d V} \sum_{x,\mu} \frac{\mathrm{Tr}}{2} \left[A_\mu^{log}\left(x + a\frac{\hat{\mu}}{2}\right) A_\mu^{log}\left(x + a\frac{\hat{\mu}}{2}\right) \right]. \tag{6.27}$$

Taylor expanding the link matrices to the order of the linear field definition, we can see that the linear field cost function can be described by,

$$F^{lin}(U) = \frac{1}{N_d V} \sum_{x,\mu} F_\mu(x). \tag{6.28}$$

as is shown by,

$$\begin{aligned} F_\mu(x) &= 1 - \frac{\mathrm{Tr}}{2N_c} \left[U_\mu\left(x + a\tfrac{\hat{\mu}}{2}\right) + U_\mu\left(x + a\tfrac{\hat{\mu}}{2}\right)^\dagger \right], \\ U_\mu\left(x + a\tfrac{\hat{\mu}}{2}\right) &= 1 + iA_\mu\left(x + a\tfrac{\hat{\mu}}{2}\right) - \frac{1}{2}A_\mu\left(x + a\tfrac{\hat{\mu}}{2}\right)^2 + O(a^3), \\ U_\mu\left(x + a\tfrac{\hat{\mu}}{2}\right)^\dagger &= 1 - iA_\mu\left(x + a\tfrac{\hat{\mu}}{2}\right) - \frac{1}{2}A_\mu\left(x + a\tfrac{\hat{\mu}}{2}\right)^2 - O(a^3), \\ F_\mu(x) &= \frac{\mathrm{Tr}}{2N_c} \left[A_\mu\left(x + a\tfrac{\hat{\mu}}{2}\right)^2 \right] + O(a^4). \end{aligned} \tag{6.29}$$

Therefore our gauge fixing functional for the linear definition of the gauge fields is,

$$F^{lin}(U) = 1 - \frac{1}{N_c N_d V} \sum_{x,\mu} \Re\left(\mathrm{Tr}\left[U_\mu\left(x + a\tfrac{\hat{\mu}}{2}\right)\right]\right). \tag{6.30}$$

Effective minimisation of this quantity, means effective maximisation of the link trace, this is not necessarily true for the log fields.

The gauge fixing algorithm to fix the logarithmic links is exactly the same as the algorithm for fixing the Hermitian projected. With the caveat that in practice one should use either the Vandermonde approximate (Log-B) definition or the Hermitian projected definition (Log-A) for the logarithm of the matrix for very early convergence times (we use the Vandermonde approximation for $\Theta > 0.1$, Eq.6.33).

A similar issue was found in [108]. This is likely due to the finite difference approximation being a poor estimate for large fluctuations of the fields and is simply a numeric difficulty, the generic Vandermonde method compared to the analytic method (Eq.A.20) is favoured as it is likely to underestimate field fluctuations but still represent the analytical logarithm of the link more accurately than the Hermitian projection (Log-A) (as can be seen in Fig.A.1), this method *heuristically* always converges, although this is never guaranteed.

6.4 Measuring the gauge fixing accuracy

Controlling the algorithm and knowing at what accuracy to stop is a vital aspect of minimisation routines. If one does not fix to a high enough precision there is a possibility that you cannot accurately match to continuum perturbation theory in a specific gauge. This will be discussed in greater detail in Chapter 2, in the context of the measurement of gluonic two and three point correlation functions.

Now, I will address several ways to measure the convergence of the algorithm, and the merits of each. One should probably check many of these in conjunction to be satisfied with the result.

We have shown in Sec.6.3, Eq.6.30 that for the linear definition of the fields (Log-A) the cost function is the maximisation of the average link trace, we can use this to monitor the gauge fixing accuracy Φ, by the term,

$$\begin{aligned} \Phi &= 1 - \frac{\bar{U}'}{\bar{U}}, \\ \bar{U} &= \frac{1}{N_c N_d V} \sum_{x,\mu} \Re \left(\mathrm{Tr} \left[U_\mu \left(x + a\frac{\hat{\mu}}{2} \right) \right] \right). \end{aligned} \tag{6.31}$$

Where the primed link is the updated link of the procedure. Apart from needing to calculate the average link trace at every step, this method also requires subtraction from unity and numerical division. This is problematic as we will only be able to describe the gauge fixing accuracy to the order of the unit in the last place (ULP) before this measure becomes unstable, this is the measurement made by the Chroma software library [77] in their implementation of a Landau gauge fixing routine . It should also be noted that this method cannot be used to measure the accuracy of a logarithmic field definition gauge fixing routine as the gauge fixing functional is different, and trace maximisation does not necessarily mean minimisation of the logarithmic field functional.

Another method to monitor the accuracy would be to note that at each iteration of the update, the gauge transformation matrices should tend to the identity matrix because each update is $\exp\left(ia\Delta_\mu A_\mu(x)\right)$ and we are minimising $a\Delta_\mu A_\mu(x)$. The measure would be,

$$\Omega = 1 - \frac{1}{N_c V} \sum_x \Re \left(\mathrm{Tr} \left[g(x) \right] \right). \tag{6.32}$$

This method is a factor of N_d cheaper than the Φ measure (Eq.6.31), as the sum runs over sites and not links, which require a sum over polarisations as well. The same arguments about numerical stability apply to this method as the Φ measure, because we are performing a comparison with 1. Unlike the Φ method, this measure is not dependent on the definition of the field.

The method that we choose to determine the accuracy of our gauge fixing procedure is a direct lattice measurement of the gauge condition (i.e. the absolute-valued squared lattice average of the divergence of the fields),

$$\Theta = \frac{2}{N_c V} \sum_x \mathrm{Tr} \left[\left(a\Delta_\mu A_\mu(x) \right)^2 \right]. \tag{6.33}$$

We choose this for several reasons, first the quantity $\left(a\Delta_\mu A_\mu(x)\right)^2$ is purely real and is equivalent to (the factor of 2 disappears due to Eq.3.18),

$$\Theta = \frac{1}{N_c V} \sum_x \sum_a^{N_c^2-1} |a\Delta_\mu A^a_\mu(x)|^2. \tag{6.34}$$

i.e. The sum of every Lie element of the matrix multiplied by its conjugate, which is computationally cheap to perform. The second reason for using this quantity to monitor the accuracy is that $a\Delta_\mu A_\mu(x)$ is already computed in the algorithm, and Θ can easily be computed in step. Thirdly, this measure does not suffer from the same numerical accuracy problems as the two above, as long as each $a\Delta_\mu A_\mu(x)$ in the sum is of approximately similar magnitude (which is the case) this measure is stable. This measure by definition incorporates the field and derivative definition.

There is also another measure that can be used to illustrate the accuracy of the gauge fixing procedure, advocated in [134] and first suggested in [123] and seen from the zero momentum temporally polarised gluon propagator in [102], this involves a check of the constancy of the sum of temporal fields per time slice,

$$\Gamma = \frac{1}{(L_t - 1)\left(N_c^2 - 1\right)} \sum_{i \in x,\, y,\, z.. \neq t,\, t \neq 0} \left| A_t(i, t=0) - A_t(i,t) \right|. \tag{6.35}$$

this is a very similar measure to that of Eq.6.33, as the minimisation procedure suggests,

$$A_t\left(i, t + a\frac{1}{2}\right) - A_t\left(i, t - a\frac{1}{2}\right) = 0. \tag{6.36}$$

and hence for periodic boundary conditions this implies constancy between time-slices. This is an expensive measure and is not well suited for monitoring the accuracy as the algorithm progresses, but it is a useful check to ensure sufficient gauge fixing accuracy. It is also dependent on the definition of the gauge fields used in the steepest descent derivative.

Fig.6.1 illustrates the methods that could be used to determine the gauge fixing accuracy. The Θ (green, second from the top) measure is the one we use, and is seen to be pessimistic compared to the Ω and Φ (red and black, bottom two lines). The Ω and the Φ measures are consistent, but suffer from round-off error at the order of

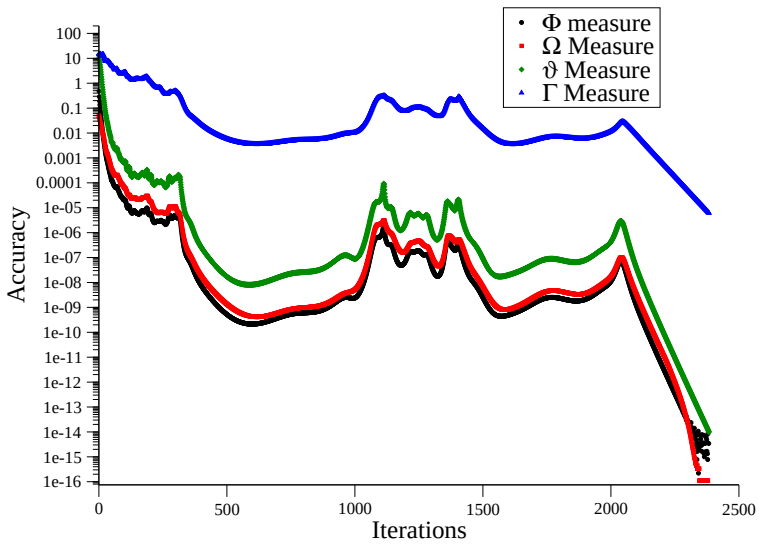

Figure 6.1 *The gauge fixing accuracy measures* Φ, Ω, Θ *and* Γ *for an arbitrary* $16^3 \times 32$ *configuration, fixed to Landau gauge using the Fourier-accelerated algorithm.*

the double precision ULP (10^{-16}).

6.5 Lattice Coulomb gauge

Much of the discussion for the Landau gauge fixing is applicable for fixing to the Coulomb gauge, as the Coulomb condition is very similar to the Landau,

$$a\Delta_i A_i(x) = 0, i \in x,\ y,\ z, .. \neq t. \tag{6.37}$$

where instead of Greek indices I use Latin indices to signify that we are working in spatial coordinates.

The Fourier acceleration algorithm is again,

$$\begin{aligned} g(x) = exp\left(\tilde{F}_{N_d-1}\,\frac{i\alpha p^2_{N_d-1,\mathrm{Max}}}{L^3 p^2_{N_d-1}}\,F_{N_d-1}\,a\Delta_i A_i(x)\right), \\ U_\mu\left(x + a\frac{\hat{i}}{2}\right) = g(x)U_\mu\left(x + a\frac{\hat{i}}{2}\right)g(x + a\hat{\mu})^\dagger. \end{aligned} \tag{6.38}$$

It has been written this way to illustrate that although we are minimising the spatial derivative, we still need to gauge transform the temporal links to ensure we are applying a pure gauge transform. The momenta are spatial in extent and the Fourier transforms are on the $N_d - 1$ subspace. The computation of the gauge transformation matrices is completely t-independent and this allows for a time-slice by time-slice procedure, this

turns out to be a fast and computer memory-wise cheap method.

The method I propose requires the storing of three time-slice's worth of gauge transformation matrices, and contrary to the Landau gauge fixing procedure (where the links are overwritten each iteration) the gauge transformation to rotate the links is performed only after convergence. This requires the storage of the gauge transformation matrices as the accumulated product,

$$g^{(n)}(x) = g'^{(n)}(x)g'^{(n-1)}(x).....g'^{(0)}(x), \qquad g'^{(0)}(x) = I. \tag{6.39}$$

Where the index "n" means the nth iteration of the gauge fixing algorithm and the prime means the gauge transformation generated by that iteration. This means that the fields $U_\mu\left(x + a\frac{\hat{\mu}}{2}\right)'$ and $U_\mu\left(x - a\frac{\hat{\mu}}{2}\right)'$ must be computed within the derivative of the steepest descents. Moving to a slice-by-slice iteration scheme is a big advantage, as we see that the number of iterations to convergence varies considerably on a slice-by-slice basis (see Fig.6.2). If we proceeded as in the Landau case performing an N_d-dimensional Fourier transform and not regarding the temporal independence, we would waste iterations on time-slices that have already converged to our desired accuracy.

We require three temporary time slice's worth of gauge transformation matrices because the rotation of the temporal links needs to be performed, and so one must converge the algorithm on the above time-slice so that this can be performed (we employ this technique as a computer memory saving procedure in the context of link smearing in Chapter 4).

The layout for this algorithm is as follows. First we set the three time-slice wide gauge transformation matrices to the identity we will call these "gauge slice end, gauge slice" and "gauge slice up". Second, one must compute the gauge transformation matrices of the time-slice $t = 0$ and the one above it at $t = 1$. We put the gauge transformation matrices of time $t = 0$ in "gauge slice end" and $t = 1$ in "gauge slice".

We then gauge transform the link matrices on the time-slice $t = 0$. We then loop over the rest of the time-slices from $t = 2$ up to $t = L_t - 1$, setting "gauge slice up" to the identity and computing the gauge transformation at $t + 1$ (we already have the gauge transformation matrices at t in "gauge slice"). Then gauge transforming the links for t and copying the matrices from "slice gauge up" to "slice gauge" and repeating. The final gauge transformation at time-slice $t = L_t - 1$ is performed using the matrices in "slice gauge up" and "slice gauge end". It should be noted that the link matrices "$U(t)$" are all of the matrices on the timeslice "t".

The algorithm for this is shown in Algorithm 3, where it should be understood that the function "Fourier accelerate" produces the gauge transformation matrices on that

Algorithm 3 *The slice-by-slice iterative Coulomb gauge fixing algorithm.*

gauge slice end $\leftarrow$ gauge slice $\leftarrow I_{N_c \times N_c}$
Fourier Accelerate(gauge slice end , U(t=0))
Fourier Accelerate(gauge slice , U(t=1))
gauge transform(gauge slice end , U(t=0) , gauge slice)
for $t = 2 \rightarrow L_t - 1$ **do**
    gauge slice up $\leftarrow I_{N_c \times N_c}$
    Fourier Accelerate(gauge slice up , U(t))
    gauge transform(gauge slice , U(t - 1) , gauge slice up)
    gauge slice $\leftarrow$ gauge slice up
end for
gauge transform(gauge slice , U(t) , gauge slice end)

time-slice via Eq.6.38 accumulating them until convergence á la Eq.6.39, and "gauge transform" performs the gauge transformation for all of the links on that time-slice.

Variations in the procedure

To illustrate the slice-by-slice variation of the Coulomb gauge fixing procedure we plot a graph of the average (estimated from a bootstrap procedure) number of iterations required to meet $\Theta < 10^{-14}$. Also plotted are the maximum and minimum variations from this average for 50 Gribov copies on the same, example $16^3 \times 32$ configuration. This is shown in Fig.6.2.

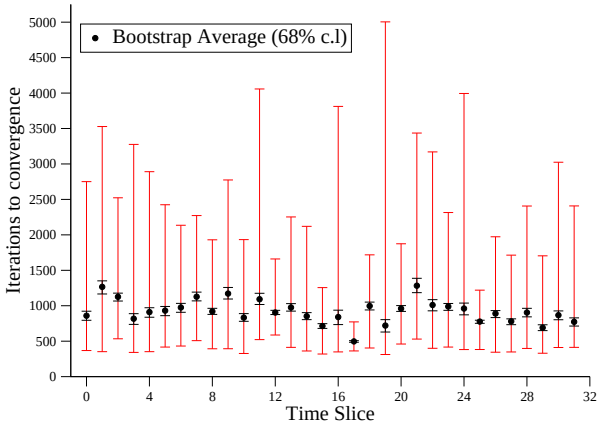

Figure 6.2 *Average iterations to convergence per time-slice for Fourier Accelerated Coulomb gauge fixing, black circles show the average and 68% confidence limit from a bootstrap analysis. The error bars illustrate the maximum and minimum number of iterations from this value. The distribution is created with a single configuration over 50 random gauge transformations of the initial configuration.*

Fig.6.2 shows that the slice-by-slice variation can be very large, the minimum number

of iterations was 327 and the maximum 5004, which is over 14× larger. Although the average number of iterations is small and does not fluctuate much per slice, illustrative of a convergence issue with some initial starting fields which should be avoided.

6.6 The tuning parameter

To obtain the best performance from the algorithm the parameter α must be tuned sufficiently. We consider many copies of the same $\beta = 2.13$, Iwasaki gauge, $16^3 \times 32$ configuration as a simple example, and claim there is a very mild lattice spacing dependence for the tuning.

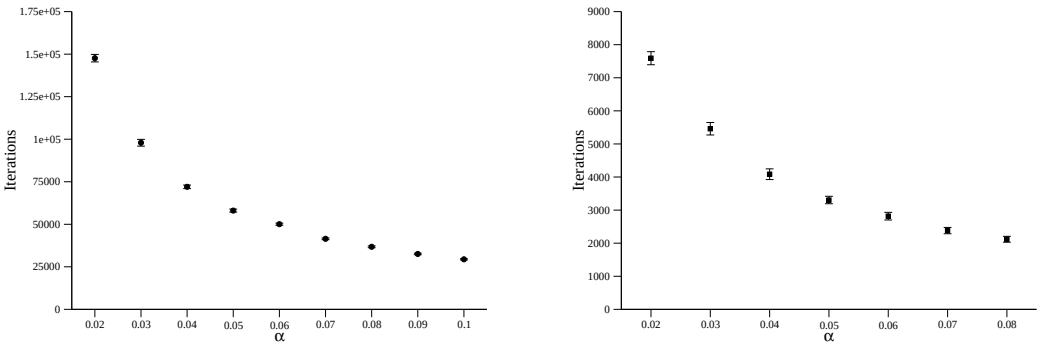

(a) *Coulomb tuning.* **(b)** *Landau tuning.*

Figure 6.3 *Variation of the tuning parameter α versus the total number of iterations of the algorithm for the Coulomb (Fig.(a)) and the Landau (Fig.(b)) gauge fixing procedures to attain an accuracy of $\Theta < 10^{-14}$ with Fourier acceleration for an example $16^3 \times 32$ configuration.*

Fig.6.3 shows the total number of iterations needed to attain an accuracy of $\Theta < 10^{-14}$ for the Fourier Accelerated Coulomb and Landau gauge fixing routines versus the tuning parameter α, the error bars are from a bootstrap analysis over 150 Gribov Copies of a thermalised $16^3 \times 32$, $\beta = 2.13$ Iwasaki gauge $N_f = 2 + 1$ Domain Wall fermion configuration. We see that poor selection of the tuning parameter could yield a slow-down in the algorithm of a factor of 4 for the Landau and nearly a factor of 5 for the Coulomb. Although the Coulomb gauge fixing takes many more iterations to achieve the required accuracy, each iteration over the (N_d-1) spatial hypercube is much cheaper than a Landau iteration, it may be surprising to note that the Coulomb gauge fixing routine converges in about half the time of the Landau gauge fixing routine. Effective tuning of the parameter α can lead to a $\approx 3\times$ speed up for the procedure.

6.6.1 A note on convergence

One would hope that the algorithm succeeds at fixing the gauge to some (appropriately chosen) accuracy, but we would not want our algorithm to continue indefinitely, especially if it gets stuck in a local minimum and does not reach convergence.

We could enforce a flexible cut-off on the number of iterations that we perform the Fourier acceleration with, stressing that it should be semi-definite because we should allow leeway if we are close to our convergence criteria, due to the cost in restarting. We can then use our the fact that our algorithm is local to our advantage, if the algorithm has not converged we start again but perform a random gauge transformation of the fields deforming the initial state with the goal of attaining an easier path to convergence.

We allow for only a small number of these random transformation steps after non-convergence to again stop the algorithm from continuing forever, which could happen with a particularly poor choice of the tuning parameter. Usually, a maximum cut-off on the number of iterations ($O(8000)$ over the whole lattice for Landau or per slice for Coulomb) and the maximum number of restarts being around seven has been enough to obtain convergence on all of our ensembles. Although there does exist very minor volume dependence for the Fourier accelerated algorithm compared to the number of iterations required to meet fixed convergence (As is seen later in Fig.6.8), so some care is needed to tune the maximum number of iterations for the procedure also.

This method is very beneficial for fixing to Coulomb gauge. As can be seen in Fig.6.2, the variations in the procedure are large but the average is orders of magnitude lower than the extrema. Putting an upper limit on the number of iterations allows for faster convergence of the algorithm, by removing the need to converge exceptional, ill-convergent initial configurations. As our routine is a time-slice by time-slice implementation, only a random restart on that time-slice is necessary. Making this a cheap technique.

It is quite common for our Coulomb gauge fixing routine to have time slices not converge, for a set of 12 $64^3 \times 128$, $\beta = 2.25$ configurations fixed to $\Theta = 10^{-14}$ accuracy with maximum number of iterations 9000 and with 10^2 leeway for convergence, around 7% of the time-slices failed to converge.

6.7 Improvements in smooth lattice gauge fixing

In this section I detail various improvement measures investigated to allow for computationally faster or more accurate fixing procedures. I discuss first algorithmic

improvements and finish with theoretical improvement techniques such as smeared preconditioning, Maximal Axial Gauge fixing as a precomputation step and residual gauge fixing for a post-processing step only available for Coulomb gauge fixing.

6.7.1 Accelerating the accelerator

If we consider the algorithm in Eq.6.21, we note that the parameter $\frac{i\alpha p^2_{\mathrm{Max}}}{Vp^2}$ is independent of the stage of the procedure and can be precomputed as a look up table at the beginning. For the next improvement we specialise to SU(3).

The matrix $dA(x) = a\Delta_\mu A_\mu(x)$ is guaranteed to be traceless and Hermitian and has the structure,

$$\begin{pmatrix} dA[0] & dA[1] & dA[2] \\ dA[1]^* & dA[4] & dA[5] \\ dA[2]^* & dA[5]^* & -(dA[0]+dA[4]) \end{pmatrix}. \tag{6.40}$$

For the Fourier acceleration, there is no need in Fourier transforming all of the elements backward and forward, instead only the elements 0, 1, 2, 4 and 5 need to be transformed as after the backward transform we can rebuild the resulting Hermitian matrix by symmetry. This accounts to performing 10 (5 forward and backward) complex to complex FFTs instead of 18. We can save on one more FFT each way (bringing the total to 8) by noting that the elements A[0], A[4] and hence A[8] are necessarily real. This means that a complex to complex transform on A[0] or A[4] is wasting its time Fourier transforming the imaginary part which is 0. What we do is pack the real element of A[4] into the imaginary part of A[0]. In general, for $SU(N_c)$ we only perform the FFTs on the $(N_c(N_c+1)/2-1$ independent elements of the Hermitian matrix, where the -1 comes from the fact that we can reproduce the last element by tracelessness.

The Fourier accelerated algorithm should be considered to be two distinct parts. The gauge transformation part should perform generically as $O(V)$ where V is the lattice volume, but the Fourier acceleration part should perform as $O(V\log(V))$. At large enough volume we will be spending most of our time performing Fourier transforms and so effectively minimising the number we perform is vital for decent volume scaling.

Thread parallelism

Effective parallelism can be achieved in two ways. As we are Fourier transforming each element of the matrix separately, each Fourier transform could be performed by a single thread. In fact, it is more pertinent to let each thread perform the forward and backward Fourier transform, as there are fewer calls for synchronisation. This method

works well for a small small number of threads, logically when the number of threads is greater than $N_c(N_c+1)/2-1$ (where integer division has been used) then some of the threads are being left idle. Some Fourier transform libraries (such as v3.3 of FFTW [84]) allow for parallel FFTs to be performed, which is preferred when many threads are available and the problem size is large.

6.7.2 Maximal Axial Gauge improvement

To help alleviate theoretical problems due to Gribov copies in our gauge fixing procedure, one could attempt to gauge fix to an absolute (or as near as possible) gauge to locate a singular gauge orbit and then apply the smooth gauge fixing procedure with the hope that one stays on that gauge orbit. We considered the improvement of fixing to the Maximal Axial Gauge (MAG) which sets many gauge links to unity in a gauge invariant manner, as detailed in [160].

This gauge is achieved by selecting a starting point at index "0". And rotating all of the links in the x-direction to the identity, which is done by setting the gauge transformation matrix at site $x + a\hat{x}$ to be the product of the links previously and the gauge transformation matrix at site 0 to be the identity.

$$g(0) = I, \qquad g(x) = \prod_{i}^{x-1} U_\mu \left(i + a\frac{\hat{\mu}}{2} \right). \tag{6.41}$$

This leaves the link at $x = L_x - a\frac{\hat{x}}{2}$ to hold all of the gauge-invariant information such as the Polyakov loop. The algorithm sets all of the links in the y-direction to the identity in the same way, by starting from the sites with links rotated in the x direction (and setting the gauge transformation matrices at these sites to the identity) and travelling up the y-direction rotating the links. This is repeated for the rest of the directions, this improvement can be used in conjunction with the Landau gauge fixing procedure as it does not completely fix the lattice degrees of freedom and so can be performed with random restarts to control convergence.

It is impractical to use this when fixing to Coulomb gauge using our implementation, because to use MAG fixing we need to converge each slice fully without randomly restarting, and so we remove many benefits from having a convergence cut-off.

Fig.6.4 shows two overlain histograms of the distribution of Gribov copies' functionals, one (the blue) having been preconditioned with the MAG treatment, and the other (the red) being from the standard gauge fixing treatment. We see that the MAG preconditioning for Landau gauge fixes us to minima, which do not for the majority

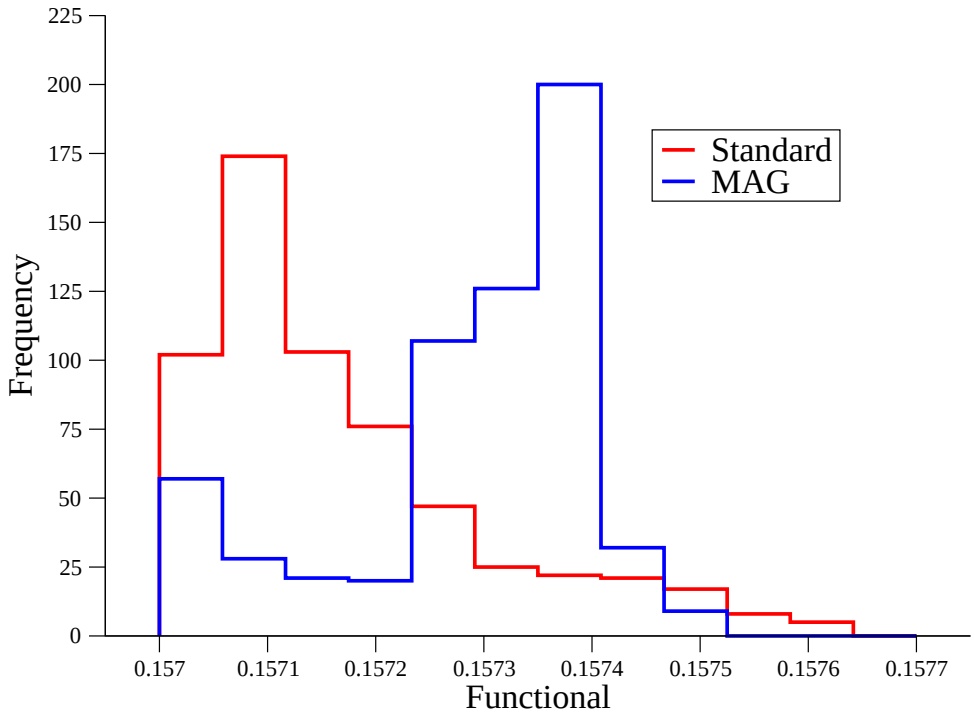

Figure 6.4 *Histogram of the gauge functional histogram from 600 Landau gauge Gribov copies for an example* $16^3 \times 32$ $\beta = 2.13$ *Iwasaki gauge,* $N_f = 2 + 1$ *DWF configuration. Showing the functional from the MAG preconditioning and the Fourier accelerated gauge fixing algorithm, and using the Hermitian projection of the links and the symmetric finite difference derivative.*

of copies minimise the the functional effectively compared to the un MAG fixed. This is in our opinion a detrimental effect, and so MAG improvement will not be discussed further.

6.7.3 Smeared-preconditioned improvement

We also looked at a smeared "preconditioned" improvement, whereby one smears the original gauge field using some procedure (the details of smearing procedures will be introduced in Chapter 4) to obtain a smoother background field. This field is then gauge fixed to some accuracy and the complete gauge transformation matrices from the smeared and fixed fields are used to gauge rotate or "precondition" the original configuration. This was first suggested in [106] and the usual gauge fixing method was then run on top of the preconditioned field. This method was first seen to provide a unique Gribov copy for several randomly gauge transformed versions of the same very small lattices.

The idea behind this procedure is that the algorithm on "rough" gauge ensembles gets stuck in one of the many local minima and so the smearing transformation smooths the gauge field by reducing UV fluctuations in the gauge field (by a kind of neighbouring field average which minimises the gauge action). So that it is easier for the algorithm to find a global maximum, with the hope that the information of the original field is not lost. By rotating our original field with the solution to the smeared gauge field we attempt to start the configuration in a space that is likely closer to the global maximum.

In practice this method does not and cannot guarantee a global minimum, but can often provide a better minimum of the gauge fixing functional. This procedure can be randomly restarted, but this must occur at the beginning of the algorithm and so is expensive as a re-read, and re-smear and fix must be performed.

I propose a method whereby we use the smearing preconditioning over several random gauge transforms of the original ensemble and select the one which minimises the functional the best, this is empirically seen to be better than obtaining copies from just a random transform. The gauge fixing for both the smearing and the comparing of copies can be done "roughly" i.e. to a small accuracy of $\Theta \approx 10^{-8}$ and then the final best copy can be fixed to the desired accuracy. This makes the algorithm considerably cheaper.

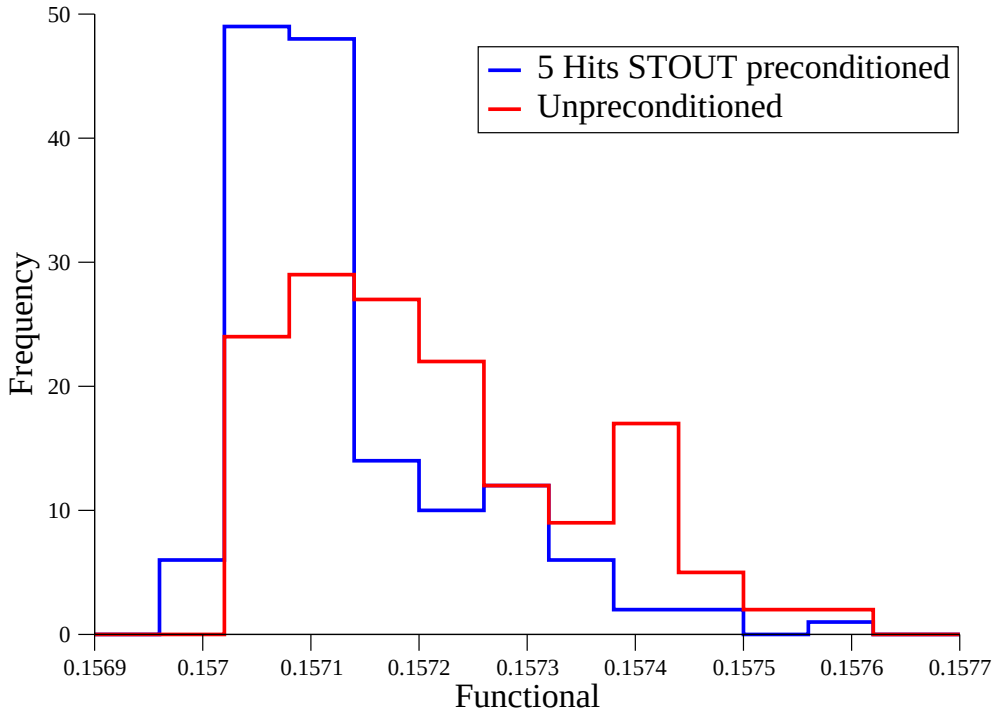

Figure 6.5 *Smeared preconditioning improvement compared with the normal Fourier accelerated gauge fixing algorithm for 150 copies of a* $16^3 \times 32$, $\beta = 2.13$, $N_f = 2 + 1$, $am_l = 0.01$ *DWF thermalised configuration.*

Fig.6.5 illustrates the ability for this method to find better Gribov copies than the unpreconditioned. As there is a much greater frequency of copies with a lower functional for the smeared-preconditioned, and a few copies with lower functionals than the unpreconditioned. Upon comparison of the best copies from the preconditioned compared to the best copies from the unpreconditioned for 20 more configurations and 150 Gribov copies we see that 14 out of the 20 of the smeared-preconditioned best copies had a lower functional than the unpreconditioned.

For the same reason the MAG precomputation has incompatibilities with the slice-by-slice Coulomb gauge fixing technique, smeared-preconditioning also cannot be effectively used.

6.7.4 Fixing the residual gauge degrees of freedom

As the continuum Coulomb gauge expression suggests ($\partial_i A_i = 0$), we have not put any constraints on the temporally polarised gauge fields. One might be concerned that as we are allowing for an unaccounted-for extra degree of freedom in our procedure, we might have large fluctuations of the field in the unfixed direction. The proposed solution ([46, 59] and [130]) is to fix to the so-called lattice Minimal Coulomb Gauge, by a procedure of fixing the residual degree of freedom. This technique is gauge invariant and can easily be performed as a post-processing step in the gauge fixing.

Once we have our Coulomb gauge fixed fields, we compute the quantity,

$$Y(t) = Proj_{SU(N_c)} \left(\frac{1}{L_x L_y L_z ... L_{N_d-2}} \sum_x U_{N_d-1}(x,t) \right) \tag{6.42}$$

Where the projection is a trace maximisation routine as described in Sec.A.2.1. We then perform the gauge transformation,

$$\begin{aligned} U'_t \left(x + a\frac{\hat{t}}{2} \right) &= g(t) U_t \left(x + a\frac{\hat{t}}{2} \right) g(t+1)^\dagger \\ U'_i \left(x + a\frac{\hat{i}}{2} \right) &= g(t) U_i \left(x + a\frac{\hat{i}}{2} \right) g(t)^\dagger. \end{aligned} \tag{6.43}$$

Where the gauge transformation matrices are defined by the recurrence,

$$g(t+1) = g(t)Y(t), \qquad g(0) = I. \tag{6.44}$$

And hence set the quantity $Y(t)$ to the identity for every time-slice but the last. This is akin to the method for fixing to a lattice axial gauge insofar as we are selecting rotations that automatically rotate the links in one direction to the identity, and the

gauge invariant information exists in the final links.

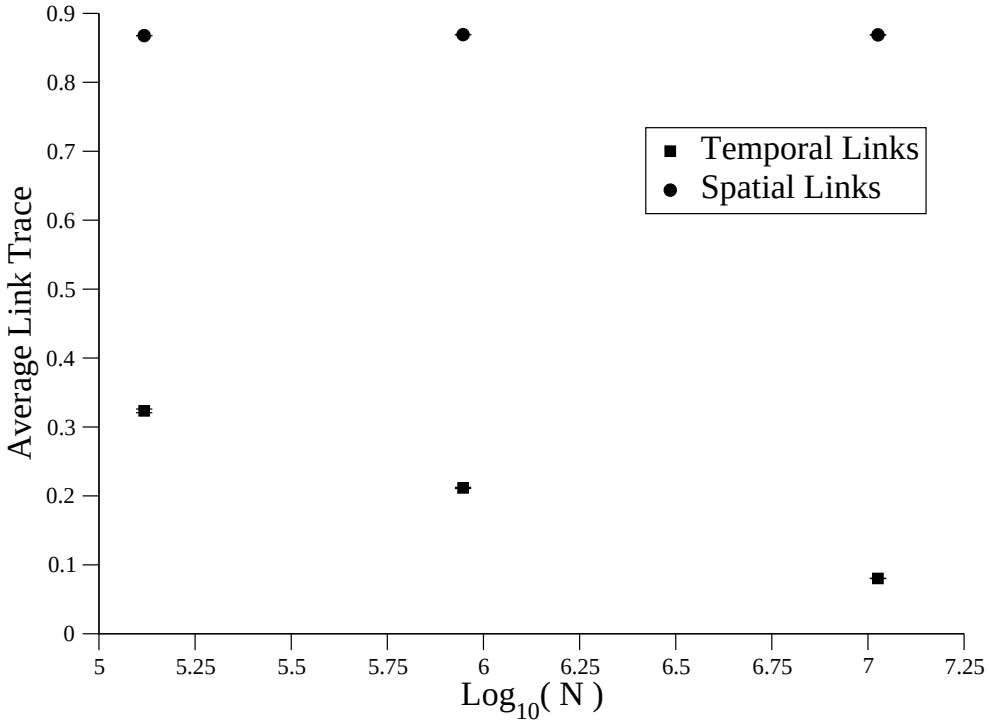

Figure 6.6 *The average spatial and temporal link trace for* $16^3 \times 32$, $24^3 \times 64$ *and* $48^3 \times 96$, $\beta = 2.13$ *Iwasaki gauge,* $N_f = 2+1$ *Domain Wall Fermion configurations against the logarithm of the number of lattice sites.*

Fig.6.6 shows the average spatial and temporal links after Coulomb gauge fixing and residual gauge fixing post-processing for fixed β and hence lattice spacing. We see that in this regime the spatial link value is constant with volume, but the temporal link varies strongly with volume. Similar scaling with lattice volume was seen in [130]. Without residual gauge fixing the average temporal link will be consistent with 0.

6.8 Benchmarks

I consider four different types of Landau gauge fixing to investigate various states of improvement, and investigate their tuning and the relative computational cost. The four types considered are all Fourier accelerated variants and the difference between each is the definition of the field, the order of the exponentiation for the gauge transformation matrices and the order of the derivative.

We call Fixing-α the standard Fourier-accelerated Cornell approach, being the usual symmetric difference derivative of the Log-A definition of the fields and reunitarisation (A.2.2) in the exponentiation. Fixing-β is the same field definition and exponentiation,

but with the $O(a^5)$ next-nearest neighbour derivative term (6.15). Fixing-χ is the Log-C (A.1.3) definition of the fields with symmetric derivative and exact exponentiation (A.2.3) for the gauge transformation matrix. Fixing-δ is the same as Fixing-χ but with the next-nearest neighbour derivative.

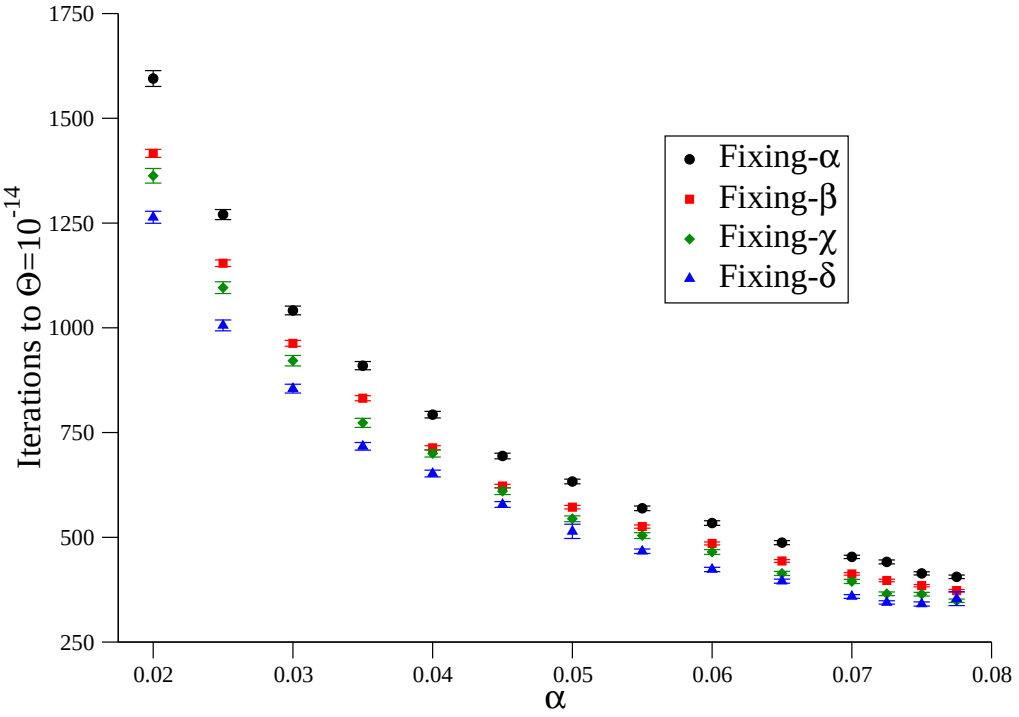

Figure 6.7 *The tuning parameter α, and the number of iterations to reach sufficient convergence $\Theta = 10^{-14}$ for a single $4^3 \times 8$, $\beta = 2.13$ $N_f = 2+1$ DWF ensemble, and a sample over 250 Gribov copies.*

Fig.6.7 shows the number of iterations required to reach sufficient convergence, for a test $4^3 \times 8$ ensemble. The level of theoretical improvement can be read from top to bottom. As can be seen, going to an all orders exponential and an exact field definition does speed up convergence compared to the standard procedure (Fixing-χ vs. Fixing-α), its average speed up over all of the α's is about 15%. If Fixing-χ takes less than 15% more time per iteration than Fixing-α then it would be pertinent to use the Log-C field definition in the gauge fixing, as long as the definition does not change the physics.

We will see in Chapter 3 that changing the gauge field definition amounts to a multiplicative renormalisation factor in the gluon fields for Landau gauge as was seen in [93, 108]. I investigate the cost of each fixing method by computing the time taken per iteration of the procedure as a percentage of the time taken for the Fixing-α procedure which is presumed fastest. The results are in Tab.6.1.

Tab.6.1 shows that although one can speed up the gauge fixing procedure by improving the field approximation, incorporating a higher order approximation to the derivative and exponentiation of the fields the methods' computational cost far outweighs their

Fixing	cost per iteration (%)	speed-up (%)
β	33	10
χ	363	15
δ	671	24

Table 6.1 *The computational cost of implementing several different Landau gauge fixing methods. The cost per iteration is as a percentage increase in the time taken for the routine compared to the Fixing-α method. The speed up is derived from Fig.6.7 as the percentage decrease in the number of iterations required to attain a fixed accuracy compared to the Fixing-α method.*

benefit if just being used to speed up the procedure.

6.8.1 Scaling with Volume

We have investigated the scaling of the gauge fixing procedure with and without Fourier Acceleration for the Fixing-α method, for fixed $\beta = 2.13$ and a wide range of lattice sizes from the very small $4^3 \times 8$ to the intermediate $16^3 \times 32$ and $24^3 \times 64$ and finally our largest, physical point ensemble (on this renormalisation trajectory) $48^3 \times 96$. We plot the logarithm of the number of iterations required to gauge fix to an accuracy of $\Theta = 10^{-14}$ versus the logarithm of the number of sites on the lattice. The results are shown in Fig.6.8.

Fig.6.8 illustrates the vast difference between Fourier accelerated Landau gauge fixing and the standard steepest descents approach. In both cases the number of iterations required to meet an acceptable accuracy grows as a power-law behaviour with the volume, because as the volume grows the degrees of freedom grows allowing for greater freedom in the algorithm and greater difficulty in converging to a minimum. It is surprising that the Fourier acceleration does a very good job of ameliorating critical slowing down considering it uses an Abelian approximation of the field content.

The least-squares fit results to the data are,

$$\begin{aligned} \log_{10}[Iterations(SD)] &= 1.9009 + 0.55778\ \log_{10}(V), \\ \log_{10}[Iterations(FA)] &= 1.6618 + 0.33096\ \log_{10}(V) \end{aligned} \tag{6.45}$$

We did not compute the number of iterations required for the un-accelerated algorithm for our largest volume ($48^3 \times 96$) because it was taking too long. We can use the fits to predict the result though and it gives an estimate of 660,479 iterations. If we compare this estimate to the number of iterations required for the Fourier accelerated algorithm

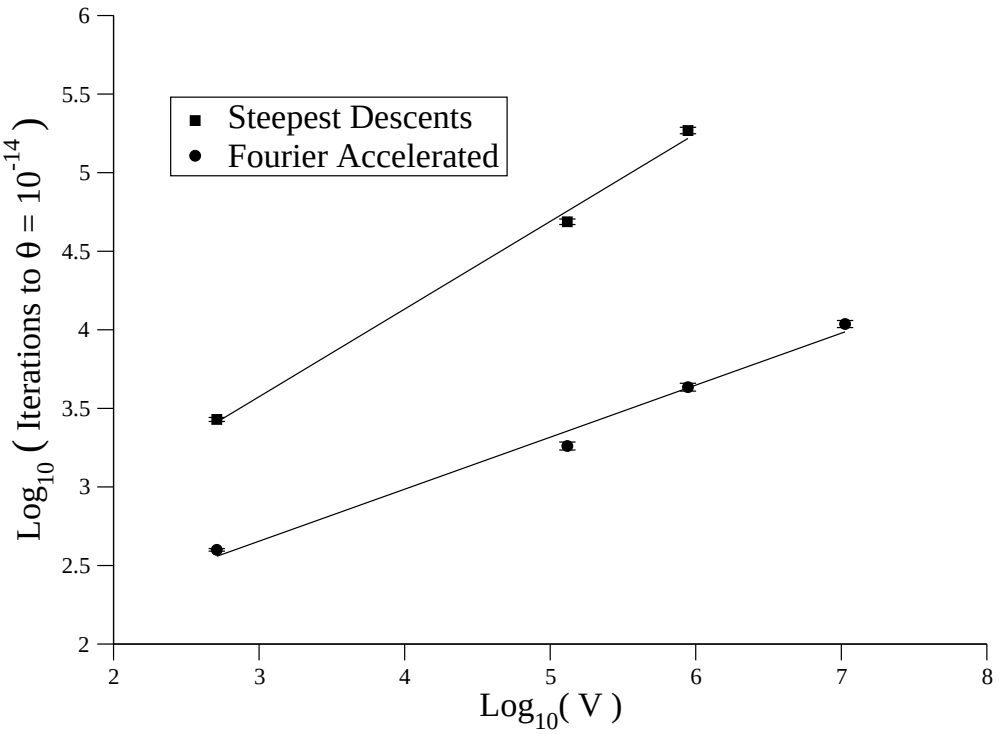

Figure 6.8 *The logarithm of the average number of iterations from 50 Gribov copies required to reach an accuracy of* 10^{-14}*, versus the logarithm of the number of lattice sites for fixed* β *for our Iwasaki gauge* $N_f = 2{+}1$ *DWF configurations and fixed tuning parameter* $\alpha = 0.08$*. Errors are from a Jackknife analysis and the straight lines are linear least squares fits.*

(10,900(600)) we are getting a 60× speed up (and even more for large volumes) with Fourier acceleration.

These measures are at a fixed β but dependence on the lattice spacing is benign. We could use our fits to predict the the number of iterations to gauge fix our largest $64^3 \times 128$ configuration. The predicted number for the steepest descents is 1,255,000. And for the Fourier accelerated 14,207, giving a projected speed up factor of 88. I have made many mild assumptions, including continual power law behaviour between these two measures at large volumes and that a Fourier acceleration step continues to be the same as the steepest descent step, this is clearly an approximation as the Fourier acceleration is the steepest descent with two Fourier transforms sandwiched in the middle.

The most time spent in this algorithm is in the gauge transformation step after each iteration, according to the profiler Callgrind [67], up to moderately large volumes ($24^3 \times 64$), and the Fourier Acceleration part of the iteration is nearly negligible. At some point the FFT's $O(V \log(V))$ behaviour will dominate, but we have not reached this region even on our largest lattices.

We have discussed in some detail some of the techniques to fix to a smooth covariant gauge on the lattice. We have introduced methods for classical improvement of the gauge fixing technique using exact logarithmic methods, improved derivatives and exact exponentiation, and we see that while these methods do allow for improvement in the convergence of the procedure they are computationally expensive. We have discussed the implementation of both Landau and Coulomb Fourier accelerated gauge fixing and seen that its ability to ameliorate critical slowing down is impressive, especially as the lattice volume is increased. We have illustrated that there is still some mild volume dependence in the procedure, and it is our opinion that comparisons at fixed accuracy and not at fixed number of iterations should be made when illustrating the properties of this algorithm.

In comparison to a naïve steepest descent (Los-Alamos) method of the Columbia Physics System (CPS) and fixing to Coulomb gauge for our largest $64^3 \times 128$ configuration, our implementation took ≈ 9 hours to fix to an accuracy of $\Theta = 10^{-14}$ on a 32-core AMD Opteron system, whereas the CPS implementation took four rack-days on the BlueGene/Q supercomputer at the Argonne National Research Facility.

Chapter 7

Conclusions

In this thesis we have discussed our implementation for fixing to a smooth covariant gauge, and discussed the method of Fourier acceleration. We have found that Fourier acceleration does a good job of ameliorating critical slowing down, but the algorithm still does scale with some small power of the lattice volume. Gauge fixing in lattice gauge theories is an important tool for the matching of lattice QCD measurements to perturbative physics and renormalising quantities non-perturbatively. For large volumes it can become performance critical.

We investigated procedures in the attempt to improve the gauge fixing algorithm. We found that upon applying higher order derivative terms and exact exponentiation in the steepest-descent method for the evaluation of the gauge transformation matrices was beneficial in reducing the average number of iterations to convergence of a configuration, although the computational effort required to use such improvements seemingly outweighed their benefits. In performing this evaluation we identified a method (the "exact Hermitian projection") for taking the logarithm of SU(2) and SU(3) matrices in a more efficient and numerically stable manner.

We applied the gauge fixing techniques to perform a first-principles measurement of the renormalised QCD strong coupling α_s using the amputated triple gluon vertex, without the benefit of our fast gauge fixing implementation we would not have been able to perform this calculation. We have called into question the validity of the measurement using the exceptional $\widetilde{\text{MOM}}$gg scheme, due to its amputation with a zero momentum gluon propagator. We believe such an amputation to have very large finite volume errors. This motivated us to perform the first computation of the non-exceptional

(MOMggg scheme) amputated triple gluon vertex coupling, with results,

$$\alpha_{nf=3}^{MOMggg}(3\ GeV) = 0.476(16)_{\rm stat}, \qquad \alpha_{nf=5}^{\overline{\rm MS}}(\rm M_Z) = 0.1273(9)_{\rm stat}(110)_{\rm pert}.$$

Even with the difficulties in locating sufficient momentum configurations satisfying the kinematic, at the scale 3 GeV our continuum extrapolated measurement has statistical error of 3%. Our evaluation (omitting systematic errors) of the nf=5 coupling in $\overline{\rm MS}$ at $\rm M_z$ is far from the world average of 0.1184(7) [27]. This is due to the low energy scale at which we are forced to perform our matching to continuum perturbation theory, and the low order of the series we can use to match our result to $\overline{\rm MS}$ with. We have performed the first measurement of the coupling for a non-SM theory, hence showing its applicability for possible BSM scenarios.

We have introduced the method of smearing and discussed its link with the Wilson flow. We have investigated the smearing radius for the first time using the non-perturbative ratio of Landau gauge fixed gluon propagators, and found values that are significantly lower than predicted by fat link perturbation theory. We have implemented a two-step adaptive routine for the numerical integration of the Wilson flow, and shown at large flow times it is far more performant than the fixed step-size integration usually used. The adaptive routine has shown that for aggressive gauge actions and smearing methods, much smaller step-sizes for integration accuracy $O\left(10^{-6}\right)$ are required than have been quoted in the literature [37, 120]. We have computed the continuum parameter W_0 from our ensembles,

$$W_0 = 0.1806(14)(fm), \qquad W_0(a) = 0.1806(14) - 0.0209(44)a^2.$$

We use the straight line extrapolation to compute the lattice spacing as if defined by the Pion, Kaon and Omega for our scaling trajectory using the fit results to evaluate a hitherto unknown lattice spacing of our ensembles. We used the adaptive Wilson flow to discuss fast lattice spacing evaluations in the context of step-scaling and the possibility of new simulation runs.

Our final topic was the evaluation of the SUSY-basis bag parameters B_i's and ratios R_i's renormalised non-perturbatively in the RI-MOM scheme and matched at 3 GeV in the continuum $\overline{\rm MS}$ scheme. Our evaluation is the first continuum limit of the full basis of (D=6) irrelevant operators with dynamical Domain Wall Fermions. We have computed the renormalised SM bag parameter $B_K^{\overline{\rm MS}}(3\ GeV) = 0.531(25)(4)$ (and the RGI bag parameter $\hat{B}_K(\mu = 3GeV) = 0.754(35)$)) and our result agrees within error of previous determinations [11]. Our final continuum extrapolated results are shown in Tab.5.9, and we see similarity with previous evaluations, and have inferred the areas where improvements to the method can be made.

Appendix A

Of matrices and their logarithms

Considering the parallel transport matrices of Eq.2.10, it is often the case that we want to perform operations on the underlying gluon field $A_\mu\left(x + a\frac{\hat{\mu}}{2}\right)$. This chapter discusses some of the various techniques available for approximating the logarithm of $SU(N_c)$ matrices and exponentiating the Lie fields back to $SU(N_c)$. The introduction of these methods is considered necessary for attempts to improve algorithms and techniques, such as those used in link smearing (Chapter 4 or gauge fixing (Chapter 6).

The techniques defined here will be of great importance for the following chapters on gauge fixing (Chapter 6), gluonic observables (Chapter 3) and link smearing (Chapter 4). I first discuss the technique for approximating the logarithm and finish with a discussion on exactly exponentiating the resulting Lie matrix.

A.1 Defining $A_\mu\left(x + a\frac{\hat{\mu}}{2}\right)$ from link variables

I discuss and compare several techniques for computing the logarithm (or an approximation thereof) of an arbitrary matrix $U \in SU(N_c)$, $U = e^{iA}$, $A \in \mathfrak{su}(N_c)$. I discuss two simple cases, SU(2) and SU(3). And try to make clear the extensions and possible difficulties with generalising the procedures to $SU(N_c)$ matrices.

A.1.1 Hermitian projection (Log-A)

Lattice gauge fields are often represented using the "Hermitian projection" or "linear definition", which is a sine approximation to the exact field. We call this "Log-A" for

disambiguation later.

$$A = \frac{1}{2i}\left(\left(U - U^\dagger\right) - \frac{1}{N_c}\mathrm{Tr}\left[U - U^\dagger\right] I_{N_c \times N_c} \right) + O(A^3). \tag{A.1}$$

Where $I_{N_c \times N_c}$ is the $N_c \times N_c$ identity matrix. In comparison to the lattice gauge links of Eq.2.10, we note that we have absorbed the factor ag_0 into the definition of $A_\mu\left(x + a\frac{\hat{\mu}}{2}\right)$ to make it dimensionless, this is commonplace in lattice calculations as in renormalised quantities such factors must cancel.

It should be clear that this Hermitian projection P (Eq.A.1) is a distributive function, i.e.

$$P(A + B) = P(A) + P(B). \tag{A.2}$$

In all of our computations we store the full $SU(N_c)$ matrix as a flat, one dimensional array in row major format in computer memory. Often I will discuss elements of our matrices in terms of the element index which I will indicate with a [.]. This storage procedure cuts down on the number of operations required for matrix addition and multiplication at the cost of computer memory[1].

Considering the access of the $N \times N$ matrix's (M) element, i,j where i is the column index and j is the row index. We can access this element using $M[i + j * N]$ for the linearised matrix array.

For SU(2) the Log-A (Eq.A.1) of the matrix $U = e^{iA}$ can be directly written as[2],

$$A = \begin{pmatrix} \Im(U[0]) & -iU[1] \\ A[1]^* & -A[0] \end{pmatrix}. \tag{A.3}$$

Where I have used the tracelessness and Hermiticity of the matrix A. As well as the SU(2) symmetry of the matrix U $U[1] - U[2]^* = 2U[1]$.

For SU(3) matrices, one can again use the symmetries of the problem to alleviate the number of operations. The Log-A of the matrix U in terms of its linearised matrix

[1] It is common to represent $SU(N_c)$ matrices without their final row, as it can be completed by the signed minors. For access to an element of the matrix on the bottom row, e.g. for matrix addition, the minor must be computed which requires more floating point operations. By storing the whole matrix we avoid this.

[2] Where I have assumed the procedure will be performed sequentially and the element A[0] will be computed before the element A[3].

indices which run from $0 \rightarrow 8$ inclusive in row-major order can be directly written as,

$$A = \begin{pmatrix} \frac{1}{3}\left(2\Im(U[0]) - \Im(U[4]) - \Im(U[8])\right) & \frac{1}{2i}\left(U[1] - U[3]^*\right) & \frac{1}{2i}\left(U[2] - U[6]^*\right) \\ A[1]^* & \frac{1}{3}\left(2\Im(U[4]) - \Im(U[0]) - \Im(U[8])\right) & \frac{1}{2i}\left(U[5] - U[7]^*\right) \\ A[2]^* & A[5]^* & -A[0] - A[4] \end{pmatrix}. \tag{A.4}$$

For generic $SU(N_c)$ matrices, the procedure should compute only the upper or lower triangular portion of A (we always use the upper) and fill in the rest by Hermiticity and tracelessness.

Log-A is computationally the fastest method to calculate the Lie matrices of U, but is inexact. The methods discussed in the following section are exact techniques to obtain the principle logarithm of the matrix.

A.1.2 The exact matrix logarithm (Log-B and Log-C)

The exact logarithm of U can be taken numerically either by diagonalisation (which a variant will be called Log-D), an iterative process as described in the appendix of [75], a rational approximation [86] or by specialised identities (which turn out to be much faster numerically). I now describe the procedure for taking the exact logarithm of $SU(3)$ and $SU(2)$ matrices, by first introducing a theorem.

Cayley Hamilton theorem

Cayley-Hamilton theorem states that "any matrix is a solution to its own characteristic equation" ($p(\lambda) = \det(U - \lambda I)$). Hence an N_c-dimensional square matrix will have at most only N_c elements in its Taylor-expansion,

$$U = e^{iA} = f_0 I_{N_c \times N_c} + f_1 A + ... + f_{N_c - 1} A^{N_c - 1}. \tag{A.5}$$

One can substitute for higher powers ($\geq N_c$) in the expansion with lower powers via the characteristic equation. All the information about the matrix is encapsulated in the f-constants, which are necessarily complex for $SU(N_c)$.

We can obtain the f-constants by considering the diagonalisation of A,

$$A = M \Lambda_A M^{-1}. \tag{A.6}$$

Where Λ_A is defined below, where the q_i's are the eigenvalues of A.

$$\Lambda_A = \begin{pmatrix} q_1 & 0 & 0 & \cdots & 0 \\ 0 & q_2 & 0 & \cdots & 0 \\ 0 & 0 & q_3 & \cdots & 0 \\ \cdots & \cdots & \cdots & \cdots & \cdots \\ 0 & 0 & 0 & \cdots & q_N \end{pmatrix}. \tag{A.7}$$

The matrix Λ_A can be written again as a Taylor expansion using the Cayley-Hamilton theorem,

$$e^{i\Lambda_A} = f_0 I_{N_c \times N_c} + f_1 \Lambda_A + ... + f_{N_c-1} \Lambda_A^{N_c-1}. \tag{A.8}$$

If we multiply by the same diagonalising matrices we obtain the equation for the Cayley-Hamilton theorem in Eq.A.5. The important point here is that the f-constants are exactly the same for both $e^{i\Lambda_A}$ and e^{iA}, if we know the eigenvalues $e^{iq_1}, e^{iq_2}, ..., e^{iq_N}$ we can calculate the f_i's and exponentiate the matrix A, or obtain the principle logarithm of the matrix e^{iA} if U is known. It is important to note that although in the discussion we have introduced the diagonalisation matrices, this method requires no explicit diagonalisation.

If we consider Eq.A.8, we see that it can be compactly expressed as a Vandermonde system.

$$\begin{pmatrix} 1 & q_1 & q_1^2 & \cdots & q_1^{N-1} \\ 1 & q_2 & q_2^2 & \cdots & q_2^{N-1} \\ 1 & q_3 & q_3^2 & \cdots & q_3^{N-1} \\ \cdots & \cdots & \cdots & \cdots & \cdots \\ 1 & q_N & q_N^2 & \cdots & q_N^{N-1} \end{pmatrix} \begin{pmatrix} f_0 \\ f_1 \\ f_2 \\ \cdots \\ f_{N-1} \end{pmatrix} = \begin{pmatrix} e^{iq_1} \\ e^{iq_2} \\ e^{iq_3} \\ \cdots \\ e^{iq_N} \end{pmatrix}. \tag{A.9}$$

The solution to this system of equations can either be calculated via a generic Vandermonde equation solver e.g.[96]. This is what we call "Log-B" or in the case of exponentiation the general Vandermonde method.

In the case of small, dense matrices the f_i's can be obtained from analytically smooth functions, which are more resistant to round-off errors. Using these for the logarithm is what we call "Log-C". We use these techniques instead of diagonalisation by an e.g LU decomposition because they are seen to be numerically stable and because they are not general they will be computationally faster.

A.1.3 Exact hermitian approximation (Log-C)

We can use Cayley-Hamilton theorem to compute the exact logarithm of matrices. A process we call the "exact hermitian projection" and label Log-C in the text. The procedure for two cases of interest, (SU(3) and SU(2) matrices) is detailed here, because only for SU(3) and SU(2) are these methods computationally competitive with iterative methods and more general techniques. The Log-B method uses the definition of the logarithm from this method, the only difference between the two is whether the f_i's are computed by analytically smooth functions or by the generic Vandermonde equation solver.

The SU(3) case

To compute the log of the matrix U using Matrix A.9, we must first calculate the eigenvalues of U, as they are the complex exponential of the eigenvalues of A.

Vieta's formula [153] for the characteristic equation of general 3×3 matrices (with eigenvalues q_i) is

$$\lambda^3 - (q_1 + q_2 + q_3)\lambda^2 + (q_1q_2 + q_1q_3 + q_2q_3)\lambda - (q_1q_2q_3) = 0. \tag{A.10}$$

And using the identities,

$$\mathrm{Tr}\left[U\right] = \sum_i q_i, \qquad \det\left(U\right) = \prod_i q_i, \qquad \mathrm{Tr}\left[U^{-1}\right] = \sum_i \frac{1}{q_i}. \tag{A.11}$$

We obtain the characteristic equation of an arbitrary 3×3 matrix U.

$$\lambda^3 - \mathrm{Tr}\left[U\right]\lambda^2 + \det\left(U\right)\mathrm{Tr}\left[U^{-1}\right]\lambda - \det\left(U\right) = 0. \tag{A.12}$$

Solving for λ yields the eigenvalues. This problem is a cubic equation which can be solved numerically using a numerically stable version of Cardano's method from [138], and when the matrix U is very close to the identity we switch to eigenvalue solutions for U-1, whose expressions are numerically better suited for small arguments [74] (we describe this method below). Restricting to SU(3) group, the determinant is guaranteed 1 and the trace of the inverse is the complex conjugate of the trace.

The solution we use for the roots of the SU(3) characteristic equation is based on the value of one variable,

$$a = \frac{1}{3}\mathrm{Tr}[U]. \tag{A.13}$$

If we then compute the variables Q and R,

$$\begin{aligned} S = (a^2 + a^*), \qquad R = a\left(S + \frac{a^*}{2}\right) - \frac{1}{2}, \\ T = R^2 - S^3. \end{aligned} \tag{A.14}$$

And then compute the variable t,

$$t = \begin{cases} \left(R + \sqrt{T}\right)^{1/3} ; \Re\left(T^*\sqrt{T}\right) > 0 \\ \left(R - \sqrt{T}\right)^{1/3} ; \Re\left(T^*\sqrt{T}\right) < 0 \end{cases}$$

Where the square root and cube-root can be computed by taking the first available root using de-Moivre's formula. We can then build the two variables P and M,

$$P = -t - \frac{S}{t}, \qquad M = \sqrt{3}\left(-t + \frac{S}{t}\right). \tag{A.15}$$

If t is exactly zero, $\frac{S}{t}$ is set to zero. We can immediately write down the eigenvalues,

$$\begin{aligned} q_0 &= P - a, \\ q_1 &= \frac{1}{2}(M - P) - a, \\ q_2 &= q_1 - M. \end{aligned} \tag{A.16}$$

This defines the round-off resistant form for solving the SU(3) characteristic equation. If a is very close to 1 (we use $1 - a < 10^{-12}$ and always work in double precision) all we need to do is switch the values of R and S to (these expressions are designed for $\mathrm{Tr}\,[U] \approx 3$)[74],

$$\begin{aligned} a &= 1 - \frac{1}{3}\mathrm{Tr}(U), \\ S = -(a^* + a(2 - a)) \qquad R &= \frac{3}{2}\left(a\left(1 - a^* - 2a\left(1 - \frac{a}{3}\right)\right) + a^*\right). \end{aligned} \tag{A.17}$$

Where I have written the polynomial in "a" using Horner's rule. The solution procedure for the eigenvalues is the same as before, but we need to add 1 to each eigenvalue at the end as we were solving for the eigenvalues of $U - I_{3\times3}$.

We now wish to compute the f_i's of Eq.A.5. Generically this is a case of solving an interpolating polynomial problem and a numerically fast algorithm is available from [96], but this is known to have numerical difficulties [138] especially when the eigenvalues of A become near-degenerate. The way around this is to compute the f_i's using the eigenvalues of A by taking the logarithm of the eigenvalues of U, for which there are smooth, numerically stable, standard methods which we borrow from the technique of exact exponentiation [129], which will be discussed in Sec.A.2.3.

Once the eigenvalues of U are computed their complex argument is taken to determine the eigenvalues of A. This is allowed because the eigenvalues of U are explicitly constrained to live on the circumference of the unit circle in the complex plane. We need not compute all 3 of the eigenvalues of U as the final one "q_3" is $(q_1 q_2)^*$.

If we consider Eq.A.8 for a generic SU(3) matrix and its conjugate transpose we obtain,

$$\begin{aligned} U &= f_0 I + f_1 A + f_2 A^2, \\ U^\dagger &= f_0^* I + f_1^* A^\dagger + f_2^* \left(A^\dagger\right)^2. \end{aligned} \tag{A.18}$$

We know that A is hermitian and so $\left(A^\dagger\right)^2 = A^2$ and so upon multiplying top and bottom lines by f_0^* and f_0 respectively and subtracting, we get,

$$f_2^* U - f_2 U^\dagger = (f_0 f_2^* - f_0^* f_2) + (f_1 f_2^* - f_1^* f_2) A, \tag{A.19}$$

which can be used to define the A matrix by,

$$A = \frac{f_2^* U - f_2 U^\dagger - \Im(f_0 f_2^*)}{\Im(f_1 f_2^*)}. \tag{A.20}$$

We have defined a method to exactly compute the logarithm for a generic $SU(3)$ matrix which does not need explicit diagonalisation and is observed to be numerically stable, as shown in the plots in Sec.A.1.5. This method was introduced because it allows for the taking of the logarithm without matrix multiplication and without iterative methods.

The SU(2) case

A generic SU(2) matrix "U" has the form,

$$U = \begin{pmatrix} a & b \\ -b^* & a^* \end{pmatrix}. \tag{A.21}$$

Which has characteristic equation,

$$\begin{aligned} \lambda^2 - \lambda(a^* + a) + (aa^* + bb^*) &= 0, \\ \lambda^2 - \lambda(\mathrm{Tr}\,[U]) + \det(U) &= 0. \end{aligned} \tag{A.22}$$

Which is just Vieta's formulae for 2x2 matrices. We know that for SU(2) the determinant is 1 and the combination $a^* + a$ is real, so solving the characteristic equation

we have,

$$q_{\pm} = \frac{2\Re\left(a\right) \pm \sqrt{4\Re\left(a\right)^2 - 4}}{2}. \tag{A.23}$$

We know that the rows and columns are normalised, so the quantity $\sqrt{4\Re\left(a\right)^2 - 4}$ is purely imaginary or 0. Taking the complex square root is expensive so we pull the complex part out,

$$q_{\pm} = \Re(a) \pm i\sqrt{(1 - \Re(a)^2)}. \tag{A.24}$$

And so we can solve the system from Matrix A.9 exactly. With solutions,

$$\begin{aligned} \theta &= \arg\left(q\right), \\ f_0 &= \cos(\theta) = \Re(q), \\ f_1 &= i\frac{\sin\left(\theta\right)}{\theta} = i\frac{\Im\left(q\right)}{\theta}. \end{aligned} \tag{A.25}$$

Some care is needed for the numerical stability of the parameter f_1 when q goes to 0 (this is the case when the matrix U approaches the identity), and a Taylor expansion of the sinc function is needed when q is below a small value (0.05 in practice is acceptable). Again, we can take the complex argument to get the eigenvalues of A, because the eigenvalues of U are on the unit circle in the complex plane. The only trigonometric function used in this definition is that of the "atan2" in the complex argument, so this routine is computationally fast.

Taking the logarithm is much simpler than the SU(3) case, and can be computed with,

$$\begin{aligned} U &= f_0 I_{2\times 2} + f_1 A, \\ A &= \frac{U - f_0 I_{2\times 2}}{f_1}. \end{aligned} \tag{A.26}$$

Both the SU(3) and SU(2) methods work well, but smooth analytic solutions for $N_c > 3$ for the f_i's are yet to be found, and the quintic polynomial does not have a direct solution for the analytic determination of the eigenvalues. Generic methods for the eigenvalues will have to be used for larger N_c.

A.1.4 Diagonalisation logarithm (Log-D)

The final logarithm method (Log-D), is based on diagonalisation and is taken from [75]. It is however, not based on generic LU decomposition as one would expect (as in practice these are observed to have numerical stability issues), but rather direct eigenvalue methods as the Log-B and Log-C. Its implementation for SU(3) and SU(2) shares a

lot of similarity to the Log-C method, as it uses direct solving of the characteristic equation. Its extension to generic $SU(N_c)$ with a generic eigen-solver is more tractable than Log-B and Log-C.

Any square matrix can be diagonalised as $U = V\Lambda_U V^{-1}$, and we know that $\Lambda_U = e^{i\Lambda_A}$. Upon taking the logarithm of the diagonal elements of Λ_U and multiplying back through by the diagonalisation matrices we obtain the matrix A.

What we require are the eigenvalues of U and the matrix V to perform this. The diagonalisation matrix V has the eigenvectors of U as its column entries. We find the eigenvectors by considering the eigenvalue problem (for eigenvalue q_i and eigenvectors v^i),

$$S^{(i)} = (U - q_i I_{N_c \times N_c}) \qquad S^{(i)} v^{(i)} = 0. \tag{A.27}$$

The matrix S is singular. If we take its Adjugate (or Classical Adjoint defined by the cofactor matrix built of the signed minors of U), and use the definition of the Adjugate of a matrix,

$$S^{(i)} adj\left(S^{(i)}\right) = \det\left(S^{(i)}\right) I. \tag{A.28}$$

We see that the Adjugate of S satifies the eigenvalue equation $S^{(i)} adj\left(S^{(i)}\right) = 0$, and we conclude that the non-zero column of the Adjugate matrix must be proportional to an eigenvector of the matrix U. In practice, we must normalise the resulting non-zero column to obtain the eigenvector for the eigenvalue "i".

We use the solutions for the characteristic equations outlined in Sec.A.1.3 to compute the eigenvalues, or a general method for $SU(N_c)$. We then compute the Adjugate of S for each eigenvalue to determine its corresponding eigenvector. We can then take the logarithm of our eigenvalues and multiply them through with the diagonalisation matrices with columns built from the eigenvectors to obtain the principal logarithm of U.

An issue with this method is that occasionally we end up on the wrong Riemann sheet for the logarithm [75], which is represented by the trace of Q ($Q = -i\log(U)$) being -2π or 2π. This is never the case for the Log-B and Log-C method. To remove this issue, we must add 2π to an eigenvalue if the trace is negative, and subtract 2π if it is positive, and re-perform the multiplication with the diagonalisation matrices. We do not need to recompute the diagonalisation matrix though, as it the same.

As an aside, the first matrix multiplication $\Lambda_A v^\dagger$ does not need to call a full matrix multiply method, as the result is the top row of $v^\dagger$ is multiplied by q_1 the second by q_2 and so on.

A.1.5 Comparison of the field definitions

If we take the exact Hermitian projection (Log-C, Eq.A.20), the Hermitian projection (Log-A, Eq.A.1) or directly solving the generic Vandermonde equation for the f_i's and using these for the logarithm evaluation defined in Log-C (Log-B, Eq.A.9), or by the diagonalisation (Log-D). Then use the technique of exact exponentiation from [129] (which is discussed in A.2.3), for Log-B,Log-C and Log-D one would expect that we should recover the same matrix that we started with up to round off errors, and naïvely expect a small difference for Log-A because it is only an $O(A^3)$ approximation to the logarithm of the link.

The way we test this is to compute,

$$\epsilon(x) = \frac{1}{N_d N_c^2} \sum_{\mu} \sum_{a=0}^{N_c^2-1} ||U[a]' - U[a]||, \tag{A.29}$$

where the prime denotes the logarithm and subsequent exponentiation. And the ||..|| denotes the complex absolute value and the "a" is a matrix element index.

Figs.A.1 and A.2 illustrate the invertibility (or lack thereof) of our four methods for determining the logarithm of our link matrices using the measure from Eq.A.29. The "diagonalisation logarithm" (Log-D) does a good job of providing an invertible map between the two procedures, the "exact Hermitian projection" (Log-C) analytical method within appreciable numerical tolerance appears to accurately represent the inverse of the exact exponentiation technique and is arguably more accurate than the Log-D. As seen by having a narrower histogram and smaller fluctuations (extrema). In Fig.A.1(e) the generic Vandermonde solver looks to be reproducing an invertible map, but on occasion suffers from sizable numerical instabilities seen in Fig.A.1(f), and the Hermitian projection (Log-A) method does not reproduce the original matrix at all under exact exponentiation.

Either Log-D or Log-C seem to be good candidates for an exact logarithm, with Log-C being a slightly more accurate determination. Log-B performs an accurate approximation but is unstable in its extreme cases, using generic Vandermonde methods for the calculation of the f constants is dangerous.

Table.A.1 shows our implementation speeds for the numerical matrix logarithms, normalised by the fastest method (Log-A) for SU(3) and SU(2), to illustrate the cost of these techniques. Generally, we see that as the complexity of the problem increases (N_c grows) the cost of performing the exact logarithm grows much faster than for taking the hermitian projection. For both SU(3) and SU(2) Log-B and Log-C are computationally cheaper to perform, this is due to not having to perform the diagonalisation and not

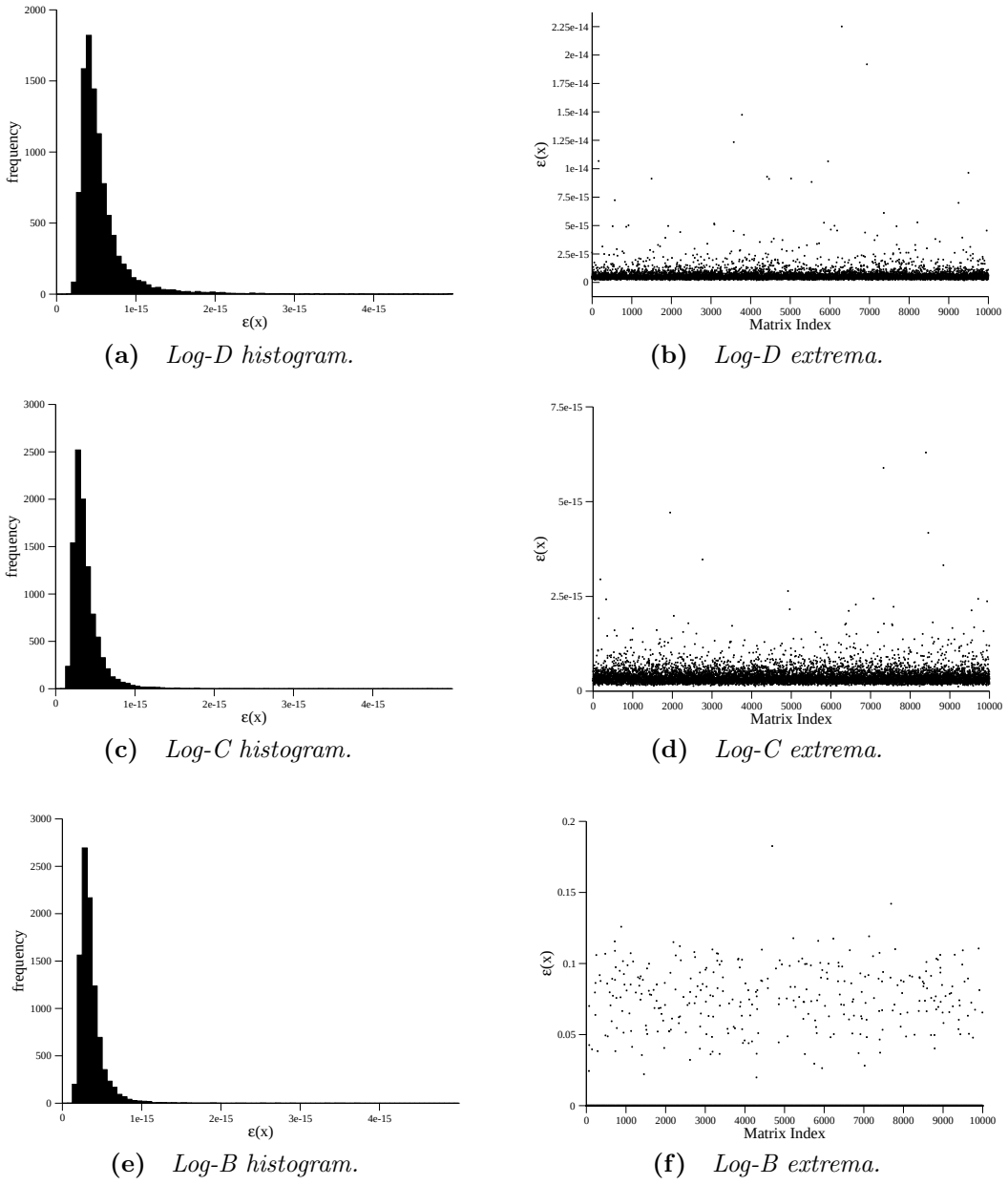

(a) *Log-D histogram.* **(b)** *Log-D extrema.*

(c) *Log-C histogram.* **(d)** *Log-C extrema.*

(e) *Log-B histogram.* **(f)** *Log-B extrema.*

Figure A.1 *Invertibility tests for various logarithm procedures, using Eq.A.29 and 40,000 random SU(3) matrices.*

having to re-perform operations depending on whether the output matrix is traceless. It could be surprising that the generic Vandermonde solver is almost twice as slow for SU(2) than the analytic solution, but this is due to the fast identities discussed earlier and the fact that calling a generic routine to solve a small, dense matrix problem is inherently costly.

From the information in Tab.A.1 and the invertibility graphs for SU(3) as shown in Fig.A.1, we choose to use the Log-C definition for the exact logarithm of the matrix for SU(3) and SU(2) because it is the fastest of the numerically stable techniques. To

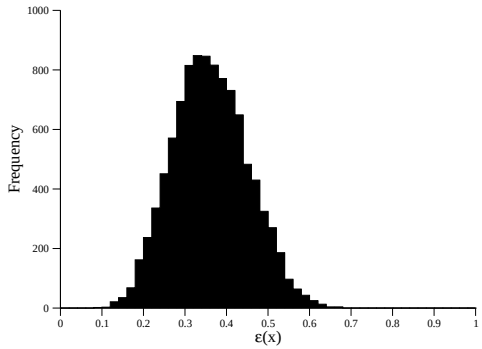

Figure A.2 *Invertibility of the Log-A procedure from 40,000 random SU(3) matrices using Eq.A.29.*

Logarithm definition	SU(3)	SU(2)
Log-A (hermitian projection)	1.0	1.0
Log-B (Vandermonde logarithm)	28.6(3)	17.0(3)
Log-C (exact hermitian projection)	29.2(3)	9.9(2)
Log-D (diagonalisation)	41.2(4)	22.7(4)

Table A.1 *The computational cost of logarithm definitions, normalised by the time taken for the Hermitian projection. Errors are from a jackknife analysis over 250 measurements of the time taken to take the logarithm of 525,000 random SU(3) and SU(2) matrices.*

our knowledge this is the first implementation of this method for taking the logarithm of these small, dense matrices.

A.2 Projection and exponentiation

I now move on to discuss the method for projecting general matrices to $SU(N_c)$, and Lie matrices by exponentiation. The first method is for arbitrary projection to $SU(N_c)$. The second method is for approximating the exponential for Lie matrices and the final is for computing the exact exponential for Lie matrices back into the group.

A.2.1 Projection to SU(N)

Projection of an arbitrary matrix V to $SU(N_c)$ is often performed by a trace maximisation routine [77], and fields which have been projected this way are not usable in the HMC field update [159] due to not having a smooth derivative. For the update

of a link variable it can be defined by the iterative procedure,

$$V = V\left(U'\right)^{\dagger}. \tag{A.30}$$

Where the matrix V is not $SU(N_c)$. The matrix $U' \in SU(N_c)$ is the matrix which maximises the trace of V. The replacement method is iterative and stops once the difference between successive traces has reached some tolerance (for single precision we use 10^{-6} and double precision 10^{-14}). If this method is being used in a projection for e.g. the APE smearing update, the original link matrix is replaced by U'.

The matrix U' is updated via successive SU(2), Cabbibo-Marinari [47] or (generalised for $SU(N_c)$ group) Givens rotations [96] via the procedure (where S_i is an SU(2) subgroup),

$$U' = S_i U'. \tag{A.31}$$

As a concrete example, for SU(3) the subgroup matrices are,

$$S_1 = \frac{1}{\sqrt{s_0 s_0^* + s_1 s_1^*}} \begin{pmatrix} s_0 & s_1 & 0 \\ -s_1 * & s_0^* & 0 \\ 0 & 0 & 1 \end{pmatrix}, S_2 = \frac{1}{\sqrt{s_0 s_0^* + s_1 s_1^*}} \begin{pmatrix} 1 & 0 & 0 \\ 0 & s_0 & s_1 \\ 0 & -s_1^* & s_0^* \end{pmatrix},$$

$$S_3 = \frac{1}{\sqrt{s_0 s_0^* + s_1 s_1^*}} \begin{pmatrix} s_0 & 0 & s_1 \\ 0 & 1 & 0 \\ s_1^* & 0 & s_0^* \end{pmatrix}.$$

Where the s_i's are built from (in terms of the linearised matrix indices $0 \to N_c^2 - 1$),

$$\begin{aligned} (S_1)\ s_0 &= V[0] + V[4]^* \qquad s_1 = V[1] - V[3]^*, \\ (S_2)\ s_0 &= V[4] + V[8]^* \qquad s_1 = V[5] - V[7]^*, \\ (S_3)\ s_0 &= V[0] + V[8]^* \qquad s_1 = V[2] - V[6]^*. \end{aligned} \tag{A.32}$$

Note that the V's on the second and third line of Eq.A.32 have been multiplied by the previous subgroup rotation due to Eq.A.31. As a speedup for SU(3), we see that there are many zeros in the rotation matrices and so we have hand-unrolled computations for the subgroup updates that implicitly do not compute multiplications with exact zeros (this meant a 2× speed up in the projection).

For generic $SU(N_c)$ this update requires the computation of the $N_c(N_c-1)/2$ rotation matrices. Otherwise the procedure is the same as SU(3). As N_c grows we have seen that this procedure requires more iterations to converge to an adequate solution, similar issues have been seen in the context of large N_c heat bath updates in [82]. As an aside, the matrix multiplication $U' = S_i U' \in SU(N_c)$, whereas the multiplication $V = V S_i^{\dagger}$ is

not. If one were to use group-specific matrix multiplies there is some speed up available in the first matrix multiply.

As the matrix multiplication of the rotation matrices only affects the same rows of the matrix we are multiplying (columns if performing the daggered operation) we have the following two functions to compute the SU(2) subgroup multiplications. Where the

Algorithm 4 *Computes* $U = S_i U$.

for $j = 0 \rightarrow N_c$ **do**
$U[N_c row(S_i[s_0]) + j] \leftarrow s_0 U[N_c row(S_i[s_0]) + j] + s_1 U[N_c row(S_i[s_1^*]) + j]$
$U[N_c row(S_i[s_1^*]) + j] \leftarrow -s_1^* U[N_c row(S_i[s_0]) + j] + s_0^* U[N_c row(S_i[s_1^*]) + j]$
end for

Algorithm 5 *Computes* $V = V S_i^\dagger$.

for $j = 0 \rightarrow N_c$ **do**
$V[col(S_i[s_0]) + jN_c] \leftarrow s_0^* V[col(S_i[s_0]) + jN_c] - s_1 V[col(S_i[s_1]) + jN_c]$
$V[col(S_i[s_1]) + jN_c] \leftarrow s_1^* V[col(S_i[s_0]) + jN_c] + s_0 V[col(S_i[s_1]) + jN_c]$
end for

functions *row* and *col* indicate which row or column index the element of the rotation matrix would have, the matrices are assumed to be stored in the usual row-major format and the element $S_i[s_1^*]$ is to be understood as the index of the matrix S_i for the element s_1^*. For instance $S_3[s_1^*]$ for SU(3) is the array element [6]. Upon using these functions instead of the general matrix multiplies we got a 10× speed up for our APE smearing procedure for SU(8).

A.2.2 Expansion and reunitarisation

The first method for exponentiating the Lie matrix A to SU(N) is a trivial Taylor expansion of the exponential in $U = e^{iA}$ and a reunitarisation. This method is used extensively in the gauge fixing procedure discussed in Chapter 6, where we wish to compute gauge transformation matrices of the form $g(x) = e^{i\partial_\mu A_\mu(x)}$. Considering our generic U matrix again, the technique is to compute,

$$U = 1 + iA + O(A^2). \tag{A.33}$$

And reunitarise. The method we choose for reunitarising the matrix (because it is the fastest) is to normalise a column or row of the matrix U (denoted u) in A.33, and compute the orthogonal column/row vector to that and normalise (denoted v). This gives us two columns/rows which are orthonormalised, and we can force the determinant to be unity by computing the signed conjugate minors of the two, i.e. the matrix

U in SU(3) can be considered as $U = (u, v, (u \times v)^*)$. As only one Gram-Schmidt orthonormalisation is needed for SU(3), numerical stability is not an issue. For $SU(N_c)$ a modified, stable Gram-Schmidt method is required [96].

This technique is not unique, and if being used to project gauge links, not gauge covariant. And so cannot be used in a smearing procedure where we are reunitarising the parallel transport matrix, which lies between sites. This technique is fine [62] for small perturbations of the gauge transformation matrices though, which live on the sites.

A.2.3 Exact exponentiation

As mentioned in Sec.A.1.2 by Cayley-Hamilton theorem, the exponential of an NxN, invertible matrix can be written as,

$$U = e^{iA} = f_0 I_{N_c \times N_c} + f_1 A + \cdots + f_{N_c-1} A^{N_c-1}.$$

And the f_i's can be found once the eigenvalues are known by solving the generic Vandermonde system (Eq.A.9).

For exponentiation, we solve for the eigenvalues of A to compute the f_i's, and use Eq.A.34 to compute the resulting matrix U. I will provide an example of the technique for SU(2), with Hermitian matrix A being exponentiated to $U \in SU(2)$, as the method for SU(3) is well described in the original paper [129].

The eigenvalues of $A \in \mathfrak{su}(2)$ are,

$$q_\pm = \pm\sqrt{\Re\left(A[0]\right)^2 + A[1]A[1]^*}. \tag{A.34}$$

The argument of the square root is real and positive. And hence so the eigenvalues are real. The f_i's are,

$$f_0 = cos(q), \qquad f_1 = i\frac{sin(q)}{q}. \tag{A.35}$$

Care must be taken when the values of z are small (this problem arises in SU(3) also [129]), and is alleviated by taking the Taylor expansion of the sinc function when $z < 0.0001$ (0.05 for SU(3)). If $z < 0.0001$, we use the form (polynomial expansion using Horner's rule),

$$f_1 = i\left(1 - \frac{q}{6}\left(1 - \frac{q}{20}\left(1 - \frac{q}{42}\right)\right)\right). \tag{A.36}$$

We are left with the resulting matrix for U,

$$\begin{pmatrix} f_0 + f_1 \Re\left(A[0]\right) & f_1 A[1] \\ f_1 A[1]^* & f_0 - f_1 \Re\left(A[0]\right) \end{pmatrix}.$$

Since f_0 is purely real and f_1 is purely imaginary we can readily see that $f_1 A[1]^* = -(f_1 A[1])^*$ and that $f_0 - f_1 \Re\left(A[0]\right) = (f_0 + f_1 \Re\left(A[0]\right))^*$, satisfying the SU(2) symmetry requirements.

For our implementation, because analytic expressions exist only for the exact exponentiation to SU(2) and SU(3) a more general method is required. For which we have two options. One is to compute the matrix exponential in a brute-force fashion by Taylor Series in A (for a more refined approach see the appendices in [75]), which is iterative and requires control over the convergence. Or we use a library such as Lapack [7] or GSL [88] to compute the Eigenvalues of the Hermitian matrix A and use the generic Vandermonde solver to compute the f_i's. Caution is necessary with this method though, because as we have seen from using the generic Vandermonde solver in the case for taking the Logarithm (Log-C) there are occasional large instabilities corresponding to close eigenvalues, and so this should only be used in a HMC update with vary careful error handling.

Appendix B

Renormalisation of operators

Unphysical quantities such as the Kaon bag parameter must be renormalised in some scheme using non-perturbative renormalisation before extrapolating the lattice spacing to 0. The method of renormalisation we use is called the Rome-Southampton regularisation invariant momentum scheme, or RI-MOM for short [124]. As we have seen previously in the context of gluonic non-perturbative renormalisation (Chapter 3), the general idea is to have a renormalisation factor $Z(\mu)$ that when multiplied with an amputated, non-perturbative vertex function in some amenable gauge (such as Landau) with sensible momentum transfer/renormalisation scale $p^2 = \mu^2$, is equal to its tree level continuum perturbative value. Again, with direct parallel to the gluonic measurement in Chapter 3, we must [23, 31] fix to Landau gauge to make a comparison to continuum perturbation theory.

The renormalisation of flavour non-singlet quark bilinears is simple, and will provide an illustrative example that can be utilised in the discussion of the renormalisation of the four quark operators.

The renormalised quark bilinear is related to the bare one by (with arbitrary Dirac matrix Γ),

$$[\bar{s}\Gamma d]_{\text{renormalised}} = Z_\Gamma(\mu)\,[\bar{s}\Gamma d]_{\text{bare}}\,. \tag{B.1}$$

We define the momentum-space propagators by taking the Fourier transform of Landau gauge fixed point source propagators,

$$S(x_0, p) = \sum_x e^{ip_\mu(x_\mu - x_0)} S(x; x_0). \tag{B.2}$$

The Fourier transform is over all dimensions. We then compute the vertex function,

$$V_\Gamma(p)_{\text{bare}} = S(x_0,p)\Gamma\left(\gamma_5 S(x_0,p)^\dagger\gamma_5\right). \tag{B.3}$$

The vertex function is finally amputated by the ensemble averages (denoted $\langle.\rangle$) of the quark propagator legs to give,

$$\Pi(p)_{\Gamma,\text{bare}} = \langle S(x_0,p)\rangle^{-1}\langle V_\Gamma(p)_{\text{bare}}\rangle\langle\gamma_5 S(x_0,p)^\dagger\gamma_5\rangle^{-1} \tag{B.4}$$

The amputated vertex function is projected so that,

$$\Lambda_{\Gamma,\text{bare}}(p) = \left[\Pi(p)_{\Gamma,\text{bare}}P_\Gamma(p)\right]. \tag{B.5}$$

P(p) is a projection operator designed to ensure the renormalisation condition,

$$\frac{Z_\Gamma(p)}{Z_q(p)}\Lambda_{\Gamma,\text{bare}}(p) = 1. \tag{B.6}$$

Where $Z_q(p)$ is the quark field renormalisation factor, which is defined from $q(x)_{\text{renormalised}} = \left(Z_q(\mu)\right)^{1/2} q(x)_{\text{bare}}$. Eq.B.6 allows for the computation of the renormalisation factor $Z_\Gamma(p)$. The extension to the renormalisation of bilinears, to that of the four quark operators follows similarly.

First, we define the renormalisation condition,

$$\frac{Z_{\Gamma\Gamma}(p)}{Z_q(p)^2}\Lambda_{\Gamma\Gamma,\text{bare}}(p) = 1. \tag{B.7}$$

Again Λ is the amputated, projected vertex function. We then define the momentum space vertex function for our operators,

$$V_{\Gamma\Gamma}(p)_{abcd} = \left[S(x_0,p)\Gamma\left(\gamma_5 S(x_0,p)^\dagger\gamma_5\right)\right]_{ab}\left[S(x_0,p)\Gamma\left(\gamma_5 S(x_0,p)^\dagger\gamma_5\right)\right]_{cd}. \tag{B.8}$$

Where the indices abcd are combined spin-color indices and so range from 1 to 12. We must contract the four legs of this vertex using the ensemble averaged inverse propagators,

$$\begin{aligned}\Pi_{\Gamma\Gamma}(p)_{efgh} = \langle S(x_0,p)\rangle^{-1}_{ea}\langle S(x_0,p)\rangle^{-1}_{fb}\left(V_{\Gamma\Gamma}(p)_{abcd}\right)\\ \times\langle\gamma_5 S(x_0,p)^\dagger\gamma_5\rangle^{-1}_{cg}\langle\gamma_5 S(x_0,p)^\dagger\gamma_5\rangle^{-1}_{dh}.\end{aligned} \tag{B.9}$$

The amputated vertex function for the four quark interpolating operators is based on the summation of its constituent vertex functions, i.e.

$$\Pi_{SS+PP}(p)_{efgh} = \Pi_{SS}(p)_{efgh} + \Pi_{PP}(p)_{efgh}. \tag{B.10}$$

Recalling from the introduction that four quark operator contractions have two separate contributing parts, the "trace" and the "trace-trace" (Eq.2.61). The renormalisation factor $\Lambda_{SS+PP}(p)$ is projected with,

$$\Lambda_{SS+PP}(p) = P_{efgh}(p)\left(\Pi_{SS+PP}(p)_{efgh} - \Pi_{SS+PP}(p)_{eghf}\right). \tag{B.11}$$

Where (although for the RI-MOM scheme there is no momentum dependence on the projector, it is possible to define schemes with momentum dependent projectors),

$$P_{efgh}(p) = \frac{1}{3072}\left(\delta_{ef}\delta_{gh} + (\gamma_5)_{ef}(\gamma_5)_{gh}\right). \tag{B.12}$$

We have the renormalisation condition for each operator,

$$\frac{Z_{\Gamma\Gamma+\Gamma'\Gamma'}(p)}{Z_q(p)^2}\Lambda_{\Gamma\Gamma+\Gamma'\Gamma'}(p) = 1. \tag{B.13}$$

For the normalisation of the bag-parameters, the B_i's are defined by the ratio of the four quark operator normalisation to the two correlators with appropriate normalisation. For $B_k = B_1$, the correlators in the denominator of Eq.5.21 under renormalisation pick up a factor of $\frac{Z_A^2}{Z_q^2}$ and for the B_i's a factor of $\frac{Z_P^2}{Z_q^2}$. The normalisation factors for the bag-parameters are then,

$$Z_{B_1} = \frac{Z_{VV+AA}}{Z_A^2} \qquad Z_{B_{2,3,4,5}} = \frac{Z_{2,3,4,5}}{Z_P^2}. \tag{B.14}$$

The renormalisation factors can be handily written as a matrix equation.

The renormalisation of the other higher dimensional operators follows from the above discussion, if chiral symmetry is broken then all of the operators in the renormalisation basis mix with one another under renormalisation. Otherwise, in the renormalisation basis for the massless theory the $VV + AA$ channel is a singlet (in the (27,1) representation) of the $SU(3)_L \otimes SU(3)_R$ flavour symmetry group for the valence quarks. The $VV - AA$ and $SS - PP$ mix as part of the $(6, \bar{6})$ representation and the $SS + PP$ and TT transform under the $(8, 8)$. The renormalisation matrix $Z_{ij}(\mu)^{RI-MOM}$, for the mixing of operators under renormalisation for valence quarks with chiral symmetry (Domain Wall or Overlap) should be block diagonal [17] up to discretisation effects (such as length of the fifth dimension for DWF),

$$\begin{bmatrix} Q_1 \\ Q_2 \\ Q_3 \\ Q_4 \\ Q_5 \end{bmatrix}_{\text{renormalised}} = \begin{bmatrix} Z_{11} & 0 & 0 & 0 & 0 \\ 0 & Z_{22} & Z_{23} & 0 & 0 \\ 0 & Z_{32} & Z_{33} & 0 & 0 \\ 0 & 0 & 0 & Z_{44} & Z_{45} \\ 0 & 0 & 0 & Z_{54} & Z_{55} \end{bmatrix} \begin{bmatrix} Q_1 \\ Q_2 \\ Q_3 \\ Q_4 \\ Q_5 \end{bmatrix}_{\text{bare}}. \tag{B.15}$$

The mixing matrix for the 1 loop matching to $\overline{\text{MS}}$ from the RI-MOM scheme in Landau gauge at some scale μ is [45],

$$
\begin{aligned}
Z_{11}^{\overline{\text{MS}}}(\mu) &= 1 - \alpha_s^{\overline{\text{MS}}}(\mu)\left\{(7 - 12\log(2))\left(1 - \frac{1}{N_c}\right)\right\}, \\
Z_{22}^{\overline{\text{MS}}}(\mu) &= 1 - \frac{\alpha_s^{\overline{\text{MS}}}(\mu)}{4\pi}\left\{\frac{1}{N_c}(1 + \log(2))\right\}, \\
Z_{23}^{\overline{\text{MS}}}(\mu) &= -\frac{\alpha_s^{\overline{\text{MS}}}(\mu)}{4\pi}\left\{4(1 + \log(2))\right\}, \\
Z_{32}^{\overline{\text{MS}}}(\mu) &= -\frac{\alpha_s^{\overline{\text{MS}}}(\mu)}{4\pi}\left\{\log(2) - 1\right\}, \\
Z_{33}^{\overline{\text{MS}}}(\mu) &= 1 - \frac{\alpha_s^{\overline{\text{MS}}}(\mu)}{4\pi}\left\{\frac{2}{N_c}(1 + \log(2)) - 4N_c\right\}, \\
Z_{44}^{\overline{\text{MS}}}(\mu) &= 1 - \frac{\alpha_s^{\overline{\text{MS}}}(\mu)}{4\pi}\left\{7 + \frac{1}{N_c}(5 + 2\log(2)) - 4(N_c + \log(2))\right\}, \\
Z_{45}^{\overline{\text{MS}}}(\mu) &= -\frac{\alpha_s^{\overline{\text{MS}}}(\mu)}{4\pi}\left\{2\left(\frac{1}{12}\left(5 - \frac{13}{N_c}\right) - \frac{\log(2)}{3}\left(2 + \frac{5}{N_c}\right)\right)\right\}, \\
Z_{54}^{\overline{\text{MS}}}(\mu) &= -\frac{\alpha_s^{\overline{\text{MS}}}(\mu)}{4\pi}\left\{\frac{1}{2}\left(4(1 - 8\log(2)) - \frac{12}{N_c}(1 - 5\log(2))\right)\right\}, \\
Z_{55}^{\overline{\text{MS}}}(\mu) &= 1 - \frac{\alpha_s^{\overline{\text{MS}}}(\mu)}{4\pi}\left\{\frac{7}{3}(1 - 4\log(2)) - \frac{1}{3N_c}(5 - 26\log(2))\right\}.
\end{aligned}
\tag{B.16}
$$

For our study we use the value of the coupling $\alpha(Mz)^{\overline{\text{MS}}} = 0.1184$ and numerically run 3.2 using the four loop beta function [140], and using appropriate threshold matching to obtain the three flavour $\overline{\text{MS}}$ strong coupling at 3 GeV, which will be our renormalisation scale. We measure our operators Q_k^{bare} from our simulation and renormalise to continuum $\overline{\text{MS}}$ with,

$$
Q_i^{\overline{\text{MS}}}(\mu) = Z_{ij}^{\overline{\text{MS}}}(\mu) Z_{jk}^{\text{RI-MOM}}(\mu) Q_k^{\text{bare}}. \tag{B.17}
$$

Where in practice, we perform the matrix multiplication between the non-perturbative renormalisation and the continuum perturbative matching implicitly.

Bibliography

[1] Albanese, M., et al. "Glueball Masses and String Tension in Lattice QCD." *Phys.Lett.* B192: (1987) 163–169.

[2] Alexandrou, C., P. de Forcrand, and E. Follana. "Gluon propagator without lattice Gribov copies." *Phys. Rev. D* 63: (2001) 094,504. `http://link.aps.org/doi/10.1103/PhysRevD.63.094504`.

[3] Allés, B., D. S. Henty, H. Panagopoulos, C. Parrinello, C. Pittori, and D. G. Richards. "α_s from the non-perturbatively renormalised lattice three-gluon vertex." *Nuclear Physics B* 502: (1997) 325–342.

[4] Allton, C., et al. "Physical Results from 2+1 Flavor Domain Wall QCD and SU(2) Chiral Perturbation Theory." *Phys.Rev.* D78: (2008) 114,509.

[5] Allton, C., L. Conti, A. Donini, V. Gimenez, L. Giusti, et al. "B parameters for Delta S = 2 supersymmetric operators." *Phys.Lett.* B453: (1999) 30–39.

[6] Altarelli, G. "The QCD Running Coupling and its Measurement." *PoS* Corfu2012: (2013) 002.

[7] Anderson, E., Z. Bai, J. Dongarra, A. Greenbaum, A. McKenney, J. Du Croz, S. Hammerling, J. Demmel, C. Bischof, and D. Sorensen. "LAPACK: a portable linear algebra library for high-performance computers." In *Proceedings of the 1990 ACM/IEEE conference on Supercomputing*. Los Alamitos, CA, USA: IEEE Computer Society Press, 1990, Supercomputing '90, 2–11.

[8] Antonio, D. J., et al. "Localization and chiral symmetry in three flavor domain wall QCD." *Phys.Rev.* D77: (2008) 014,509.

[9] Antonio, D., et al. "First results from 2+1 Flavor Domain Wall QCD: Mass Spectrum, Topology Change and Chiral Symmetry with L(s) = 8." *Phys.Rev.* D75: (2007) 114,501.

[10] Aoki, S., and Y. Taniguchi. "One loop renormalization for the axial Ward-Takahashi identity in domain wall QCD." *Phys.Rev.* D59: (1999) 094,506.

[11] Aoki, Y., R. Arthur, T. Blum, P. Boyle, D. Brommel, et al. "Continuum Limit of B_K from 2+1 Flavor Domain Wall QCD." *Phys.Rev.* D84: (2011) 014,503.

[12] Aoki, Y., T. Blum, N. Christ, C. Cristian, C. Dawson, et al. "Domain wall fermions with improved gauge actions." *Phys.Rev.* D69: (2004) 074,504.

[13] Aoki, Y., P. Boyle, N. Christ, C. Dawson, M. Donnellan, et al. "Non-perturbative renormalization of quark bilinear operators and B(K) using domain wall fermions." *Phys.Rev.* D78: (2008) 054,510.

[14] Aoki, Y., et al. "Continuum Limit Physics from 2+1 Flavor Domain Wall QCD." *Phys.Rev.* D83: (2011) 074,508.

[15] Arthur, R. personal communication, 2012.

[16] Arthur, R., and P. Boyle. "Step Scaling with off-shell renormalisation." *Phys.Rev.* D83: (2011) 114,511.

[17] Arthur, R., P. Boyle, N. Garron, C. Kelly, and A. Lytle. "Opening the Rome-Southampton window for operator mixing matrices." *Phys.Rev.* D85: (2012) 014,501.

[18] Arthur, R., P. Boyle, S. Hashimoto, and R. Hudspith. "A note on Rome-Southampton Renormalization with Smeared Gauge Fields." .

[19] Arthur, R., et al. "Domain Wall QCD with Near-Physical Pions." .

[20] Atiyah, M. F., and I. M. Singer. "The index of elliptic operators on compact manifolds." *Bull. Amer. Math. Soc.* 69: (1963) 422–433.

[21] Babich, R., N. Garron, C. Hoelbling, J. Howard, L. Lellouch, et al. "K0 - anti-0 mixing beyond the standard model and CP-violating electroweak penguins in quenched QCD with exact chiral symmetry." *Phys.Rev.* D74: (2006) 073,009.

[22] Bailey, J. A., T. Bae, Y.-C. Jang, H. Jeong, C. Jung, et al. "Beyond the Standard Model corrections to $K^0 - \bar{K}^0$ mixing." *PoS* LATTICE2012: (2012) 107.

[23] Becirevic, D., and G. Villadoro. "Remarks on the hadronic matrix elements relevant to the SUSY K0 - anti-K0 mixing amplitude." *Phys.Rev.* D70: (2004) 094,036.

[24] Beringer, J., et al. "Review of Particle Physics (RPP)." *Phys.Rev.* D86: (2012) 010,001.

[25] Bernard, C. W., and T. A. DeGrand. "Perturbation theory for fat link fermion actions." *Nucl.Phys.Proc.Suppl.* 83: (2000) 845–847.

[26] Bertone, V., et al. "Kaon Mixing Beyond the SM from Nf=2 tmQCD and model independent constraints from the UTA." *JHEP* 1303: (2013) 089.

[27] Bethke, S. "World Summary of α_s (2012)." *Nucl.Phys.Proc.Suppl.* 234: (2013) 229–234.

[28] Bilson-Thompson, S. O., D. B. Leinweber, and A. G. Williams. "Highly improved lattice field strength tensor." *Annals Phys.* 304: (2003) 1–21.

[29] Blossier, B., P. Boucaud, M. Brinet, F. De Soto, X. Du, et al. "Lattice measurement of α_s with a realistic charm quark." *Nucl.Phys.Proc.Suppl.* 234: (2013) 217–220.

[30] Blum, T., P. Chen, N. H. Christ, C. Cristian, C. Dawson, et al. "Quenched lattice QCD with domain wall fermions and the chiral limit." *Phys.Rev.* D69: (2004) 074,502.

[31] Blum, T., N. Christ, C. Cristian, C. Dawson, G. Fleming, G. Liu, R. Mawhinney, A. Soni, P. Vranas, M. Wingate, L. Wu, and Y. Zhestkov. "Nonperturbative renormalization of domain wall fermions: Quark bilinears." *Phys. Rev. D* 66: (2002) 014,504. `http://link.aps.org/doi/10.1103/PhysRevD.66.014504`.

[32] Blum, T., and A. Soni. "Domain wall quarks and kaon weak matrix elements." *Phys.Rev.Lett.* 79: (1997) 3595–3598.

[33] Bogolubsky, I., V. Bornyakov, G. Burgio, E. Ilgenfritz, M. Muller-Preussker, et al. "Improved Landau gauge fixing and the suppression of finite-volume effects of the lattice gluon propagator." *Phys.Rev.* D77: (2008) 014,504.

[34] Bona, M., et al. "Model-independent constraints on Δ F=2 operators and the scale of new physics." *JHEP* 0803: (2008) 049.

[35] Bonnet, F. D., P. O. Bowman, D. B. Leinweber, A. G. Williams, and J. M. Zanotti. "Infinite volume and continuum limits of the Landau gauge gluon propagator." *Phys.Rev.* D64: (2001) 034,501.

[36] Bonnet, F. D., D. B. Leinweber, A. G. Williams, and J. M. Zanotti. "Improved smoothing algorithms for lattice gauge theory." *Phys.Rev.* D65: (2002) 114,510.

[37] Borsanyi, S., S. Durr, Z. Fodor, C. Hoelbling, S. D. Katz, et al. "High-precision scale setting in lattice QCD." *JHEP* 1209: (2012) 010.

[38] Boucaud, P., G. Burgio, F. Di Renzo, J. Leroy, J. Micheli, et al. "Lattice calculation of 1 / p**2 corrections to alpha(s) and of Lambda(QCD) in the MOM scheme." *JHEP* 0004: (2000) 006.

[39] Boucaud, P., F. De Soto, A. Le Yaouanc, J. Leroy, J. Micheli, et al. "The Strong coupling constant at small momentum as an instanton detector." *JHEP* 0304: (2003) 005.

[40] Boucaud, P., A. Le Yaouanc, J. Leroy, J. Micheli, O. Pene, et al. "Testing Landau gauge OPE on the lattice with a $\langle A*A2\rangle$ condensate." *Phys.Rev.* D63: (2001) 114,003.

[41] Boucaud, P., J. P. Leroy, J. Micheli, O. Pene, and C. Roiesnel. "Lattice calculation of alpha(s) in momentum scheme." *JHEP* 10: (1998) 017.

[42] Boucaud, P., J. Leroy, H. Moutarde, J. Micheli, O. Pene, et al. "Preliminary calculation of alpha(s) from Green functions with dynamical quarks." *JHEP* 0201: (2002) 046.

[43] Boyle, P., N. Garron, and R. Hudspith. "Neutral kaon mixing beyond the standard model with $n_f = 2+1$ chiral fermions." *Phys.Rev.* D86: (2012) 054,028.

[44] Buras, A. J. "Weak Hamiltonian, CP violation and rare decays." 281–539.

[45] Buras, A. J., M. Misiak, and J. Urban. "Two loop QCD anomalous dimensions of flavor changing four quark operators within and beyond the standard model." *Nucl.Phys.* B586: (2000) 397–426.

[46] Burgio, G., M. Quandt, and H. Reinhardt. "Coulomb gauge gluon propagator and the Gribov formula." *Phys.Rev.Lett.* 102: (2009) 032,002.

[47] Cabibbo, N., and E. Marinari. "A New Method for Updating SU(N) Matrices in Computer Simulations of Gauge Theories." *Phys.Lett.* B119: (1982) 387–390.

[48] Cabibbo, N. "Unitary Symmetry and Leptonic Decays." *Phys.Rev.Lett.* 10: (1963) 531–533.

[49] Callan, J., Curtis G., and J. A. Harvey. "Anomalies and Fermion Zero Modes on Strings and Domain Walls." *Nucl.Phys.* B250: (1985) 427.

[50] Capitani, S., S. Durr, and C. Hoelbling. "Rationale for UV-filtered clover fermions." *JHEP* 0611: (2006) 028.

[51] Chetyrkin, K. G., and A. Retey. "Three-loop three-linear vertices and four-loop MOM beta functions in massless QCD." .

[52] Chetyrkin, K., B. A. Kniehl, and M. Steinhauser. "Strong coupling constant with flavor thresholds at four loops in the MS scheme." *Phys.Rev.Lett.* 79: (1997) 2184–2187.

[53] Chetyrkin, K., J. H. Kuhn, and M. Steinhauser. "RunDec: A Mathematica package for running and decoupling of the strong coupling and quark masses." *Comput.Phys.Commun.* 133: (2000) 43–65.

[54] Christenson, J. H., J. W. Cronin, V. L. Fitch, and R. Turlay. "Evidence for the 2π Decay of the K_2^0 Meson." *Phys. Rev. Lett.* 13: (1964) 138–140.

[55] Ciuchini, M., E. Franco, G. Martinelli, and L. Reina. "The S = 1 effective hamiltonian including next-to-leading order {QCD} and {QED} corrections." *Nuclear Physics B* 415, 2: (1994) 403 – 459. `http://www.sciencedirect.com/science/article/pii/055032139490118X`.

[56] Ciuchini, M., V. Lubicz, L. Conti, A. Vladikas, A. Donini, et al. "Delta M(K) and epsilon(K) in SUSY at the next-to-leading order." *JHEP* 9810: (1998) 008.

[57] Clark, M., and A. Kennedy. "Accelerating dynamical fermion computations using the rational hybrid Monte Carlo (RHMC) algorithm with multiple pseudofermion fields." *Phys.Rev.Lett.* 98: (2007) 051,601.

[58] Cucchieri, A., and T. Mendes. "Constraints on the IR behavior of the gluon propagator in Yang-Mills theories." *Phys.Rev.Lett.* 100: (2008) 241,601.

[59] Cucchieri, A., and D. Zwanziger. "Numerical study of gluon propagator and confinement scenario in minimal Coulomb gauge." *Phys.Rev.* D65: (2001) 014,001.

[60] Curci, G., P. Menotti, and G. Paffuti. "SYMANZIK'S IMPROVED LAGRANGIAN FOR LATTICE GAUGE THEORY." *Phys.Lett.* B130: (1983) 205.

[61] Dagotto, E., A. Kocic, and J. Kogut. "FINITE SIZE, FERMION MASS AND N(f) SYSTEMATICS IN COMPUTER SIMULATIONS OF QUANTUM ELECTRODYNAMICS." *Nucl.Phys.* B331: (1990) 500–514.

[62] Davies, C. T. H., G. G. Batrouni, G. R. Katz, A. S. Kronfeld, G. P. Lepage, K. G. Wilson, P. Rossi, and B. Svetitsky. "Fourier acceleration in lattice gauge theories. I. Landau gauge fixing." *Phys. Rev. D* 37, 6: (1988) 1581–1588.

[63] DeGrand, T., and C. DeTard. *Lattice Methods for Quantum Chromodynamics*. World Scientific Publishing Company Incorporated, 2006. `http://books.google.co.uk/books?id=V48ddclvbioC`.

[64] Del Debbio, L., A. Patella, and C. Pica. "Higher representations on the lattice: Numerical simulations, SU(2) with adjoint fermions." *Phys. Rev. D* 81: (2010) 094,503. `http://link.aps.org/doi/10.1103/PhysRevD.81.094503`.

[65] Della Morte, M., et al. "Computation of the strong coupling in QCD with two dynamical flavors." *Nucl.Phys.* B713: (2005) 378–406.

[66] Deuzeman, A., and U. Wenger. "Gradient flow and scale setting for twisted mass fermions." *PoS* LATTICE2012: (2012) 162.

[67] Developers, V. "Callgrind Manual." http://valgrind.org/docs/manual/cl-manual.html, Accessed June 2012.

[68] Dietrich, D. D., and F. Sannino. "Conformal window of SU(N) gauge theories with fermions in higher dimensional representations." *Phys.Rev.* D75: (2007) 085,018.

[69] de Divitiis, G., R. Petronzio, and N. Tantalo. "On the discretization of physical momenta in lattice QCD." *Phys.Lett.* B595: (2004) 408–413.

[70] Donini, A., V. Gimenez, L. Giusti, and G. Martinelli. "Renormalization group invariant matrix elements of Delta S = 2 and Delta I = 3/2 four fermion operators without quark masses." *Phys.Lett.* B470: (1999) 233–242.

[71] Duane, S., A. Kennedy, B. Pendleton, and D. Roweth. "Hybrid Monte Carlo." *Phys.Lett.* B195: (1987) 216–222.

[72] Duncan, A., E. Eichten, and H. Thacker. "Electromagnetic splittings and light quark masses in lattice QCD." *Phys.Rev.Lett.* 76: (1996) 3894–3897.

[73] Durr, S., Z. Fodor, C. Hoelbling, S. Katz, S. Krieg, et al. "Lattice QCD at the physical point: Simulation and analysis details." *JHEP* 1108: (2011) 148.

[74] Durr, S. "Gauge action improvement and smearing." *Comput.Phys.Commun.* 172: (2005) 163–186.

[75] ———. "Logarithmic link smearing for full QCD." *Comput.Phys.Commun.* 180: (2009) 1338–1357.

[76] Edwards, R., U. M. Heller, and T. Klassen. "Accurate scale determinations for the Wilson gauge action." *Nucl.Phys.* B517: (1998) 377–392.

[77] Edwards, R. G., and B. Joo. "The Chroma software system for lattice QCD." *Nucl.Phys.Proc.Suppl.* 140: (2005) 832.

[78] Efron, B. *The Jackknife, the Bootstrap, and Other Resampling Plans*. CBMS-NSF regional conference series in applied mathematics. Society for Industrial and Applied Mathematics (SIAM, 3600 Market Street, Floor 6, Philadelphia, PA 19104), 1982. `http://books.google.co.uk/books?id=RY_m7GKbnhkC`.

[79] Falcioni, M., M. Paciello, G. Parisi, and B. Taglienti. "AGAIN ON SU(3) GLUEBALL MASS." *Nucl.Phys.* B251: (1985) 624–632.

[80] Follana, E., et al. "Highly improved staggered quarks on the lattice, with applications to charm physics." *Phys.Rev.* D75: (2007) 054,502.

[81] de Forcrand, P., M. Garcia Perez, and I.-O. Stamatescu. "Improved cooling algorithm for gauge theories." *Nucl.Phys.Proc.Suppl.* 47: (1996) 777–780.

[82] de Forcrand, P., and O. Jahn. "Monte Carlo overrelaxation for SU(N) gauge theories." 67–73.

[83] Frezzotti, R., P. A. Grassi, S. Sint, and P. Weisz. "Lattice QCD with a chirally twisted mass term." *JHEP* 0108: (2001) 058.

[84] Frigo, M., and S. G. Johnson. "The Design and Implementation of FFTW3." *Proceedings of the IEEE* 93, 2: (2005) 216–231. Special issue on "Program Generation, Optimization, and Platform Adaptation".

[85] Furman, V., and Y. Shamir. "Axial symmetries in lattice QCD with Kaplan fermions." *Nucl.Phys.* B439: (1995) 54–78.

[86] Furui, S., and H. Nakajima. "Infrared features of unquenched Lattice Landau Gauge QCD." *Few Body Syst.* 40: (2006) 101–128.

[87] Gabbiani, F., E. Gabrielli, A. Masiero, and L. Silvestrini. "A Complete analysis of FCNC and CP constraints in general SUSY extensions of the standard model." *Nucl.Phys.* B477: (1996) 321–352.

[88] Galassi, M., J. Davies, J. Theiler, B. Gough, G. Jungman, M. Booth, and F. Rossi. *Gnu Scientific Library: Reference Manual*. Network Theory Ltd., 2003.

[89] Garcia Perez, M., A. Gonzalez-Arroyo, J. R. Snippe, and P. van Baal. "Instantons from over - improved cooling." *Nucl.Phys.* B413: (1994) 535–552.

[90] Gattringer, C., and C. Lang. *Quantum Chromodynamics on the Lattice: An Introductory Presentation*. Lecture Notes in Physics. Springer, 2009. `http://books.google.co.uk/books?id=l2hZKnlYDxoC`.

[91] Ginsparg, P. H., and K. G. Wilson. "A Remnant of Chiral Symmetry on the Lattice." *Phys.Rev.* D25: (1982) 2649.

[92] Giusti, L., M. Paciello, C. Parrinello, S. Petrarca, and B. Taglienti. "Problems on lattice gauge fixing." *Int.J.Mod.Phys.* A16: (2001) 3487–3534.

[93] Giusti, L., M. Paciello, S. Petrarca, B. Taglienti, and M. Testa. "On the definition of gauge field operators in lattice gauge fixed theories." *Phys.Lett.* B432: (1998) 196–202.

[94] Giusti, L., and A. Vladikas. "RI / MOM renormalization window and Goldstone pole contamination." *Phys.Lett.* B488: (2000) 303–312.

[95] Gockeler, M., R. Horsley, H. Oelrich, H. Perlt, D. Petters, et al. "Nonperturbative renormalization of composite operators in lattice QCD." *Nucl.Phys.* B544: (1999) 699–733.

[96] Golub, G. H., and C. F. Van Loan. *Matrix computations (3rd ed.)*. Baltimore, MD, USA: Johns Hopkins University Press, 1996.

[97] Gottlieb, S., W. Liu, D. Toussaint, R. L. Renken, and R. L. Sugar. "Hybrid-molecular-dynamics algorithms for the numerical simulation of quantum chromodynamics." *Phys. Rev. D* 35: (1987) 2531–2542. `http://link.aps.org/doi/10.1103/PhysRevD.35.2531`.

[98] Gracey, J. A. "Two loop QCD vertices at the symmetric point." *Phys. Rev. D* 84: (2011) 085,011. `http://link.aps.org/doi/10.1103/PhysRevD.84.085011`.

[99] Gracey, J. "Power corrections to symmetric point vertices in Gribov-Zwanziger theory." *Phys.Rev.* D86: (2012) 105,029.

[100] Gribov, V. "Quantization of Nonabelian Gauge Theories." *Nucl.Phys.* B139: (1978) 1.

[101] Gross, D., and F. Wilczek. "Asymptotically Free Gauge Theories. 1." *Phys.Rev.* D8: (1973) 3633–3652.

[102] Gupta, R., G. Guralnik, G. Kilcup, A. Patel, S. R. Sharpe, et al. "THE HADRON SPECTRUM ON A 18**3 x 42 LATTICE." *Phys.Rev.* D36: (1987) 2813.

[103] Hasenfratz, A., and F. Knechtli. "Flavor symmetry and the static potential with hypercubic blocking." *Phys.Rev.* D64: (2001) 034,504.

[104] Hausdorff, F. *Die symbolische Exponentialformel in der Gruppentheorie*, Ber Verh Saechs Akad Wiss Leipzig, 1906, volume 58, 19–49.

[105] Herrlich, S., and U. Nierste. "The Complete —delta S— = 2 - Hamiltonian in the next-to-leading order." *Nucl.Phys.* B476: (1996) 27–88.

[106] Hetrick, J., and P. de Forcrand. "Smeared gauge fixing." *Nucl.Phys.Proc.Suppl.* 63: (1998) 838–840.

[107] Ilgenfritz, E.-M., M. Laursen, G. Schierholz, M. Muller-Preussker, and H. Schiller. "First Evidence for the Existence of Instantons in the Quantized SU(2) Lattice Vacuum." *Nucl.Phys.* B268: (1986) 693.

[108] Ilgenfritz, E.-M., C. Menz, M. Muller-Preussker, A. Schiller, and A. Sternbeck. "SU(3) Landau gauge gluon and ghost propagators using the logarithmic lattice gluon field definition." *Phys. Rev.* D83: (2011) 054,506.

[109] Inami, T., and C. Lim. "Effects of Superheavy Quarks and Leptons in Low-Energy Weak Processes k(L) mu anti-mu, K+ pi+ Neutrino anti-neutrino and K0 anti-K0." *Prog.Theor.Phys.* 65: (1981) 297.

[110] Itzykson, C., and J. Zuber. *Quantum Field Theory.* Dover books on physics. Dover Publications, Incorporated, 2012.

[111] Kaplan, D. B. "A Method for simulating chiral fermions on the lattice." *Phys.Lett.* B288: (1992) 342–347.

[112] Kobayashi, M., and T. Maskawa. "CP Violation in the Renormalizable Theory of Weak Interaction." *Prog.Theor.Phys.* 49: (1973) 652–657.

[113] Landau, D., and K. Binder. *A Guide To Monte Carlo Simulations In Statistical Physics.* Cambridge University Press, 2005. `http://books.google.co.uk/books?id=HbxQxS7tHiYC`.

[114] Leinweber, D. B., J. I. Skullerud, A. G. Williams, and C. Parrinello. "Gluon propagator in the infrared region." *Phys.Rev.* D58: (1998) 031,501.

[115] Leinweber, D. B., J. I. Skullerud, and C. Williams, Anthony G.and Parrinello. "Asymptotic scaling and infrared behavior of the gluon propagator." *Phys. Rev. D* 60, 9: (1999) 094,507.

[116] Liang, Y., K.-F. Liu, B.-A. Li, S. Dong, and K. Ishikawa. "Lattice calculation of glueball matrix elements." *Phys.Lett.* B307: (1993) 375–382.

[117] Lin, M., and E. E. Scholz. "Chiral limit and light quark masses in 2+1 flavor domain wall QCD." *PoS* LAT2007: (2007) 120.

[118] Luscher, M. "Topology of Lattice Gauge Fields." *Commun.Math.Phys.* 85: (1982) 39.

[119] ———. "Properties and uses of the Wilson flow in lattice QCD." *JHEP* 1008: (2010) 071.

[120] ———. "Trivializing maps, the Wilson flow and the HMC algorithm." *Commun.Math.Phys.* 293: (2010) 899–919.

[121] Luscher, M., R. Narayanan, P. Weisz, and U. Wolff. "The Schrodinger functional: A Renormalizable probe for nonAbelian gauge theories." *Nucl.Phys.* B384: (1992) 168–228.

[122] Maltman, K., D. Leinweber, P. Moran, and A. Sternbeck. "The Realistic Lattice Determination of alpha(s)(M(Z)) Revisited." *Phys.Rev.* D78: (2008) 114,504.

[123] Mandula, J., and M. Ogilvie. "The gluon is massive: A lattice calculation of the gluon propagator in the Landau gauge." *Physics Letters B* 185, 12: (1987) 127 – 132. `http://www.sciencedirect.com/science/article/pii/0370269387915413`.

[124] Martinelli, G., C. Pittori, C. T. Sachrajda, M. Testa, and A. Vladikas. "A General method for nonperturbative renormalization of lattice operators." *Nucl.Phys.* B445: (1995) 81–108.

[125] McNeile, C., C. Davies, E. Follana, K. Hornbostel, and G. Lepage. "High-Precision c and b Masses, and QCD Coupling from Current-Current Correlators in Lattice and Continuum QCD." *Phys.Rev.* D82: (2010) 034,512.

[126] McNeile, C. "Strong coupling and quark masses from lattice QCD." .

[127] Montvay, I., and G. Münster. *Quantum Fields on a Lattice.* Cambridge Monographs on Mathematical Physics. Cambridge University Press, 1997. `http://books.google.co.uk/books?id=NHZshmEBXhcC`.

[128] Moran, P. J., and D. B. Leinweber. "Over-improved stout-link smearing." *Phys.Rev.* D77: (2008) 094,501.

[129] Morningstar, C., and M. Peardon. "Analytic smearing of $SU(3)$ link variables in lattice QCD." *Phys. Rev. D* 69, 5: (2004) 054,501.

[130] Nakagawa, Y., A. Voigt, E.-M. Ilgenfritz, M. Muller-Preussker, A. Nakamura, et al. "Coulomb-gauge ghost and gluon propagators in SU(3) lattice Yang-Mills theory." *Phys.Rev.* D79: (2009) 114,504.

[131] Narayanan, R., and H. Neuberger. "A Construction of lattice chiral gauge theories." *Nucl.Phys.* B443: (1995) 305–385.

[132] Okamoto, M., et al. "Equation of state for pure SU(3) gauge theory with renormalization group improved action." *Phys.Rev.* D60: (1999) 094,510.

[133] Oliveira, O., and P. Silva. "Does The Lattice Zero Momentum Gluon Propagator for Pure Gauge SU(3) Yang-Mills Theory Vanish in the Infinite Volume Limit?" *Phys.Rev.* D79: (2009) 031,501.

[134] Parrinello, C. "Exploratory study of the three-gluon vertex on the lattice." *Phys. Rev. D* 50, 7: (1994) R4247–R4251.

[135] Peskin, M. E., and T. Takeuchi. "Estimation of oblique electroweak corrections." *Phys.Rev.* D46: (1992) 381–409.

[136] Pich, A. "Review of alphas determinations." *PoS* ConfinementX: (2012) 022.

[137] Politzer, H. D. "Reliable Perturbative Results for Strong Interactions?" *Phys.Rev.Lett.* 30: (1973) 1346–1349.

[138] Press, W. H., S. A. Teukolsky, W. T. Vetterling, and B. P. Flannery. *Numerical recipes in C (2nd ed.): the art of scientific computing.* New York, NY, USA: Cambridge University Press, 1992.

[139] Rinaldi, E. personal communication, 2013.

[140] van Ritbergen, T., J. Vermaseren, and S. Larin. "The Four loop beta function in quantum chromodynamics." *Phys.Lett.* B400: (1997) 379–384.

[141] Sachrajda, C., and G. Villadoro. "Twisted boundary conditions in lattice simulations." *Phys.Lett.* B609: (2005) 73–85.

[142] Schmidt, B., and M. Steinhauser. "CRunDec: a C++ package for running and decoupling of the strong coupling and quark masses." *Comput.Phys.Commun.* 183: (2012) 1845–1848.

[143] Shintani, E., S. Aoki, H. Fukaya, S. Hashimoto, T. Kaneko, et al. "Strong coupling constant from vacuum polarization functions in three-flavor lattice QCD with dynamical overlap fermions." *Phys.Rev.* D82: (2010) 074,505.

[144] Silva, P., and O. Oliveira. "Gribov copies, lattice QCD and the gluon propagator." *Nucl.Phys.* B690: (2004) 177–198.

[145] Skullerud, J., and A. Kizilersu. "Quark gluon vertex from lattice QCD." *JHEP* 0209: (2002) 013.

[146] Skullerud, J. I., P. O. Bowman, A. Kizilersu, D. B. Leinweber, and A. G. Williams. "Nonperturbative structure of the quark gluon vertex." *JHEP* 0304: (2003) 047.

[147] Sommer, R. "A New way to set the energy scale in lattice gauge theories and its applications to the static force and alpha-s in SU(2) Yang-Mills theory." *Nucl.Phys.* B411: (1994) 839–854.

[148] Sternbeck, A., E.-M. Ilgenfritz, M. Muller-Preussker, and A. Schiller. "Towards the infrared limit in SU(3) Landau gauge lattice gluodynamics." *Phys.Rev.* D72: (2005) 014,507.

[149] Sternbeck, A., and M. Mller-Preussker. "Another look at the Landau-gauge gluon and ghost propagators at low momentum." *PoS ConfinementX* PoS: (Confinement X) 074, 2013.

[150] Sturm, C., Y. Aoki, N. Christ, T. Izubuchi, C. Sachrajda, et al. "Renormalization of quark bilinear operators in a momentum-subtraction scheme with a nonexceptional subtraction point." *Phys.Rev.* D80: (2009) 014,501.

[151] Suman, H., and K. Schilling. "A Comparative study of gauge fixing procedures on the connection machines CM2 and CM5." .

[152] Takaishi, T. "Heavy quark potential and effective actions on blocked configurations." *Phys.Rev.* D54: (1996) 1050–1053.

[153] Viète, F., and F. van Schooten. *Francisci Vietae Opera mathematica in vnum volumen congesta ac recognita, Opera atque studio Francisci aSchooten ...* Diapositivas (Biblioteca Histórica UCM). ex Officina Bonaventurae & Abrahami Elzeviriorum, 1646.

[154] Vink, J. C., and U.-J. Wiese. "Gauge fixing on the lattice without ambiguity." *Phys.Lett.* B289: (1992) 122–126.

[155] Wennekers, J. "Neutral Kaon Mixing Beyond the Standard Model from 2+1 Flavour Domain Wall QCD." *PoS* LATTICE2008: (2008) 269.

[156] Wilson, K. G. "Confinement of Quarks." *Phys.Rev.* D10: (1974) 2445–2459.

[157] Wilson, K., and J. B. Kogut. "The Renormalization group and the epsilon expansion." *Phys.Rept.* 12: (1974) 75–200.

[158] Wolfenstein, L. "Parametrization of the Kobayashi-Maskawa Matrix." *Phys. Rev. Lett.* 51: (1983) 1945–1947. http://link.aps.org/doi/10.1103/PhysRevLett.51.1945.

[159] Zanotti, J., S. O. Bilson-Thompson, F. Bonnet, P. Coddington, D. Leinweber, et al. "Novel fat link fermion actions." *Nucl.Phys.Proc.Suppl.* 109A: (2002) 101–105.

[160] Zhestkov, Y. "Domain wall fermion study of scaling in nonperturbative renormalization of quark bilinears and B(K)." .